Development of novel sensing solutions for coating wear measurement

Nan Xu

Submitted in accordance with the requirements for the degree of

Doctor of Philosophy

The University of Leeds

School of Mechanical Engineering

March 2022

The candidate confirms that the work submitted is his own, except where work which has formed part of jointly authored publications has been included. The contribution of the candidate and the other authors to the work has been explicitly indicated below. The candidate confirms that appropriate credit has been given within the thesis where reference has been made to the work of others.

The work in Chapter 5 and 6 of the thesis has been accepted in publication as follows:
Nan Xu, Chun Wang, Liuquan Yang, Eric Kumi Barimah, Gin Jose, Anne Neville, and Ardian Morina, Nano-scale coating wear measurement by introducing Raman-sensing underlayer, Journal of Materials Science & Technology, 2022, 96, 285–294.
Candidate's contribution - conceptualization, methodology, all experimental work, preparing samples for and performing all the tests and analysis in this work, writing the manuscript, and producing all figures and tables therein. Chun Wang - assisted with data collection of Raman tests and commented on the manuscript. Liuquan Yang - assisted with coating deposition and commented on the manuscript. Eric Kumi Barimah, Gin Jose, and Anne Neville - all provided comments on the manuscript. Ardian Morina - initial concept, supervision, methodology, and provided extensive manuscript review.

The work in Chapter 7 of the thesis has been accepted for publication as follows:
Nan Xu, Chun Wang, Liuquan Yang, Gin Jose, and Ardian Morina, Probing the Tribochemical Impact on Wear Rate Dynamics of Hydrogenated Amorphous Carbon via Raman-Based Profilometry. ACS Appl. Mater. Interfaces 2022, 14 (1), 2071–2081.
Candidate's contribution - conceptualization, methodology, all experimental work, preparing samples for and performing all the tests and analysis in this work, writing the

manuscript, and producing all figures and tables therein. Chun Wang - assisted with data collection of Raman tests and commented on the manuscript. Liuquan Yang - assisted with coating deposition and commented on the manuscript. Gin Jose - provided comments on the manuscript. Ardian Morina - initial concept, supervision, methodology, and provided extensive manuscript review.

Acknowledgments

I would like to express my deepest appreciation and gratitude to my supervisors Professor Ardian Morina, Professor Anne Neville, and Professor Gin Jose for their support, guidance and encouragement all through the project. Many thanks to Dr. Liuquan Yang, Dr. Chun Wang, and Dr Eric Kumi Barimah for their expertise and technical support. I am indebted to Dr. Ivan Kolev of IHI Hauzer Techno Coating B.V. for coating techniques.

I would like to thank the helpful assistance for FIB, SEM, and TEM tests by Mr. John Harrington, Mrs. Zebeada Aslam, and Mr. Stuart Micklethwaite from Leeds Electron Microscopy and Spectroscopy Centre (LEMAS), University of Leeds. Special thanks to my colleagues and friends of Institute of Functional Surface (IFS), in particular, Guizhi, Kris, Gerda, Frank, Sam, Yajing, Ryan, Paul, Jordan for their help and encouraging talks.

To my family, and in particular my wife Ningning – thanks for your endless support during PhD study, and without your support, it would not have been possible for me to finish this thesis in time. Also, my son Zhongchi - thanks for bringing so much happiness for me. Finally, to parents and relatives – thanks for giving support, care, and encouragement. After all the ups, downs, and sleepless nights of the last few years, I hope I've managed to do it justice.

Abstract

Wear of coatings, particularly on key components, critically affects the service life and reliability of systems/devices. To gain key and necessary information of wear condition and failure prediction, it is necessary to develop accurate and reliable coating wear measurement techniques, particularly at the nanoscale level and with in-situ monitoring potential. In this study, a high-sensitively in-situ Raman-based profilometry has been developed to achieve accurate coating thickness quantification. This developed method is based on a bilayer coating system: a top target layer of hydrogenated amorphous carbon film as light attenuating and anti-wear layer, and an underlayer of silicon as Raman-sensing layer. Through constructing the relationship between the thickness of a-C:H and Raman intensity of attenuated silicon signal, the coating thickness quantification method was established and successfully applied to quantify coating wear in the friction process.

This approach can effectively avoid remarkable deviations caused by tribo-induced effects in the interface regions, demonstrating its advantage in error tolerance. Details about these tribo-induced effects were also elucidated by a combination of Raman spectroscopy, optical profilometer, EELS, and TEM. In particular, the proposed approach enables measuring coating wear with oil film on top, which breaks an important limitation of existing wear measurement methods, i.e., incapable of applying in oil-lubricated conditions.

In addition, this approach was applied to detect tribofilms derived from lubricant additive and explore their influence on coating wear behaviour. It was suggested that tribochemical

products with distinct optical properties were formed in different wear-stages and resulted in extra attenuated intensities of Raman signals from silicon under-layer, in the form of measurement deviations of wear depth. By monitoring deviation variation, critical information of tribofilm compositions could be obtained, helping to understand the coating wear mechanisms under oil-lubricated conditions. The detailed structure and composition analysis of tribofilms were also performed by a combination of TEM, FIB and FFT.

After demonstrating the reliability and accuracy of Raman-based profilometry, a wear-sensing coating system, composed of a-C:H and crystalline silicon coatings, was successfully deposited on steel substrates. Then, Raman-based profilometry was employed to measure the wear depth values across the wear track. Compared with the results deriving from the optical profilometer, the Raman-based method could provide accurate wear depth values based on the wear-sensing coating system. As this wear-sensing coating system could be deposited on the substrate with various materials and shapes, it has the potential to open a new pathway for realizing in-situ and real-time wear measurement in diverse engineering applications.

Contents

List of Figures

List of Tables

Abbreviations

a	Hertzian contact circle radius (m)
A	Real contact area
AFM	Atomic Force Microscope
BE	Binding Energy (eV)
DLC	Diamond Like Carbon
E	Young's Modulus (Pa)
EDX	Energy Dispersive X-ray
F	Friction force (N)
h	Height of the sphere of pin worn after the wear test (m)
h_{min}	Minimum film thickness (m)
H	Hardness (Pa)
k	Dimensional wear coefficient ($m^3N^{-1}m^{-1)}$
L	Phase transition energy (Jkg^{-1})
MoDTC	Molybdenum Dithiocarbamate
p	Pressure (Pa)
p_o	Maximum Hertzian Pressure (pa)
p_m	Mean Hertzian Pressure (Pa)
PVD	Physical Vapor Deposition
PECVD	Plasma Enhanced Chemical Vapor Deposition
r	Radius of the wear scar (m)
R	Radius of Curvature (m)
R_q	Root Mean Square Roughness
T	Operating Temperature (°C)
U	Entrainment speed (ms^{-1})
V	Velocity (ms^{-1})
V_L	Loss of material (m^3)
W	Normal load (N)
XPS	X-ray Photoelectron Spectroscopy
ZDDP	Zinc dialkyldithiophosphate
ν	Specific volume (m^3kg^{-1})
α_p	Viscosity-pressure coefficient (Pa^{-1})
η_o	Viscosity of oil at ambient pressure (Pa-s)
γ	Poisson ratio
λ	Lambda ratio
μ	Friction coefficient
σ	Normal stress (Pa)
τ	Shear stress (Pa)
PAO	Polyalphaolefins
BL	Boundary Lubrication
ML	Mixed Lubrication
EHL	Elastohydrodynamic Lubrication
HL	Hydrodynamic Lubrication
a-C:H	hydrogenated amorphous carbon
CVD	Chemical Vapor Deposition
RF	Radio Frequency

SEM	Scanning Electron Microscopy
TEM	Transmission Electron Microscopy
FIB	Focused Ion Beam
WLI	White Light Interferometer
a-C	Amorphous carbon
ta-C	Tetrahedral amorphous carbon

Chapter 1

Introduction

1.1. Background and motivation

1.1.1. Automation manufacturing in Industry 4.0

In Industry 4.0, machines in smart factories are getting highly networked. The main challenge for cooperating in a more robust and autonomous way is minimizing the downtime caused by unpredicted failure [1-4]. In view of this fact, the maintenance strategies in modern manufacturing industries are transforming from traditional reactive practices to predictive and preventive methodologies, which has driven numerous efforts to develop reliable techniques for wear monitoring [3,5] due to its increasing critical role in the maintenance strategies. Reactive maintenance describes the repairing strategy only after the components has broken down or been run to the point of failure. Preventive maintenance consists of maintenance tasks performed while the equipment is under normal operation to avoid unexpected breakdowns and the associated downtime and costs. Predictive maintenance connects the working condition of components to the computerized maintenance management system through sensor data, directly monitoring the performance during normal operation to anticipate and predict failures.

The main aim of wear monitoring is to detect the wear evolution rather than just recognize severe wear or breakage [6,7]. Through continuously monitoring, the wear stage (e.g.,

running-in, steady state and severe wear) can be determined, which is crucial to predicting the service life and failure. To date, most approaches for wear monitoring estimate the wear condition based on the operation signals which are indirectly correlated to wear [3-9]. As these approaches monitor wear conditions without machine interruption, they have been widely adopted in the online monitoring system. However, their inherent drawbacks, deriving from signal noise and lack of direct or visual wear information, always lead to the inevitable reduction in the measurement reliability and accuracy [2,6,9]. In addition, since these methods are incapable of direct application in a distinct process condition (e.g., material variation, different working conditions), model retraining for a new working condition become necessary, which requires extensive tests to obtain various operation parameters for estimating the wear level [4,5,7]. Therefore, it is necessary to develop novel wear monitoring approaches capable of providing more accurate and direct wear information under various working conditions.

1.1.2. Novel lubrication strategies

As a promising way for energy savings and emission control, combination of solid and liquid lubricants in the tribological systems have attracted considerable research attentions in diverse engineering fields, including lightweight design, manufacturing, aeronautics, marine equipment, automobiles [10-15]. This approach can effectively integrate the advantages of solid and liquid lubricants while minimizing their individual drawbacks through interaction [10]. To meet the requirements of increasingly demanding lubricating conditions in the future, it is therefore necessary to develop novel solid-liquid composite lubricating systems. Considering most of the existing liquid lubricants are tailored for ferrous-base surfaces [13], in-depth studies of the interaction between non-ferrous surfaces

and liquid lubricants are therefore essential for developing high-performance lubricating systems and understanding further mechanisms.

To date, the majority of experimental studies on friction and wear mechanisms of boundary lubricated systems are mainly based on understanding the tribofilm nature (e.g. chemical composition, structure, and mechanical properties) and their tribochemical interaction with contact surfaces [16-18]. To reveal the impact of tribochemical products, various surface analytical techniques have been applied to identify the composition and microstructure of additive-derived tribofilms formed on coating surfaces [13, 19-21]. Although a significant progress has been achieved in understanding the chemical nature of tribofilms, the friction and wear mechanisms are still not fully understood. The main reason is the difficulty in continuously or periodically obtaining the tribofilm composition during the friction process. It is well-known that friction process is always accompanied with the formation and evolution of tribochemical products. In different stages, there exists specific tribochemical products dominating the tribological behavior. It is therefore of great importance to verify the tribofilm composition in the correlated stage. However, this remains a significant challenge for conventional surface analytical approaches due to their limitations in accessing the tribofilms in friction process or low signal intensities of thin tribofilms with nanometers thickness [16].

1.2. Aims and Objectives

Inspired by the coating system with built-in wear sensing layer as reported in the previous studies [22, 23], this project aims to develop a multilayer coating system with the potential of in-situ and real-time wear detection by introducing a Raman sensing layer. By monitoring the Raman signal during the friction process, this system is expected to report

the wear depth and failure warning. In addition, wear detection can also provide valuable insight on the wear mechanisms of coatings under oil-lubricated condition, which can lead to the development of effective solid-liquid lubricating systems.

The main objectives of this study are summarized in the following:

1: To build coating wear quantification method based on Raman signal.

2: To investigate the formation mechanisms of additive-derived tribofilm based Raman-based method.

3: To study the friction and wear mechanisms of coatings under oil-lubricated condition based on the tribofilm formation mechanism.

4: To develop Raman sensing layer with strong Raman signal.

5: To construct coating systems on metallic substrates and conduct wear measurement based on this coating systems.

1.3. Thesis Outline

This thesis is divided into eleven chapters including introduction. Chapter 2 presents basic theories in tribology and coating deposition techniques. The literature review of wear monitoring techniques and tribochemical interaction between DLC coating and additives is presented in Chapter 3. The detailed information of tribotest, coating deposition methods, and characterization and analysis techniques used in this project are listed in Chapter 4. The coating thickness quantification method based on Raman signal is constructed in Chapter 5, which is then used to measure the wear of a-C:H coatings under dry and oil-lubricated conditions in Chapter 6. In Chapter 7 and 8, this Raman-based method is employed to explore the formation mechanisms of additive-derived tribofilm on coating surface and their influence on final wear and friction behaviors. In Chapter 9, Raman sensing layer of

crystalline silicon is developed by pulsed-DC magnetron sputtering and used in constructing wear-sensing coating system for realizing wear measurement based on Raman-based method. Discussions on key findings are presented in Chapter 10. Main conclusions from this study and recommendations for future work are presented in Chapter 11.

Chapter 2

Basic Theories of Tribology, Lubrication, Coating Deposition

2.1. Tribology

The definition of tribology is "the science and technology of two interacting surfaces in relative motion and of related subjects and practices" [24, 25], which includes the research and application of the fundamentals in the fields of friction, wear and lubrication. It is an interdiscipline, involving mechanical engineering, materials science, physics, chemistry, mathematics, and biology. Classical tribology mainly covers the applications in mechanical engineering, like ball bearings, gear drives, clutches, brakes, etc. But it has been expanded to some important applications in the last decades, particularly the micro- and nanotechnology as well as biology and medicine. The word "*tribology*" derives from the Greek roots of "*tribo*" and "*logia*", which mean "*rubbing or sliding*" and "*study of or knowledge of*", respectively. Peter Jost first used the word "*tribology*" in the Jost Report in 1966, which highlights the huge cost to the UK economy related to friction, wear and corrosion. It was estimated over £500 million annually could be saved for the UK industry through gaining deep insights into the tribological behaviors in diverse engineering fields and improving the corresponding lubricating strategies [26-30].

Intensive research attention has been attracted in tribology since Jost Report for achieving energy saving and emission control. Recently, considerable attempt was made to quantify

the impact of wear and friction worldwide in the main sectors of energy consumption, including manufacturing, power generation, transport, and residential.

- In total, around 23 percent of energy consumption in the world derives from tribological contacts. 20 percent of that figure is to overcome friction and the other 3 percent for remanufacturing or replacing components and standby equipment due to wear and wear-related causes.
- Through employing the effective strategies for reducing friction and wear in the mechanical components, energy consumption caused by friction and wear in vehicles and machine equipment worldwide can be reduced by 40 percent in the long term and 18 percent in the short term. The potential savings would amount to 1.4 percent of global GDP and 8.7 percent of total energy consumption annually in the long term.
- The largest potential of energy savings in the short term is expected in the fields of transport (25 %) and power generation (20 %) while that of manufacturing and residential sectors are estimated to be around 10 %. In the long term, potential savings are estimated at 55%, 40%, 25%, and 20%, respectively.
- It was estimated the global emission of carbon dioxide could be reduced by as much as 1,460 million tons of carbon dioxide equivalent (MtCO2) by employing advanced tribological strategies, leading to cost saving of 450,000 million Euros in the short term. In the long term, it is expected that the reduction of emission could be 3,140 MtCO2 and the cost savings could be up to 970,000 million Euros.

2.2. Friction

Friction is the force that resists the relative movement between the friction pairs [30]. In general, friction is represented as the friction coefficient which is denoted as μ. The friction

coefficient can be calculated according to the ratio of F_M/F_N, where F_M is the frictional force between the contact surfaces and F_N is applied load. The desirable friction coefficient depends on the application conditions. For example, high friction is desirable for braking system while low friction is the basic requirement for most lubricated mechanical components, like gears and bearings. Depending on lubricating condition, friction can be clarified into dry friction, fluid friction and mixed friction. Reducing the friction is one of critical functions of lubrication. Uncontrollable friction can lead to severe wear and catastrophic failure of equipment. Meanwhile, friction has a high correlation with the type of the relative movement (e.g., sliding and rolling). Table 2.1 shows the friction coefficient under different lubricating conditions and types of relative movements [31].

Table 2.1 Friction coefficient under different conditions.

Friction regime	Friction coefficient (μ)	Wear
Dry friction (sliding)	0.300	High
Dry friction (rolling)	0.005	Very Low
Mixed friction (rolling)	0.005-0.300	Noticeable
Fluid friction	0.005-0.100	Practically zero

2.3. Lubrication

Lubrication can be interpreted as a process or technique that employs lubricants to separate the contact surfaces for reducing wear and energy consumption deriving from friction [32]. Effective lubrication can reduce the downtime and improve the operation efficiency of equipment, while lubrication failure will result in destructive damage on mechanical components and the significantly reduced machine life. In general, lubricants can be clarified into five groups, including liquid (e.g., mineral oil, synthetic oil and vegetable oil),

semi-solid (e.g., lubricating grease), solid (e.g., coatings), gas (e.g., air) and supercritical fluid (e.g., supercritical carbon dioxide).

2.3.1. Lubrication regimes

Based on the film thickness ratio λ and friction coefficient, a Stribeck curve is established as shown in Figure 2.1. According to the λ, the lubrication regimes can be classified into four types, including hydrodynamic, elastohydrodynamic, mixed, and boundary lubrications [33]. Here, the film thickness ratio can be calculated via the following equation:

$$\lambda = \frac{h_{\min}}{\sqrt{R_{q1}^2 + R_{q2}^2}} \qquad 2\text{-}1$$

where R_{q1} and R_{q2} are the surface roughness values of two contact surfaces and h_{min} is the minimum thickness of lubricant films which can be obtained by the following equation [34]:

$$h_{\min} = 3.63 \times R \times U_{\Sigma}^{0.68} \times G_{\Sigma}^{0.49} \times W_{\Sigma}^{-0.073}(1 - e^{-0.68k_e}) \qquad 2\text{-}2$$

where $U_{\Sigma} = \frac{\eta_0 U}{E^* R}$, $G_{\Sigma} = \alpha_p E^*$, $W_{\Sigma} = \frac{W}{E^* R^2}$, U is the entraining surface velocity (m/s), R is the reduced curvature radius (m), α_p is the viscosity-pressure coefficient (m^2/N), W is the contact load (N), η_o is the dynamic viscosity of the lubricant at atmospheric pressure (Pa•s), E^* is the reduced Young's modulus and k_e is the elliptical parameter. For the contact condition of ball on disc, k_e = 1.0339.

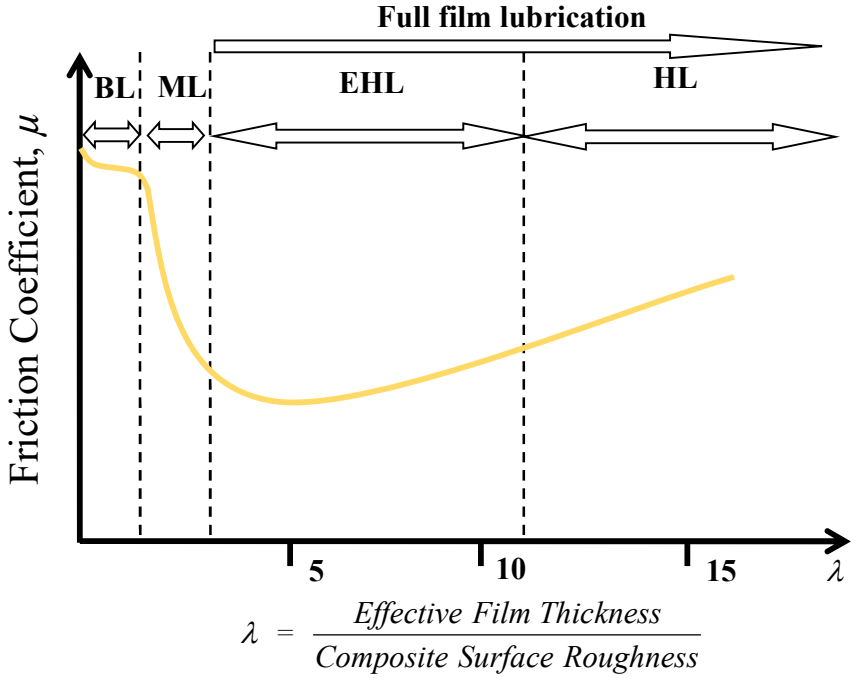

BL = Boundary Lubrication, ML = Mixed Lubrication,
EHL = Elastohydrodynamic Lubrication, HL = Hydrodynamic Lubrication

Figure 2.1. Modified Stribeck curve and the lubrication regimes [33].

As displayed in Figure 2.2a, when $\lambda > 10$, the contact surfaces are separated completely by lubricant films under hydrodynamic lubrication. There is no wear under this lubrication and the friction mainly depends on the viscosity of lubricating oil.

Figure 2.2b. displays the elastohydrodynamic lubrication (EHL, $4 < \lambda < 10$). Although the contact surfaces are also separated by lubricant films, the thickness of films is much thinner (0.5 – 5 μm) than that under hydrodynamic lubrication due to high local contact pressure. It can result in the remarkable elastic deformation of contact surfaces, further affecting the distribution of lubricant film. The flow features of lubricants still dominate the final tribological performances.

With decreasing the speed or increasing the load, the lubrication regime will transform from EHL to mixed lubrication with $1 < \lambda < 4$. As displayed in Figure 2.1, it an

intermediary condition between hydrodynamic and boundary lubrication. Under mixed lubrication, the potential of asperity contacts increases with the decrease of the thickness of lubricant films. The influence of surface roughness on the tribological performance become obvious while the flow features of lubricant have a weaker effect compared that under EHL. The shear forces on the asperity contacts can lead to the formation of tribochemical films which also play a critical role in the final tribological performances.

Under boundary lubrication, the λ is below 1. The thickness of lubricating film is less that the surface roughness, leading to large number of asperity contacts. The high local pressure happened on the top of asperities can result in plastic deformation and the formation of new contact surfaces by triggering tribochemical reaction between lubricants and the surface materials. The friction and wear performances mainly depend on the tribochemical films formed under shear forces. In general, boundary lubrication prefers to happen under high load, low speed, and high temperature conditions.

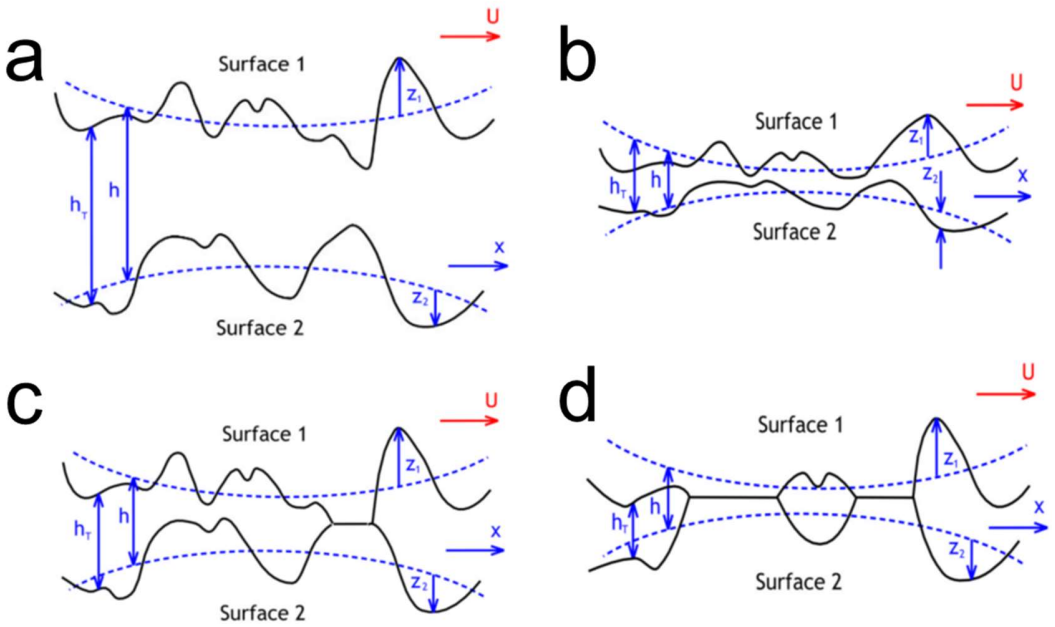

Figure 2.2. (a) Hydrodynamic lubrication. (b) Elastohydrodynamic lubrication. (c) Mixed lubrication. (d) Boundary lubrication. [35]

2.3.2. Lubricating oil

Lubricating oil are used between contact surfaces to reduce friction and wear. It is composed of base oil and diverse additives. There are different types of base oils, including mineral oil, synthetic oil and vegetable oil [31]. They can be grouped into five groups as shown in Table 2.2. The physical and chemical properties of lubricating oil can affect the effectiveness of additives in lubricating oil. The formulation of lubricating oil should be designed according to the requirement of application conditions.

Table 2.2. Base oil categories [31].

Base oil	Description	Sulphur (%)	Saturates (%)	Viscosity index
Group-I	Solvent refined oil	> 0.03	⩽ 90	80 -120
Group-II	Mineral oils	< 0.03	⩾ 90	80 - 120
Group-III	Mineral oils	< 0.03	⩾ 90	> 120
Group-IV	All polyalfaolefins (PAOs)			
Group-V	All base oil not in Group-I-IV			

To meet the requirements of diverse working conditions, different types of lubricating additives were developed to improve the properties of lubricating oils, like friction modifier, antiwear additive, corrosion inhibitor, oxidation inhibitor and so on. Figure 2.3 displays the development process of the most common lubricating additives.

2.3.2.1. Antiwear and extreme pressure additives

Antiwear and extreme pressure additives are employed to reduce friction and prevent severe wear under boundary or mixed lubrication [31]. In general, the extreme pressure additive contains active elements like sulphur and/or phosphorus, which could react with the surface materials to form a protective layer. In addition, antiwear additive with polar

head and long molecular chains (e.g., fatty oils, acids, esters) could form an absorbed layer to protect the contact surfaces. ZDDP (Zinc dialkyldithiophosphates) is one of the most crucial anti-wear/extreme pressure additives [36]. The shear forces under boundary lubrication can result in the tribochemical reactions between ZDDP and ferrous surface. ZDDP can form surface-bonded pad-like tribofilms of a gradient structure with a short-chain glassy phosphate near the ferrous surface and a thin outer layer of long-chain polyphosphates.

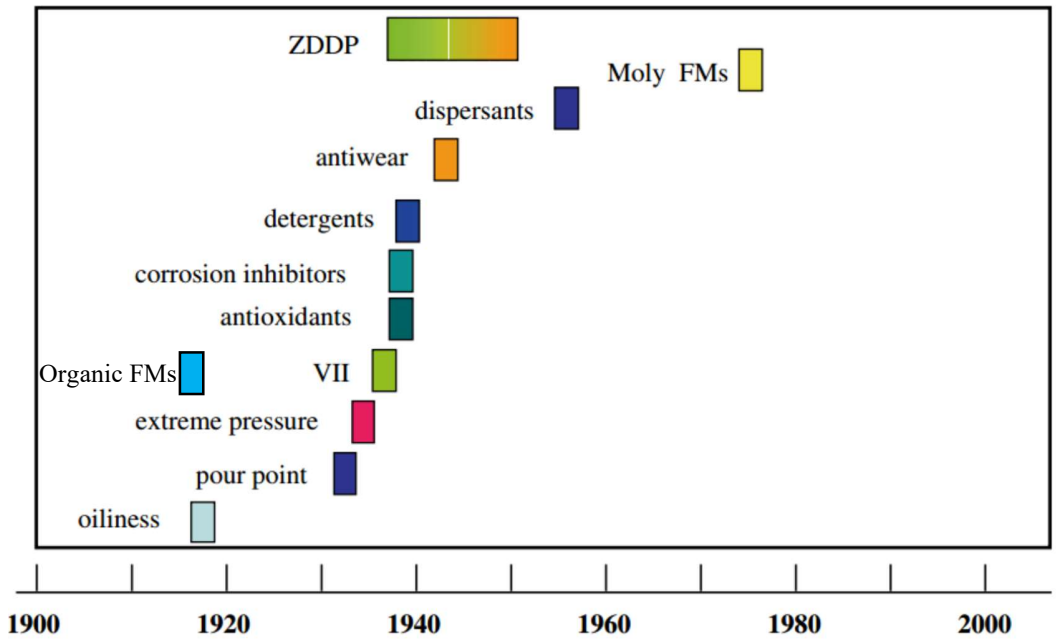

Figure 2.3. Chronology of the development of the most common additives. Modified from [36].

2.3.2.2. Friction modifiers

The main functions of friction modifier are reducing friction and increasing the strength of lubricating films. There are two types of friction modifiers [31, 37]. One take effect through physically absorbing on the contact surface (e.g., fatty acids and amides). The

other one functions via additive-derived products. In the case of MoDTC (molybdenum dialkyldithiocarbamate), they have been widely employed in engine oils as a classic friction modifier (FM) which decomposes into molybdenum disulphide (MoS_2) sheets and molybdenum trioxide (MoO_3) under the action of friction forces. For ferrous-base contact surfaces, its effectiveness in friction-reduction can be attributed to the formation of tribofilms, containing nano-MoS_2 sheets with layer-lattice structure and weak interlaminar shear forces.

2.3.2.3. Oxidation inhibitors

Oxidation inhibitor is used to prevent the oxidation of lubricating oil, especially under high temperature conditions [31, 37]. It can be classified into three types, including hydroperoxide decomposers, free radical scavengers, and metal deactivators. The commonly used oxidation inhibitors are organic sulphur and organic phosphorus compounds, zinc dialkyldithiophosphates (ZDDP), hindered phenols, alkylated arylamines, ethylenediaminetetraacetic acid (EDTA), and salicylaldoxime. In the initial, the oxidation can result in the darkening and thickening of lubricating oil, followed by the formation of polymeric materials in the form of varnish deposits with the increased oxidation degree. The detrimental effect caused by the oxidation will shorten the service life of lubricating oil and the lubricating failure.

2.3.2.4. Viscosity Index Improvers

The main function of viscosity index improver is to increase the viscosity index of lubricating oil by increasing the viscosity at high temperature and decreasing the viscosity at low temperature [31, 37]. In general, the viscosity index improvers are composed of

polymers with high molecular weight, like polyalkylmethacrylates, hydrogenated styrene-diene copolymers and olefin copolymers.

2.3.2.5. Detergents

Detergents can neutralize the acidic products from combustion and lubricant oxidation and increase the solubility of the deposit precursors and contaminants in oil, minimizing the deposit formation on the lubricated parts [31, 37]. Specifically, the base group of detergents help neutralize acids while their soap content makes the polar products suspending in oil. The commonly used detergents are alkali metal or alkaline earth metal salts of organic acids, with or without the base group. The acids could be alkylbenzenesulfonic acids, alkylphenols, and fatty carboxylic acids.

2.5.2.6. Other Additives

In addition to the additives stated above, there exist some other important additives, including dispersants, corrosion inhibitors, emulsifiers, pour point depressants, and antifoaming agents [31, 37]. The main functions of these additives are protecting the contact surface or improve the chemical or physical properties of lubricating oil.

2.4. Wear

Wear is a progressive damage process toward contact surfaces which is accompanied by surface materials loss due to shear forces in the friction process [38]. The deformation and materials loss on the component surface can result in the loss of dimensional precision, further leading to the mismatch of contact surfaces and increased vibration. This can accelerate the surface wear and cause early failure of lubricated components. Therefore, the wear mechanisms are always the hotspots in the tribology and intensive investigations have

been made on developing new ways for decreasing and/or controlling the wear. Currently, the wear mechanism can be classified into five types as following [31, 39]:

- Adhesive wear, as the most common wear form, is recognized as the least preventable, which can result in plastic deformation and even welding on the contact surface. Severe adhesive wear will result in galling or scuffing phenomena, further leading to catastrophic damage to contact surfaces.

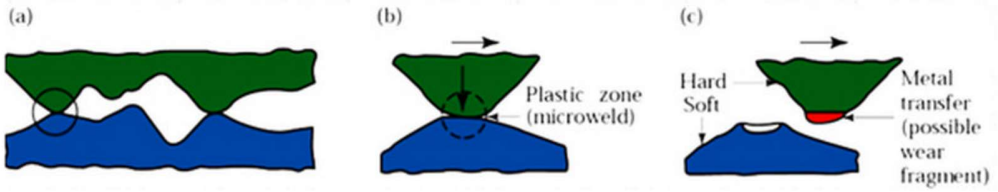

Figure 2.4. Adhesive wear. [40]

- Abrasive wear is the wear phenomena happened on the softer surface, which is caused by the existence of hard particles between contact surfaces or hard contact asperities on the hard surfaces. In general, abrasive wear can derive from micro fatigue, micro-fracture, micro-cutting, and loss of material grains. Meanwhile, abrasive wear can be classified into two body abrasive wear and three body abrasive wear as shown in Figure 2.5

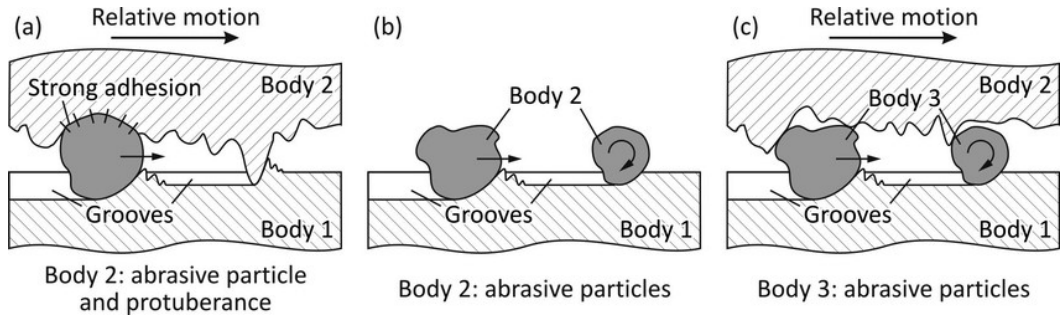

Figure 2.5. Abrasive wear (two body and three body). [41]

- Fatigue wear is caused by repetitive stress over a working time, which can lead to significantly loss of surface materials. Fatigue wear often happens in the application with

cyclic loading, like rolling bearing, gears, cam/follower system and so on. It generally starts with micro-pitting.

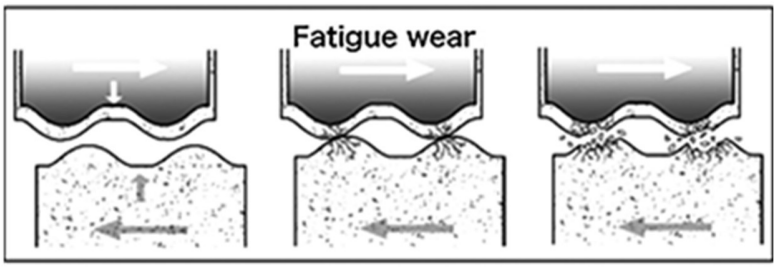

Figure 2.6. Fatigue wear. [42]

- For a typical corrosive wear process, surface corrosion occurs at the initial stage when contaminants present in the lubricants (e.g., acid, water, reactive lubricating additive), which generally decrease the anti-wear property of surface materials (e.g., oxide films). Then the wear process will be accelerated in the form of abrasive wear or adhesive wear under shear forces. Fretting is a typical wear form deriving from the combined action of corrosive, adhesive and abrasive wear.

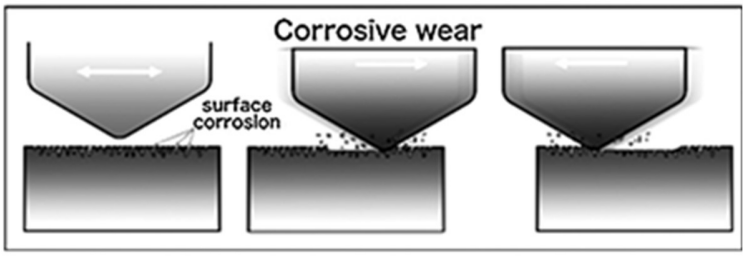

Figure 2.7. Corrosive wear. [42]

- Erosive wear is a degradation process of surface materials caused by the abrasion of high-speed particles which could be solid or liquid. The wear mechanisms largely depend on the physical parameters of particles, including particle size, impact velocity, impact angle and the materials.

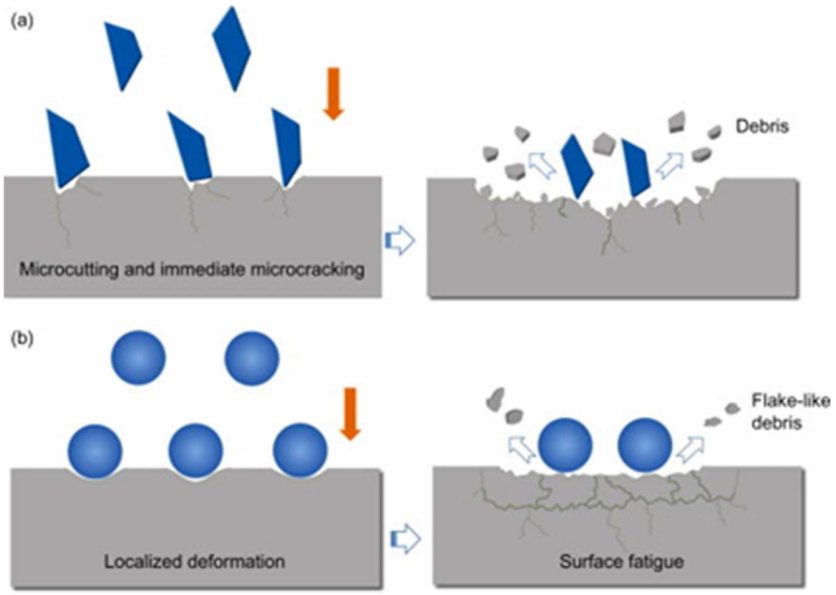

Figure 2.8. Erosive wear. [43]

According to the Archard's law, the volume of worn material removed V as a result of a tribological interaction is directly proportional to the load N and also to the total sliding distance S. However, since less wear is observed when the hardness of the softer member of the tribological couple increases, V can also be regarded as inversely proportional to the hardness H of the material being worn away. In symbols, the above is represented as

$$V = K\frac{SN}{H} \qquad 2\text{-}3$$

Both K and H reveal the material response and thus can be grouped in a single parameter, called the wear rate, $k = V/SN$, which is used to replace the wear coefficient K. The equation can be transformed into:

$$V = kSN \qquad 2\text{-}4$$

The friction force is proportional to applied load and can be expressed:

$$F = \mu N \qquad 2\text{-}5$$

A proportional relationship between wear volume and the friction force can be established as:

$$V \propto FS \qquad 2\text{-}6$$

Based on this equation, the volume of wear is proportional to the energy dissipated by friction and the wear rate can be calculated from the energetic approach [44].

2.5. Tribochemistry

Tribochemistry is defined as the chemical reactions which happen between the lubricant and contact surfaces under the shear stress [45]. The lubricant can degrade into small molecular groups which react with surface materials to form tribofilm to replace the original surface. In addition, tribochemical reactions can result in the mechanical and physico-chemical changes on the contact surfaces. The formation of tribofilm and property changes on the contact surface can affect the wear and friction behaviors.

Two mechanisms were proposed for driving the tribochemical reactions: i, thermally activated reactions occur at the contact asperities with high flash temperature; ii, stress-induced reactions happen on the contact asperities with high local contact pressure.

2.5.1 Thermally activated reactions

In general, the reaction rate of thermally activated reactions depends on the reactant concentration and temperature. It is accepted that flash high temperature on the contact asperities under boundary lubrication can promote the increase of the reaction rate.

The thermally activated reactions can be explained by the activated complex theory, which can be expressed by the following equation. According to this theory, the product C can be

synthesized via a reaction where an activated complex [AB]‡ of the reactants A and B is formed.

$$A + B \rightleftharpoons [AB]^{\ddagger} \rightarrow C \qquad 2\text{-}7$$

The formation rate of C is given by:

$$\frac{d[C]}{dt} = r = k_{thermo}[A][B] \qquad 2\text{-}8$$

Where [A] and [B] are the concentrations of A and B. k_{thermo} is the reaction constant and is given by:

$$k_{thermo} = \zeta \frac{k_B T}{h} e^{\frac{\Delta S^{\ddagger}}{R}} e^{\frac{-\Delta H^{\ddagger}}{RT}} \qquad 2\text{-}9$$

Where ζ is the transmission coefficient, $\Delta H^{\ddagger}$ is the activation enthalpy, $\Delta S^{\ddagger}$ is the activation entropy, h is the Planck constant, k_B is the Boltzmann constant, T is the absolute temperature, and R is the gas constant.

2.5.2 Stress-induced reactions

Stress-induced reactions can happen under low temperature due to the decreased activation energy under shear stress [45, 46]. Several models were proposed to calculate the reaction rates dominated by stress activation. According to the modified Arrhenius equation, the degradation rate of the additives under shear stress can be obtained by the following equation:

$$k_{tribo} = \mathrm{A}_o \, exp^{\frac{\sigma V - E_a}{k_B T}} \qquad 2\text{-}10$$

Where A_o is the pre-exponential factor, V is the material constant, σ is the shear stress, k_B is the Boltzmann constant, E_a is the activation energy, and T the temperature.

2.6. Coating deposition techniques

2.6.1 Physical vapour deposition (PVD)

PVD is a thin film deposition process which is used to deposit diverse coatings (e.g., metals, alloys and ceramics) with thickness ranging from nanometers to several micrometres [47]. In the deposition process, the target materials transform from a condensed phase to a vapor phase and then back to a condensed phase in the form of coatings on substrate. The most common PVD techniques are sputtering and evaporation.

In a sputtering process, the sputtered atoms will be ejected from the target by the bombardment of high energy ions (e.g., Ar^+) and fly in straight lines to impact on the substrate under high vacuum condition. DC magnetron sputtering is one typical sputtering method. Magnetrons, which are placed behind the cathodes, are employed to provide strong electric and magnetic fields to confine the plasma gas (e.g., Ar^+) near the target surface. The high electric field between target (cathode) and the substrate (anode) can cause the ionization of the gas atoms (e.g., Ar to Ar^+) and the occurrence of sputtering process.

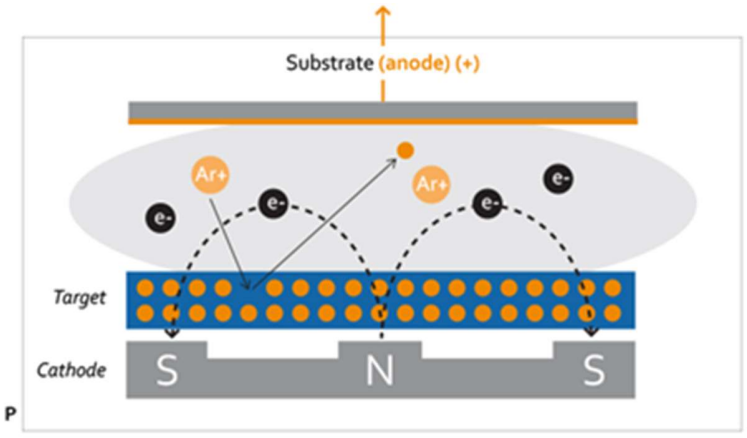

Figure 2.9. Magnetron sputtering deposition.

Evaporation deposition includes two basic processes: i, the target materials are evaporated by the energy source (e.g., electron-beam, filament); ii, evaporated atoms condense on the substrate. This deposition method needs a high vacuum condition to prevent collisions and reactions of evaporated atoms with residual gas molecules.

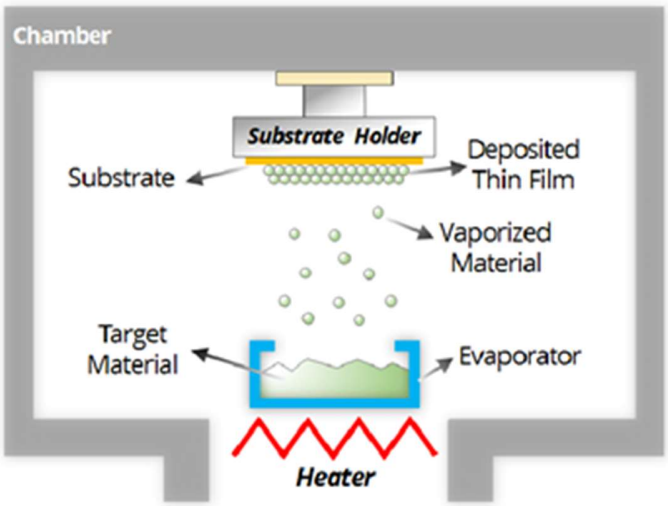

Figure 2.10. Thermal evaporation deposition. [48]

2.6.2 Chemical vapor deposition (CVD)

CVD is a deposition process where one or more precursors react and/or decompose on the substrate surface to form coatings [49]. This technique is often employed in the semiconductor industry to produce thin films. There are different types of CVD methods, like plasma-enhanced CVD (PECVD), atomic-layer CVD (ALCVD), laser CVD (LCVD) and so on.

In the plasma enhanced chemical vapor deposition (PECVD), plasma deriving from precursors is generated first by radio frequency (RF) or direct current (DC) discharge between electrodes. Then chemical reactions happen on the substrate to form coatings. PECVD employs plasma to

increase the reaction rates of the precursors. Meanwhile, it allows low temperature deposition, which is critical in the semiconductor industry.

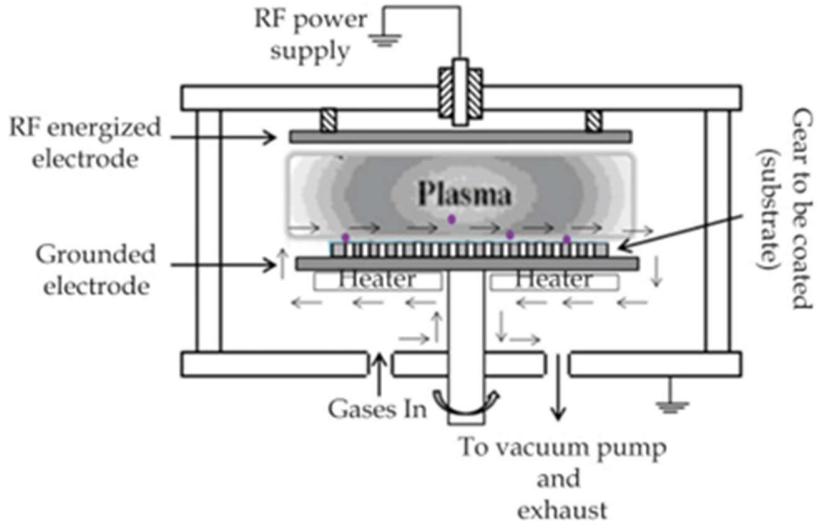

Figure 2.11. Plasma Enhanced Chemical Vapour Deposition. [50]

Chapter 3

Literature Review

In this chapter, a comprehensive literature review will be conducted on wear monitoring techniques. Then, coating deposition techniques of DLC and crystalline silicon coatings will be described. In addition, the nature of tribofilms derived from MoDTC and ZDDP additives and their interactions with DLC will be presented. This review will also show the challenges for in-service wear monitoring techniques and surface analytical method of identifying the tribofilm.

3.1. Wear monitoring techniques

With the increasing demands for manufacturing automation, the wear monitoring technique plays an increasing critical role in the machine maintenance strategies, as it yields necessary and key information of the service condition and fault prediction [1-4]. It is known that the machines in the smart factories are getting highly networked, and the main challenge for cooperating in more robust and autonomous way is how to minimize the downtime caused by unpredicted failure.

Depending on the average downtime and fault frequency of various machine components, it can be classified into four different groups as shown in Figure 3.1 [3]. The components with long average downtime and high fault frequency in the upper right group can be perfectly omitted in the design stage of modern machines. For the components with short

average downtime and high fault frequency in the upper left group, the periodic maintenance plan can be applied. A regular maintenance for the components in the lower left group is enough considering their low fault frequency and short maintenance time. The most critical components are the lower right group which have long downtime and low fault frequency. The monitoring techniques in machine health management systems are mainly developed for this kind of components, including tools, bearings, gears, electric motors, and etc.

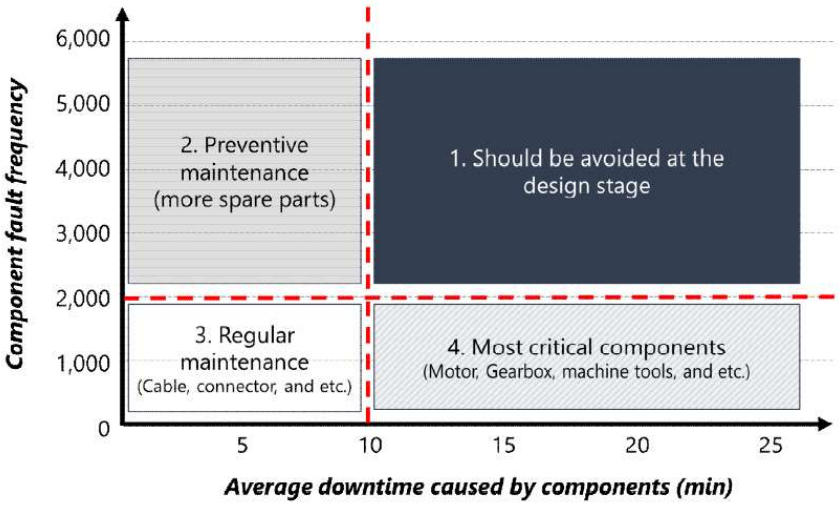

Figure 3.1 Average downtime and fault frequency of diverse components. [3]

In view of this fact, the maintenance strategies in modern manufacturing industry are transforming from traditional reactive practices to predictive and preventive methodologies, which has driven numerous efforts for developing reliable techniques for wear monitoring. The main aim of wear monitoring is to detect the wear evolution rather than just recognize severe wear or breakage [6, 7]. Through continuously monitoring the wear, the wear stage (e.g. running-in, steady state and severe wear) can be determined, which is crucial to predicting the service life and failure. Up to now, the wear monitoring techniques can be classified into two categories: indirect method and direct method.

3.1.1. Indirect wear monitoring techniques

To date, most approaches for the wear monitoring usually estimate the wear condition based on the operation signals which are indirectly correlated to wear, such as acoustic emission, cutting force, vibration and motor power (Figure 3.2) [3-9]. More specifically, these signals are processed to extract features related to the wear conditions which are classified according to predefined conditions or trained monitoring model, and then the maintenance decisions are made based on the status assessment [1, 3]. As these approaches monitor conditions without machine interruption and extraction, they have been widely adopted in the online monitoring system.

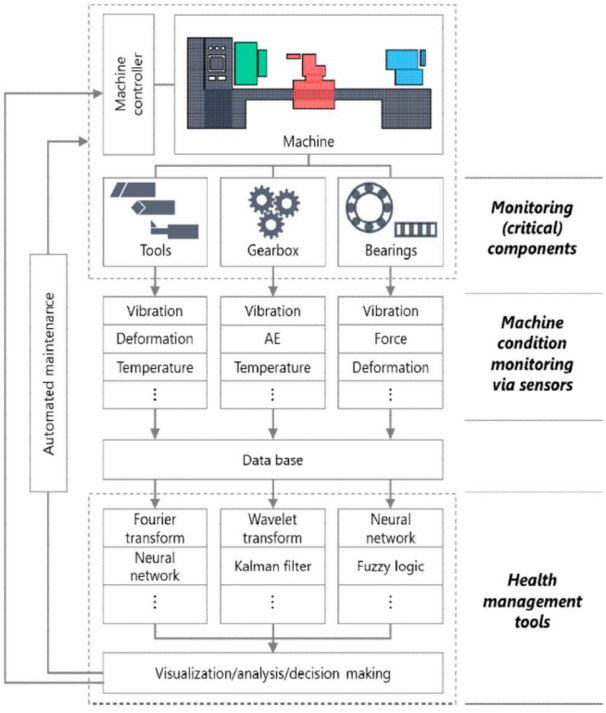

Figure 3.2. Machine health management system. [3]

In addition, since these methods are incapable of direct application in a distinct process condition (e.g., material variation, different working conditions), model retraining become

necessary for a new working condition, which requires extensive tests to obtain various operation parameters for estimating the wear level [4, 5 ,7].

3.1.2. Direct wear monitoring techniques

Direct wear monitoring techniques can be classified into two types: offline and online. Offline methods can only be used in the offline condition while online methods can provide wear information during friction process.

3.1.2.1. Offline methods

Currently, there are two typical modes of offline approaches widely used in industrial fields: contact and non-contact optical profilometers [51, 52]. Highly reliable and accurate topographic analysis of surface wear can be achieved via these approaches in the form of two- or three-dimensional wear profiles. The significant advantage of contact approach is that it captures real physical depth profile by using touch trigger probes. However, it cannot provide continuous online measurements because the contact regions of moving parts are generally inaccessible during running process.

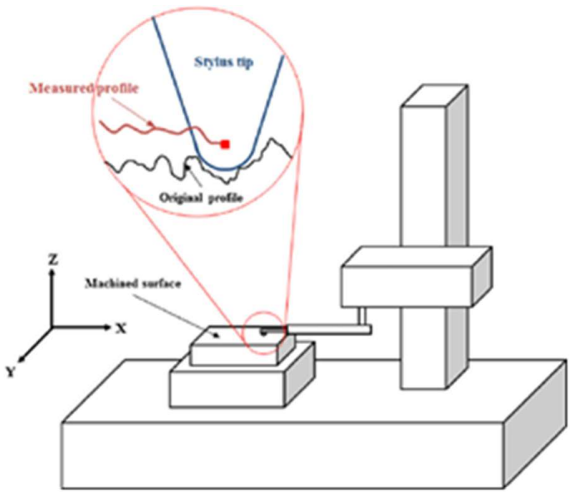

Figure 3.3. Working principle of contact profilometer. [51]

The non-contact optical approach builds up three-dimensional topographic map by collecting array signals of light interference of reflected light. Although highly accurate surface analysis at nanoscale can be achieved for as-grown coatings via non-contact optical approach, remarkable measurement errors will appear when characterizing the tribo-tested coatings. Since non-contact optical approach possesses high sensitivity on the light signals, tribo-induced variation of optical properties on the coating surface, which can be termed as tribo-induced polishing effect, can significantly affect reflected light signal, further leading to remarkable measurement errors.

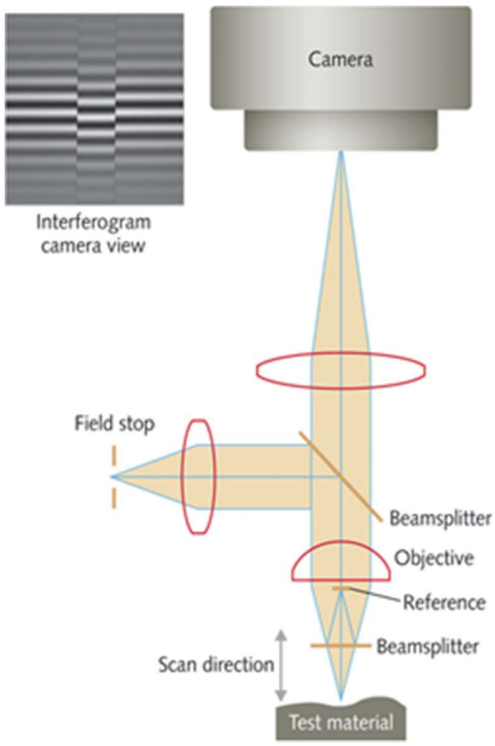

Figure 3.4. Working principle of non-contact optical profilometer. [53]

3.1.2.2. Online methods

Wear monitoring techniques which have been used in online monitoring mainly include wear debris detection and radioactive tracer technology. This part begins with wear debris monitoring techniques used in lubricating oil. Depending on the measurement principles,

online debris detection can be classified into four types: magnetic, resistive-capacitive, optical and acoustic methods [54, 55].

Magnetic method has been widely employed in oil debris monitoring due to the simple structures and anti-interference capacity. It contains two categories: i, magnetic chip detectors; ii, inductive sensors. The magnetic chip detector can count the ferrous metal amount based on the principle of magnetic collection. One representative product is Quantitative Debris Monitor (QDM) as shown in Figure 3.5. The core components are a permanent magnet and an inductive coil. When the oils pass through the magnetic field, the ferrous metallic debris will be attracted to the sensor tip. Then different pulse signals are outputted by inductive coil and analysed to determine the generation rate and the amount of wear debris. Additionally, by employing a vortex pump, entrained air and wear debris can be separated from the lubricating oil.

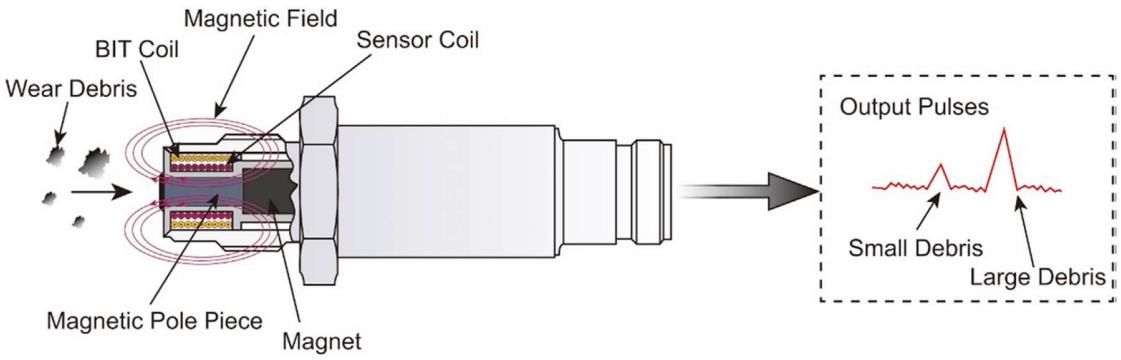

Figure 3.5. Schematic diagram of QDM sensor. [55]

Inductive sensor can measure the changes of the inductance and inductive voltage of inductive coils caused by wear debris. This method is based on electromagnetic method. The variation of the inductive voltage and inductance largely depends on the debris size and materials. Figure 3.6 displays the working principle of a typical inductive sensor called

in-line Metal Particle Detector (MPD). It can be observed that the debris materials can be identified based on the wave forms of signals (e.g., ferromagnetic, and non- ferromagnetic).

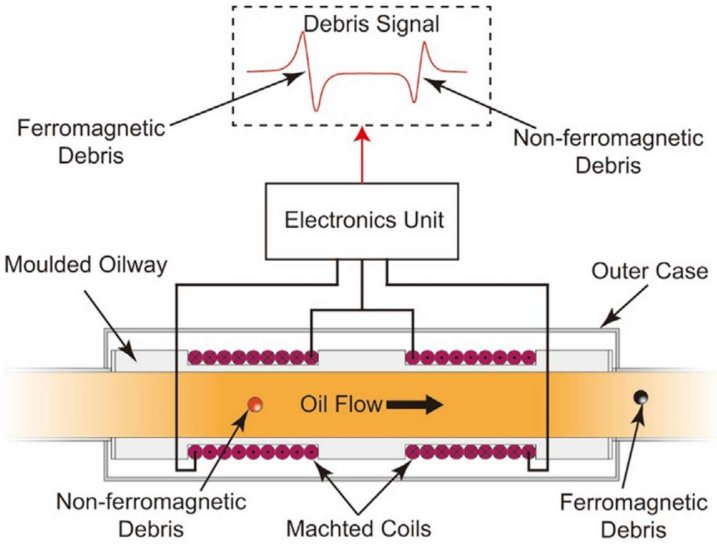

Figure 3.6. Schematic diagram of in-line MPD. [55]

Figure 3.7 displays the principle of resistive-capacitive method. A pair of poles, located on both sides of oil flow, is used to produce electrical field. When wear debris pass through the electrical field, they can be detected by monitoring the variation of resistance or capacitance between the poles. Although the sensor structure is very simple, this method is not widely used considering that the strong electrical field can result in the acceleration of oil deterioration.

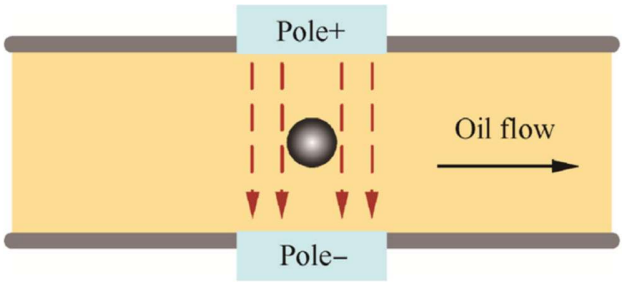

Figure 3.7. Schematic diagram of the resistive-capacitive method. [54]

The key components of the optical method are light source and photosensor. As shown in Figure 3.8, when wear debris particles pass through the light path, it can cause the changes of light intensity. Although, this method has high sensitivity, obvious errors can be caused by low oil transparency and the existence of bubbles.

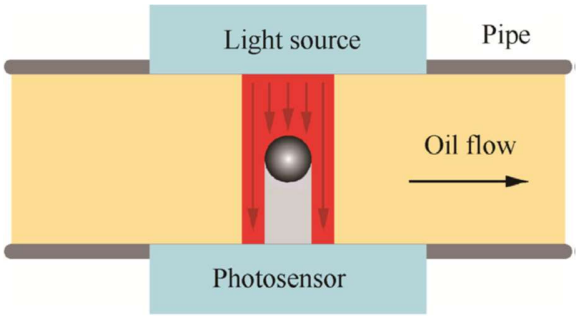

Figure 3.8. Schematic diagram of the optical method. [54]

The key components of the acoustic method are the acoustic transmitter and receiver, which are located on both sides of oil flow as shown in Figure 3.9. When wear debris particles pass through, the transmitted waves can be distorted with generating reflex waves. Based on the information of acoustic waves, the debris size could be obtained.

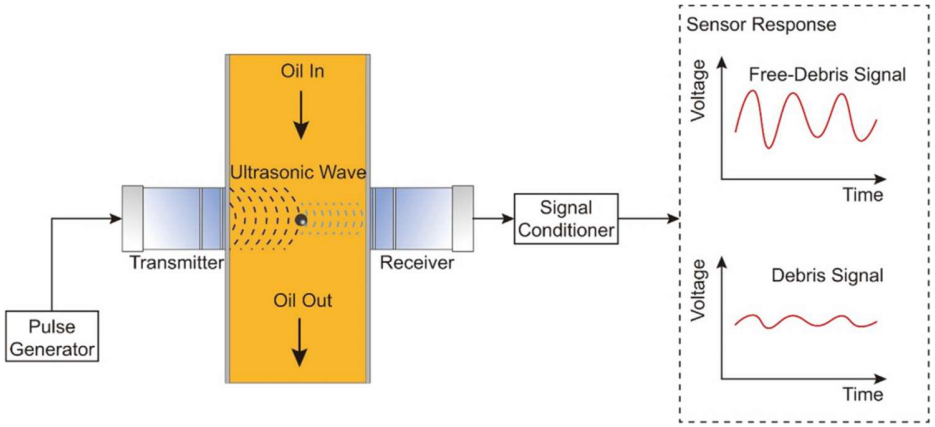

Figure 3.9. Schematic diagram of the acoustic method. [55]

Radioactive tracer technology has been employed as a highly sensitive method for real-time wear and corrosion measurement [56, 57]. Through this approach, radioactive isotopes are

tagged on the tribopairs by either direct activation on the component or implantation of radioactive isotopes. In the friction process, the surface materials with radioactive atoms are removed and dispersed in the lubricating oil. Real-time wear measurement can be achieved by monitoring the increased radioactivity in the lubricating oil, or the reduced radioactivity of the component surface.

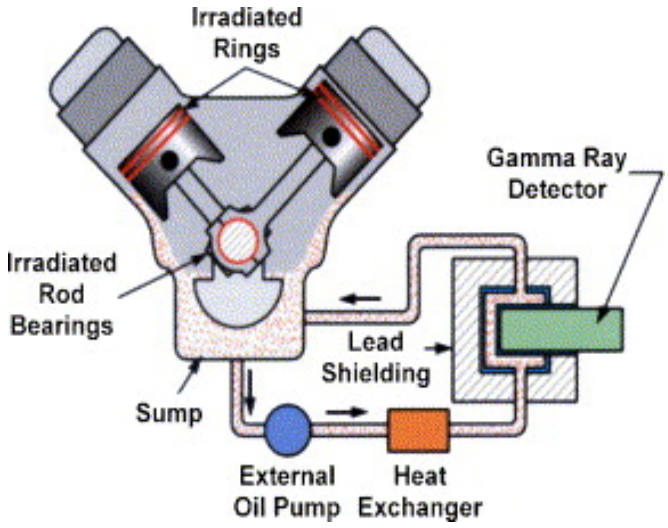

Figure 3.10. Schematic diagram of radioactive tracer technology. [56]

Fourier transform infrared (FTIR) spectroscopy has potential to be used to evaluate the online condition of lubricating oils. When exposed to infrared radiation, molecules absorb radiation at specific wavelengths in term of absorption peaks, which can be used to identify the antioxidants, water, soot, wear debris in the lubricating oil. Meanwhile, the intensity of absorption peak is a direct indication of the content of specific materials, which can be employed to provide wear information by detecting the absorption peaks corresponding to the materials of contact surfaces [58].

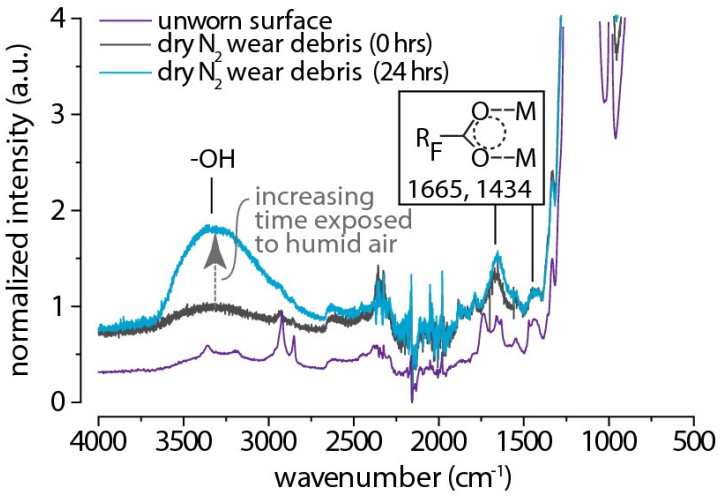

Figure 3.11. FTIR spectra for analysing the content of wear debris. [58]

3.1.2.3. Coating thickness measurement methods

Apart from the above techniques, there are two methods which can be used to measure the coating wear. As reported in the literature, luminescence spectra were used to detect the coating wear by monitoring the intensity of spectra from the layers composed of luminescent materials [22, 23]. As the upper layers of coating were removed in the wear process, the intensity of spectra from the sensing layers increased. When luminescent layers were damaged, the characteristic spectra disappear. This wear information could be used to predict the coating life and report failure warning. However, the relationship between the Raman signal intensity of sensor layer (sublayer) and the thickness of upper layer has remained unexplored

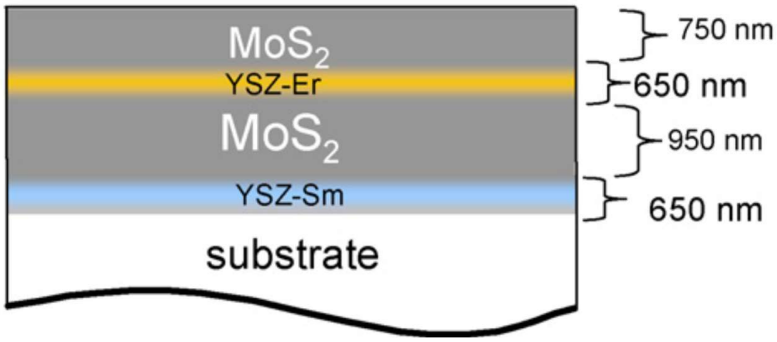

Figure 3.12. Multi-layered coating with embedded, luminescent wear sensor layers. [22]

Several studies by Thomas et al. proposed a Raman scattering model for quantifying the thickness of Raman active coating (i.e., diamond-like nanocomposite (DLN)) [59-61]. By clarifying the correlation between DLN thickness and the Raman intensity of carbon signal of DLN in equations, this model allows us to present more detailed wear information in the form of wear depth profiles, which show good agreement with measured results of the stylus profilometer. However, the influence of tribo-induced effects on measurement accuracy was not considered in these studies, which could lead to remarkable measurement errors, especially for the long-term tribological tests. We note that the challenges posed by the long term tribo-test include revealing the effect of tribo-induced variation of chemical composition and optical property of coatings and lifting the error tolerance of wear quantification method.

Specifically, the tribo-induced effect can result in enhancement of sp^2 phase (i.e., the increase and local clustering of sp^2-C phase). Since the Raman spectra of carbon of a-C:H are dominated by scattering of sp^2 phase due to its high polarizability. Slight enhancement of the sp^2 phase, especially ordering or clustering, could result in the remarkable increase of the Raman intensity [62], further leading to obvious measurement errors in the

transformation areas and low reliability in monitoring the coating thickness in the friction process.

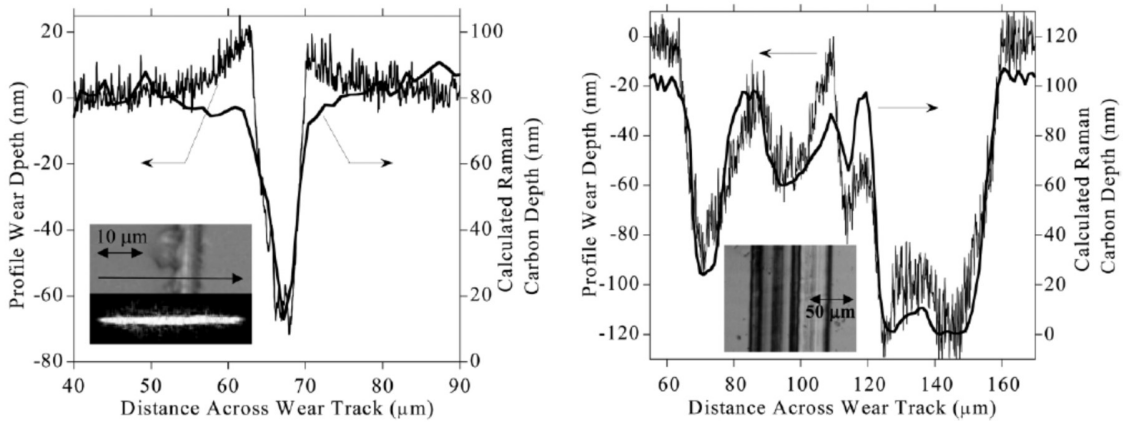

Figure 3.13. Calculated and measured profile wear depth of a DLN coating based on Raman signal of carbon. [59]

3.2. Diamond-like carbon (DLC) coatings

3.2.1. Structure of DLC coatings

In general, amorphous carbon (a-Cs) is composed of three bondings (i.e., sp^3, sp^2, and even sp^1) with the hydrogen content up to 60 at. % [62]. Figure 3.14 displays the ternary phase diagram of a-Cs, which is based on the content ratio of sp^3, sp^2, and hydrogen. The a-Cs with extreme high sp^2 ratio and disordering graphitic structure located in the lower left corner, including soot, glassy carbon, and evaporated a-C. With increasing the hydrogen content, the content of C-C networks decreases significantly with the formation of hydrocarbon polymers (e.g., polyethylene). Amorphous carbon and hydrogenated amorphous carbon with a significant ratio of sp^3 bonding are defined as diamond-like carbon (DLC). When the sp^3 content is up to 80 %, it is termed as ta-C (tetrahedra amorphous carbon) and ta-C:H (hydrogenated tetrahedra amorphous carbon). In addition,

the clustering degree of sp^2 phase is considered as the fourth key parameter which can significantly affect the electronic, optical, and mechanical properties of a-Cs [63, 64].

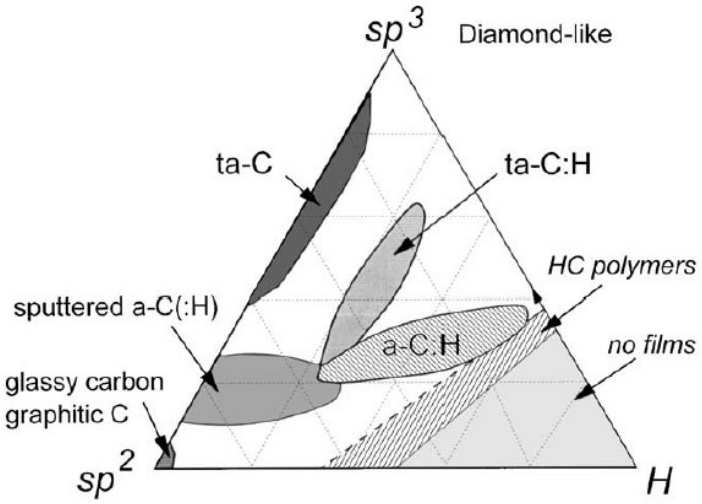

Figure 3.14. Ternary phase diagram of in amorphous carbon. [62]

For DLC, sp^2 sites can from small clusters which are embedded in sp^3 matrix. The mechanical properties and chemical stability of DLC are generally dominated by the sp^3 bonding, while the optical and electrical properties depend on the content and orientation of sp^2 phases [65]. The relative ratio sp^2/sp^3 determines the overall properties of DLC coatings. Depending on the composition and structure, the properties of DLC can range from soft coatings with a wide optical gap to coatings with diamond-like mechanical properties and low optical gap. Therefore, the DLC properties can be tailored for different engineering applications. In addition, it should be pointed that hydrogen content critically affects the properties of DLC coatings. Increasing the hydrogen content leads to the increase of the optical band gap and transmittance, and the decrease of hardness and wearing resistance [66].

Table 3.1. Comparison of major properties of amorphous carbons. [62]

	sp^3 (%)	H (%)	Density (g cm^{-3})	Gap (eV)	Hardness (GPa)
Diamond	100	0	3.515	55	100
Graphite	0	0	2.267	0	
C_{60}	0	0		1.6	
Glassy C	0	0	1.3–1.55	0.01	3
Evaporated C	0	0	1.9	0.4–0.7	3
Sputtered C	5	0	2.2	0.5	
ta-C	80–88	0	3.1	2.5	80
a-C:H hard	40	30–40	1.6–2.2	1.1–1.7	10–20
a-C:H soft	60	40–50	1.2–1.6	1.7–4	<10
ta-C:H	70	30	2.4	2.0–2.5	50
Polyethylene	100	67	0.92	6	0.01

3.2.2 Deposition methods of DLC coatings

DLC coatings with different composition and structure can be deposited by PVD or CVD methods as displayed in Figure 3.15 [62]. Depending on the deposition method, the range of deposition parameters (e.g., deposition pressure, bias voltage, and temperature) varies over broad ranges. For most tribological applications, DLC coating should have high adhesive ability towards substrates to prevent fracture and delamination under high shear forces or applied load in the sliding process. The adhesive ability of DLC strongly depends on the chemical nature of substrate materials. Strong adhesion can be obtained on the substrates of carbide- and silicide-forming materials (e.g., Si, Ti, W and Cr). For the substrates with low adhesion, interlayer is suggested to be deposited on these substrates before DLC deposition in the same batch to minimize the point defects and chemical impurities. These interlayers are also composed of strong carbide- or silicide-forming materials, which can react with the substrate materials to form strong bonding.

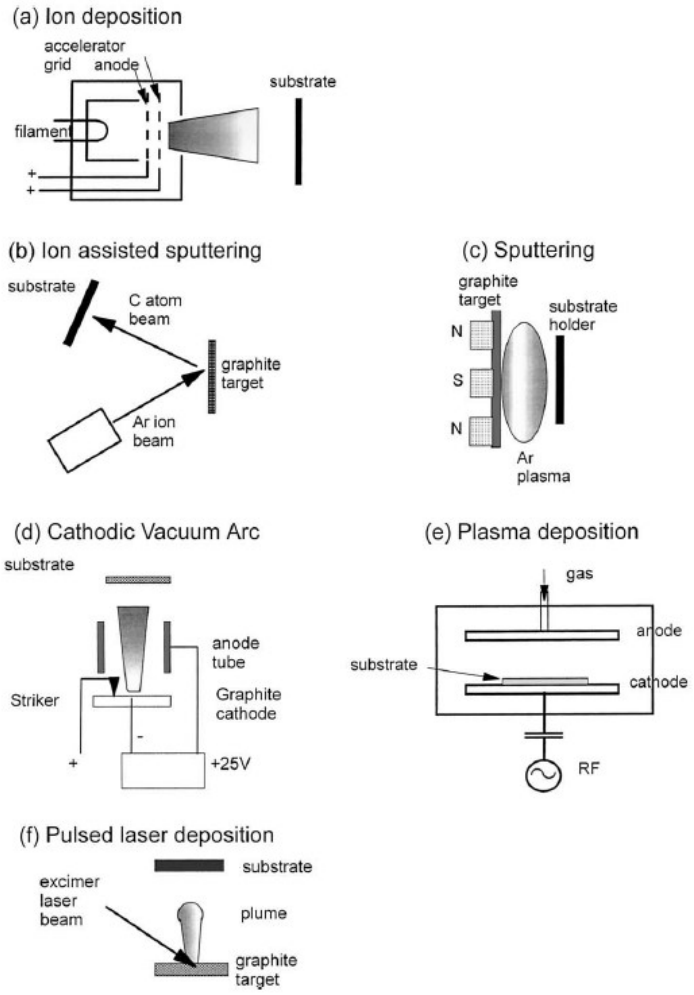

Figure 3.15. Schematics of various deposition systems for DLC. [62]

3.2.3. Raman spectra of DLC coatings

As a fast and non-destructive method, Raman spectroscopy has been employed to characterize the chemical structure of a series of carbon materials as shown in Figure 3.16 [62-64]. In general, the main signals of carbons can be collected in the 800-2000 cm^{-1} region of Raman spectra. The G and D peaks locate at around 1560 and 1360 cm^{-1}, respectively. The G peak is caused by the stretching vibration of sp^2 bonding in both C=C chains and aromatic rings, while the D peak corresponds to the breathing modes of sp^2 bonding only in rings as shown in Figure 3.17.

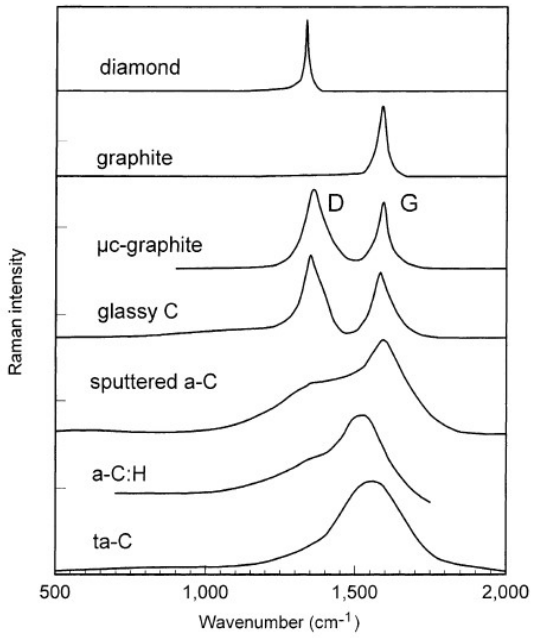

Figure 3.16. Comparison of typical Raman spectra of carbons. [62]

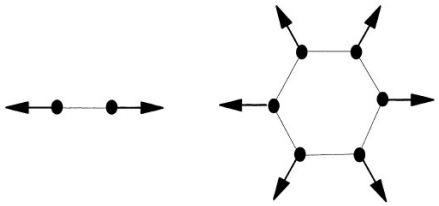

Figure 3.17. Eigenvectors of the Raman G and D modes in graphite and amorphous carbon. [62]

The Raman spectra of a-Cs are dominated by scattering of sp^2 phases due to its higher polarizability. It gives the sp^2 phase a 50-230 times larger Raman intensity than that of sp^3 phases. Slight enhancement of sp^2 phases, especially ordering or clustering, could result in a remarkable increase in the Raman intensity. The Raman spectrum mainly depends on (i) clustering of the sp^2 phase, (ii) ordering of sp^2 phase, (iii) sp^2/sp^3 ratio. These factors act as competing forces on the shape of the Raman spectra as shown in Figure 3.18.

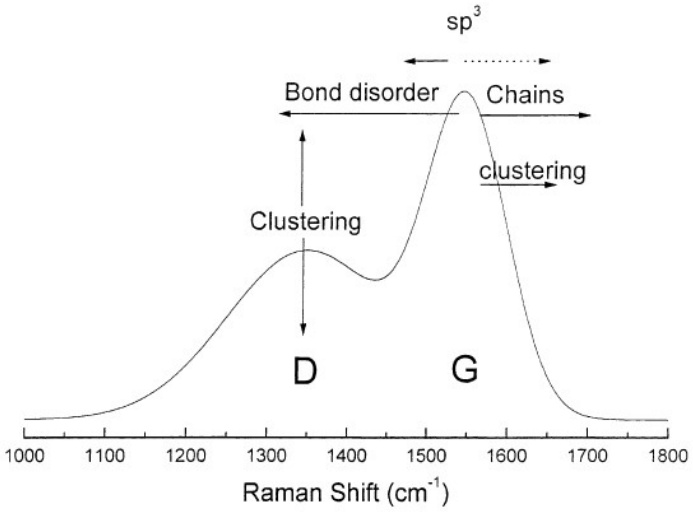

Figure 3.18. Schematic of the factors affecting the position and heights of the Raman G and D peaks of amorphous carbon. [62]

For obtaining the bonding information based on Raman spectra, it is important to select appropriate fitting method. Currently, there are three methods for shape fitting of Raman spectra of carbon materials, including all Gaussians fitting, all Lorentzians fitting, and the method employing the Breit-Wigner-Fano (BWF) fitting for G peak and the Lorentzian fitting for the D peak [67]. For crystalline carbon materials (e.g., disordered graphite), Lorentzian fitting is suitable considering the finite lifetime broadening. For hydrogenated amorphous carbons with a significant photoluminescence background, all Gaussian fitting works better than BWF method.

After obtaining the fitting peaks of G and D, I(D)/I(G) ratio is used to reflect the structure features of carbon materials. When using BWF and Lorentzian fitting method, the I(D)/I(G) ratio is the ratios of peak height while it is peak area ratio for all Gaussian fitting. The difference between height ratio and area ratio is not obvious for disordered graphite due to the similar peak widths. For amorphous carbons, there is significant difference. For example, the wider size distribution and disordering of sp^2 clusters can result in the broadening of the D peak. In addition, after the fitting procedure is decided, it is suggested

to use the same procedure for data analysis as it enables the result comparison between different samples.

3.2.4. Optical properties of DLC coatings

DLC coatings have high transparency in the infrared wavelength and the absorption coefficient increases with decreasing the wavelength, as shown in Figure 3.19 [62]. There are three hybridizations in DLC (i.e., sp^3, sp^2 and sp^1). In the sp^3 configuration, four sp^3 orbitals are formed in a carbon atom and bonding with adjacent atoms via strong σ bonds. In the sp^2 configuration, there are three sp^2 orbitals to form σ bonds and one pπ orbital to form a π bond.

As displayed in Figure 3.20, the σ states in the valence band and empty σ^* states in the conduction band formed by σ bonds are separated by a wide σ- σ^* gap, while π states and π^* states of π bonds show a much narrower gap [68]. Therefore, the final band gap of DLC is mainly determined by the π bonds from sp^2 phases. Depending on the configurations of sp^2 clusters, sp^2 phases have variable band gaps. The final band-gap is given by the average band gap of each sp^2 clusters. The wide distribution of cluster sizes can lead to a broad absorption tail. The arrangement of sp^2 phases dominates the electronic and optical properties, while the sp^3 matrix determines the mechanical properties.

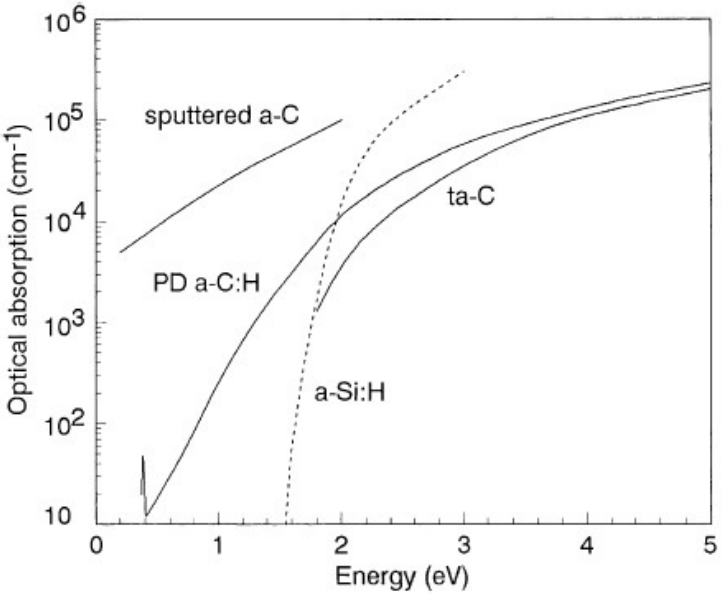

Figure 3.19. Optical coefficients of a sputtered a-C, ta-C and an a-C:H coatings. [62]

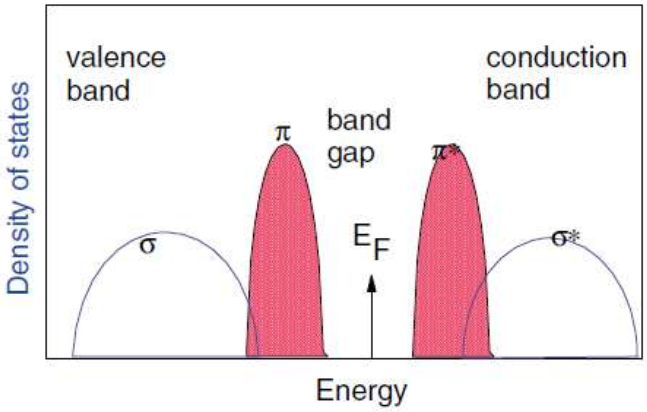

Figure 3.20. Schematic DOS of amorphous carbon. [68]

The band-gap of crystalline materials is defined as the minimum energy gap between the occupied and empty states. For the amorphous semiconductor, there is no true gap, and an arbitrary definition is used. For determining the band gap of DLC coatings, the E_{04} gap and Tauc gap are employed. E_{04} gap is defined as the energy when the optical absorption coefficient α is 10^{-4} cm^{-1} (Figure 3.21), and Tauc gap (E_g) is deduced by extrapolating the linear behavior of $(\alpha E)^{1/2}$ as a function of photon energy E (Figure 3.22) based on the following equation [64]:

$$\alpha E = B(E - Eg)^2 \qquad 3\text{-}1$$

Meanwhile, the band-gap of DLC coatings strongly correlates with their sp^2 fractions while hydrogen has a little direct effect as the C-H states lie away from the band-gap region.

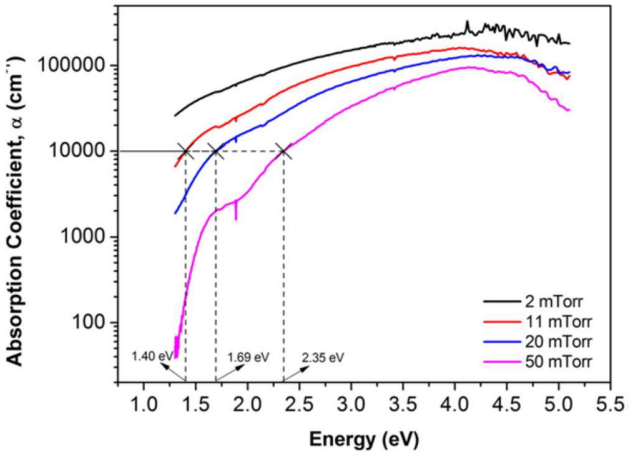

Figure 3.21. Absorption coefficients as a function of energy for DLC films prepared at different working pressures on glass substrates at room temperature. E_{04} gaps are also shown in the figure. [65]

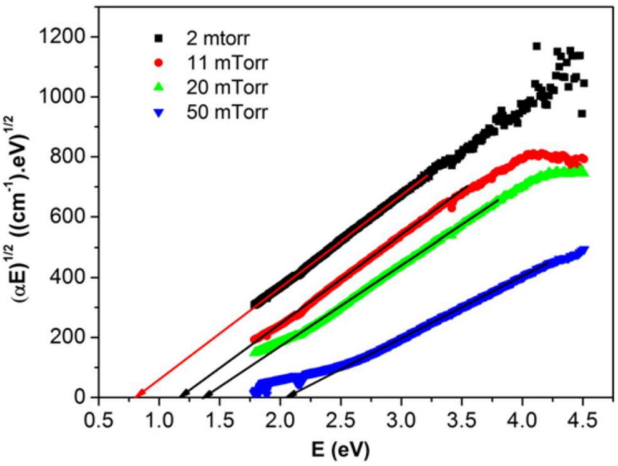

Figure 3.22. Tauc plots of DLC films prepared at different working pressures on glass substrates at room temperature. [65]

DLC coatings can be deposited by diverse deposition methods [69, 70]. Though controlling the deposition parameters, the optical properties can be adjusted according to application requirements. For example, the gas pressure (e.g., Ar) in magnetron sputtering, as an

important deposition parameter, significantly affects the energy of the sputtered atoms arriving at the substrate, further determining the coating properties. As shown in Figure 3.23, working pressure has an important influence on the bonding properties, strongly influencing the optical properties of the deposited films.

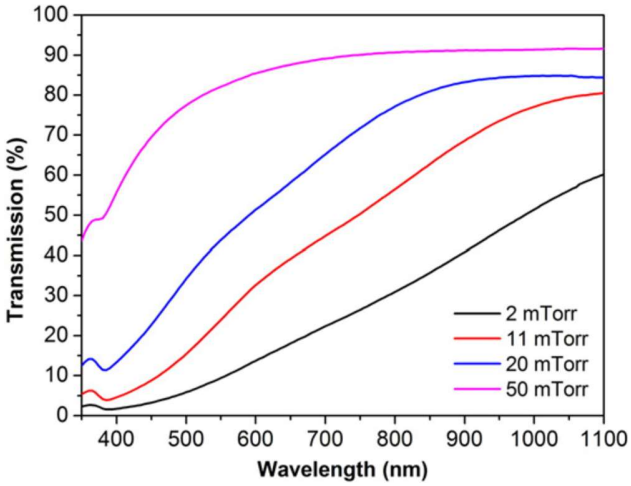

Figure 3.23. Optical transmission spectra of DLC films prepared at different working pressures on glass substrates at room temperature. [65]

3.3. DLC/additives interactions

Additives are the crucial components of liquid lubricants and their tribochemical products formed on coating surfaces in the form of tribofilm critically affect the wear and friction behaviors. However, the mechanisms governing the tribofilm growth on coating surfaces are not well understood since most of existing lubricating additives are developed for ferrous surfaces [71]. It can result in severe wear and early failure of key components when using the conventional lubricating solutions. It is therefore necessary to deepen the understanding of tribochemical interactions between lubricating additives and coatings, and the growth mechanisms of additive-derived tribofilm on coating surfaces, which can significantly contribute to developing effective lubricating solutions for diverse coatings.

3.3.1. MoDTC/a-C:H interaction

Molybdenum dithiocarbamate (MoDTC) has been widely employed in engine oils as a classic friction modifier (FM) which decomposes into molybdenum disulphide (MoS_2) sheets and molybdenum trioxide (MoO_3) under the action of friction forces. For ferrous-base contact surfaces, its effectiveness in friction-reduction can be attributed to the formation of tribofilms, containing nano-MoS_2 sheets with layer-lattice structure and weak interlaminar shear forces [72]. Figure 3.24 displays the corresponding chemical structure of MoDTC and MoS_2.

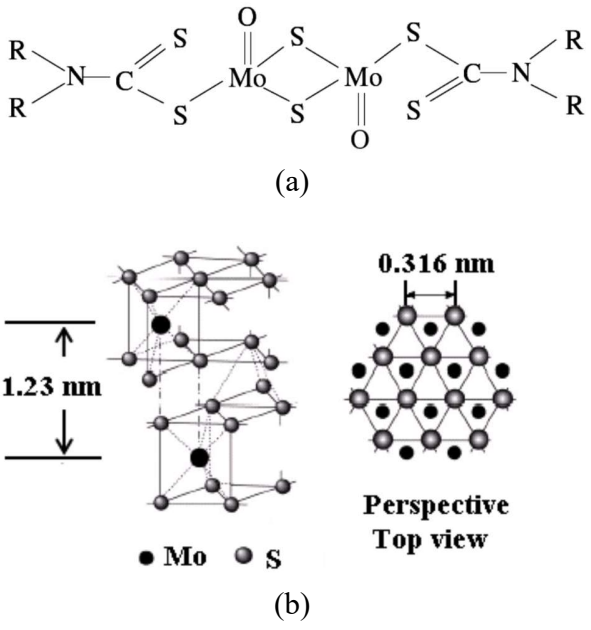

Figure 3.24. (a) Molecular structure of MoDTC, (b) MoS_2 Structure.

When applying MoDTC-containing oil on the steel/DLC contacts, it dramatically accelerated the wear rate of DLC, further triggering coating failure [73-77]. It is well accepted that MoDTC-derived tribochemical products play a critical role in this detrimental effect. Figure 3.25 displays the decomposition process of MoDTC. It can be observed that the main products are molybdenum disulphide (MoS_2) sheets and molybdenum trioxide.

The wear acceleration mechanisms of MoDTC on DLC surfaces in previous studies can be summarized as follows: i, oxidation-reduction reaction between DLC and molybdenum oxides [77]; ii, abrasive wear of molybdenum oxides [69]; iii, abrasive wear of molybdenum carbides formed via tribochemical reaction [76]; iv, re-hybridization of C-C bonding from sp^3 to sp^2 under severe tribological conditions and delamination of this sp^2-rich carbon layer [75]. It should be also pointed that some of the above mechanisms (e.g., abrasive wear mechanism of molybdenum oxides and re-hybridization mechanism of C-C bonding) remain controversial [74]. More importantly, it is still unclear which type of tribochemical products dominates the coating wear behavior in different wear-stages when lubricated with MoDTC.

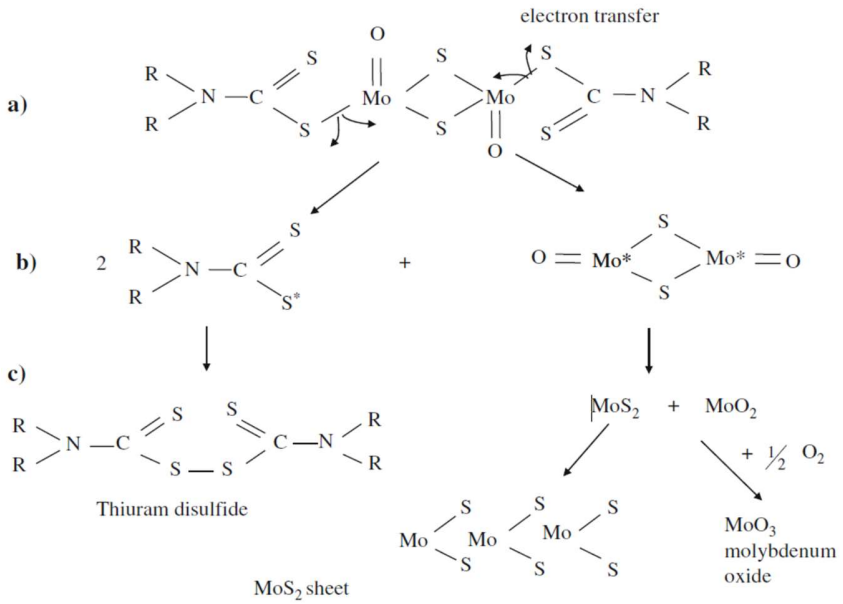

Figure 3.25. Decomposition process of MoDTC. [78]

3.3.1.1 Raman spectra of MoS_2

MoS_2 is one of main decomposition products of MoDTC and plays a critical role in the tribological performances. Raman spectroscopy has been applied to identify the formation of MoS_2 based on the Raman peaks. Figure 3.26 displays diverse vibration modes of MoS_2

lattice structure, including Raman active, infrared active and inactive as listed in Table 3.2 [79]. The Raman peaks corresponding to the Raman active vibration modes E^2_{2g}, E_{1g}, E^1_{2g} and A_{1g} locate at 34, 287, 383 and 409 cm^{-1}, respectively [80]. Among these four vibration modes, E^1_{2g} and A_{1g} possess strong Raman intensities.

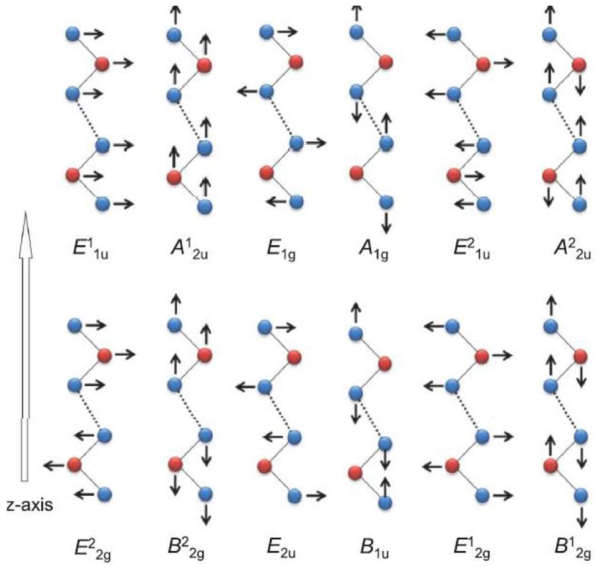

Figure 3.26. Vibration modes of MoS_2 lattice structure. [79]

Raman peaks of MoS_2 has been employed to investigate the disordering and size of MoS_2 crystals. It is indicated that disordering and size reduction of crystals can lead to the peak broadening [81, 82]. Meanwhile, the peak shifts and width could be used to reflect the thickness variation of MoS_2 [83-85]. With increasing the MoS_2 thickness from one layer to four layers, red shifts (to lower wavenumbers) of E^1_{2g} peak and blue shifts (to higher wavenumbers) of A_{1g} peak were observed. The A_{1g} peak width (FWHM) was found to decrease with the increase of MoS_2 layers.

Table 3.2. Classification of vibration modes of MoS_2. [79, 80]

	Infrared active	Raman active	Inactive
In-plane	E^1_{1u}	E^2_{2g}	E_{2u}
	E^2_{1u}	E_{1g}	
		E^1_{2g}	
Out of plane	A^1_{2u}	A_{1g}	B^2_{2g}
	A^2_{2u}		B_{1u}
			B^1_{2g}

In addition, the Raman peaks of MoS_2 are significantly influenced by pressure, temperature, and laser power. Figure 3.27 displays the Raman spectra of MoS_2 under different pressures [86]. It can be observed that increasing the stress can result in the bule shifts of both E^1_{2g} and A_{1g} peaks due to the pressure-induced disordering of lattice structure [86-88].

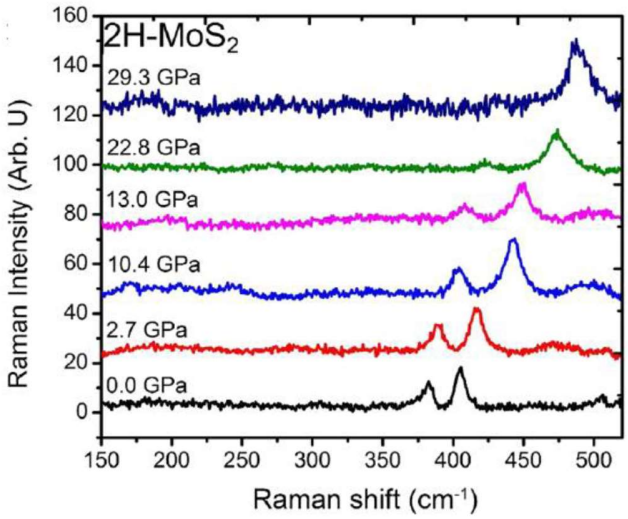

Figure 3.27. Pressure-induced shift of Raman peaks of MoS_2. [86]

Temperature is also a key factor affecting the Raman peaks of MoS_2 [89-92]. Figure 3.28 shows the Raman spectra of MoS_2 under different temperature. It was found that the positions of E^1_{2g} and A_{1g} peaks decrease linearly with increasing the temperature from 83 to 473 K. It was also indicated that a non-linear relationship between frequency shift and temperature was observed at higher temperatures [92]. Meanwhile, the broadening of peak widths was observed with raising the test temperature. Additionally, high laser power can cause a sharp rise of local

temperature on MoS_2 crystals, which results in adjustment of lattice structure and influences the vibration. Red shifts of A_{1g} peaks were observed with increasing the laser power. Excessive laser power can even result in the oxidation of MoS_2 into MoO_3.

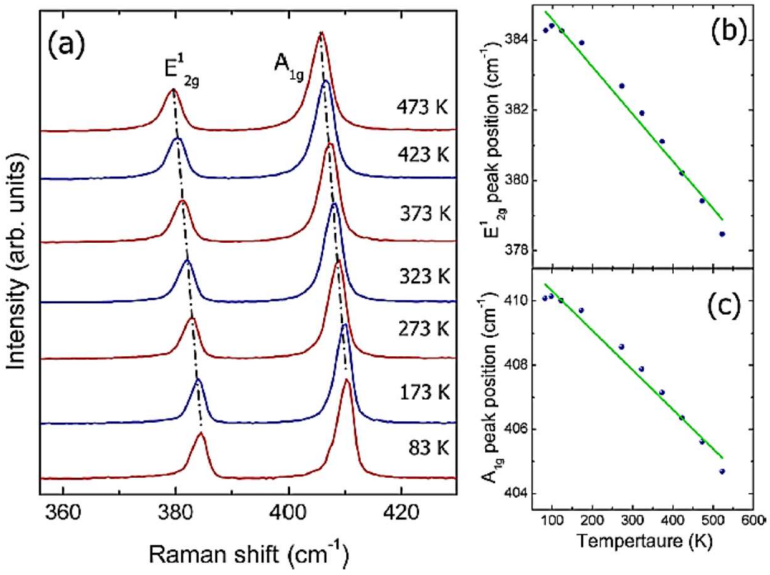

Figure 3.28. The influence of temperature on Raman peaks of MoS_2. [89]

3.3.2. ZDDP/a-C:H interaction

In the past decades, a significant progress has been achieved in identifying the structure and growth mechanisms of additive-derived tribofilm via advanced surface analysis techniques. Particular attention is paid on the governing factors in the tribofilm growth of ZDDP which is one of the most crucial anti-wear additives, highlighting the critical role of contact pressure and temperature in the tribochemical reactions [93-95].

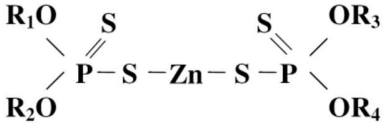

Figure 3.29. The molecular structure of ZDDP.

As indicated in the literature, the growth process of ZDDP-derived tribofilm on ferrous surface includes three stages, including nucleation, growth, and thickness saturation [93]. It well accepted that ZDDP can form surface-bonded pad-like tribofilms with a gradient structure with a short-chain glassy phosphate near the ferrous surface and a thin outer layer of long-chain polyphosphates [93, 95]. Some studies indicated that this reaction was driven by the Lewis acid-base interaction between phosphate (hard Lewis base) and oxidized surface layer (Fe^{3+} is hard Lewis acid) based on the HSAB principle [94-99].

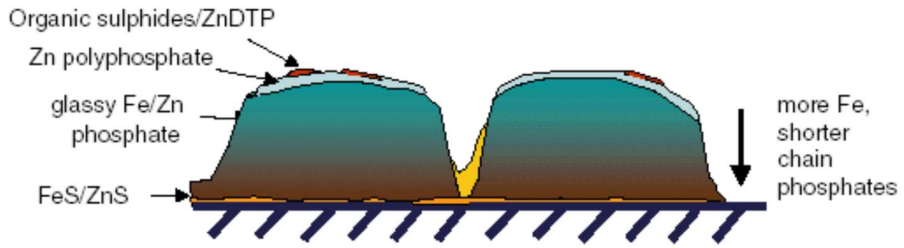

Figure 3.30. Schematic diagram of pad structure and composition of ZDDP derived tribofilm [94].

As indicated in the literature, when employing DLC coatings with different chemical structure (e.g., hydrogen content and sp^2/sp^3 ratio) and mechanical properties as contact surfaces, the tribofilm growth process of ZDDP is still dominated by effective local contact pressure rather than the chemical structure of coatings [100]. However, it is interesting note that the tribofilms formed on DLC surface are less durable than those formed on ferrous surfaces [101, 102]. Meanwhile, by comparing the results of element composition on ferrous and DLC surfaces, it is found that ZDDP tribofilms prefer to form on ferrous surface [103, 104].

Table 3.3. XPS quantification of tribofilms for a-C/ CI (cast iron) contacts. [104]

Lubricants	Surfaces	Element composition (at. %)				
		C 1s	O 1s	Fe 2p	P 2p	Zn 2p
PAO+ZDDP	Plates (carbon)	86.1	8.5	0	1.8	2.3
	Pins (CI)	50.9	33.9	2.5	3.5	5.5

3.3.3. Governing factors in the growth process of additive-derived tribofilms

Stress-activated and thermal activated tribochemical mechanisms have been well accepted on understanding the tribological behaviors of lubricating additives. Carpick et al. used AFM to monitor the growth process of ZDDP-derived tribofilms on ferrous substrate [93]. It was found that the thickness of ZDDP tribofilm increased with sliding cycles. More importantly, with increasing the contact pressure and temperature, the growth rate of tribofilm increased significantly as show in Figure 3.31. The growth rate can be calculated by the following equation:

$$\tau_{growth} = \tau_0 \, exp^{\frac{\sigma \Delta V - E_a}{k_B T}} \qquad 3\text{-}2$$

Where τ_0 depends on the volume of the growth species and attempt frequency, ΔV is the activation volume, σ is the average stress component, E_a is the activation energy, k_B is the Boltzmann constant and T is the temperature. It was indicated that the energy barrier of the tribochemical reaction of ZDDP on contact surface becomes lower where the local stress is higher and increasing the reaction temperature could promote the formation of tribofilms.

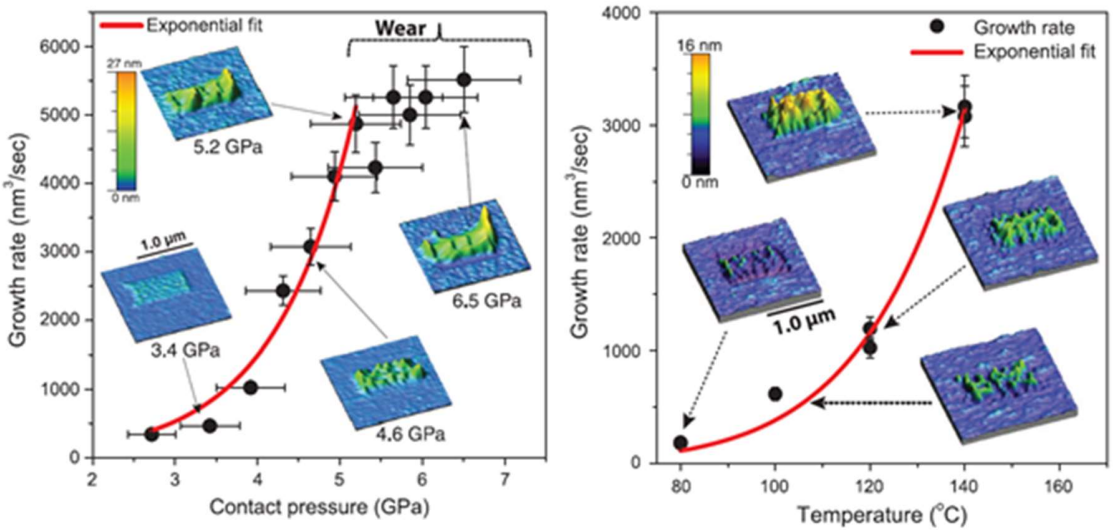

Figure 3.31. The influence of pressure and temperature on the growth rate of ZDDP tribofilms. [93]

Recently, De Barros Bouchet et al. reported the critical influence of surface nano-topography of DLC coatings on the tribological performances with ZDDP as additives [100]. It is indicated that under the same macroscopic hertzian contact pressure, different surface topographies of diverse DLC coatings result in distinct local contact pressures, further leading to the decomposition of ZDDP into different tribochemical species. For low contact pressure is below 3 GPa, the Zn-S bonds were broken under shear forces with the formation of Zn-C bonds to form chemical absorption films in the initial stage. During this stage, ZDDP decomposed into dithiophosphates. Then the antiwear films composed of polyphosphates were formed via accumulation and cross-linking. When the local contact pressure exceeds 9 GPa, ZDDP can decompose into small sulphur-rich species as shown in Figure 3.32(b). High shear forces promote the doping of sulphur into the sub-surface of DLC which weakens the DLC matrix and further leads to massive wear.

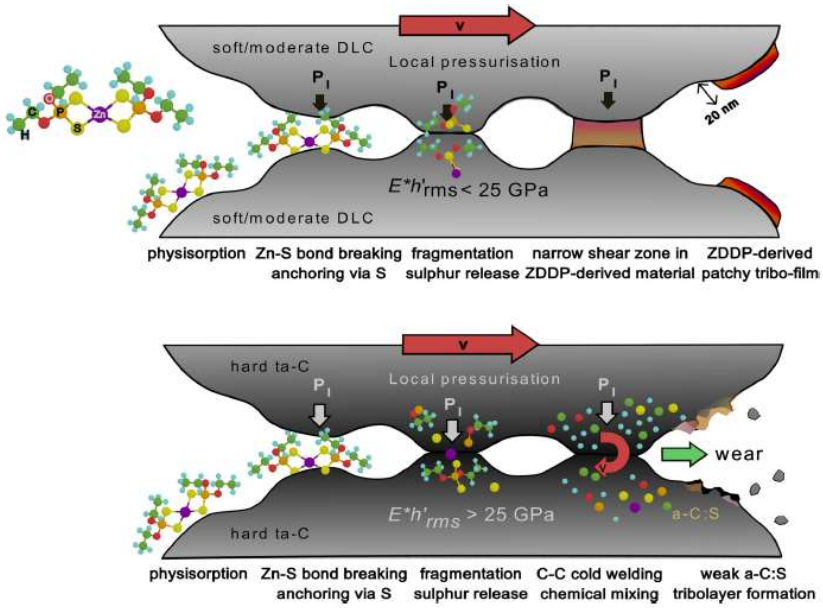

Figure 3.32. Tribochemcial mechanisms of ZDDP on DLC under different contact pressure. [100]

3.3.4. Effect of Hydrogen

As reported in the literature, hydrogen content of DLC coating plays a key role in the interaction between DLC and additives [105, 106]. Although the effect of hydrogen content attracts intense research attention, the mechanisms are still unclear. Carbon atoms on the diamond surface have dangling bond which can be passivated by oxygen and hydrogen elements from absorbed water molecules, leading to the decreased friction [107]. This mechanism is also employed to explain the tribochemical behaviors of DLC lubricated by different additives.

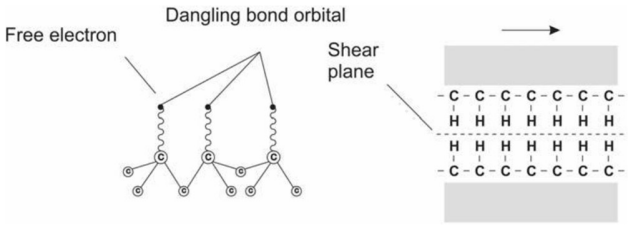

Figure 3.33. Schematic illustration of dangling bonds in diamond and weak shear plane between hydrogen-terminated diamond surfaces.

Yasuda et al. and Mabuchi et al. studied the effect of hydrogen content on the tribological performance of DLC [108, 109]. It was suggested high hydrogen content resulted in poor wettability of lubricant on the DLC surface and the high friction was due to the low absorption of additives on the DLC surface. In contrast, De Barros Bouchet et al. [110] reported the positive effect of hydrogen in the tribofilm formation on the DLC coating. It was found that a-C:H displayed lower friction than hydrogen-free a-C. XPS results indicated that the MoS_2/MoO_3 ratio of tribofilms formed on a-C:H was five times higher than that formed on a-C. Based on the chemical hardness approach (HSAB principle), it was suggested that a-C:H, which are soft bases, preferred to interact with soft acids (e.g., Mo^{4+}) to promote the formation of MoS_2. Meanwhile, a-C, which is considered as "intermediate bases", can react with Mo^{6+} with the formation of MoO_3. Equey et al. [111] reported that the ZDDP tribofilm formed on a-C:H/ a-C:H contacts could be easily removed by ultrasonic cleaning cyclohexane. It was suggested that the adhesion of ZDDP tribofilm on a-C:H was weaker than that formed on ferrous surface.

3.4. Silicon coatings

3.4.1. Deposition techniques of crystalline silicon coatings

Crystalline silicon coatings can be deposited by both CVD and PVD methods. The most common CVD methods are plasma enhanced chemical vapor deposition (PECVD) and hot-wire chemical vapor deposition (HWCVD) [112-115]. For obtaining silicon coatings with good crystallinity, hydrogen gas is introduced to dilute the source gas SiH_4, while amorphous silicon can be deposited under high SiH_4/H_2 ratio. Through PECVD, silicon coating can be deposited at high deposition rates and low substrate temperature. Note that

PECVD with capacitively coupled plasmas (CCPs) is the most prevalent deposition technique.

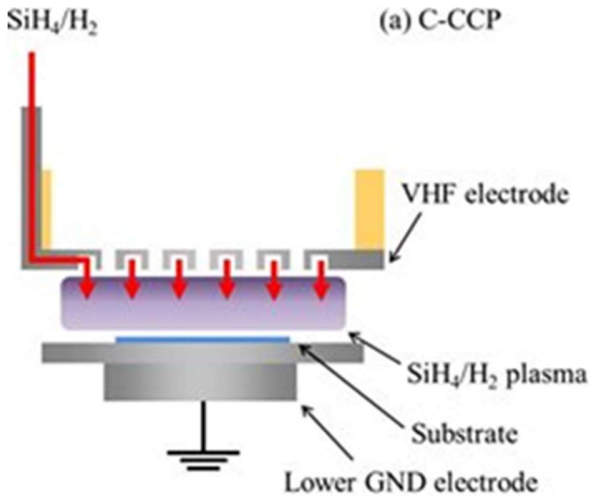

Figure 3.34. Capacitively coupled plasmas. [116]

The most common PVD method for depositing silicon coatings is the magnetron sputtering deposition, which mainly includes pulsed direct current (pulsed-DC) and radiofrequency (RF) magnetron sputtering [117, 118]. It is demonstrated that the growth of silicon coating can be significantly modified by controlling the ion-bombardment in sputtering process [119, 120]. Recently, ion-assisted sputtering deposition techniques have attracted intensive research attention for enhancing the bombardment of energetic particles and improving the quality of silicon coatings. Shin *et al*. employed inductively coupled plasma method to assist the growth of silicon coatings in an unbalanced magnetron sputtering deposition system [121].

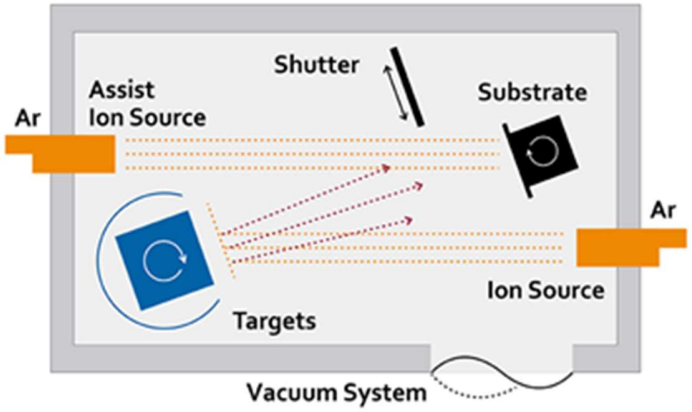

Figure 3.35. Ion beam deposition.

Reinig *et al*. reported that crystalline silicon coatings could be deposited by employing bipolar pulsed-DC magnetron sputtering deposition [122]. Meanwhile, it is demonstrated that external magnetic field can benefit the growth of crystalline silicon when using magnetron sputtering technique as it plays a critical role in adjusting the ion bombardment conditions near the substrate surface. Gerbi *et al*. employed the Helmholtz coil to control the magnetic field and the plasma density near the substrate surface, which were used to adjust the growth of silicon coatings [123].

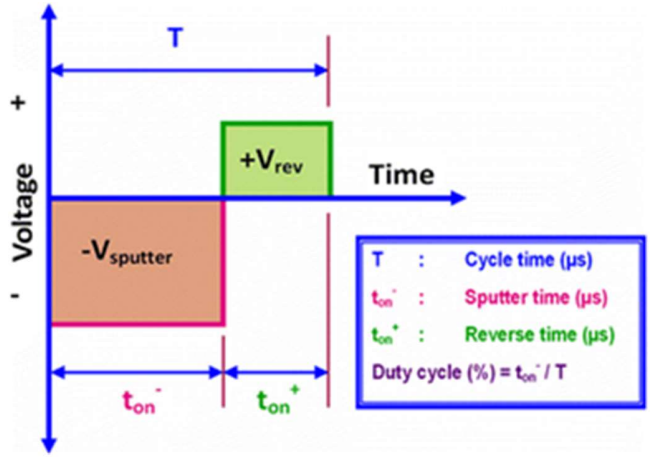

Figure 3.36. Pulsed-DC power for magnetron sputtering. [124]

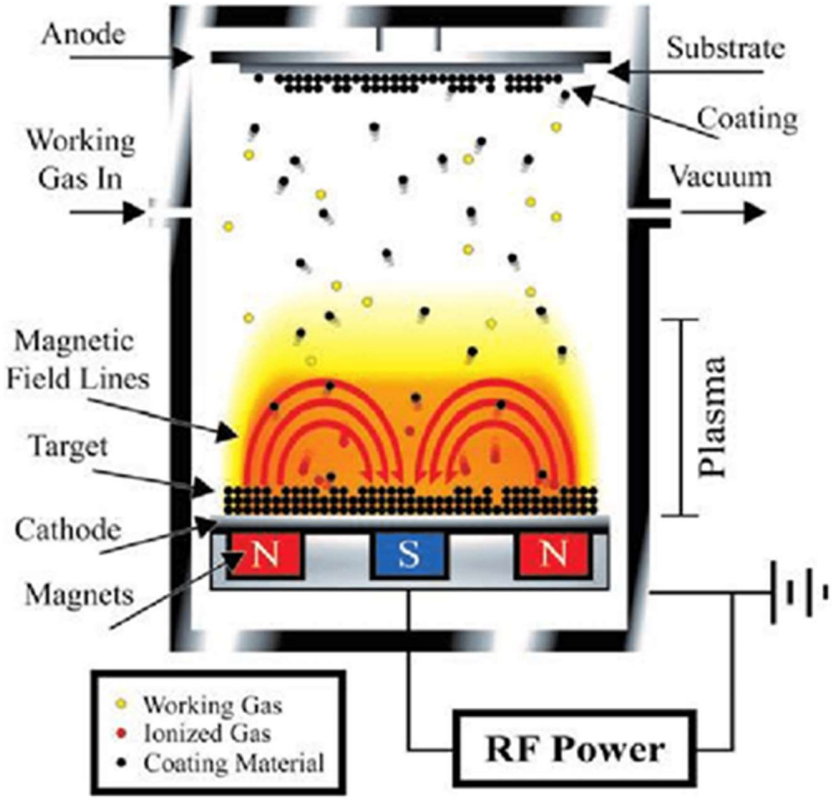

Figure 3.37. RF magnetron sputtering. [125]

3.4.2. Raman spectra of silicon coatings

The crystallinity of silicon coatings can be obtained by Raman spectroscopy as shown in Figure 3.38 [126]. Typical Raman peaks locate in the frequency range from 400 to 600 cm^{-1}, which give information of the first order scattering of the transverse optical (TO) modes of Si\Si vibrations [127]. The Raman spectrum of silicon coating can be fitted using three Gaussians. Note that Gaussian fitting is selected due to the asymmetry and broadening of Raman peaks caused by the disordering. The broad peak centred at 480 cm^{-1} corresponds to the amorphous phase. The intermediate peak centred at 505 cm^{-1} is attributed to tensile-strained Si\Si bonds at the grain boundary. The narrow and strong peak at 520 cm^{-1} originates from crystalline phase.

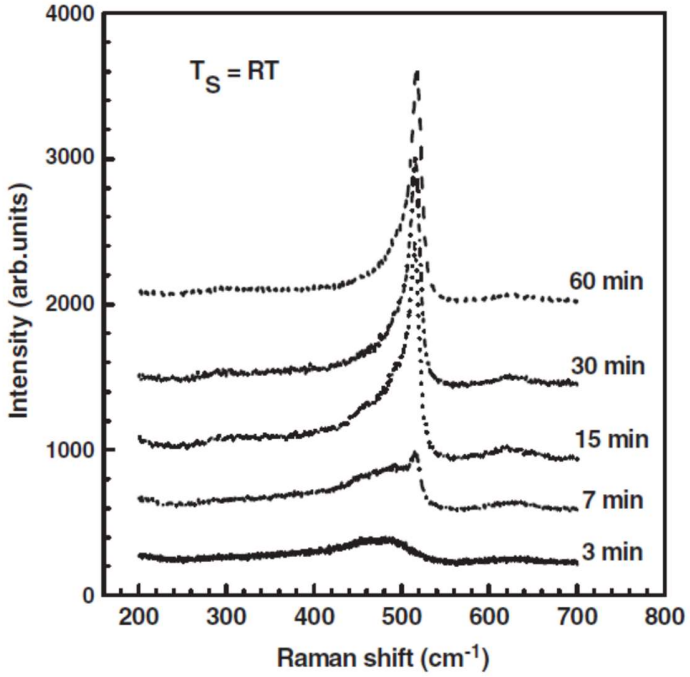

Figure 3.38. Raman spectra of silicon coatings with different crystallinity. [126]

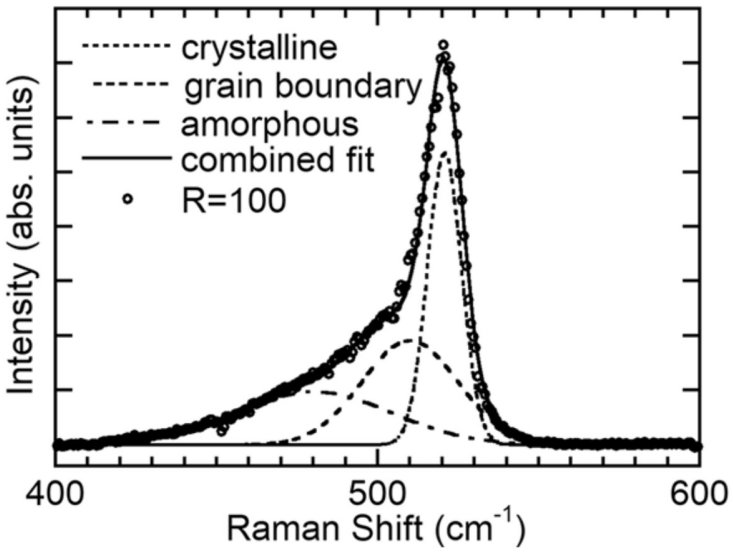

Figure 3.39. Typical Raman spectrum of silicon coatings. [128]

A typical shape fitting process of Raman spectrum is given in Figure 3.39. The crystalline content is defined as the ratio of $(A_{crystalline}+A_{boundary})/(A_{crystalline}+A_{boundary}+A_{amorphous})$, where $A_{crystalline}$, $A_{boundary}$ and $A_{amorphous}$ denote the integrated areas of crystalline, boundary, and

amorphous phases [128]. In general, the Raman intensity of silicon peak at 520 cm^{-1} will increase with increasing the crystal content.

3.5. Summary

- As indicated in the literature review, most approaches of online wear monitoring estimate wear conditions based on the multi-sensor signals which are indirectly correlated to wear, such as acoustic emission, cutting force, vibration, and motor power. Their inherent drawbacks, deriving from signal noise and lack of direct or visual wear information, always lead to an inevitable reduction in measurement reliability and accuracy. In addition, since these methods are incapable of direct application in a distinct service condition, model retraining becomes necessary, which requires extensive tests to obtain various operation parameters for estimating wear level. In comparison, highly reliable and accurate topographic analysis of surface wear can be achieved via direct wear measurement approaches in the form of two- or three-dimensional wear profiles. Currently, there are two typical modes of direct approaches widely used in industrial fields: stylus and non-contact optical profilometer. The significant advantage of the former approach is that it captures real physical depth profiles using contact trigger probes. However, it cannot provide continuous online measurements because the contact regions of moving parts are generally inaccessible during running process. The non-contact optical approach builds up a three-dimensional topographic map by collecting array signals of light interference of reflected light. Although highly accurate surface analysis at the nanoscale can be achieved for as-grown coatings via non-contact optical approach, remarkable measurement errors will appear when characterizing the tribo-tested coatings as

indicated in this study. Since the non-contact optical approach possesses high sensitivity on the light signals, tribo-induced variation of optical properties on the coating surface, which can be termed as tribo-induced polishing effect, can significantly affect reflected light signal, further leading to remarkable measurement errors. Consequently, there is a request to develop novel coating wear measurement approaches that can provide accurate wear information at the nanoscale while possessing online monitoring and high error tolerance capabilities and enabling directly implementation in various engineering fields.

- Advanced coating techniques have been increasingly applied in a wide range of tribological applications, including manufacturing, vehicles, and aeronautics. In combination with liquid lubricants, protective coatings on key mechanical components can dramatically reduce friction and extend the service lifetimes by orders of magnitude, leading to considerate materials and energy savings. Additives are the crucial components of liquid lubricants and their tribochemical products formed on coating surfaces in the form of tribofilm critically affect the wear and friction behaviors. However, the mechanisms governing the tribofilm growth on coating surfaces are not well understood since most of existing lubricating additives are developed for ferrous surfaces. It can result in severe wear and early failure of key components when using the conventional lubricating solutions. For example, when using the traditional friction modifier MoDTC, which is designed for ferrous-based surfaces, on the steel/DLC contact under ambient environment, MoDTC-derived products can cause remarkably wear acceleration on diamond-like carbon coatings (DLC). It is therefore necessary to deepen the understanding of tribochemical interactions between lubricating additives and coatings, and the growth mechanisms of

additive-derived tribofilm on coating surfaces, which can significantly contribute to developing effective lubricating solutions for diverse coatings.

Chapter 4

Materials and methods

This chapter outlines the detailed information about lubricating materials (coating, oil and additives), tribotest conditions, coating deposition methods, and analysis techniques employed in this project.

4.1. Materials

4.1.1. Additives and base oil

The base oil used in this study is PAO 4. The typical properties are listed in Table 4.1. The classic friction modifier MoDTC (molybdenum dialkyldithiocarbamate) and anti-wear additive ZDDP (zinc dialkyldithiophosphate) are employed as additives in the PAO 4. Figure 4.1 displays the molecular structures of MoDTC and ZDDP. In this study, the mechanisms of additive-derived tribofilms and their interaction with a-C:H coatings are studied by combining Raman-based method and diverse surface analysis techniques.

Table 4.1. Typical properties of PAO 4 base oil.

Properties	Typical value
Kinematic Viscosity @100°C (cSt, mm^2/s)	3.9
Viscosity Index	124
Pour Point (°C)	-57
Flash Point (°C)	204
Density @20℃ (g/cm^3)	0.82

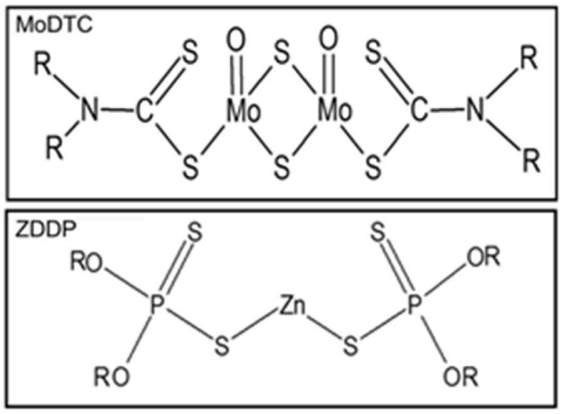

Figure 4.1. Molecular structures of MoDTC and ZDDP.

4.1.2. Coatings

The a-C:H films were deposited by a Plasma Enhanced Chemical Vapour Deposition technique (PECVD) with acetylene as gas precursor (Flexicoat 850, Hauzer Corp., Netherlands). Two kinds of substrates, n-type silicon (100) wafers (10 mm × 10 mm × 0.5 mm, Ra < 1 nm) and glass plates (25 mm × 25 mm × 1 mm, Ra < 1 nm), are employed. The a-C:H films deposited on silicon wafers were used for tribo-test, thickness quantification, and characterizations of structure and composition, while those on glass plates were for optical studies. The substrates were ultrasonically cleaned by acetone and ethanol. Before the deposition, the vacuum chamber was evacuated to a base pressure of 3.0×10^{-3} Pa and heated to 200 °C. After that, the substrate surface was etched in argon plasma at the pressure of 0.15 Pa for 5 mins. During the deposition, a pulsed DC power with bias voltage at -500 V was applied to the substrates and the chamber pressure was 0.85 Pa with acetylene as feeding gas with feeding rate at ca. 250 sccm. By controlling the deposition time, a-C:H coatings with different thickness are synthesized. Detailed information of the a-C:H film is as follows: hydrogen content of ca. 22%, hardness of ca. 21 GPa, Young's modulus of ca. 180 GPa, initial roughness of ca. 5.3 nm (Ra), and Poisson's ratio of 0.2.

A series of silicon coatings with different crystallinity were deposited on steel discs (M2 steel disc) in pure Ar atmosphere via pulsed-DC magnetron sputtering method under different deposition parameters, including gas pressure, cathode power, temperature, and substrate-target distance. Before the deposition, the vacuum chamber was evacuated to a base pressure of 6.0×10^{-3} Pa and heated to 520 ℃. During the deposition, a pulsed DC power with the frequency of 100 kHz and duty cycle of 0.8 was applied to cathode. Table 4.2 gives the detailed information of deposition parameters of silicon coatings. Here, the M2 steel is high speed steels with a hardness of 62–64 HRC. The dimension of M2 steel disc is ø 25 mm × 6 mm.

Table 4.2. Deposition parameters of silicon coatings

Sample ID	Pressure (mbar)	Power (kW)	Temp. (℃)	S-T (cm)
S-1	6.0×10^{-3}	4	520	16.5
S-2	4.0×10^{-3}	4	520	16.5
S-3	3.0×10^{-3}	4	520	16.5
S-4	4.0×10^{-3}	5	520	16.5
S-5	4.0×10^{-3}	3	520	16.5
S-6	4.0×10^{-3}	4	520	15.5
S-7	4.0×10^{-3}	4	520	20
S-8	4.0×10^{-3}	4	480	16.5

S-T, distance between substrate and target on the cathode.

4.2. Tribotest

In this study, the tribological experiments were conducted via a ball-on-disc tribometer (Bruker UMT-Tribolab) at room temperature under both dry and oil-lubricated conditions.

The samples with coatings were fixed on a reciprocating platform while employing a fixed upper ball (AISI 52100 steel, 6.35 mm in diameter, HRC 60-67) as the counterpart. In the oil-lubricated condition, base oil and oils with different additives (PAO4+0.8 wt.% ZDDP, PAO4+0.8 wt.% MoDTC, and PAO4+0.8 wt.% ZDDP and 0.8 wt.% MoDTC) were employed.

Dry tribotest conditions: a-C:H/steel contact, test time of 30 to 140 min, applied load of 1 N (580 MPa), frequency of 2.5 Hz, stroke of 2mm and ambient environment. Oil-lubricated test conditions: a-C:H/steel contact, time of 30 to 140 min, applied load of 1 N and 10 to 40 N (1.2 to 2.0 GPa), frequency of 2.5 Hz, stroke of 2mm and ambient environment.

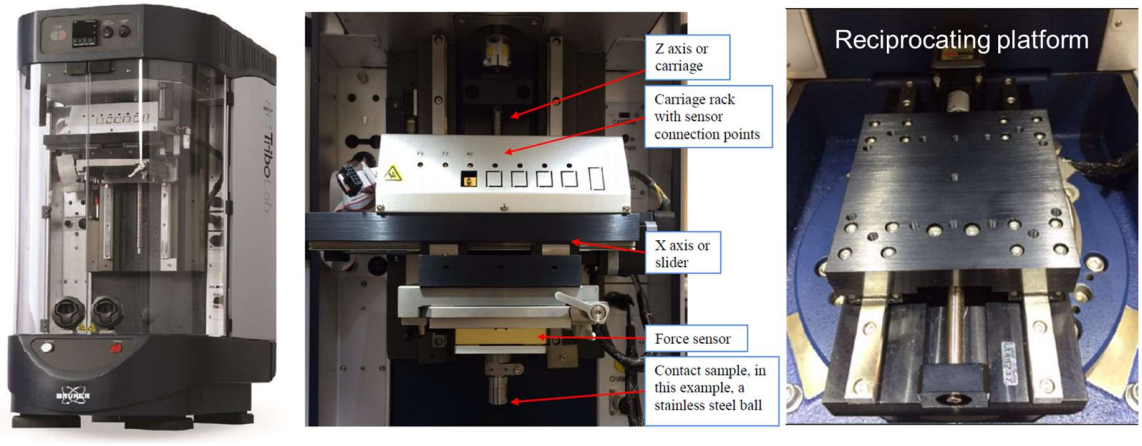

Figure 4.2. Images showing the structure of the UMT tribotester.

4.3. Raman spectroscopy

A Renishaw InVia Raman spectrometer as shown in Figure 4.3 was employed in this project. Lasers with wavelength of 488 nm and 785 nm are equipped in this equipment with the maximum lasers of 10 mW. This equipment possesses short-distance objectives of 5×, 20× and 50× and long-distance objective of 50×. Samples are fixed on the sample stage and focused. This equipment is connected to a PC for collecting and analysing data.

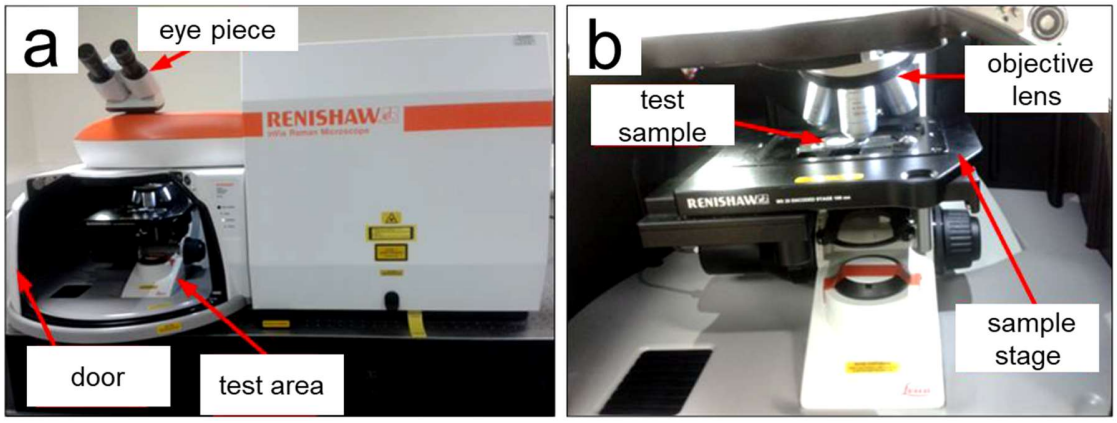

Figure 4.3. (a) Image of Renishaw InVia spectrometer. (b) Test area inside the Raman spectrometer.

Figure 4.4 shows a schematic illustration of the operating principle of the Raman spectrometer. The Raman spectrometer contains the following parts: laser sources, filters, lenses, microscope, diffraction grating and CCD camera. Scattered light is collected at 180^{o} backscattering geometry. The holographic filters blocks reflected light and allowed scattered light to go through to the diffraction grating where the light is split into different colours. The CCD camera is employed to detect the colours. The 2400 l/mm and 1200 l/mm gratings are used for the 488 and 785 nm lasers, respectively. A diffraction grating is used to separate polychromatic light into its constituent wavelengths. Raman spectrometer diffraction gratings are used to separate the constituent wavelengths of the collected Raman scatter onto different pixels of the CCD camera for detection. All Raman spectrometers will require at least one diffraction grating and will frequently be configured to contain more than one to allow the user optimum grating selection for their samples and excitation wavelength(s).

When light is scattered by molecule, the oscillating electromagnetic field of a photon induces a polarisation of the molecular electron cloud which leaves the molecule in a higher energy state with the energy of the photon transferred to the molecule. This can be considered as the formation of a very short-lived complex between the photon and molecule which is commonly

called the virtual state of the molecule. The virtual state is not stable and the photon is re-emitted almost immediately, as scattered light. In a much rarer event (approximately 1 in 10 million photons) Raman scattering occurs, which is an inelastic scattering process with a transfer of energy between the molecule and scattered photon. If the molecule gains energy from the photon during the scattering (excited to a higher vibrational level) then the scattered photon loses energy, and its wavelength increases which is called Stokes Raman scattering. Inversely, if the molecule loses energy by relaxing to a lower vibrational level the scattered photon gains the corresponding energy and its wavelength decreases, which is called Anti-Stokes Raman scattering. Quantum mechanically Stokes and Anti-Stokes are equally likely processes. However, with an ensemble of molecules, the majority of molecules will be in the ground vibrational level (Boltzmann distribution) and Stokes scatter is the statistically more probable process. As a result, the Stokes Raman scatter is always more intense than the anti-Stokes and for this reason, it is nearly always the Stokes Raman scatter that is measured in Raman spectroscopy.

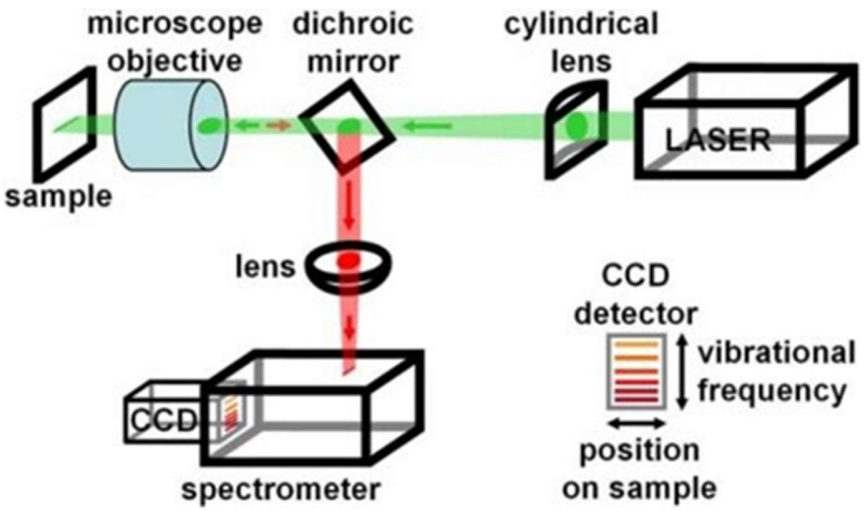

Figure 4.4. Schematic illustration of the operating principle of Raman spectrometer. [129]

In this study, samples were analysed via the short distance objective of 50×. Raman tests were conducted using 488 nm laser in two modes: i. Single spot mode: a single spectrum is

collected from a single test point on the sample. ii. Line-scanning mode: A series of spectra along the line-scanning trace are collected from different test points on the sample. In addition, peak analysis was conducted via the Renishaw WiRE software. Gaussian fitting was employed in the shape fitting of Raman peaks.

4.4. NPFLEX white light interferometer (WLI)

NPFLEX 3D non-contact optical profilometer (Bruker) was used to measure the thickness of as-grown a-C:H coatings and characterize the wear scars on tribo-tested samples. The results were analysed via Vision64 software. The optical profilometer builds up a 3D map by collecting array signals of light interference of reflected light. Since the tribo-induced variation of optical properties (i.e., reflectivity) on the top surface, termed the tribo-induced polishing effect, can affect the intensity of light signal and further results in the remarkable measurement deviation of the optical profilometer. To avoid the influence of the tribo-induced polishing effect on the measurement accuracy of the optical profilometer, an optical signal synchronization layer of iridium with uniform thickness was deposited on the tribo-tested sample by DC magnetron sputtering to provide a top surface with consistent optical properties. Then, the optical profilometer was used to characterize the tribo-tested samples. This improved profilometry with an optical signal synchronization layer of iridium was used to provide an accurate wear depth as a standard reference. A typical test result of the wear scar obtained by Vision64 is shown in Figure 4.5.

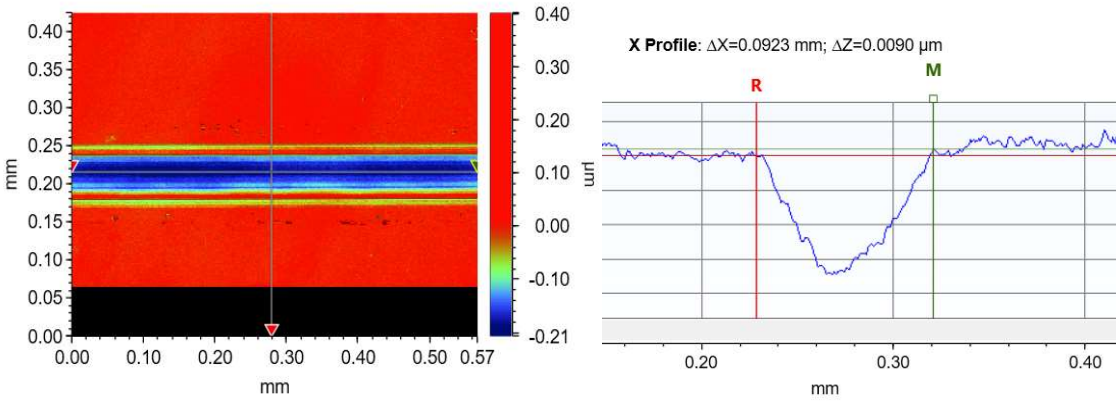

Figure 4.5. Typical NPFLEX wear measurements of wear scar.

4.5. Contact Profilometry

In this study, Talysurf 120L contact profilometer was employed to verify the feature information of wear profile (e.g., depth rising) rather than the accuracy as its low resolution could result in obvious measurement errors. In addition, surface wear profile was collected and analyzed using Talysurf ultra software. A typical wear profile is presented in Figure 4.6.

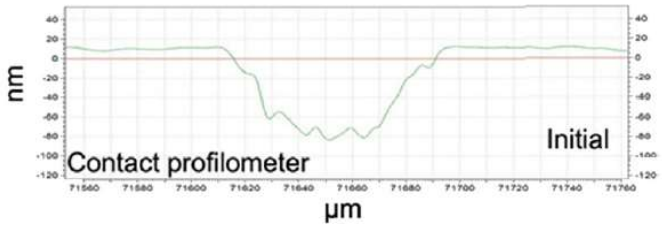

Figure 4.6. Wear profile obtained by contact profilometer.

4.6. Coating deposition system

Coating deposition was performed with the Hauzer Flexicoat 850 multi-purpose PVD/PECVD coatings system as displayed in Figure 4.7. This system is equipped with multifunction, including the closed field unbalanced magnetron sputtering, cathodic arc evaporation (CARC), high power impulse magnetron sputtering (HiPIMS), nanoparticle

source, high powered pulsed microwave source, and PECVD together with advanced plasma diagnostics including optical and Langmuir probes. Figure 4.8 displays the cathodes arrangement of Hauzer Flexicoat 850. This coating deposition system has an effective volume of 500mm x 500mm height and enables the application of diverse deposition methods in one batch.

Figure 4.7. Hauzer Flexicoat 850 coating deposition system in the School of Mechanical Engineering at the University of Leeds.

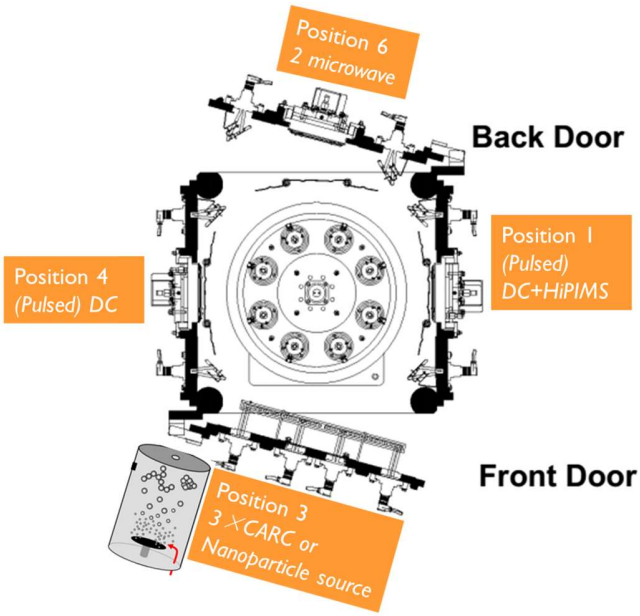

Figure 4.8. Schematic illustration of the cathode arrangement of Hauzer Flexicoat 850 in

the School of Mechanical Engineering at the University of Leeds.

4.7. Focused ion beam (FIB)

A focused ion beam (FIB, FEI Helios G4 CX DualBeam FIB-SEM) was used to prepare thin cross-sectional lamellar specimens of friction contact area for the characterizations of transmission electron microscopy (TEM), electron energy loss spectroscopy (EELS), and energy dispersive X-ray spectroscopy (EDS). Prior to FIB milling, the contact area was coated by a layer of iridium (20 nm) to eliminate contaminations. Then, samples were transferred into FIB-SEM chamber and coated by a thick Pt film (~ 1 μm) in order to protect coating structure during FIB milling (low-kV Ga+ ion milling).

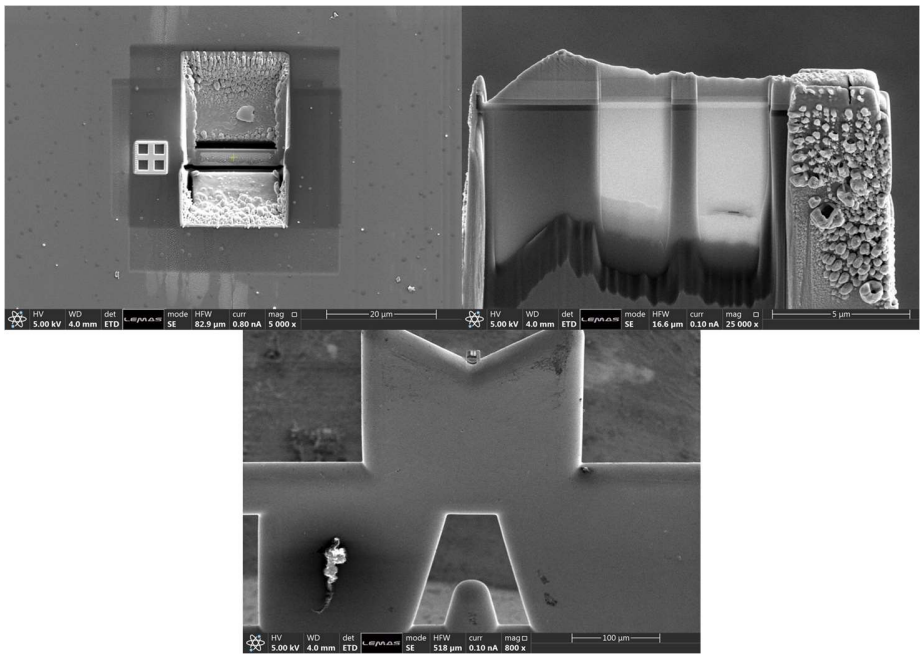

Figure 4.9. Typical FIB preparation section for TEM.

4.8. Transmission electron microscopy (TEM) / Electron energy loss spectroscopy (EELS) / Energy dispersive X-ray spectroscopy (EDS)

FEI Titan3 Themis 300 TEM/STEM (Scanning transmission electron microscopy) equipped with Gatan Quantum ER energy filter and energy dispersive X-ray spectroscopy (EDS) was employed for TEM characterization, elemental analysis, and electron energy loss spectroscopy (EELS) as shown in Figure 4.10. HAADF (high-angle annular dark-field) image was acquired in the STEM mode. Note that EELS in STEM mode could provide detailed information of bonding structure in the atomic resolution.

Gaussian peak fitting of EELS spectra was adopted to quantify the bonding fractions within the energy window of 280-310 eV through the Gatan DigitalMicrograph software. To reduce the complexity and instability during fitting, two Gaussian peaks are fitted to π* (C=C) and σ* (C-H) bonds and the residual bond fraction is then assigned to σ* (C-C). To calculate the sp^2 bond (C=C) fraction in the C-K edge, the integrated area of π* peak centred at ~ 285.5 eV is normalized to the total area (π* + σ*) integrated in the window of 280-310 eV and the ratio is then referenced to the standard value (~ 0.119) of highly oriented pyrolytic graphite (HOPG, 100% sp^2-C bonds), according to the following equation [128, 129]:

$$sp^2\% = \frac{A_s\,(\pi^*)/A_s(total)}{A_{HOPG}\,(\pi^*)/A_{HOPG}(total)} \qquad 4\text{-}1$$

where $A_s\,(\pi^*)$ and $A_{HOPG}\,(\pi^*)$ are the areas of π* peaks of the samples and HOPG, while A_s (total) and A_{HOPG} (total) are the areas integrated in the energy region of 280-310 eV. The

bond fraction of σ^* (C-H) at ~ 287 eV are also obtained by this method. EDS spectra were obtained using line-scanning mode and mapping mode. Line-scanning mode was used to verfiy the evolution of element concentraion and mapping modes were employed to verify chemical composition.

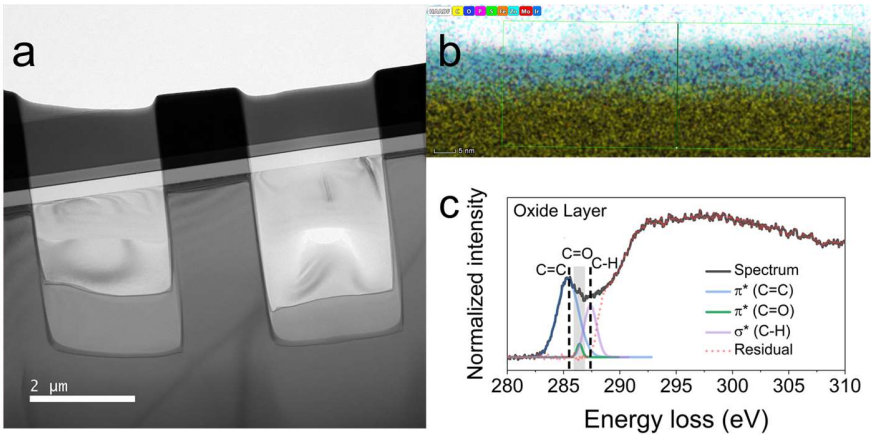

Figure 4.10. (a) TEM images of cross section fabricated by FIB. (b) EDS image. (c) EELS spectrum.

4.9. UV−vis−NIR spectrophotometer

UV-vis-NIR spectrophotometer (PerkinElmer Lambda 950) was employed to study the optical properties of a-C:H films deposited on glass plates. PerkinElmer Lambda 950 is an ultra-high UV-vis-NIR spectrophotometer withs an operating range of 175-3000 nm. It is equipped with capabilities as following: i, 2D detector (PMT and PbS Detectors, full-range wavelength coverage). ii, Universal Reflectance Accessory (Angles 8-65° with a 0.5° step size, horizontal mounting, 185-3100 nm wavelength range, Spot size up to 5×5 mm). iii, Integrating sphere (highly reflective spectralon coating, 200 to 2500 nm wavelength range, sample size up to 150mm^2).

Figure 4.11. PerkinElmer Lambda 950 UV-vis-NIR spectroscopy in the School of Chemical and Process Engineering at the University of Leeds.

Chapter 5

Coating Thickness Quantification Methodology

In this chapter, a coating thickness quantification method was established by introducing a Raman sensing layer of silicon under the target coating of a-C:H (hydrogenated amorphous carbon), which was further employed in chapter 6 to measure the coating wear in the dry and oil-lubricated condition. The chapter is divided into three sections. Section one constructs the non-linear relationship between the a-C:H thickness and Raman intensity of silicon underlayer based on Beer's law. Section two compares the thickness of as-grown a-C:H films obtained by Raman-based method and non-contact optical profilometer. Finally, section three summaries the main findings in this chapter.

5.1. Construction of coating thickness quantification method

A schematic of the wear quantification method used in this study is shown in Figure 5.1a. In the method developed in this project, Si wafers served as Raman signal provider due to the high intensity of silicon 1st band at 520 cm^{-1} and a-C:H coatings were deposited on top and employed as anti-wear and light attenuating layer. Since the light intensity will be attenuated in the a-C:H due to absorption (A) and reflection (R), the Raman intensity of silicon signal (I_s) from the silicon substrate depends on the transmittance values of both incident light (I_o) and scattered light and is given based on Beer's law by

$$I_s = I_o \beta T_o T_1 \qquad 5\text{-}1$$

where β is the light scattering rate, $I_o\beta$ is the Raman intensity of silicon 1st band of silicon substrate (Figure 5.1b), and T_o and T_1 are transmittance values of incident light and scattered light, respectively. Additionally, it should be pointed out that there exists a shift of light wavelength on the sites of Raman scattering. As shown in Figure 5.1a, b, when employing silicon substrate as Raman signal provider, the wavelength (λ_0, 488 nm) of the incident light will shift to 500 nm (λ_1, scattered light), according to the equation [132]:

$$\lambda_1 = \frac{1}{\frac{1}{\lambda_o} - \nu} \qquad 5\text{-}2$$

where ν is Raman shift (520 cm $^{-1}$ for silicon 1st band).

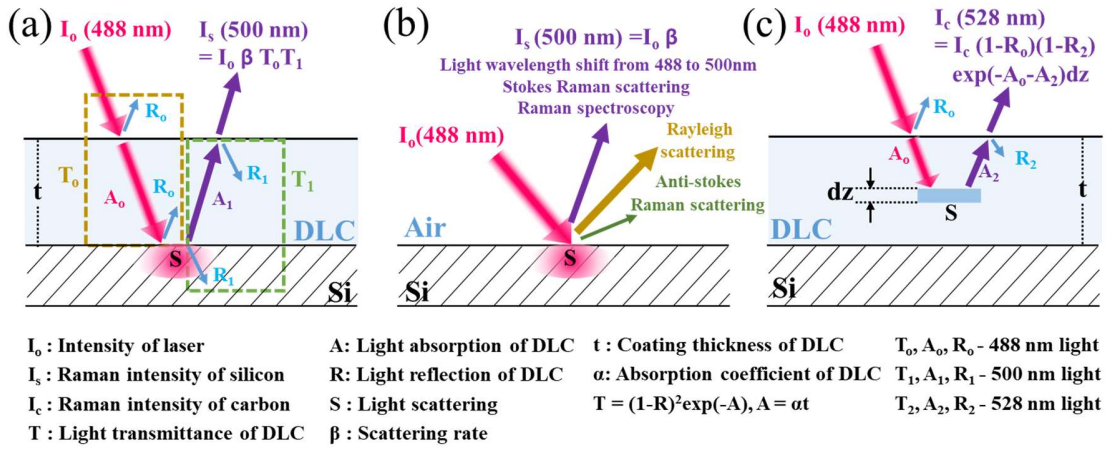

Figure 5.1. Schematic illustration of the coating thickness quantification methods under dry friction.

By substituting the transmittance (T) in the equation 5-1 with the following expression [133]:

$$T = (1-R)^2 exp(-A) = (1-R)^2 exp(-\alpha t) \qquad 5\text{-}3$$

where α is the light absorption coefficient and t is the thickness of a-C:H coating (unit: μm), the relationship between I_s and t can be constructed by:

$$I_s = I_o\beta(1-R_o)^2(1-R_1)^2 exp(-\alpha_o-\alpha_1)t \quad 5\text{-}4$$

where R_o and α_o are the reflectivity and absorption coefficient of a-C:H for incident light (488 nm), and R_1 and α_1 are that for scattered light (500 nm). The thickness of a-C:H can be obtained through rearranging the equation 5-4 as the expression:

$$t = -\frac{1}{\alpha_o+\alpha_1} ln \frac{I_s}{I_o\beta(1-R_o)^2(1-R_1)^2} = \frac{-1}{\alpha_o+\alpha_1}[lnI_s - lnI_o\beta - ln(1-R_o)^2(1-R_1)^2] \quad 5\text{-}5$$

Therefore, via independently measuring the R_o, R_1, and $I_o\beta$, and obtaining the absorption coefficients, the thickness of a-C:H coatings can be calculated based on I_s. Here, the absorption coefficient (α) of a-C:H can be obtained by

$$\alpha = \frac{1}{-t} ln \frac{T}{(1-R)^2} \quad 5\text{-}6$$

which derives from equation (3) and t is measured by optical profilometer.

For comparison, the calculated thickness of a-C:H based on the Raman signal of carbon are also provided according to the previous studies [59, 60]. The Raman intensity of carbon signal (I_G, G band at 1555 cm $^{-1}$) can be calculated by integrating contribution from each slice over thickness t (Figure 1c) by

$$I_G = I_{c\infty}(1-R_o)(1-R_2)[1-exp(-\alpha_o-\alpha_2)t] \quad 5\text{-}7$$

which can be rewritten as

$$t = \frac{-1}{\alpha_o+\alpha_2} ln\left[1 - \frac{I_G}{I_{c\infty}(1-R_o)(1-R_2)}\right] \quad 5\text{-}8$$

where $I_{c\infty}$ is the intensity obtained at saturation for infinitely thick layer, R_o and α_o are the reflectivity and absorption coefficient of a-C:H for incident light (488 nm), and R_2 and α_2 are the reflectivity and absorption coefficient of a-C:H for incident light (528 nm for the G band of carbon signal). Since G peak arises from the stretching vibration of all sp^2 sites in both aromatic rings and C=C chains while D peak only derives from sp^2 sites in rings, G peak intensity (I_G) is employed to quantify the thickness of a-C:H coatings in this study [59].

5.2. Thickness quantification of as-grown a-C:H coatings

The a-C:H coatings with different thicknesses were deposited on silicon wafers and glass plates in the same batches using the PECVD method. For transmittance and reflectivity acquisitions, the UV-vis-NIR spectroscopy was employed to characterize the samples with a-C:H deposited on glass plates, and the spectra in the wavelength region 400 to 600 nm were displayed in Figures 5.2a and b. With increasing the thickness of a-C:H coatings, a significant decrease in transmittance values was observed, while the reflectivity values fluctuated between 19 % and 25%. Table 5.1 summarizes the optical parameters at the targeted wavelength (488, 500, 528 nm), which will later be used to calculate the coating thickness.

Figures 5.3a and b display the Raman spectra of silicon 1st band and carbon band of samples (a-C:H coatings of different thicknesses deposited on silicon wafers). The Raman intensity of silicon signal corresponds to the peak value of silicon 1st band, while that of carbon signal (G peak) could be obtained through Gaussian fitting. As shown in Figure 5.3c, two Gaussian peaks fitting is used in the shape fitting of the carbon band as this works

better for hydrogenated amorphous carbon, especially for condition with a photoluminescence background [67].

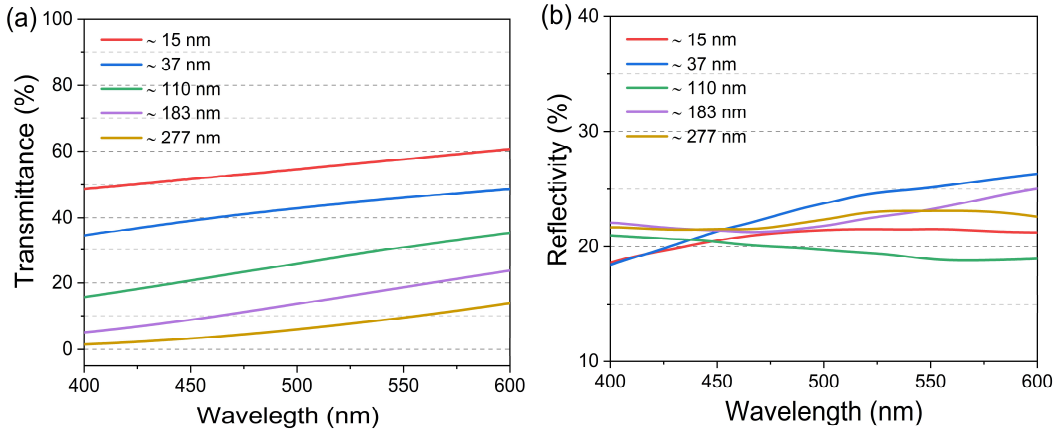

Figure 5.2. Transmittance spectra (a) and reflectivity spectra (b) of as-grown a-C:H films of different thicknesses deposited on a glass substrate.

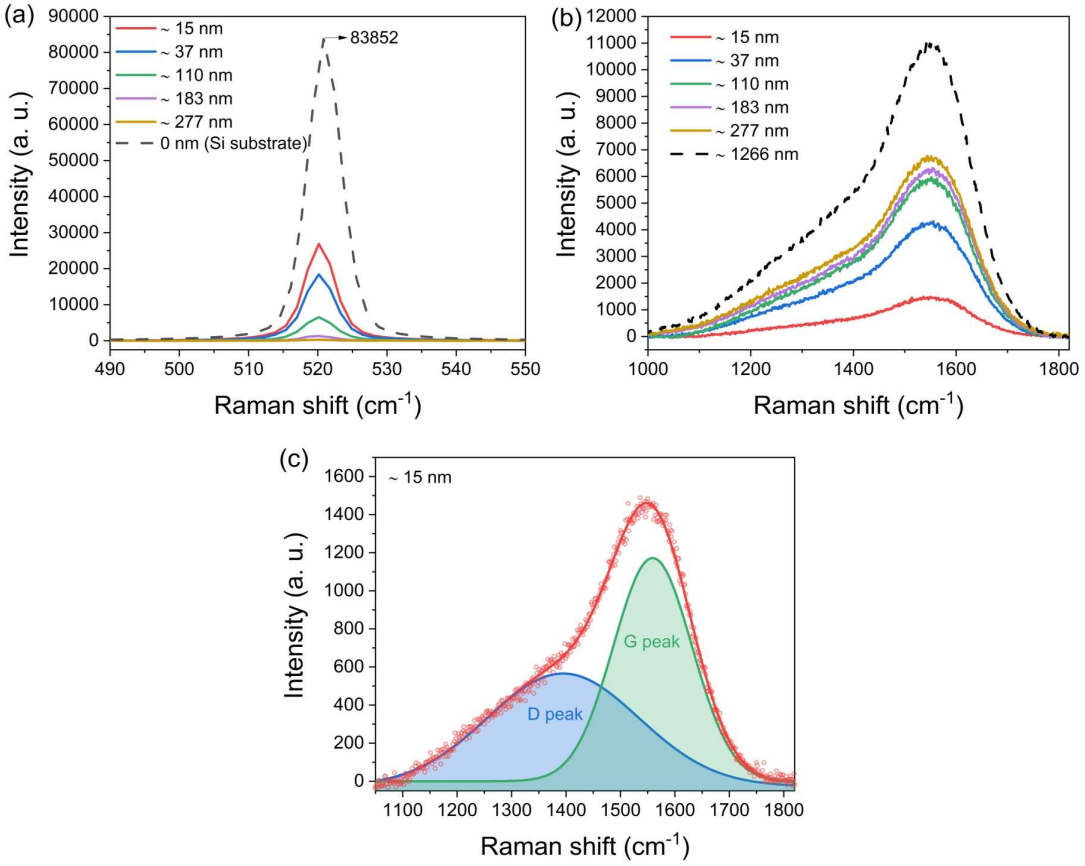

Figure 5.3. Raman spectra of as-grown a-C:H films of different thickness deposited on silicon wafers (a, silicon 1st band; b, carbon band), and fitting curves of carbon band by two Gaussians (c).

Once the optical parameters of a-C:H coatings were obtained (Table 5.1), the thickness could then be calculated based on the Raman signals according to equations (5.5) and (5.8). Figures 5.4a and b summarizes the calculated thickness based on I_S and I_G, and measured values by a non-contact optical profilometer. The calculated thickness of a-C:H coatings showed good alignment with that of the optical profilometer. Furthermore, I_G increased exponentially with the a-C:H thickness, while I_S showed an opposite trend. Additionally, the silicon wafer was partially marked for measuring the thickness of a-C:H films by NPFLEX 3D non-contact optical profilometer as shown in Figure 5.5.

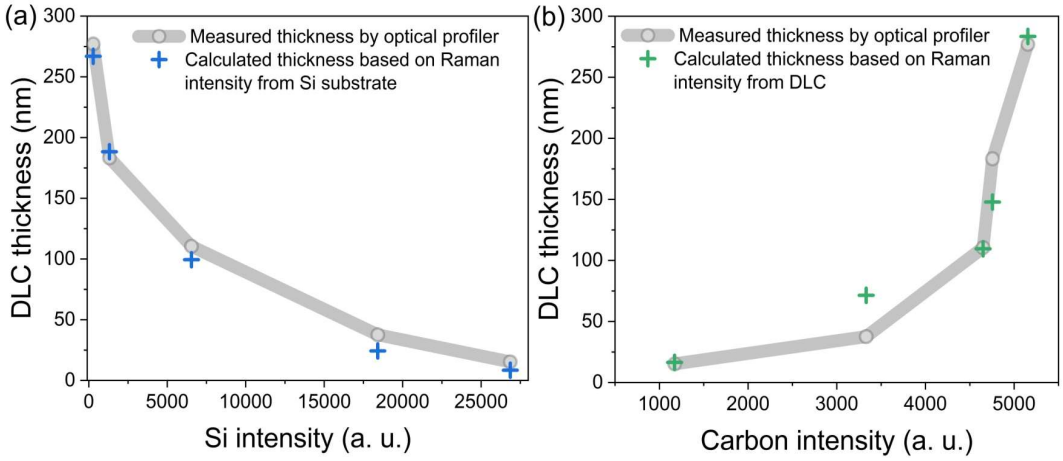

Figure 5.4. Comparison between the measured thickness of as-grown a-C:H films by optical profilometer and the calculated thickness based on Raman intensity of silicon band (a) and G peak of carbon band (b).

Table 5.1. Optical parameters of samples with a-C:H coatings of different thickness deposited on glass plates.

Thickness(nm)	T_o (%)	T_1 (%)	T_2 (%)	R_o (%)	R_1 (%)	R_2 (%)	α_o (cm^{-1})	α_1 (cm^{-1})	α_2 (cm^{-1})
15.3±1.6	53.88	54.57	56.27	21.34	21.45	21.52	9.04×10^4	8.01×10^4	5.89×10^4
37.6±2.7	42.04	42.84	44.66	23.24	23.81	24.74	8.97×10^4	8.07×10^4	6.32×10^4
110.4±2.4	24.61	25.83	28.65	19.87	19.71	19.33	8.68×10^4	8.28×10^4	7.43×10^4
183.3±3.0	12.38	13.56	16.4	21.55	21.82	22.66	8.75×10^4	8.21×10^4	7.05×10^4
277.1±2.3	5.20	5.94	7.54	22.03	22.36	23.07	8.87×10^4	8.36×10^4	7.43×10^4

Note: T_o, R_o, and α_o for 488nm light; T_1, R_1, and α_1 for 500nm light; T_2, R_2, and α_2 for 528nm light. The thickness is measured by non-contact optical profilometer.

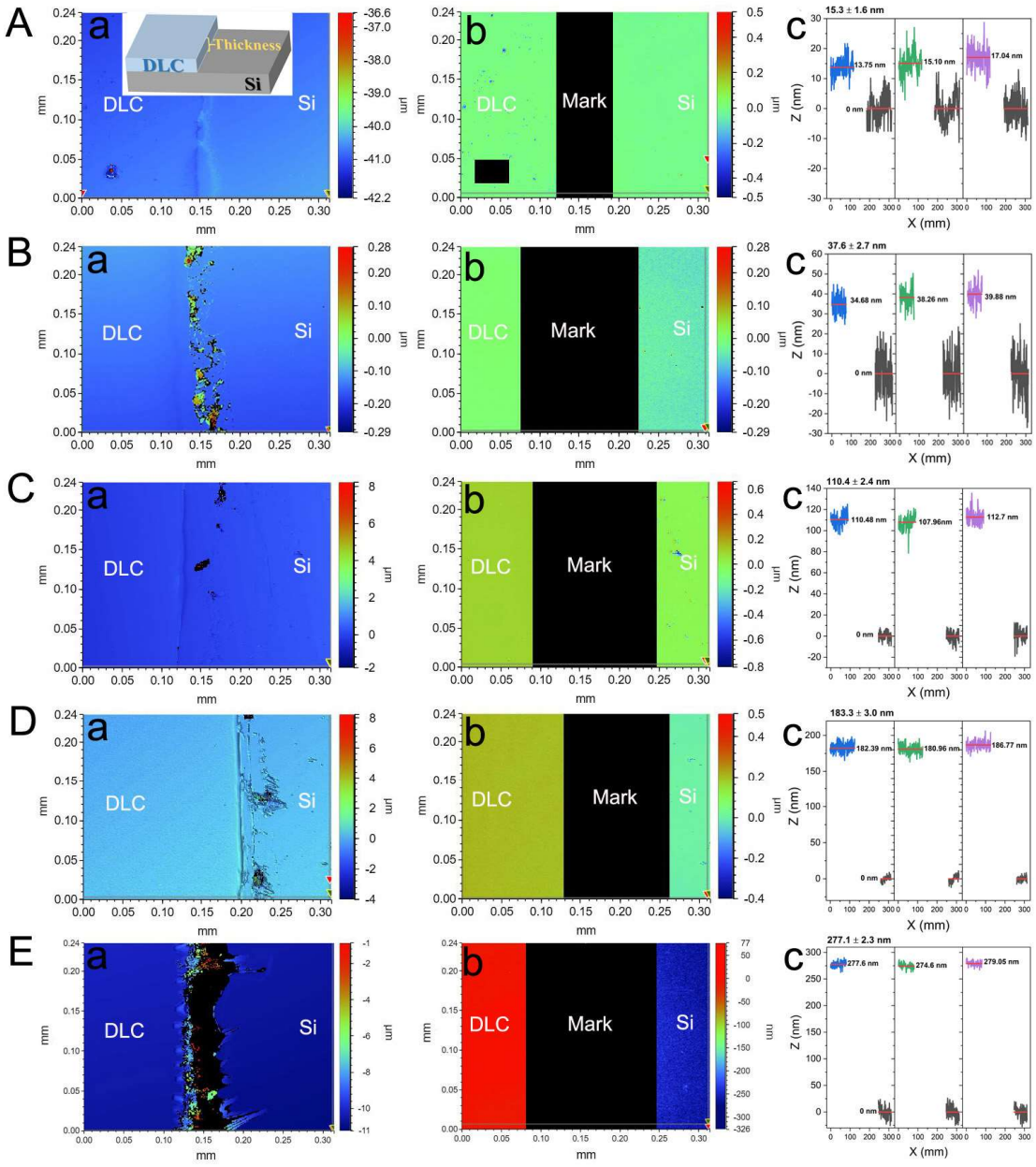

Figure 5.5. 3D optical microscopy images of samples with a-C:H coatings of different thickness deposited on Si wafers (A, 15.3 nm; B, 37.6 nm; C, 110.4 nm; D 183.3 nm; E, 277.1 nm) and the corresponding step height values (c).

5.3. Summary

The coating thickness quantification method presented in this chapter is based on a bilayer structure: a top target layer of a-C:H film is considered as a light attenuating while an

underlayer of silicon serves as Raman-sensing layer. The main findings are summarized as below:

1. Via independently measuring the R_o, R_1, and $I_o\beta$, and obtaining the absorption coefficients of a-C:H, a-C:H thickness can be calculated based on I_s.
2. The a-C:H thickness decreased logarithmically with increasing Raman intensity of silicon.
3. The calculated thickness values of a-C:H coatings obtained by the Raman-based method show good alignment with that of the optical profilometer.

Chapter 6

Wear measurement of a-C:H coating in dry and oil-lubricated conditions

In this chapter, the developed Raman-based coating thickness quantification method is applied to quantify coating wear in dry and oil-lubricated conditions. In the first section of this chapter, a tribo-tested sample was thoroughly investigated to verify the accuracy of the proposed method and error tolerance capacity by combining Raman, FIB, TEM, EELS and profilometers. In sections two and three, the proposed method is applied to quantify coating wear in dry and oil-lubricated conditions, respectively. Finally, section four summarises the main results.

6.1. Wear measurement of the a-C:H coating from a dry friction test

Tribological tests, with time ranging from 10 to 110 min, were performed directly on the sample (a-C:H of 277 nm thickness on a silicon wafer) at the applied load of 1 N (~ 550 MPa), the velocity of 10 mm/s, the room temperature around 25 °C, and atmospheric environment. Figure 6.1 shows the corresponding friction curves and optical images of middle areas of wear scars. To verify the accuracy and error tolerance capacity of the coating thickness quantification method, a typical sample (90 mins) was thoroughly investigated in this section, and the results were compared with other measurement methods to reveal the influence of tribo-induced effects on wear measurement accuracy.

Note that the tribo-induced effects can cause measurement errors for some methods (e.g., optical profilometer and Raman method based on carbon signals). Therefore, it is necessary to develop a method which is hardly affected by tribo-induced effects. This is defined as the error tolerance capacity in this thesis.

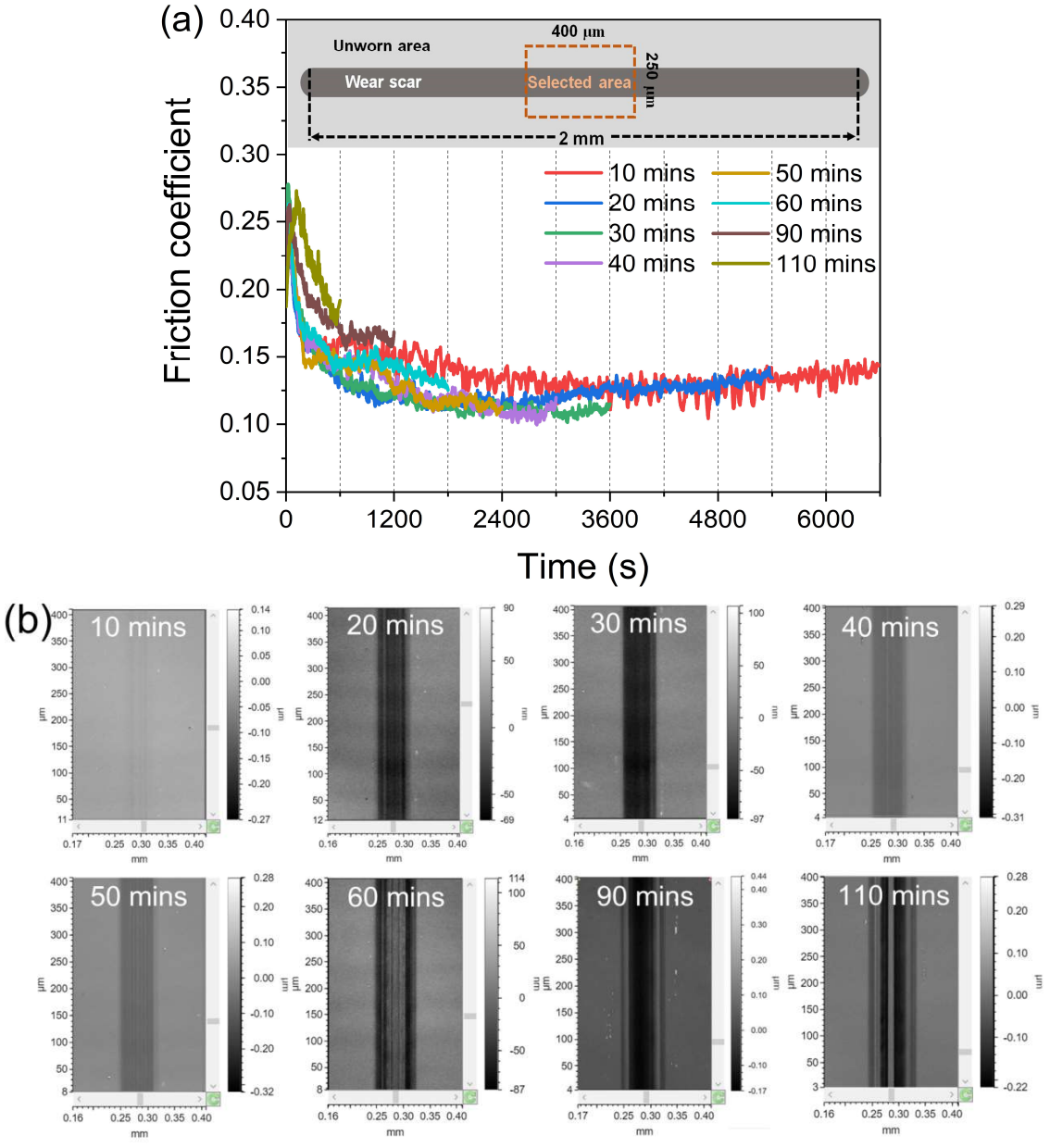

Figure 6.1. Friction curves of a-C:H film deposited on silicon wafer under different test time in the dry friction (a) and 3D optical microscopic images of the middle areas of wear scars (b).

6.1.1 Coating wear quantification via Raman spectroscopy

As shown in Figure 6.2a, a line-scanning Raman spectroscopy was conducted across the wear track, and the spectra of silicon and carbon signals are presented in Figures 6.2b and c, respectively. Figure 6.2d gives the corresponding Raman intensity values of silicon bands and carbon G peaks and A_D/A_G ratios (area ratios of D peak and G peak). Then, the coating thickness values across the wear scar could be given according to the equation (5.5) and (5.8). After subtracting the thickness value of as-grown a-C:H, the wear profile curves were obtained and displayed in Figure 6.2e. It could be observed that, at the edges of the wear scar, the wear profile deriving from the silicon signal compared well with that of the carbon signal. However, as approaching the centre region, the wear profile based on carbon signal displayed a sharp rise of coating height, while that corresponding to silicon signal displayed a consistent downward trend.

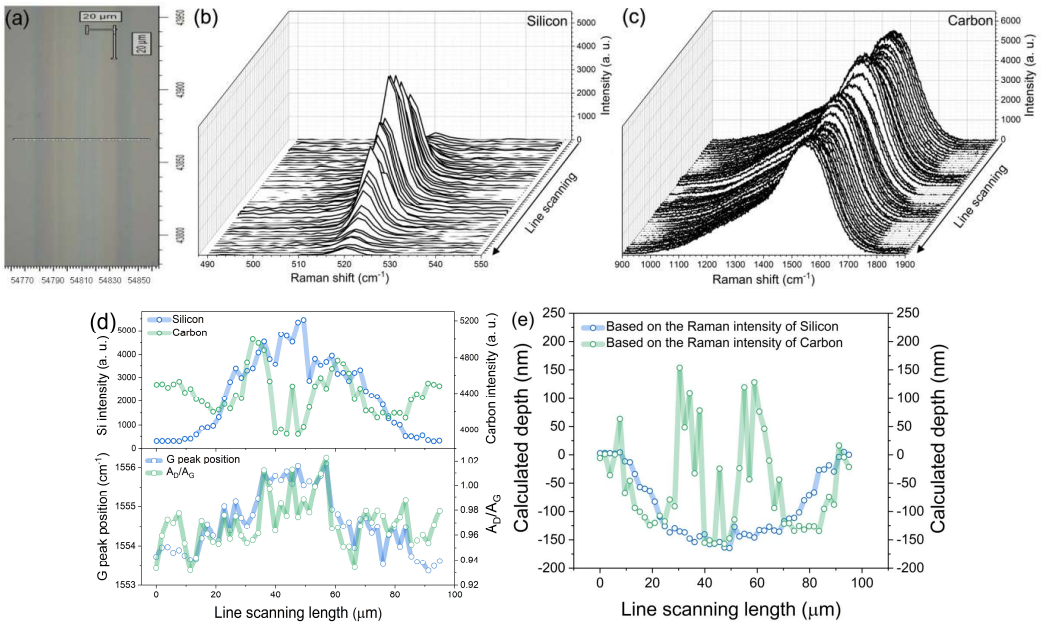

Figure 6.2**.** Detailed information of data processing based on Raman spectra of silicon and carbon bands. (a) Optical image of line-scanning trace of Raman spectroscopy across the wear track (tribo-test time: 90 mins). (b) Raman spectra of a series of silicon bands obtained from line-scanning. (c) Raman spectra of a series of carbon bands obtained from line-scanning. (d) Intensity of silicon bands, intensity and position of G peak of carbon

bands, and area ratios of D peak and G peak (A_D/A_G). A_D/A_G increases obviously in the centre region of wear track indicating the increase of sp^2 fraction. (e) Calculated wear profile curves based on the Raman intensity of silicon signal and carbon signal.

6.1.2 Coating wear quantification via profilometers

To validate the results based on Raman signals of silicon and carbon, a non-contact optical profilometer and contact profilometer were used to characterize the same sample, as shown in Figure 6.3. It is well known that a non-contact optical profilometer builds up a 3D map by collecting array signals of light interference of reflected light (for example, the highest points on the surface will cause interference first). Due to its high sensitivity towards the optical signal, the variation of optical properties (i.e., reflectivity) on the top surface, arising from tribo-induced polishing effect [134-136], could affect the intensity of the light signal, resulting in coating height mismatch with the actual profile.

As shown in Figures 6.3b and e, it was found that after depositing an iridium layer (~ 20 nm in Figure 6.4) the height spikes emerging in the wear profile disappeared. The iridium layer could provide a top surface with consistent optical properties. Here, the contact profilometer was employed to verify the feature information of wear profile (e.g., height rising) rather than the accuracy as its low resolution could result in obvious measurement errors. As shown in Figure 6.3c, the measured result of the contact profilometer confirmed the absence of height rising inside the wear scar. Since the width values obtained by contact profilometer is close to that of non-contact optical profilometer (90 μm of contact profilometer vs 87 μm of non-contact optical profilometer), the height spikes appearing in the edge should be due to the low resolution of the measuring mode of the contact profilometer.

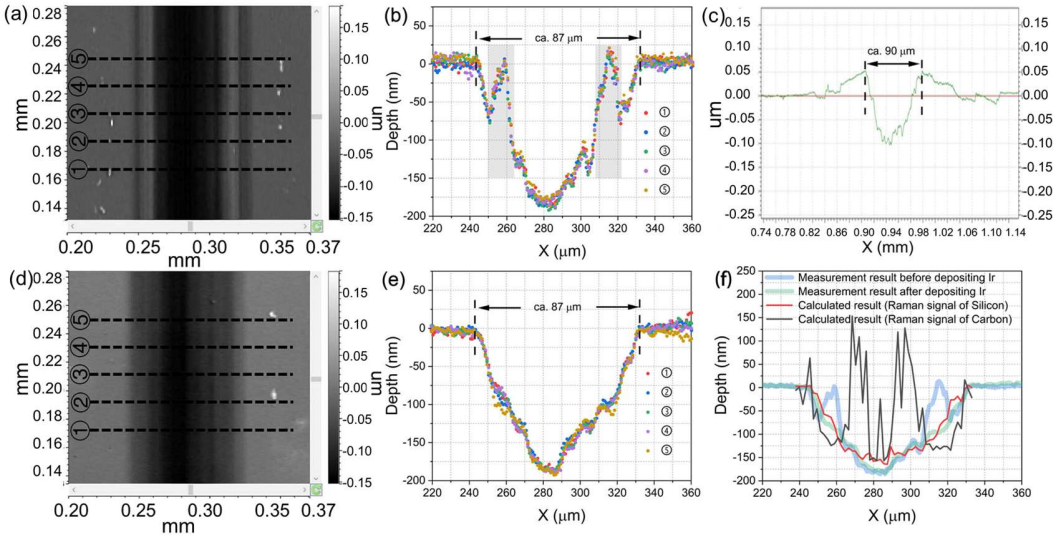

Figure 6.3. (a) 3D optical image of wear scar after 90 mins tribo-test. (b) Wear profile curves of marked lines in (a) obtained by non-contact optical profilometer. (c) Wear profile curve obtained by contact profilometer. (d) 3D optical image of wear scar of the same sample in (a) with iridium layer deposited on top. (e) Wear profile curves of marked lines in (d) obtained by non-contact optical profilometer. (f) Comparison between calculated wear profile derived from Raman intensity of silicon and carbon bands and measured wear profile characterized by non-contact optical profilometer (before and after depositing iridium layer on top of a-C:H).

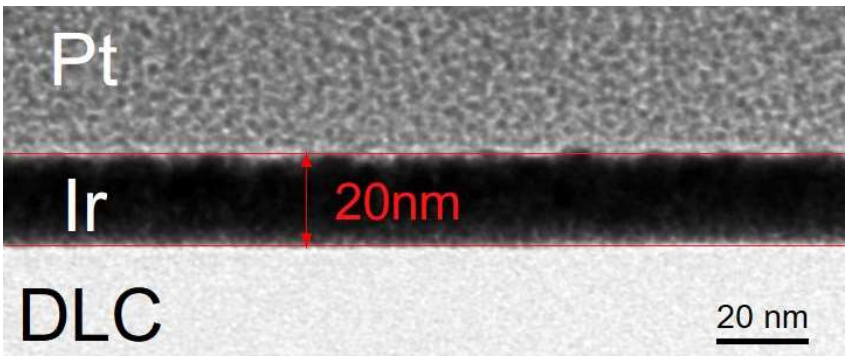

Figure 6.4. HRTEM image of cross-sectional morphology of the a-C:H surface with iridium and platinum layers. The thickness of iridium is ca. 20 nm which is employed to provide a top surface with consistent optical properties.

6.1.3 Coating wear quantification via TEM/FIB

To further verify the results of the optical profilometer, FIB with the in-situ lift-out technique was used to fabricate lamellar specimens in three typical areas of wear scar for

obtaining the actual coating thickness by a combination of TEM characterization (Figures 6.5-6.9). Figure 6.7a shows the SEM image of the lamellar specimen (FIB) in the centre area marked in Figure 6.5. Figures 6.7b and c display the corresponding TEM images and the actual coating thickness values were measured at intervals of 300 nm along the horizontal direction. Furthermore, the same process was employed to characterize the coating thickness in the side and unworn areas, as shown in Figures 6.8 and 6.9. Figure 6.6 includes the results of the non-contact optical profilometer (with iridium layer), TEM (FIB), and our quantification method for comparison. It was confirmed once again that there was no height spike in the side area as shown in Figure 6.6b. Meanwhile, it is suggested that after depositing iridium on the surface of tribo-tested sample, the optical profilometer could be used to provide the accurate wear depth and this method will be employed as standard reference to verify the results based on Raman signal in this study.

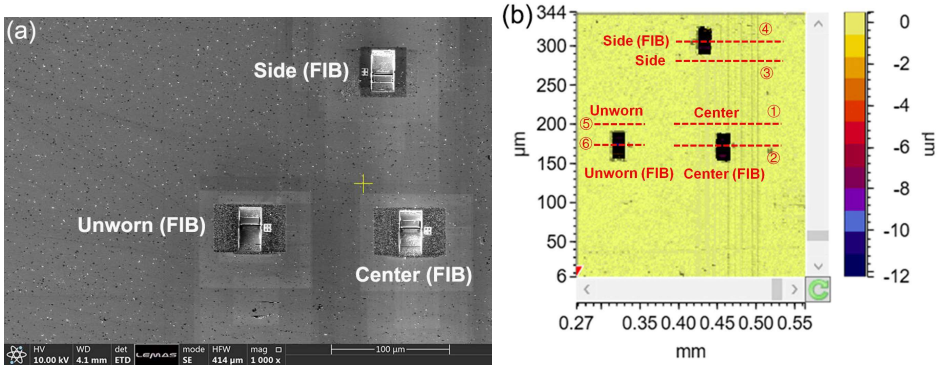

Figure 6.5. SEM image of wear scar after 90 mins tribo-test (a) and the corresponding 3D optical image obtained by optical profilometer (b). Three typical positions (centre, side and unworn areas of wear scar) were selected to provide FIB samples. A non-contact optical profilometer was used to locate actual FIB positions and give wear profile curves across and beside the FIB areas.

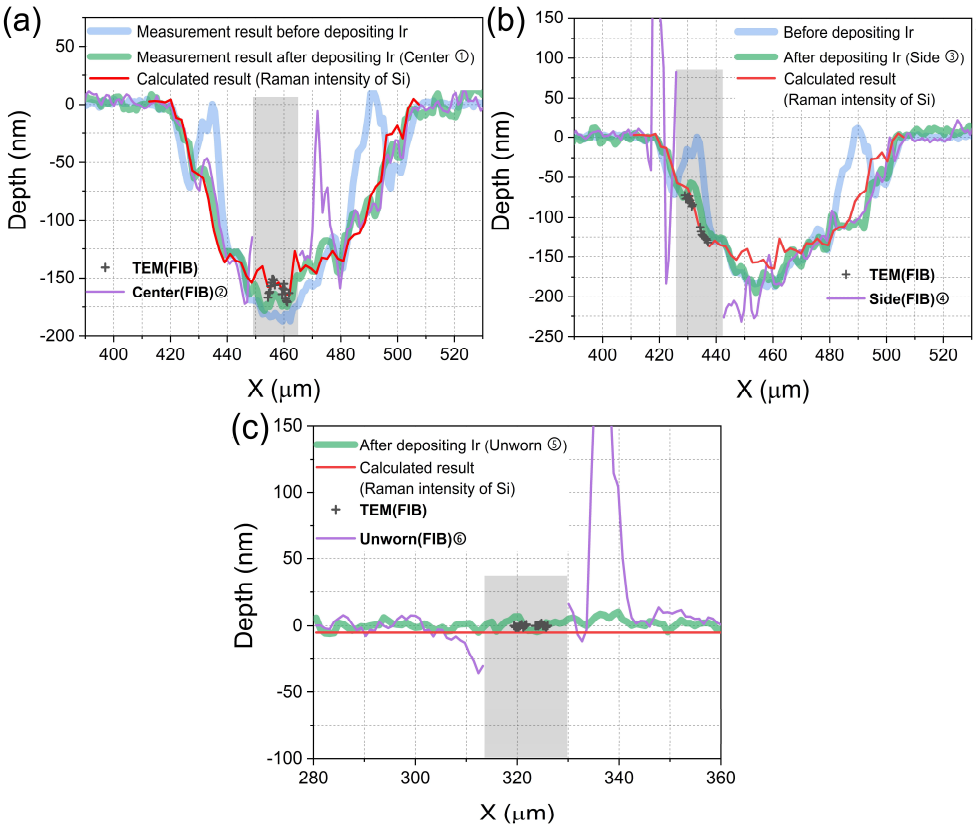

Figure 6.6. Comparison of the wear profile curves obtained by different methods (90 mins tribo-test). Non-contact optical profilometer: wear profile curves before (blue line) and after depositing iridium layer (green line), and wear profile curves in the FIB positions (purple line). Wear quantification method based on the Raman intensity of silicon signal (red line). Combination of FIB, SEM, and TEM measurements: actual thickness values (+) in the marked areas of Figure 8. Grey areas are corresponding to targeted FIB areas.

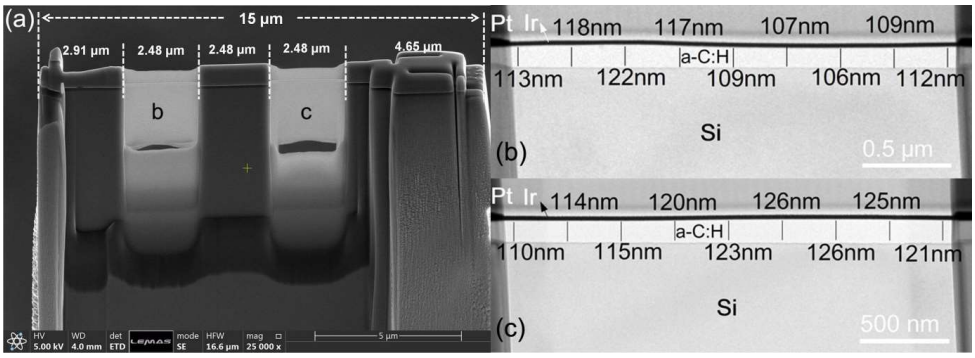

Figure 6.7. SEM image (a) of cross-sectional morphology of centre area and the corresponding TEM images ((b) and (c)) in the marked areas as shown in (a).

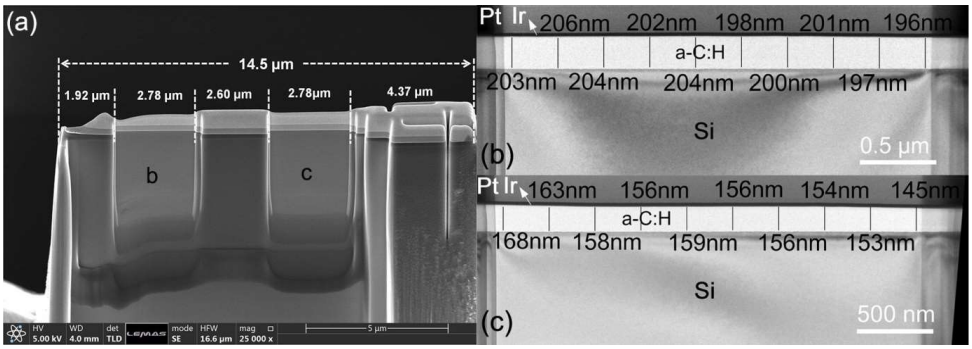

Figure 6.8. SEM image (a) of cross-sectional morphology of side area and the corresponding TEM images ((b) and (c)) in the marked areas as shown in (a).

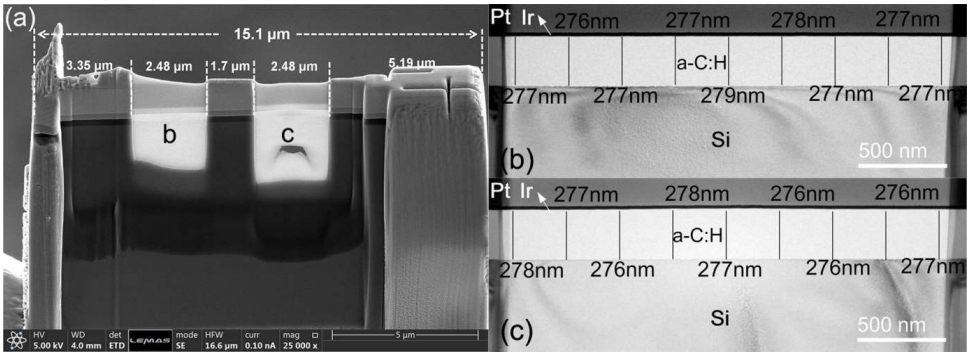

Figure 6.9. SEM image (a) of cross-sectional morphology of unworn area and the corresponding TEM images ((b) and (c)) in the marked areas as shown in (a).

6.1.4 Characterization of tribo-induced bonding transformation

Figure 6.3f includes the results from the optical profilometer, and the calculated results based on the Raman signals of carbon and silicon for comparison. It could be observed that the wear profile curve deriving from the Raman signal of silicon showed good alignment with the wear measured by optical profilometer after depositing the iridium layer, which demonstrates the accuracy of our coating thickness quantification method. While for the height spikes in the result based on the Raman signal of carbon, it should derive from the tribo-induced enhancement of sp^2 phase (i.e., the increase and local clustering of sp^2-C phase). As shown in Figure 6.2d, the enhancement of sp2 phase is confirmed by the increase of A_D/A_G and up-shift of G peak position emerging in the regions of height rising

[62, 137, 138]. This is because the Raman spectra of carbon of a-C:H are dominated by scattering of sp^2 phase due to its high polarizability. Slight enhancement of the sp^2 phase, especially ordering or clustering, could result in the remarkable increase of the Raman intensity [62], further leading to disagreement in the bonding transformation regions.

To explore the tribo-induced bonding transformation, the bonding structure of the above FIB specimens from three targeted areas were further examined by EELS. Figure 6.10 present the EELS spectra (STEM mode) of C-K core-edge collected point by point across the specimens. By fitting the C-K edges, more accurate bonding information could be obtained (Figure 6.11). Figures 6.10c, f and i display the evolution of the calculated bonds fractions in the C-K edges at targeted areas (Figure 6.5). The EELS result in Figure 6.10i confirmed the consistent bonding environment across the cross-sectional unworn area (as-grown a-C:H). The calculated sp^2-C fraction was in the range of 55-60%, with residual fraction attributed to σ* bonds (17-25% for C-H and 15-25% for C-C). While for the coating in the wear scar centre, it was divided into two sublayers according to the EELS result in Figure 6.10c: a top layer with bonding structure being similar to the case of unworn area and a bottom layer near the silicon substrate with remarkable increase of sp^2 phase (π* (C=C), up to ~72%) and decrease of σ* (C-H) fraction (down to ~10%). Similar trend could be found in the EELS result of the side area (Figure 10f). Hence, it is reasonable to conclude that the bottom layer underwent a bonding transformation of sp^3 (C-H) to sp^2 (C=C).

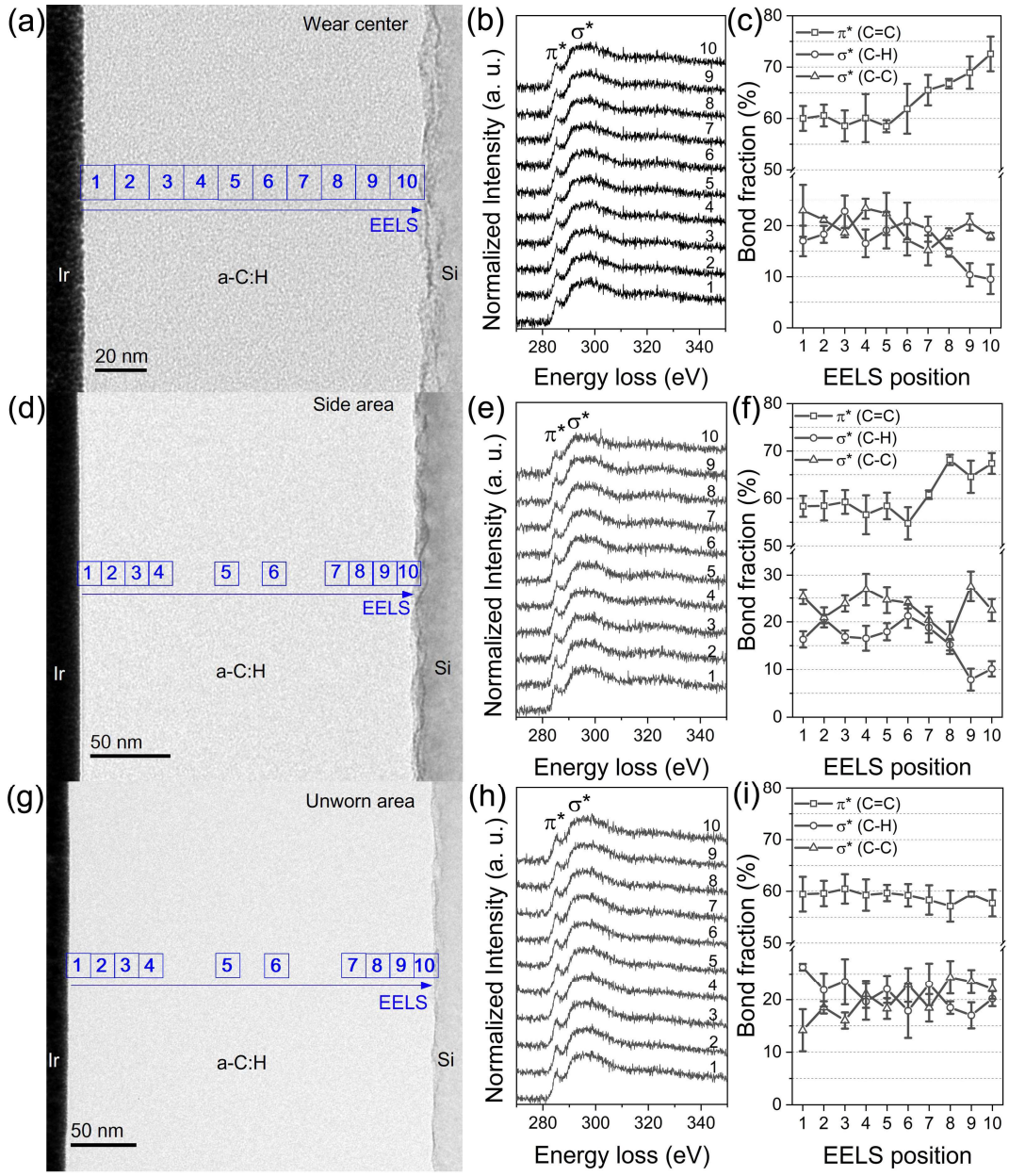

Figure 6.10. TEM images showing the cross-sectional morphology of FIB lamellar specimens from the centre area (a), side area (d) and unworn area (g), evolution of C-K EELS (STEM) core-edge spectra recorded across the cross-sectional area from the wear centre (b), side area (e) and unworn area (h) as marked in (a), (d) and (g) respectively, and evolution of the calculated EELS C-bonds fractions across the cross-sectional area from the wear centre (c), side area (f) and unworn area (i) from the EELS C-*K* edges presented in (b), (e) and (h). *Error bars* denote s.d. of calculated bond fractions.

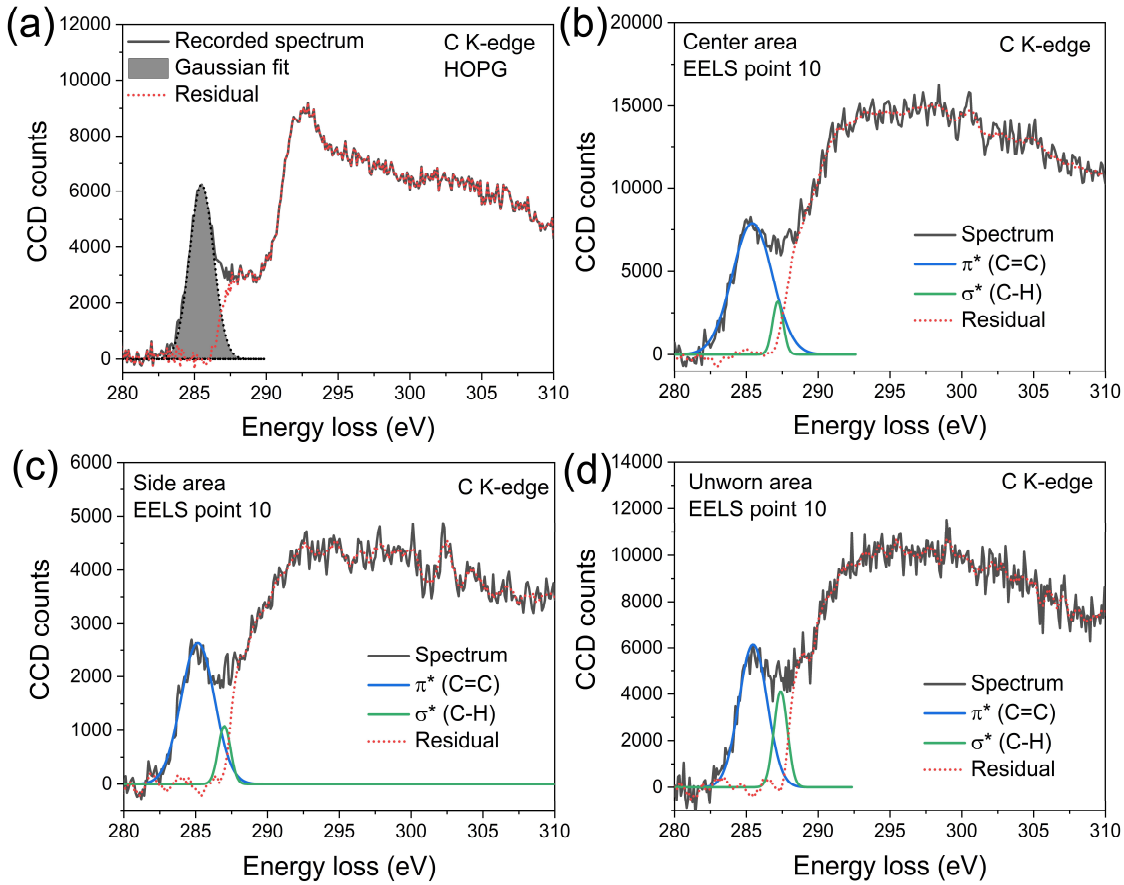

Figure 6.11. (a) C K-edge spectrum of HOPG in the energy window of 280-310 eV showing a Gaussian fit to the π* peak after background subtraction and deconvolution of the C K-edge spectrum. By normalizing the π* peak area to the integrated area in the energy window of 280-310 eV, a standard value of 0.119 is obtained. (b-d) Examples of peak fitting to the C *K*-edges from centre, side and unworn areas as marked in Figure 6.10. Two Gaussian peaks are fitted to π* (C=C) and σ*(C-H) bonds, respectively. The residual bond fraction is then assigned to σ*(C-C).

6.2. Wear measurement in dry friction test

The aim of the coating thickness quantification method is to develop a wear measurement system. Figure 6.12 shows the wear profile curves from tribological tests at different time, obtained by both optical profilometer and the wear quantification method developed in this project (Chapter 5). As discussed in section 6.1, an accurate wear profile by non-contact optical profilometer could be obtained by depositing an iridium layer on top of wear scar. This method was employed here to verify the calculated wear results deriving from the

Raman signal of silicon. Through comparison, our wear quantified results compared well with the measured results by optical profilometer in all tribo-tests. Specifically, our thickness quantification method could provide accurate values of maximum width and depth, and detailed information about depth evolution along the wear profile, which was crucial to wear monitoring and service-life prediction of coatings.

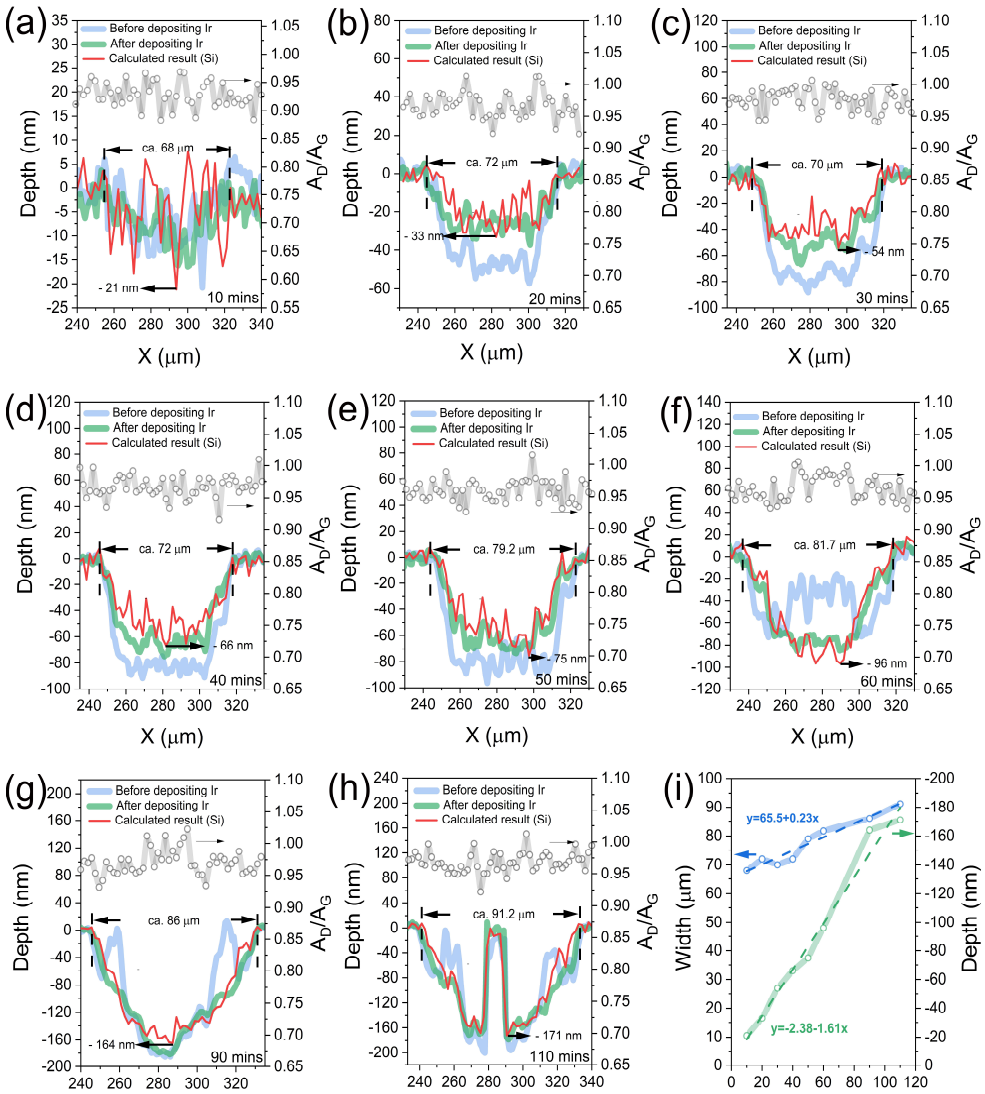

Figure 6.12. (a)-(h) Comparison of the wear profile curves obtained by different methods (dry friction with test time range 10-110 mins). Non-contact optical profilometer: wear profile curves before (blue line) and after depositing iridium layer (green line). Wear quantification method based on the Raman intensity of silicon signal (red line). The A_D/A_G ratios across the wear scars (grey line). (i) Evolution of width and depth of wear scars with test time.

In addition, Figure 6.12i displays the evolution trend of wear scar, and it is observed that the maximum width and depth of wear scars increase linearly with test time. This could be used to monitor the wear and predict the service life of coatings. On the other hand, when using an optical profilometer, there was a remarkable difference between the results before and after depositing iridium layer, which was significantly intensified by the tribo-induced polishing effect on some contact areas, especially in the long-term test (60-110 mins, Figures 6.12f - h).

6.3 Wear measurement in oil-lubricated test

The most critical finding in this study is applying the method developed in this project to quantify the coating thickness in oil-lubricated sliding conditions. Here, PAO base oil was used as a lubricant in tribo-test and the tested samples were transferred directly to Raman spectroscopy for characterization without removing PAO. The tested samples were also characterized by an optical profilometer after removing the oil film with heptane and depositing iridium layers, and the results were employed as standard references to verify the wear quantified results based on Raman signals. Figure 6.13a displays the friction behaviours with test time ranging from 30 to 110 mins. Figure 6.13b shows the Raman spectrum obtained when adding PAO oil on the top surfaces of the a-C:H coatings.

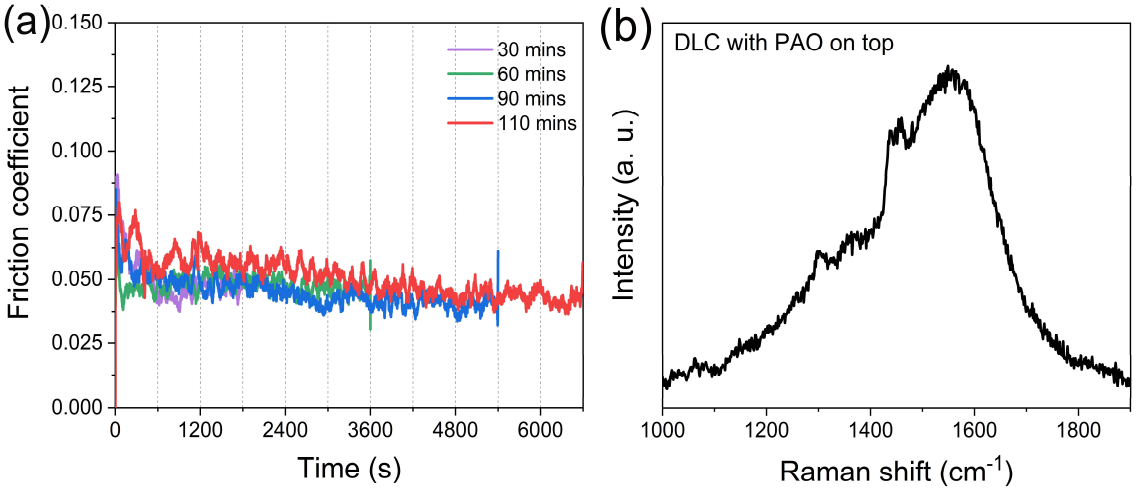

Figure 6.13. (a) Friction curves of samples with a-C:H deposited on silicon wafer under different test time under oil-lubricated condition (PAO; test time 30-110 mins). (b) Raman spectra of carbon band with oil film on the top (PAO; test time 110 mins).

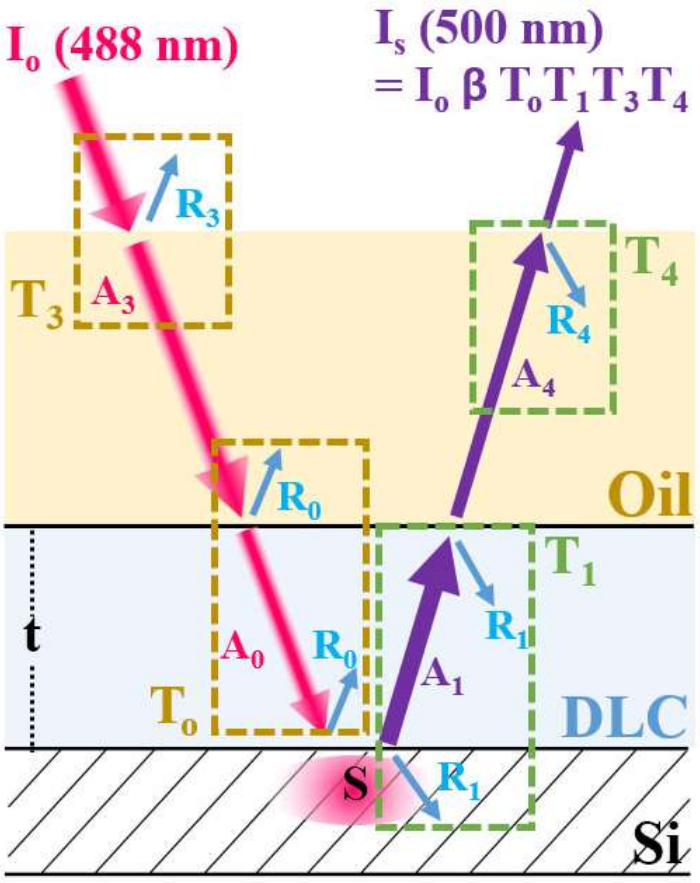

Figure 6.14. Schematic illustration of the coating thickness quantification methods under oil-lubricated condition.

Figure 6.14 illustrates the principle of coating thickness quantification under oil-lubricated condition. Based on the assumption that the oil film with the roughly same thickness could be formed on the top of the coating under stable friction process and slight thickness difference of oil film could not result in a significant deviation of quantified results due to the high transmittance of PAO, the Raman intensity of silicon signal could be obtained by

$$I_s = I_o \beta T_o T_1 T_3 T_4 \qquad 6\text{-}1$$

where β is light scattering rate, $I_o\beta$ is Raman intensity of silicon 1st band of silicon substrate, T_o and T_1 are transmittance values of incident light and scattered light in a-C:H, and T_3 and T_4 are transmittance values of incident light and scattered light in oil film. Then, the coating thickness could be given by

$$t = \frac{-1}{\alpha_o + \alpha_1}[lnI_s - lnI_o\beta - lnT_3T_4 - ln(1-R_o)^2(1-R_1)^2] \qquad 6\text{-}2$$

which could be rewritten as

$$t - \frac{lnT_3T_4}{\alpha_o + \alpha_1} = \frac{-1}{\alpha_o + \alpha_1}[lnI_s - lnI_o\beta - ln(1-R_o)^2(1-R_1)^2] \qquad 6\text{-}3$$

where the effect of oil film in the form of $\frac{lnT_3T_4}{\alpha_o + \alpha_1}$ will result in the lowering of quantified thickness than the actual value. With knowing all parameters in the right of equation (6.3) as stated in section 6.1, we could obtain $t - \frac{lnT_3T_4}{\alpha_o + \alpha_1}$. After subtracting the thickness of as-grown a-C:H, the wear profile curves were obtained as displayed in Figures 6.15a-d (black lines). Clearly, the initial calculated results were far below the measured results by the optical profilometer. Here since T_3 and T_4 were regarded as constants based on above assumption, $\frac{lnT_3T_4}{\alpha_o + \alpha_1}$ could be considered as a constant. It was therefore suggested $t - \frac{lnT_3T_4}{\alpha_o + \alpha_1}$

taken point by point across the wear scar could reflect the actual variation trend of wear depth. When the value obtained on edge (unworn area) was set as reference (for example, it is -35nm in Figure 6.15a (black line)), the expected wear profile was obtained by shifting up the reference value (red line in Figure 6.15). As displayed in Figures 6.15a - d, the revised wear profile curves compared well with that of the optical profilometer (with iridium layers) in all tested samples. Figure 6.15e shows the evolution trend of wear width and depth with test time. Compared with the results under dry conditions, the wear condition was significantly improved with the maximum width and depth reduction of ~25% and ~85%, respectively.

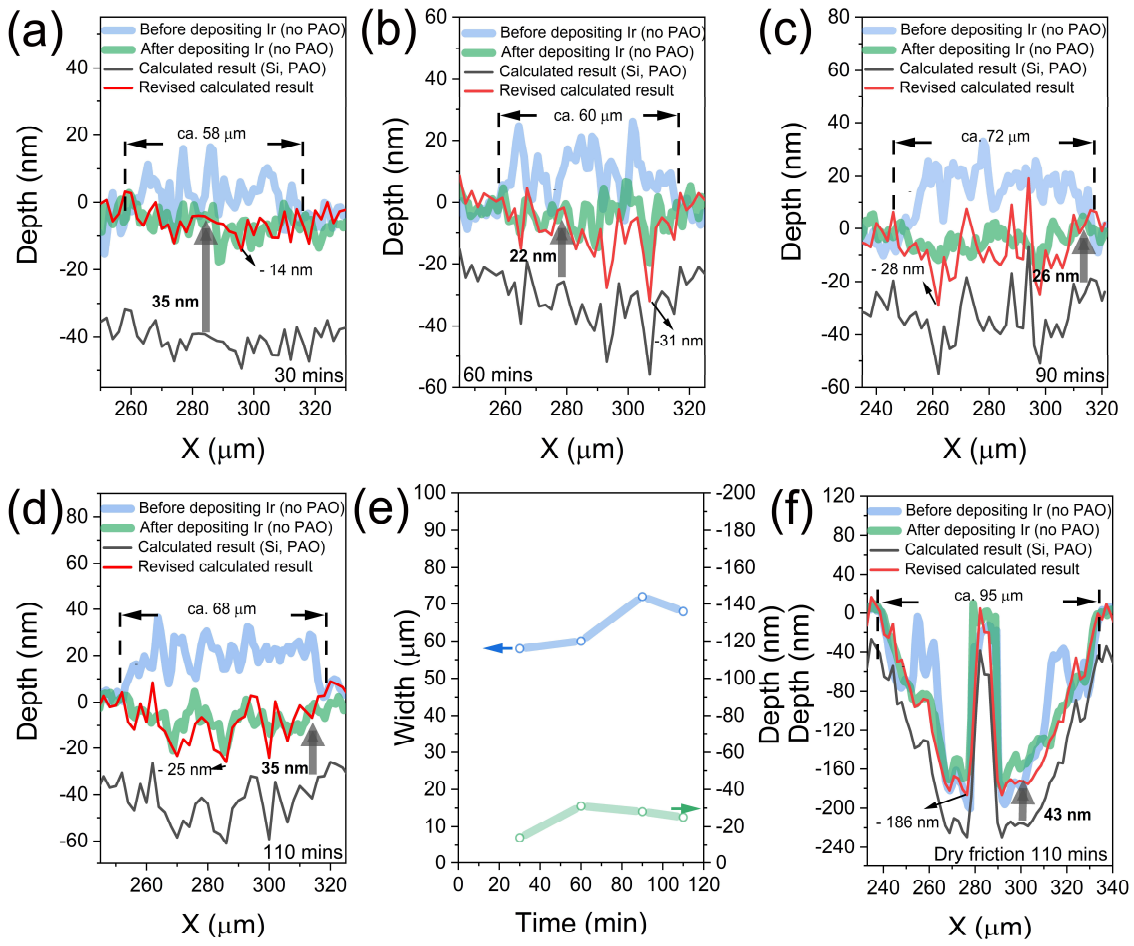

Figure 6.15. (a)-(d) Comparison of the wear profile curves obtained by different methods (oil-lubricated condition, PAO; test time 30-110 mins). Non-contact optical profilometer: wear profile curves before (blue line) and after depositing iridium layer (green line). Wear

quantification method based on the Raman intensity of silicon signal (black and red lines). (e) Evolution of width and depth of wear scars with test time. (f) Comparison of the wear profile curves obtained by different methods. Here, we drop PAO on top of the tested sample under dry friction with test time of 110 mins as shown in Figure 6.12(h). Non-contact optical profilometer: wear profile curves before (blue line) and after depositing iridium layer (green line). Wear quantification method based on the Raman intensity of silicon signal with oil on top (black and red lines).

It should be also pointed out that, when the initial quantified thickness (without tribo-test) is set as a reference, the difference between thickness obtained in the friction process and the reference value is just the wear depth and only depend on I_S according to the equation (5.5) and (6.2), as all the parameters except I_S could be regarded as constant for the same a-C:H sample. Furthermore, in view of the small wear depth under oil-lubricated condition, the sample of dry friction (110 mins) with larger wear depth (Figure 6.12h) was covered with PAO and used for verifying the quantification method under severe wear conditions. As displayed in Figure 6.15f, it was confirmed that the method developed in this project could provide accurate depth values under large wear depth. On the other hand, more prominent tribo-induced polishing effect happened under oil-lubricated condition (blues lines in Figures 6.15a - d). Compared with the results of dry friction (Figure 6.12), the polishing effect under oil-lubricated condition appeared in the earlier stage (30 mins), due to the role of liquid in accelerating the polishing process.

6.4 Summary

In this chapter, a novel strategy was introduced to achieve an accurate coating thickness quantification by employing a bilayer structure with the top layer of a-C:H as tribological and light attenuating layer and the bottom layer of silicon as Raman signal provider. This approach was successfully applied to quantify the coating wear in dry and oil-lubricated conditions. Since the Raman intensity of silicon signal varied as a function of a-C:H

thickness, wear monitoring of a-C:H could be realized during the friction process, giving the opportunity for in-situ wear measurement. The main results are summarized as below:

1. Compared with the results deriving from profilometer and Raman signal of carbon, coating thickness quantification method based on the Raman signal of silicon provided more accurate wear profile in the long term tribo-tests.

2. The remarkable errors of non-contact optical profilometer was attributed to the tribo-induced variation of optical properties on the top surface of a-C:H film, while the obvious errors of the approach based on Raman signal of carbon was due to tribo-induced bonding transformation of sp^3 (C-H) to sp^2 (C=C) in the bonding transformation regions, resulting in noticeable enhancement effect of sp^2 C-phase towards Raman intensity of carbon signal.

3. By introducing additional attenuating-layer of oil film into calculation process, this method enabled the possibility of monitoring coating wear under oil-lubricated condition.

Chapter 7

Investigation on the effect of lubricating additive on wear behaviors of a-C:H coatings via Raman-based wear quantification method

In this chapter, the proposed Raman-based coating thickness quantification method was employed for detecting tribofilms derived from lubricating additives and exploring their influence on the wear behaviour of hydrogenated amorphous carbon. It was suggested that tribochemical products with distinct optical properties were formed in different wear-stages, resulting in extra attenuated intensities of Raman signals from silicon under-layer compared with pure a-C:H, in the form of measurement deviations of wear depth. By monitoring the deviation, critical information of tribofilm compositions were obtained, which was further employed to reveal coating wear mechanisms under oil-lubricated condition. Based on this approach, a two-stage wear acceleration mechanism was proposed for the first time to clarify the detrimental effects of MoDTC (molybdenum dialkyldithiocarbamate)-derived tribofilms on a-C:H wear. The detailed structure and composition analysis of tribofilms were also performed by combination of TEM, FIB and FFT to verify this Raman-based approach.

7.1 Improved profilometry for coating wear measurement

To obtain accurate topographic information of wear scars, both non-contact optical and contact profilometers were employed to characterize the tribo-tested samples as shown in

Figure 7.1 (tribo-test conditions: a-C:H of 277 nm thickness on the silicon wafer, dry friction, time of 30 to 110 mins, applied load of 1N, frequency of 2.5 Hz, stroke of 2mm, ambient environment). Figure 7.1a gave the morphologies of the wear tracks under a test time of 30 mins. Through comparison, the wear profiles obtained by different profilometers show a similar depth evolution trend along the wear scar. However, when the test time was extended to 60 mins (Figure 7.1b), the wear profile given by the non-contact optical profilometer displayed evident depth spikes in the centre area, which was not observed in the result of the contact profilometer. It is well known that a non-contact optical profilometer builds up 3D map by collecting array signals of light interference of reflected light. Given the high sensitivity towards the optical signal, it is suggested that the tribo-induced variation of optical properties (i.e., reflectivity) on the top surface, termed tribo-induced polishing effect, may affect the intensity of the light signal, resulting in distinctive measurement deviations.

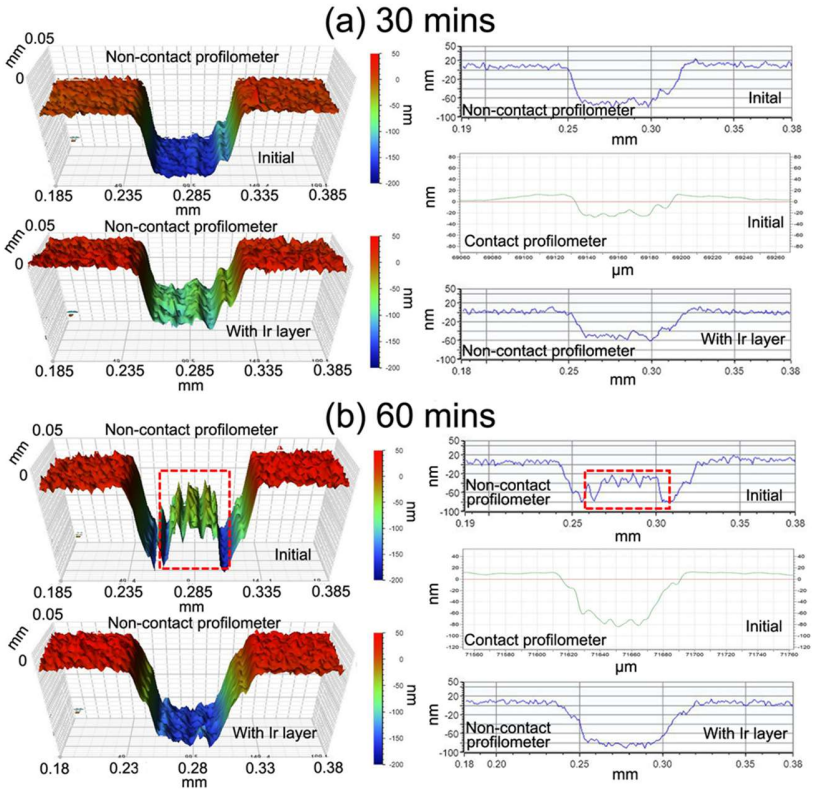

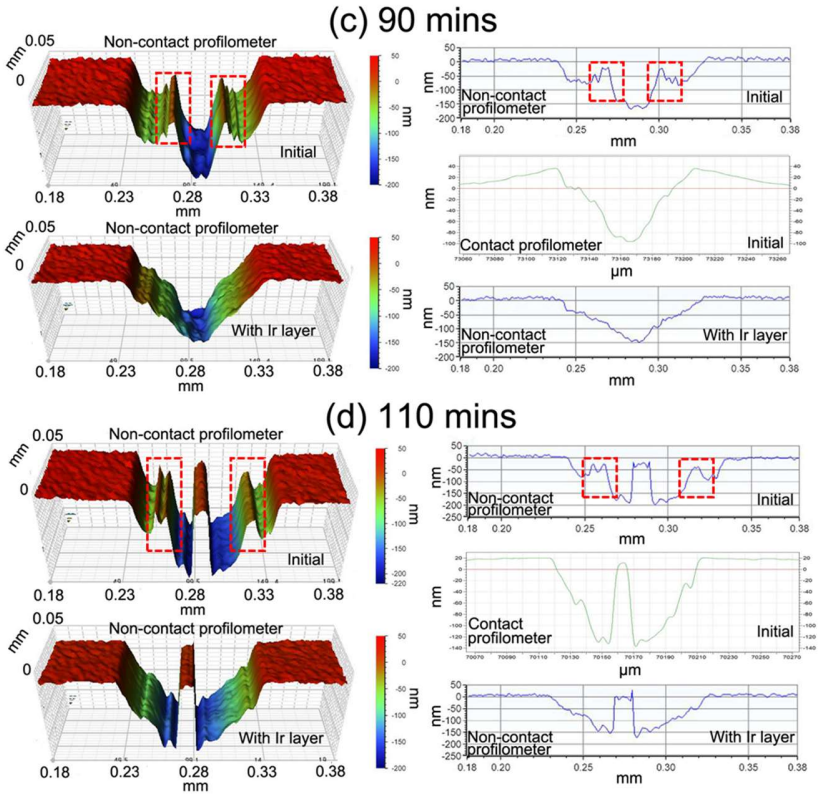

Figure 7.1. Comparison of wear profile curves obtained by non-contact optical profilometer (before and after depositing iridium layer on top of a-C:H) and contact profilometer for tribo-tested samples under dry friction (a, 1N, 30mins; b, 1N, 60mins; c, 1N, 90mins; d, 1N, 110mins). The marked areas in (b)-(c) indicated the measurement deviations of optical profilometer (before depositing iridium layers).

For verifying this finding, an optical signal synchronization layer of iridium with uniform thickness (~ 20 nm in Figure 6.4) was deposited on the sample by DC magnetron sputtering to provide a top surface with consistent optical properties. Then, an optical profilometer was used again to characterize the sample, and it was found that the depth rising in the centre area disappeared after depositing the iridium layer. As a result, the wear profile showed similar evolution trend with that of contact profilometer. Meanwhile, a similar tribo-induced effect was also observed for tribo-tested samples with test time of 90 and 110 mins as marked in Figures 7.1c and d. Therefore, it was demonstrated that the measurement deviation (depth rising) in the original result of the optical profilometer was attributed to tribo-induced polishing effect which could be avoided by depositing a top iridium layer with consistent optical properties. This improved profilometry with optical signal

synchronization layer was used in this chapter to provide accurate wear depth as standard reference to verify the quantified results based on Raman signal, benefiting the identification of additive-derived products.

7.2. Wear behavior of a-C:H under additive-lubricated condition

For gaining fundamental insights into the wear behaviour of a-C:H coatings under additive-lubricated conditions, surface topographic analysis of tribo-tested a-C:H coatings was conducted by combining improved profilometry and Raman-based wear quantification method. Here, MoDTC, as a typical lubricant additive, was employed to investigate the impact of tribofilms on the wear behaviour of a-C:H coatings. As shown in Figure 7.2, a series of tribo-tests were performed on the a-C:H/steel contact (test conditions: a-C:H of 183 nm thickness on silicon wafer, oil lubrication (PAO with 0.8 wt.% MoDTC), time of 30 to 140 mins, applied load of 1N, frequency of 2.5 Hz, stroke of 2mm, ambient environment).

After removing the oil, Raman-based approach was first used to quantify the wear depth via the same process as stated in chapter 5. Then improved optical profilometry was employed to characterize the wear scars to provide a standard reference. Compared with the results of optical profilometer, significant deviations in the form of depth difference (black bars) were observed (Figure 7.3). It is well-accepted that MoDTC tribofilm, composed of various tribo-chemical products, could be formed on the sliding surface of a-C:H [137-141]. Since they possess different optical properties compared with a-C:H, apparent deviations of Raman-based method were obtained as displayed in Figure 7.4. Meanwhile, the depth

difference between the results of optical profilometer with and without iridium layers also confirmed the formation of tribofilms with different optical properties.

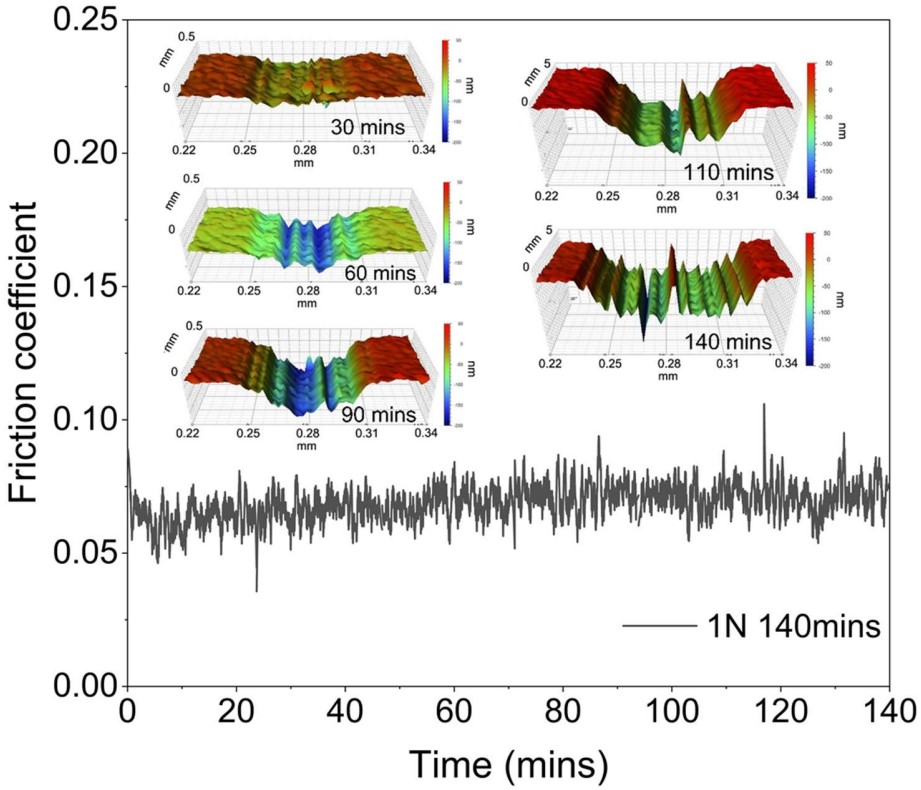

Figure 7.2. Friction behavior of a-C:H film under oil lubrication (PAO with 0.8 wt.% MoDTC) and 3D optical microscopic images of wear scars of different test time (30 to 140 mins).

Table 7.1 summarizes the optical properties of MoDTC-derived tribochemical products [144-151]. Based on equation (5.3) and (5.4) in chapter 5, it was suggested that tribofilms should be composed of products with lower transmittance than a-C:H, since decreasing the transmittance resulted in the reduction of Raman signal intensity which corresponded to the thickening of coating in the form of depth rising. As shown in Table 7.1, MoS_2, MoC, and Fe_3O_4 possessed lower transmittance (higher absorption coefficient or/and reflectivity) than a-C:H coating. Therefore, based on Raman spectra in Figure 7.3f, it was suggested that MoS_2 and MoC should be the main tribo-chemical products of MoDTC.

Note that Raman signals of MoS_2 and MoC were just detected on a small number of deviation points as marked in the Figure 7.3. This should be attributed to the low Raman intensity of small crystal size, or poor crystallinity of MoS_2 and MoC formed on other deviation points. However, as quantified wear depth based on Raman scattering signals depended on the transmittance of top coatings, this Raman-based approach could provide insight into tribofilm formation and evolution on the top sliding surface based on the measurement deviations.

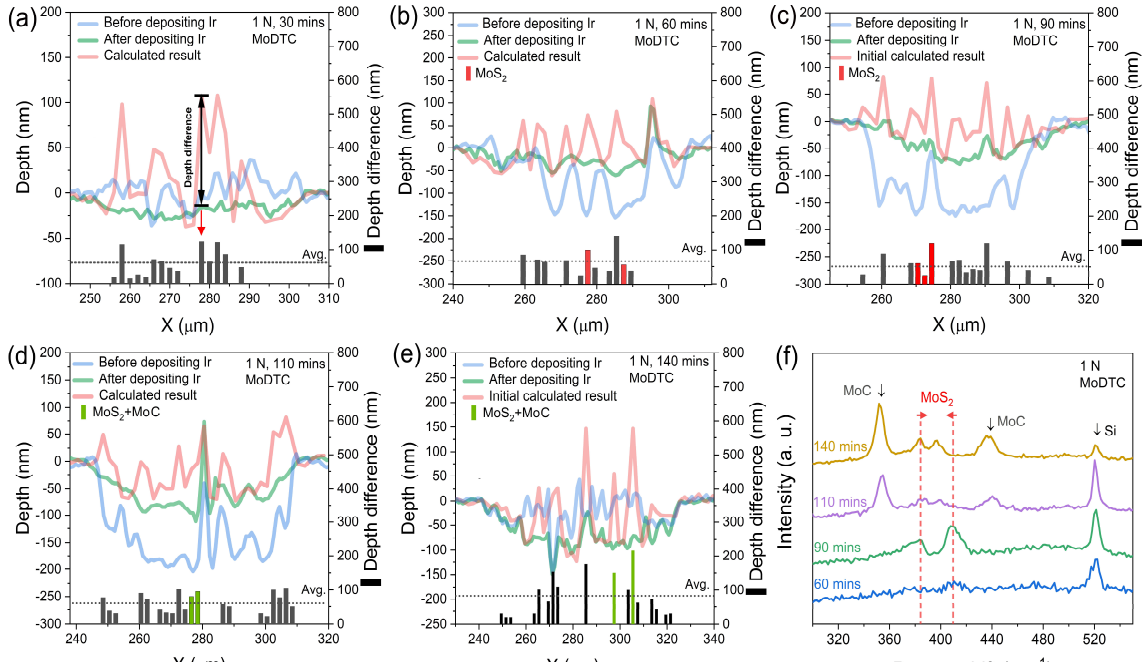

Figure 7.3. (a)-(e) Comparison between calculated wear profiles derived from Raman intensity of silicon bands and wear profiles characterized by non-contact optical profilometer (before and after depositing iridium layer on top of a-C:H) under oil lubrication (PAO with 0.8 wt.% MoDTC, test time of 30-140 mins, applied load of 1 N). Black bars displayed the depth difference of wear profile curves obtained by Raman-based method and non-contact optical profilometer (after depositing iridium layer). Red and green bars indicated the formation of MoS_2 and MoS_2 + MoC, respectively. (f) Raman spectra of MoS_2 and MoS_2+MoC detected on the tribo-tested samples under different test time.

Table 7.1. Reflectivity (R) and absorption coefficient (α) of MoDTC-derived products in the wavelength region 450-550 nm reported in the literature.

Materials	R (%)	α(cm^{-1})
MoO_3 [28,29]	~ 20	~ 4×10^4
Fe_2O_3 [30,31]	~ 10	~ 5×10^4
MoC [32, 33]	~ 50	~ 12×10^4
MoS_2 [34, 35]	~ 19	~ 15×10^4

As shown in Figure 7.3f, when test time was less than 90 mins only MoS_2 was detected, and MoC always appeared simultaneously with MoS_2 in the longer test time. Meanwhile, the blue shift of the E^1_{2g} vibration and red shift of A_{1g} vibration of MoS_2 in the Raman spectra with the formation of both MoC and MoS_2 indicated the degradation of MoS_2 crystal [152]. It was therefore suggested that MoS_2 crystals were gradually converted into MoC in the friction process. Thermal carburization of MoS_2 into MoC has been reported in the literature [153], where MoS_2 shell was broken first through the reaction between hydrogen and sulfur atoms of MoS_2, followed by CH_4 attack to form MoC. Therefore, the critical reaction conditions for MoS_2 carburization were heat, active sites on MoS_2 resulting from structure degradation as well as carbon source.

Indeed, these requirements can also be fulfilled in the friction process: (a) Tribo-contact imposed shear forces on the coating can be partly dissipated as heat. Meanwhile, tribo-induced shear stress can result in the activation energy reduction of chemical reactions, leading to the decrease of reaction temperature [154]. (b) Tribo-induced transformation or degradation of the microstructure of nano-additives can also be realized in the friction process [155-157]. (c) Some studies have demonstrated the degradation of lubricating oil into shorter chains in the friction process, which could further form solid carbon-based films [158, 159]. While for PAO oil used in this study, the degradation of olefin chains into shorter hydrocarbon fragments was also found under the action of friction

forces [158]. Additionally, CH_4 and H_2 have been demonstrated as the main products of tribo-chemical degradation from PECVD a-C:H coatings [160].

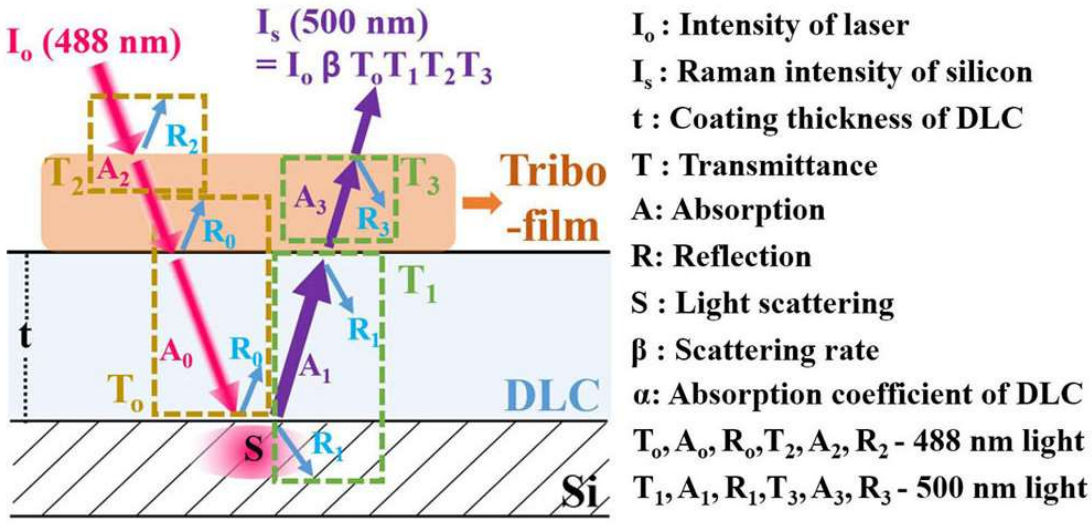

Figure 7.4. Schematic illustration of Raman-based coating thickness quantification process with additive-derived tribofilms on coating surface.

For further verifying the finding of MoS_2 and MoC formation from MoDTC, FIB with the in-situ lift-out technique was used to fabricate cross-sectional lamellar specimens of tribofilms for structure and composition characterization by TEM and FFT. As shown in Figure 7.5a, a thin tribofilm (thickness below 10 nm) with small patches of MoS_2 sheets was formed under 30 mins test time. The distance between MoS_2 layers was measured to be 0.62 nm, agreeing with the lattice structure of MoS_2 [153]. When prolonging test time to 90 mins (Figure 7.5b), a significant increase of tribofilm thickness (up to ~ 35 nm) was observed with the formation of highly crystallized MoS_2 structures (~ 3-4 layers). With extending the time to 140 mins, the formation of hybrid structures of nano-MoS_2 and nano-MoC was confirmed by TEM images and FFT patterns. The interplanar crystal spacing and intersection angle agreed very well with those of (200) and (111) planes of

cubic α-MoC (Figures 7.5c-II and III) [161, 162]. It was demonstrated that MoS_2 was formed in the initial stage and further converted to MoC.

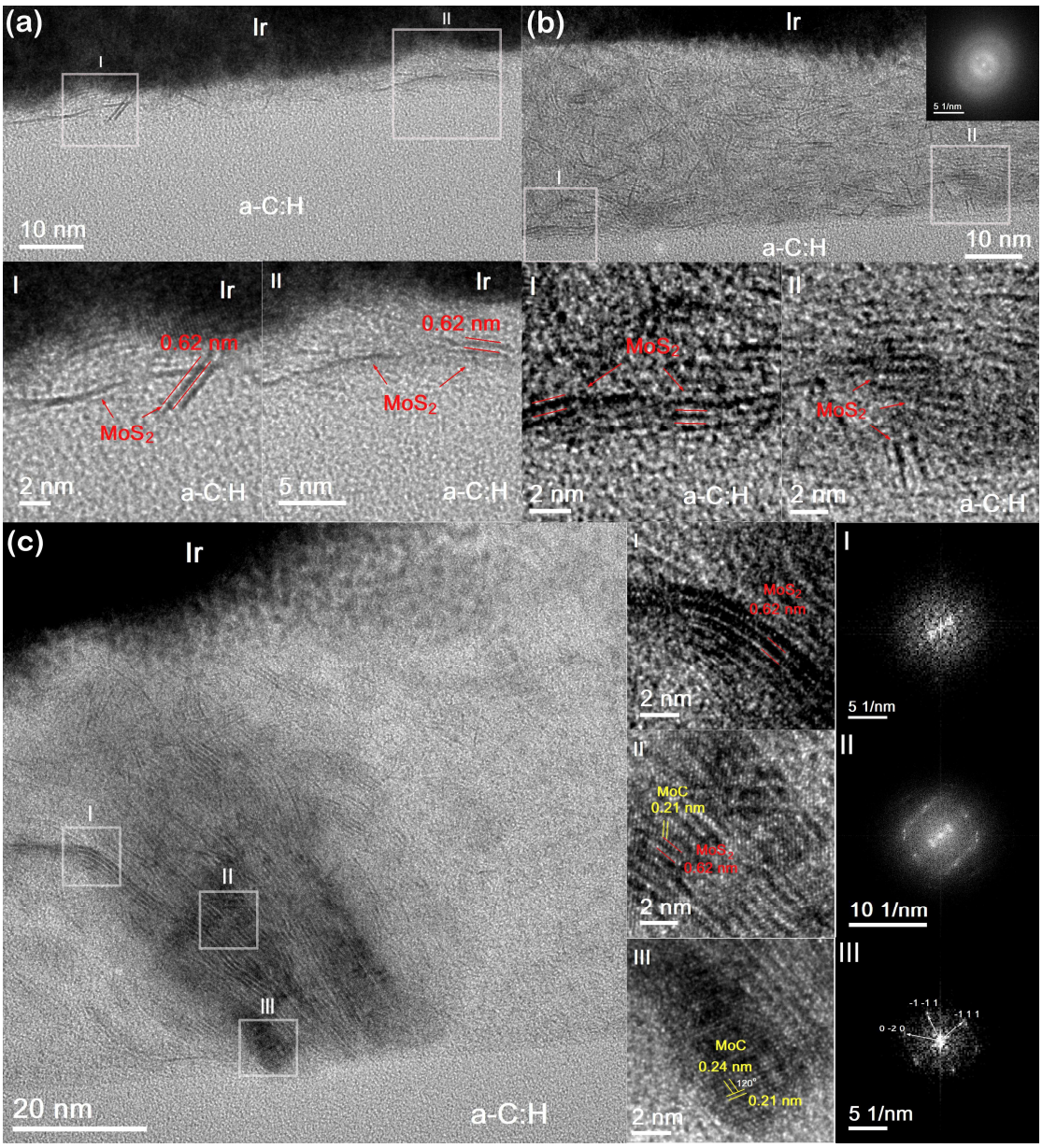

Figure 7.5. HRTEM images showing the tribofilms formed under different test time (a, 30mins; b, 90mins; c, 140 mins) and fast Fourier transform (FFT) patterns clarifying the crystal phases.

Figure 7.6a shows the evolution of maximum width and depth of wear scars with test time. It was found that the width increased linearly while depth trend could be divided into two stages. Compared with stage 1, the growth rate of wear depth in stage 2 was obviously

increased, indicating a higher wear rate. For a better understanding of the underlying mechanism, average values of depth difference between Raman-based wear measurement results and improved profilometry are given in Figure 7.6a. As the depth difference was attributed to the formation of tribofilm with different optical properties on the top surface of a-C:H, the Raman-based wear measurement method could provide valuable information about the tribofilm formation and evolution. Here the average depth difference increased remarkably in stage 2 in contrast with stage 1, indicating the formation of tribo-chemical products with lower transmittance. This agreed with the above finding of carburization of MoS_2 into MoC under the longer tribotest time, as MoC displayed lower transmittance (higher reflectivity) than MoS_2 as shown Table 1. Meanwhile, MoC can trigger abrasive wear and speed up coating wear due to its high hardness. As suggested above, the shear forces critically promoted the carburization of MoS_2 into MoC in the friction process.

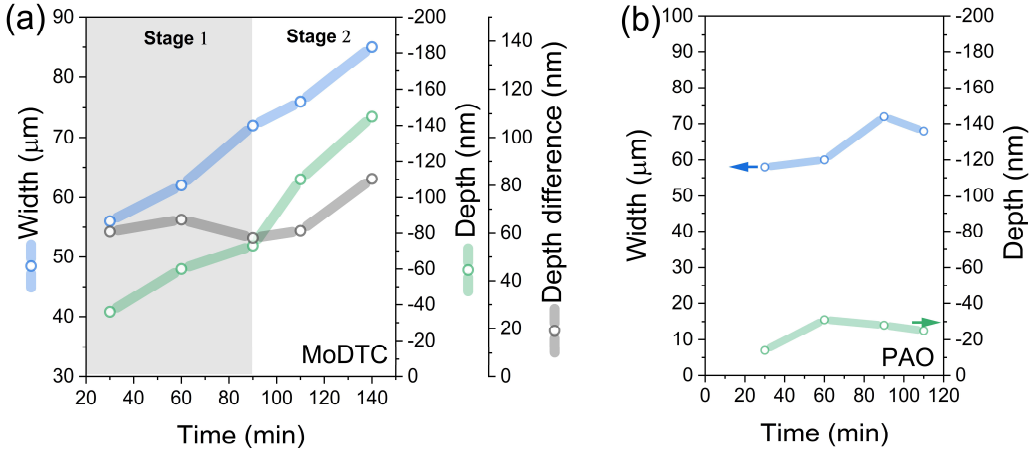

Figure 7.6. Evolution of width and depth of wear scars with test time under oil lubrication (a, PAO + 0.8 wt.% MoDTC; b, PAO). The average values of depth difference between Raman-based wear measurement results and improved profilometry in Figure 7.3 were also displayed in (a), giving information about the evolution of tribofilm composition.

To further validate this hypothesis, the wear behaviours of a-C:H lubricated by MoDTC-containing oil under high applied load (10-40 N) were investigated as shown in Figure 7.7. Similarly, the wear rate was accelerated dramatically in stage 2 accompanied by

the formation of abundant MoC (Figure 7.7d), indicating the critical role of MoC in wear acceleration of a-C:H films in the stage 2.

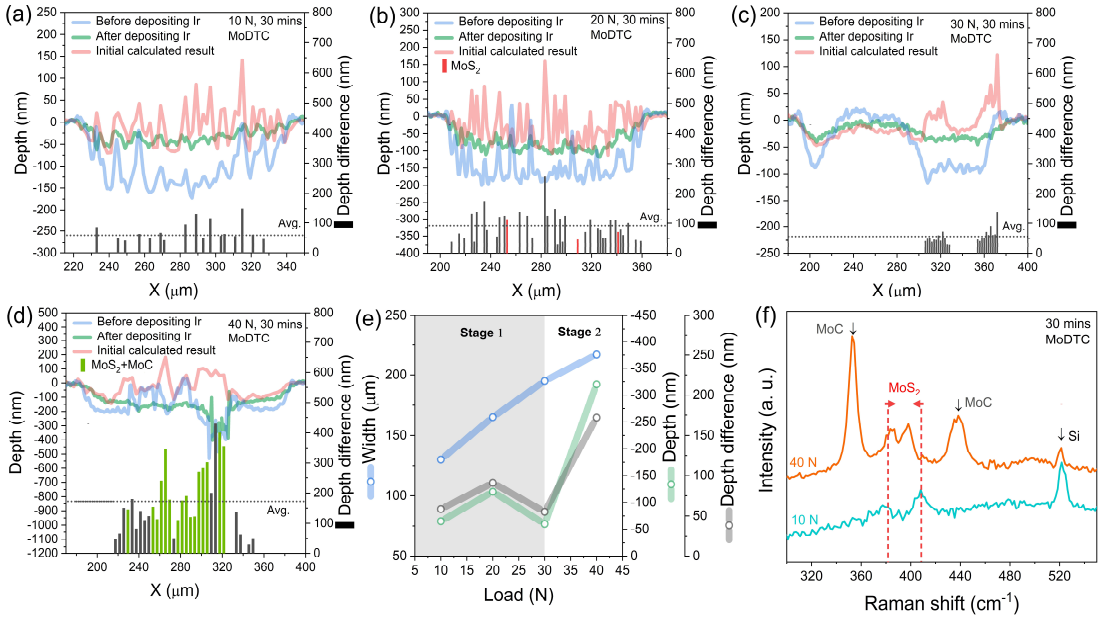

Figure 7.7. (a)-(d) Comparison between calculated wear profile derived from Raman intensity of silicon bands and wear profile characterized by non-contact optical profilometer (before and after depositing iridium layer on top of a-C:H) under oil lubrication (PAO with 0.8 wt.% MoDTC, test time of 30 mins, applied load of 10-40 N). Black bars displayed the depth difference of wear profile curves obtained by Raman-based method and non-contact optical profilometer (after depositing iridium layer). Red and green bars indicated the formation of MoS_2 and MoS_2 + MoC, respectively. (e) Evolution of width, depth, and average depth difference of wear scars with test time. The average values of depth difference between Raman-based wear measurement results and improved profilometry give information about the evolution of tribofilm composition. (f) Raman spectra of MoS_2 and MoS_2+MoC detected on the tribo-tested samples under different test time.

Based on the above results, a two-stage wear process was proposed to explain the wear acceleration mechanism. It is well accepted that MoS_2 is always formed accompanied by MoO_3 formation. It is suggested that wear acceleration in the first stage can be attributed to the catalytic effect of molybdenum [162-165]. Due to the easy-shear capability of oxidation products [165-171], only tiny oxidation layer remains on the surface with a thickness around several nanometers [167]. Considering the large probe depth of Raman (~300 nm)

and its high sensitivity towards sp^2-C phase, the bulk signal of a-C:H dominates the Raman spectra, explaining why we cannot detect the oxidation layer by Raman spectroscopy which is in line with the literature. Meanwhile, to clarify the formation of MoO_3 in tribofilm, TEM and EDS elemental mapping were used to characterize the composition and structure of tribofilm as shown in Figure 7.8. Figure 7.8a shows the HRTEM image of tribofilm formed after tribo-test (1 N, 90 mins). In the selected area, obvious accumulation zones of highly crystalline MoS_2 are observed, which are surrounded by a material with an amorphous structure.

By comparing the EDS mapping images of Mo, S and O, it is found that elements Mo and O are enriched in the areas of amorphous material, while the MoS_2 accumulation areas are abundant in Mo and S. This finding gives direct evidence of MoO_3 formation in the tribofilm and its accompanying relationship with MoS_2. In addition, the main reason why it is hard to detected MoO_3 via Raman is due to the low Raman intensity of the poor crystalline MoO_3 in the tribofilm. Meanwhile, the formation of MoDTC-derived MoO_3 in the tribological process has also been confirmed based on the XPS analysis in the literature [110, 142]. While for the second wear stage, the tribo-induced shear forces trigger the degradation of PAO into hydrocarbon fragments (carbon source) and generate heat for promoting the conversion of MoS_2 into MoC. Due to its high hardness, MoC acts like an abrasive particle to further accelerate the wear of a-C:H in the second stage.

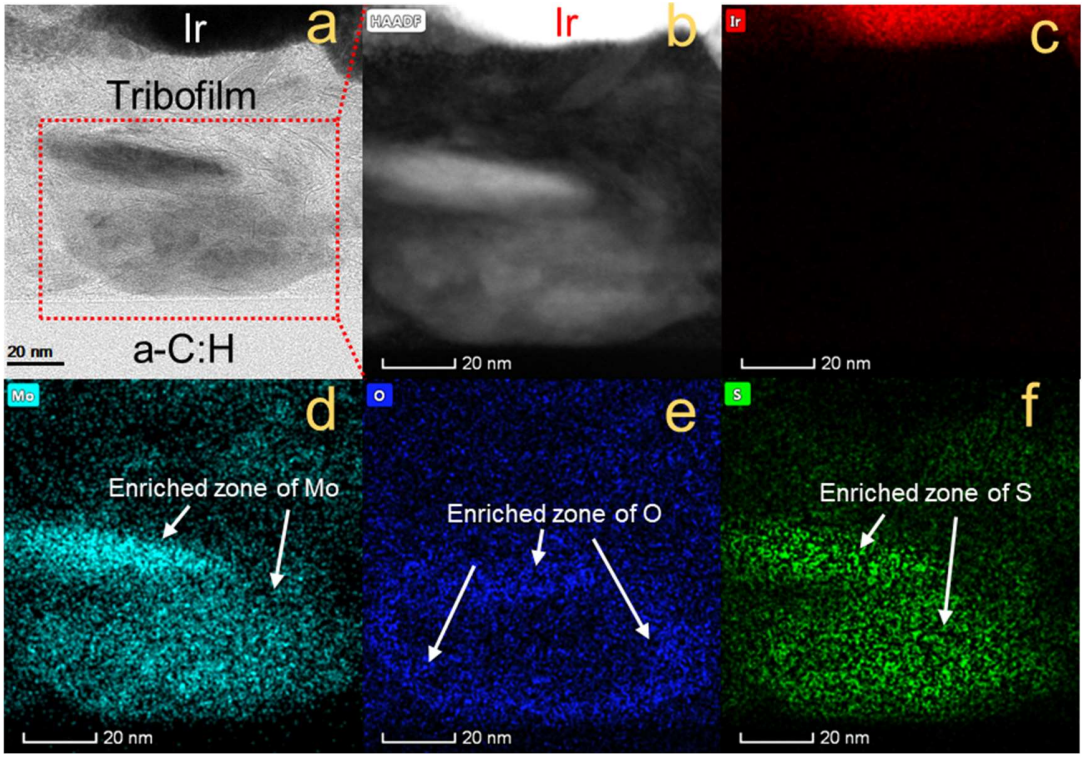

Figure 7.8. (a) HRTEM image showing the tribofilms after tribo-test (1 N, 90 mins). (b) High-angle annular dark-field (HAADF) image of selected area in (a). (c-f) The corresponding EDXS elemental mapping images of Ir, Mo, O and S.

To further verify this wear mechanism, EDS was employed to characterize the element distribution in the interface area between a-C:H and tribofilm as displayed in Figure 7.9. Figure 7.9a shows the HRTEM image of tribofilm after tribo-test (1 N, 140 mins) where a hybrid structure of nano-MoS2 and nano-MoC is observed as stated above. EDS line-scanning was conducted from the bottom of the hybrid structure to a-C:H as shown in Figure 7.9b, and the corresponding result is given in Figure 7.9c. Along the line-scanning direction, the C concentration increases continuously and achieves maximum value when it is close to the a-C:H surface, while the concentrations of Mo and S show opposite trend and drop to zero when it reaches the a-C:H surface. An interesting finding is the oxygen doping region in the subsurface of a-C:H (thickness of ca. 3 nm, a grey area in Figure 7.9c), which directly demonstrates the catalytic effect of MoO_3 on a-C:H surface under shear forces leading to significant weakening and wear of a-C:H. In addition, the accelerated

wear in the second stage is caused by the abrasive wear of hard MoC rather than the reason of sulphur doping in the subsurface area of DLC reported in the literature [100]. As shown in this literature, sulphur doping happens under high Hertzian contact pressure (> 5 GPa) and on hard DLC surface (hardness > 50 GPa) which is inapplicable to our study (Hertzian contact pressure from 580 MPa to 2.0 GPa, hardness 21 GPa).

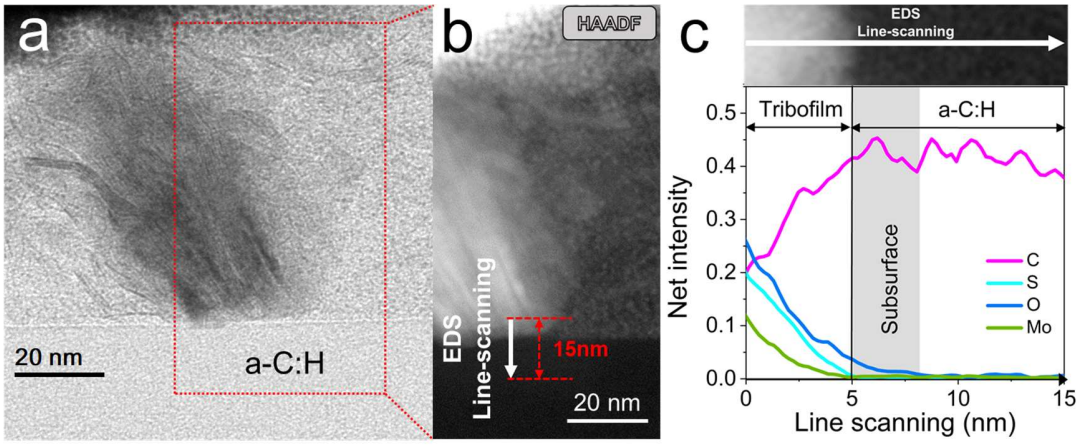

Figure 7.9. (a) HRTEM image showing the tribofilms after tribo-test (1 N, 140 mins). (b) HAADF image of selected area in (a). (c) EDS line-scanning results showing the elements distribution (C, Mo, O, and S) along the direction as marked in (b).

7.3 Summary

In summary, the evolution process of MoDTC-derived tribofilms formed on a-C:H coating surface was investigated by a combination of Raman-based profilometry, TEM and FFT. The obtained results confirmed that the remarkable deviations of Raman-based coating wear measurement were attributed to the tribofilm formation on the top surface of a-C:H due to their distinct optical properties compared with a-C:H. Formation of MoS_2 nano-sheet was observed in the initial stage, which was further converted into nano-MoC via carburization reaction under the impact of shear forces. In combination with previous studies about MoDTC-derived tribofilms, MoDTC-induced wear process on a-C:H/steel contact could be divided into two stages. In the first stage, wear acceleration was attributed

to the catalytic effect of molybdenum oxides (accompaniment of MoS_2 derived from MoDTC) in the oxidation of a-C:H and easy-shear capability of oxidation layers. While for the second stage, the tribo-induced MoS_2 carburization into hard MoC led to abrasive wear, dominating the wear acceleration process. Based on this proposed mechanism, inhibiting strategies for the detrimental effect of MoDTC were also provided. The findings of this study may open a new pathway for detecting tribofilm composition formed on coating surface and clarifying its relation to coating wear behaviour. This can help gain fundamental insights into wear mechanisms of a broad range of additives and coatings, and thus benefit the development and optimization of an effective solid-liquid lubricating system.

Chapter 8

Investigation on the growth mechanism of ZDDP-derived tribofilm on diamond-like carbon coatings via Raman-based wear quantification method

In the friction process, the additive-derived tribofilms formed on coatings will replace the original surfaces and dominate the wear and friction behaviours under boundary lubrication. Therefore, fundamental insight into the mechanisms governing the tribofilm growth significantly contribute to the design and development of high-effective lubricating systems for target coatings. To clarify the tribofilm growth mechanisms, the proposed Raman-based profilometry is used in this chapter to in-situ identify the tribochemical products of additives formed on a-C:H surfaces based on the distinct optical properties. Selective growth of additive-derived tribofilm on a-C:H surface was observed when employing different lubricating additives.

By combining detailed structural and composition analysis (EELS, EDS, and TEM) towards the tribofilms and the upper surface of a-C:H, the effectiveness of Raman-based profilometry in identifying the tribofilm compositions was verified. The obtained results suggest that the surface oxidation layer on a-C:H, which is catalysed by MoDTC-derived molybdenum oxides, plays a crucial role in the growth process of ZDDP tribofilm. The oxidation process transforms a-C:H surface from Lewis base to Lewis acid, providing active growth sites for ZDDP-derived products (phosphate-Lewis base) based on HSAB

principle (Hard Soft Acids Bases). In view of the unobservable wear on the tribofilm growth areas of a-C:H surfaces, it is suggested that the tribochemical reaction between ZDDP-derived products and a-C:H surfaces is driven by interfacial Lewis acid-base interaction rather than stress-dependent mechanism, highlighting the critical role of surface chemical property in the initial nucleation stage of tribofilm growth.

8.1. Selective growth of additive-derived tribofilms on a-C:H surfaces

As shown in Figure 8.1, tribo-tests were conducted on a-C:H/steel contact under oil lubrication with different additives. The corresponding images of wear scars are given in Figure 8.2. As displayed in Figure 8.1a, when MoDTC is introduced into the lubricating oil with ZDDP as additive, the friction-reducing property is obvious improved with friction coefficient reduced from ca. 0.125 to ca. 0.07 which is close to the condition with only MoDTC as additive. Figure 8.1b displays the wear volumes on steel ball and a-C:H coatings (plate). It can be observed that when using ZDDP as additive, the wear only takes place on the steel ball, which is caused by the sacrificial nature of ZDDP tribofilm and its significantly lower hardness compared with a-C:H. As shown in Figure 8.2a, the ZDDP-derived tribofilm could only be observed on the surface of steel ball rather than a-C:H surface under the mild tribo-test condition (contact pressure of 580 MPa). Therefore, the surface-bonded tribofilms of ZDDP on steel surface are continually sacrificed and replenished in the friction process, further resulting in obvious materials loss of steel surface (severe wear). For the condition of employing MoDTC as additives (Figures 8.1b and 8.2b), the main reason triggering the dramatical wear is attributed to abrasive wear caused by MoDTC-derived products.

Here, the interesting finding is that when both MoDTC and ZDDP were employed in the oil, obvious tribofilms were observed on a-C:H surface with only slight wear as shown in Figure 8.2c. To gain fundamental insights into this finding, a Raman-based profilometry is employed to identify the tribofilm components by combining TEM, EELS, and EDS in the later section.

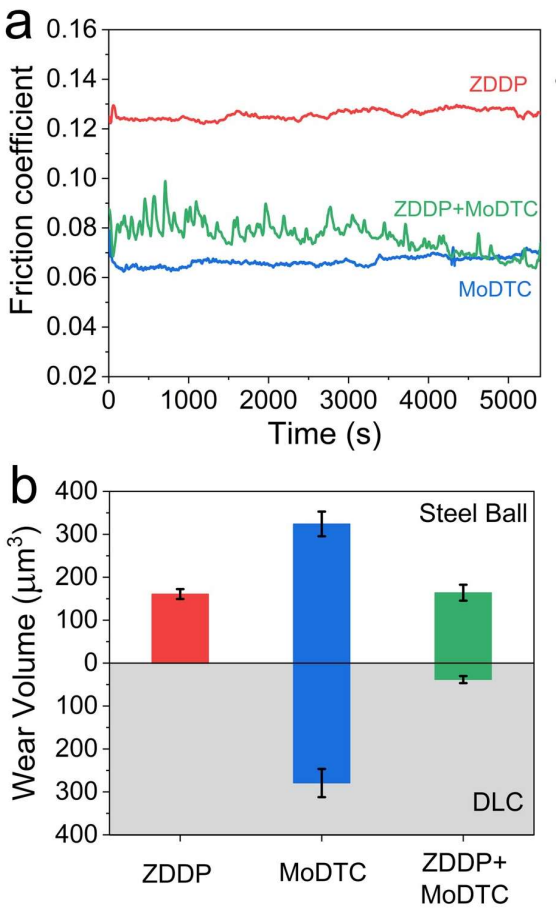

Figure 8.1. Friction and wear behaviors of a-C:H coatings under oil lubrication (PAO4+ZDDP, PAO4+MoDTC, and PAO4+ZDDP and MoDTC; test condition: 1 N, 90 mins).

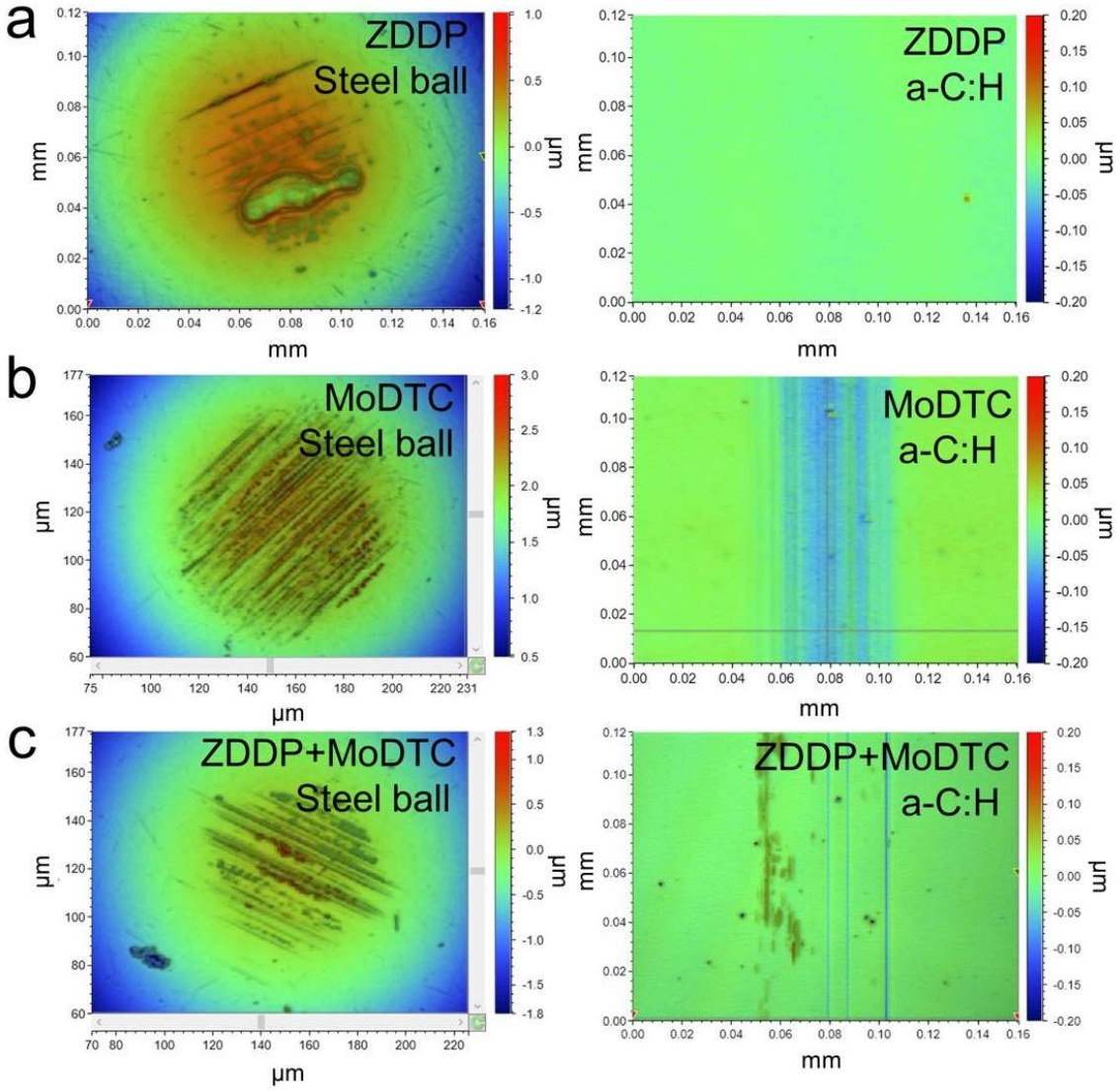

Figure 8.2. 3D optical microscopic images of wear scars of a-C:H coatings under oil lubrication (PAO4+ZDDP, PAO4+MoDTC, and PAO4+ZDDP and MoDTC; test condition: 1 N, 90 mins).

8.2. Identification of additive-derived tribofilm by Raman-based profilometry

The proposed Raman-based profilometry is employed here to identify the tribofilm components formed on a-C:H under oil-lubricated condition with both ZDDP and MoDTC as additives. As indicated in former chapter, this method could provide accurate wear depth of a-C:H under lubricating condition of base oil by monitoring the Raman signal intensity

from silicon sensing layer. When additives are introduced in the oil, the additive-derived tribofilms formed on coating surfaces can cause measurement deviations, which can provide key information of tribofilm compositions based on the known optical properties of tribochemical products.

As shown in Figures 8.3(A-D) and 8.4, a series of tribo-tests under different time were conducted on a-C:H/steel contact under oil lubrication (PAO + ZDDP and MoDTC). After removing the lubricating oil with heptane, the proposed Raman-based approach was employed to quantify the wear depth under the line-scanning mode as shown in Figure 8.6. Non-contact optical profilometer was then employed to characterize the wear scars along the same traces of Raman line-scanning (marked as dot lines in Figure 8.3(A-D)). Note that, for avoiding the measurement errors caused by tribo-induced effect and tribofilm formation, optical profilometer is used only after depositing iridium layer with uniform thickness (ca. 20 nm) on a-C:H surface and the results are employed as standard reference. By comparing the wear profiles obtained by Raman-based method and optical profilometer in Figures 8.3a - d, it is interesting to find that on the positions with tribofilm formation, optical profilometer detects obvious depth rising regions which cannot be detected through Raman-based method.

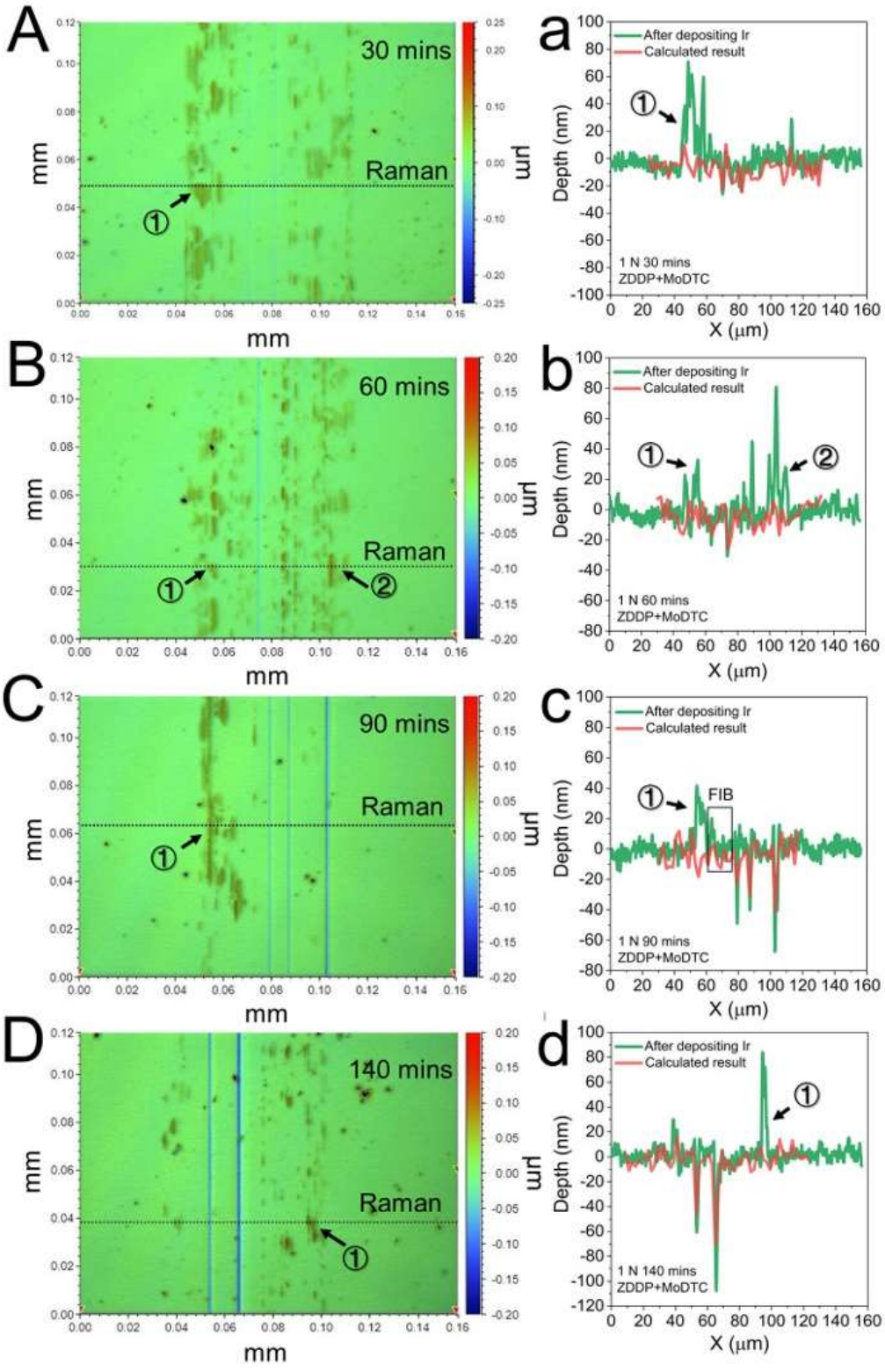

Figure 8.3. (A-D) 3D optical microscopic images of wear scars under different test time. (a-d) Comparison between wear profiles obtained by Raman-based profilometry and non-contact optical profilometer along the same traces. The dot lines marked the line-scanning trace of Raman spectroscopy. FIB test position is marked in c.

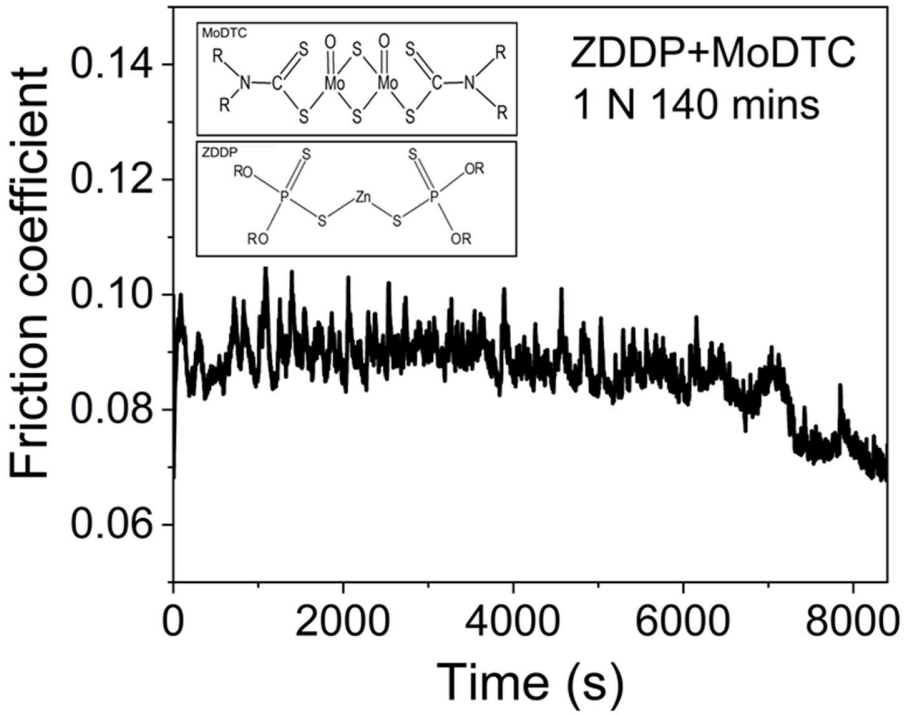

Figure 8.4. Friction behavior of a-C:H film under oil lubrication (1N, 140 mins, PAO + 0.8 wt.%ZDDP and 0.8 wt.% MoDTC).

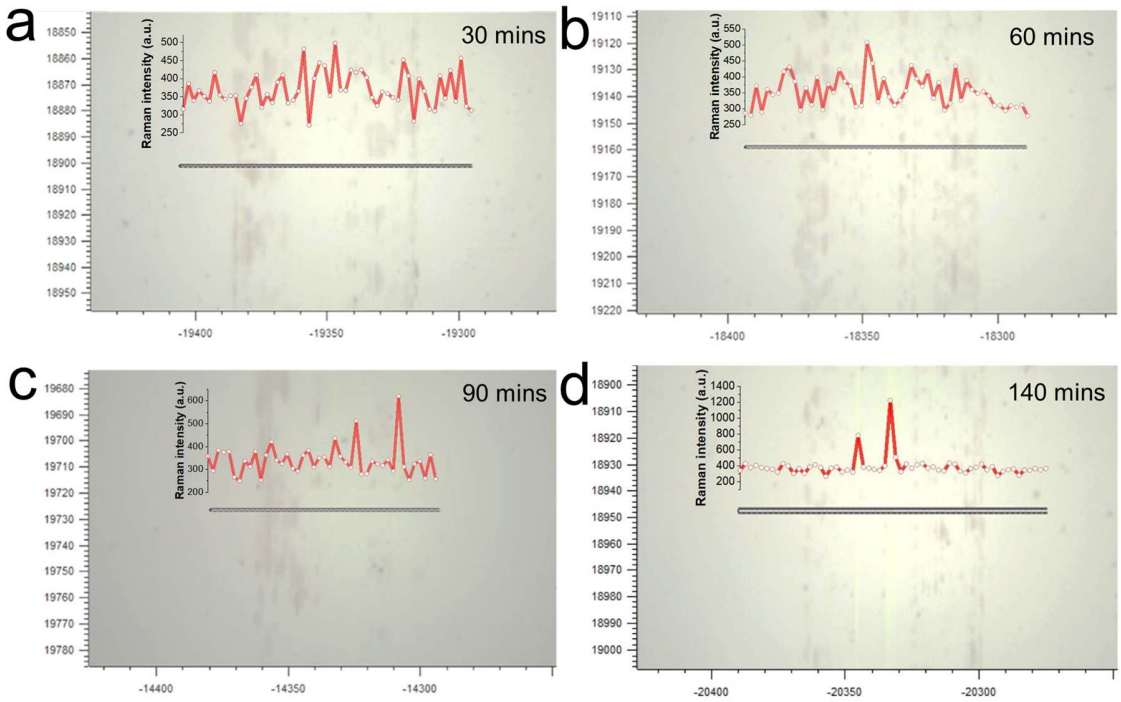

Figure 8.5. Optical images of line-scanning trace of Raman spectroscopy across the wear scars under different test time (oil lubrication: PAO + 0.8 wt.%ZDDP and 0.8 wt.%

MoDTC) and the corresponding Raman intensity of silicon signals which are used to quantify the a-C:H thickness.

As stated above, the effect of tribofilm formation on the measurement accuracy of Raman-based method depends on their optical properties (e.g., absorption coefficient and reflectivity). Specifically, tribofilms composed of tribochemical products with lower transmittance (higher absorption coefficient and reflectivity) towards Raman laser (e.g., MoDTC-derived MoS_2 and MoC) can cause extra attenuation of Raman signal intensity and consequently, remarkable measurement deviations of a-C:H thickness in the form of depth rising as indicated in chapter 7, whereas tribofilms with the high transmittance hardly affect the Raman signal intensity and accurate coating thickness can be obtained.

It is therefore suggested that the tribofilms formed on a-C:H should be composed of tribochemical products with high transmittance. Considering the optical properties of the tribochemical products from ZDDP and MoDTC, it is suggested that the main component of this tribofilm should be glassy zinc/iron phosphate derived from ZDDP.

8.3. Governing factors in the growth of additive-derived tribofilm

To verify the chemical composition of the tribofilm and exploring the growth mechanism, FIB technique was employed to fabricate cross-sectional lamellar specimens of a-C:H coating in the marked area as shown in Figure 8.3c and Figure 8.6 for structural and composition analysis by TEM, EDS and EELS. Two windows for TEM observation were displayed in Figure 8.7c. Windows 1 and 2 correspond to the tribofilm area and no-tribofilm area on a-C:H surface, respectively. Figure 8.6a and b show the TEM images of the cross-section of tribofilm area. Figure 8.6c displays the TEM image of no-tribofilm

area. Through comparison, it is found that the a-C:H thicknesses in two areas are same (ca. 276 nm). More importantly, there is no observable wear on the area with tribofilm formation, indicating that the stress-dependent mechanism of tribofilm growth is inapplicable in this study. This is because the stress-activated tribochemical reactions between additives and contact surfaces prefer to happen on the high local stress-concentrated surface areas with substantial plastic deformation and wear [93], while the tribo-test condition in this study is mild (contact pressure of ca. 580 MPa). Besides, based on the wear profiles displayed in the Figure 8.3, it was found that the there is no obvious wear in the area with tribofilm formation for all the tribo-tested samples.

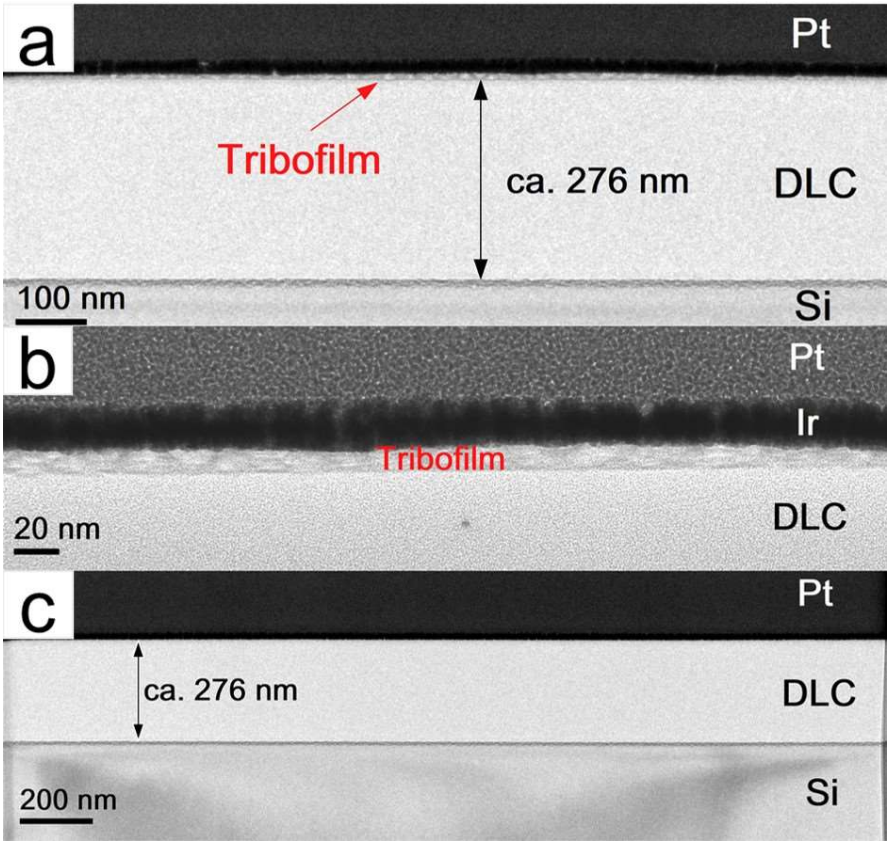

Figure 8.6. (a) TEM image showing the area with tribofilm formation, which correspond to window 1 in Figure 8.8c. (b) Enlarged TEM image showing tribofilm as marked in (a). (c) TEM image showing the area without wear and tribofilm, which corresponds to window 2 in Figure 8.8c.

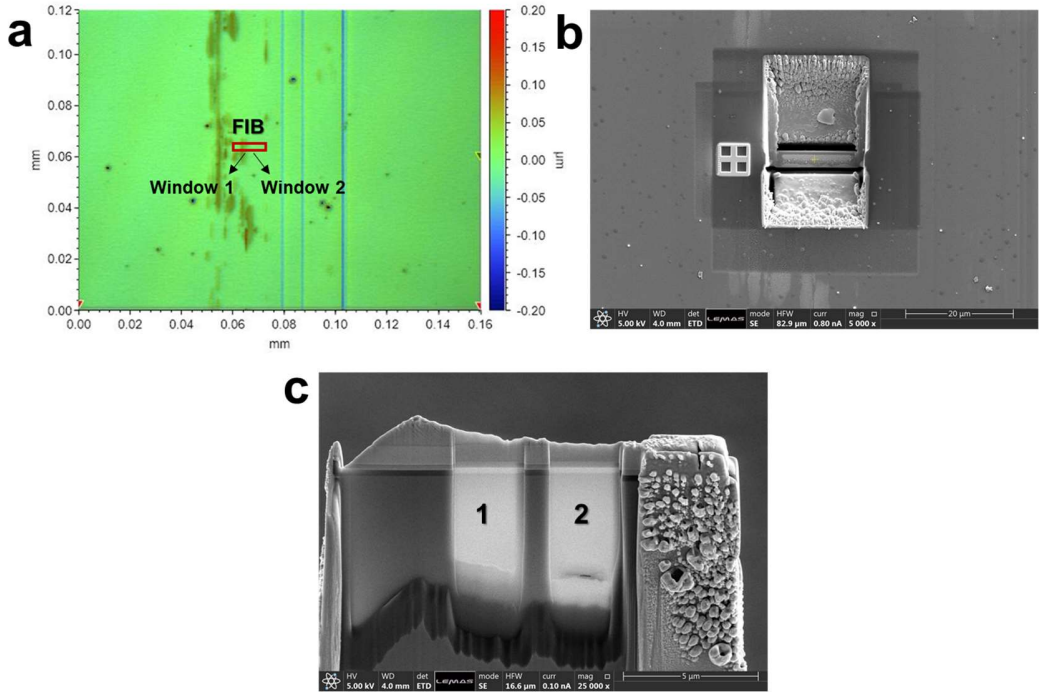

Figure 8.7. (a) 3D optical image showing FIB position. (b) SEM image of FIB position. (c) SEM image of cross-sectional morphology of marked area with two windows for TEM characterization (window 1 with tribofilm and window 2 without tribofilm).

Figure 8.8a shows a high-angle annular dark-field (HAADF) image of the cross-section of tribofilm area, showing the EDX line-scanning trace and test regions of EELS. In Figure 8.8b, the presence of elements P, Zn and O in the tribofilm is confirmed by EDX line-scanning along the trace as marked in Figure 8.8a. Therefore, the main component of tribofilm should be zinc phosphate, agreeing with the above deduction based on Raman-based profilometry. Given undetectable element Mo, the small amount of element S should result from partial substitution for O element in the chain backbone of phosphate rather than MoDTC-derived MoS_2 [94]. An interesting finding is the existence of oxidized layer on the a-C:H surface (Figure 8.8b), which can be caused by the catalytic oxidation driven by the catalytic effect of MoDTC-derived MoO_3 [171-173].

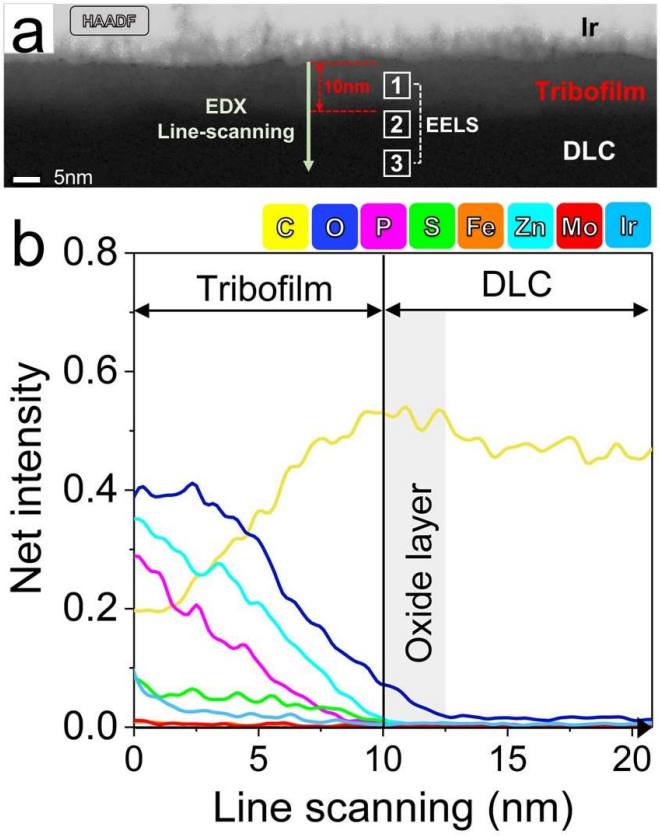

Figure 8.8. (a) HAADF image from area with tribofilm formation on a-C:H surface showing the EDX line-scanning trace and EELS test positions. (b) EDX line-scanning profile along the trace as marked in (a).

In order to clarify the chemical composition of oxidized layer on a-C:H surface, EELS analysis was carried out in three different regions as displayed in Figure 8.9. The typical bonds of C=C (sp^2, 1s-to-π*) and C-H (sp^3, 1s-to-σ*) were centred at 285.5 and 287.5 eV, respectively. It can be observed in Figure 8.9a that the main bonding structure of ZDDP-derived tribofilm is sp^3 bond, agreeing with chemical composition of zinc phosphate. Figures 8.9b and c present the EELS spectra of C-K core-edge collected from oxidized layer and sublayer of a-C:H. Gaussian peak fitting was adopted to quantify the bonding fractions and detailed fitting process was presented in the previous chapter.

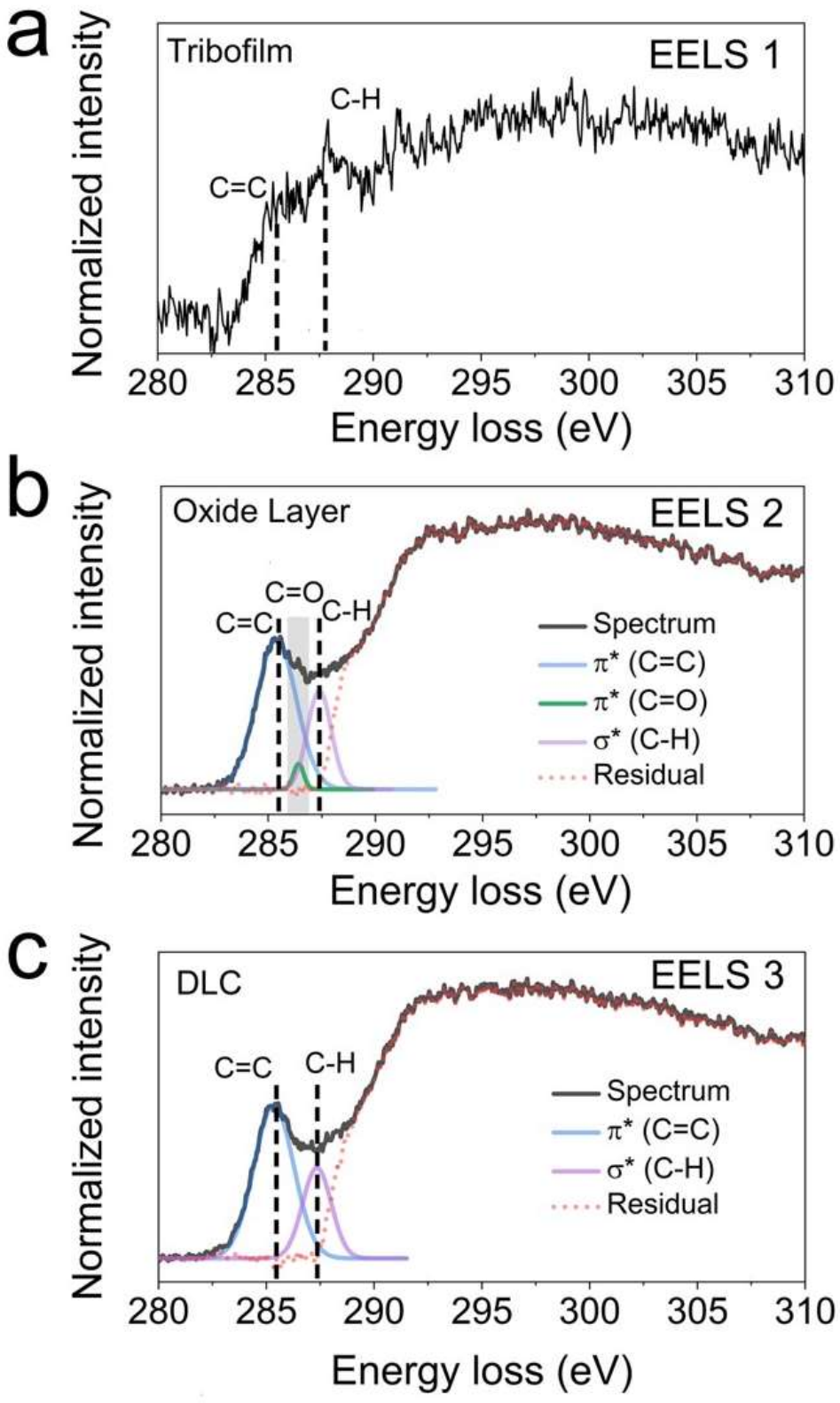

Figure 8.9. EELS C K-edge spectra in three regions of the cross-section of a-C:H (a, tribofilm; b, oxide layer (a-C:H upper surface); 3, a-C:H sublayer). The residual bond fraction is assigned to σ*(C-C, sp^3).

It can be observed that two Gaussian peaks corresponding to C=C and C-H have been well defined in both EELS spectra, but there is an additional peak on the high-energy side of C=C peak (located at -286.5, grey area in Figure 8.9b), which belongs to C=O (sp^2, 1s-to-π*) [174, 175]. Besides, the residual bond fraction is assigned to 1s-to-σ* transition of sp^3 phase (C-C). As shown in Table 8.1, the calculated sp^2 and sp^3 fractions in oxidized layer of a-C:H are 63.2 % (C=C and C=O) and 36.8 % (C-H and C-C), while that in the a-C:H sublayer are 60.2 % and 39.8 %. It can be observed that the oxidized layer underwent a bonding transformation from sp^3 to sp^2. Compared with the C-bond fractions in the sublayer, the sp^3 fraction in oxidized layer decreases by 3 %, which is close to the C=O fraction (2.6 %, sp^2). It indicates that the oxidation of carbon in a-C:H prompts the bond dissociation of C-C and C-H, and the formation of C=O bond.

Table 8.1. EELS C-bonds fractions of oxidized layer and sublayer of a-C:H.

Region	sp^2		sp^3	
	C=C	C=O	C-H	C-C
Oxidized layer	60.6 %	2.6 %	23.9 %	12.9 %
Sublayer	60.2 %	-	25.7 %	14.1 %

Based on EDX and EELS, the chemical structure of oxidized layer was confirmed, which can transform a-C:H surface from Lewis base to Lewis acid (oxidized a-C:H) according to HSAB principle [176, 177]. More importantly, the presence of surface oxidized layer on a-C:H provides active sites to promote the tribochemical reaction with phosphate (Lewis base). The above results give direct evidence that the selective growth of ZDDP tribofilms on a-C:H surface in mild tribo-test condition is driven by Lewis acid-base interaction rather than stress-dependent mechanism in view of the unobservable wear on the a-C:H surface as indicated above.

Additionally, since the oxidation process on a-C:H surface is accompanied by the rearrangement (clustering or ordering) of sp^2-hybridized carbon phase into six-fold ring-like structure (i.e., graphite-like), the oxidized layer is more prone to wear [163, 166]. Figure 8.10 presents the wear behaviors of a-C:H under different applied loads. It can be observed that the wear volumes of a-C:H under low applied load of 1 N kept at a low level for the test time ranging from 30 to 140 mins, indicating ZDDP could form effectively anti-wear tribofilms on a-C:H surfaces in the friction process. However, when increasing the applied load to 10 N (1.2 GPa) and 30 N (1.8 GPa), the coverage of ZDDP tribofilms on coating surface decreased notably (Figure 8.10b and c), resulting in a significant increase in wear volume. Compared with ZDDP-derived tribofilms formed on ferrous surfaces which show good anti-wear properties even under 5.2 GPa, the tribofilms formed on a-C:H are less durable under high applied loads which is in accordance with the literature [101, 178]. Based on above results, the less durability of ZDDP tribofilm on a-C:H is attributed to the easy-shear capability of oxidized layer.

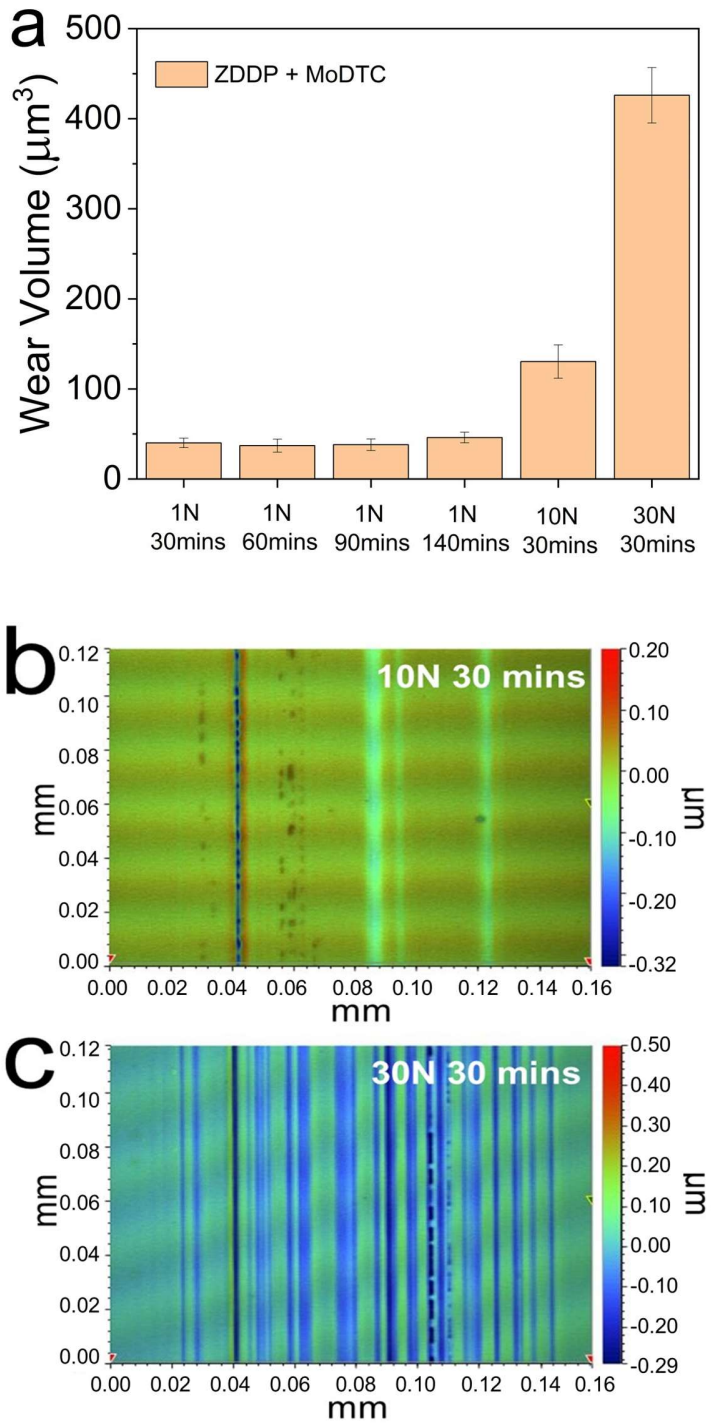

Figure 8.10. Wear behaviors of a-C:H in additive-lubricated conditions (PAO + ZDDP and MoDTC) under different time and loads. (a) Wear volumes. (b) 3D optical images under the tribo-test condition of 10 N (1.2 GPa) and 30 mins. (c) 3D optical images under the tribo-test condition of 30 N (1.8 GPa) and 30 mins.

8.4. Friction and wear mechanism of a-C:H under additive-lubricated condition

It is well accepted that friction and wear behaviors are dominated by tribofilms formed on contact surfaces [16-18]. Gaining fundamental insights into the tribofilm growth mechanism can benefit a better understanding of the tribological mechanisms. Figure 8.11 presents a schematic illustration of tribofilm growth mechanism on a-C:H surfaces with different lubricating additives based on above findings, which could be used to clarify the tribological behaviors in section 8.1. As shown in schematic illustration, when ZDDP is used alone in lubricating oil, tribofilms prefer to form on the steel surface. Since the hardness of a-C:H is obvious higher than steel [178], wear at initial stage mainly happens on steel surface and results in abundant nascent surfaces that is easily oxidized in the tribological process. These oxide areas provide active sites for the tribofilm growth based on Lewis acid-base interaction (Fe^{3+}-Lewis acid, phosphate-Lewis base). Given the Lewis base property of a-C:H, ZDDP tribofilm (Lewis base) was formed on steel surface rather than a-C:H. After that, wear mainly takes place on ZDDP tribofilm, considering its significantly low hardness (hardness: a-C:H > steel > ZDDP tribofilm). As this wear process on steel surface will be repeated constantly, remarkable wear was observed on steel ball. In addition, since the friction behavior depends on the ZDDP tribofilms, the friction coefficient is close to the condition of ferrous / ferrous contacts with ZDDP as additive [180]. When adding MoDTC into the above lubricating oil, MoDTC-derived MoO_3 performs action for catalytic oxidation of a-C:H surfaces which transforms a-C:H surface from Lewis base to Lewis acid, providing active growth sites for ZDDP tribofilms. In view

of lower hardness of ZDDP tribofilms than steel, slight wear was observed on a-C:H surface.

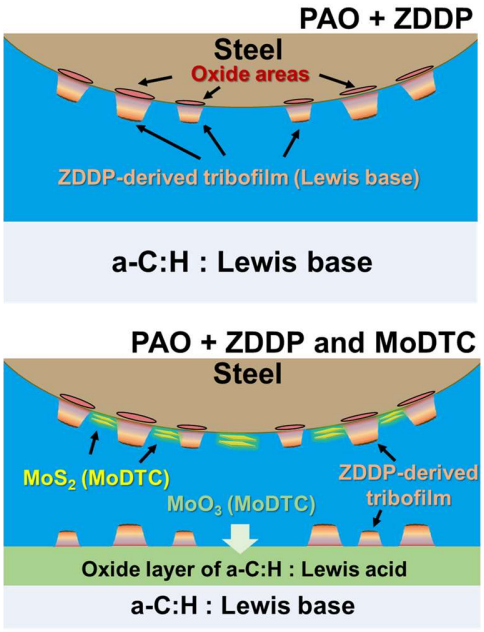

Figure 8.11. Schematic illustration of the growth mechanism of ZDDP-derived tribofilms on a-C:H surface.

As indicated in the chapter 7, tribofilms composed of tribochemical products with low transmittance (e.g., MoS_2) can introduce measurement deviations of Raman-based profilometry in the form of depth rising. Figure 8.3 presents the wear profiles obtained by Raman-based method and there is no depth rising, indicating no formation of crystal MoS_2 on a-C:H surface.

For locating the MoDTC-derived MoS_2, Raman test were conducted on the wear scar of steel ball as shown in Figure 8.12a. Compared with the lubricating condition with only MoDTC as additive, the Raman signal intensity of MoS_2 increased significantly when using MoDTC and ZDDP as additives, indicating MoDTC-derived MoS_2 crystals preferred to accumulate and grow into large size on steel surface under the existence of ZDDP. In the friction process, ZDDP decomposes into small molecular fragments with abundant sulphur

atoms which can react with ferrous surfaces to form mixtures of FeS/ZnS [110]. These mixtures provide active S^{2-} to promote the sulphuration of molybdenum oxysulphide into MoS_2 units. These units progressively grow into large lamellar sheets and cover the contact asperities, further resulting in low friction. This explains why the friction coefficient with MoDTC and ZDDP as additives kept between the values with only MoDTC or ZDDP as additive in the initial stage and decreased over time to reach the same value with MoDTC as additive.

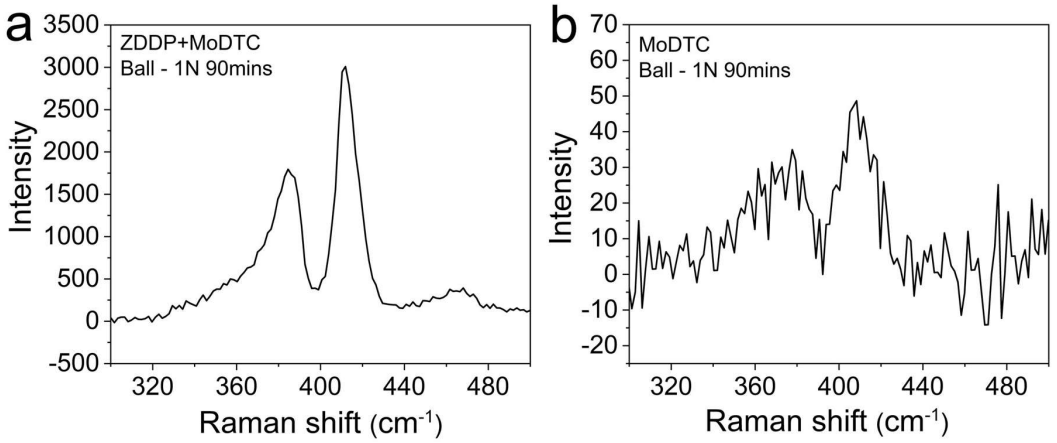

Figure 8.12. Raman spectra of MoS_2 detected on the wear scars of steel balls (counterpart) with different lubricants (a) PAO with ZDDP and MoDTC. (b) PAO with MoDTC.

As indicated in the previous chapter, MoDTC derived tribochemical products can accelerate the wear of DLC, which is attributed to the easy-shear capability of oxidized a-C:H layer caused by MoO_3 in the first stage and the abrasive wear of hard MoC formed via tribo-induced carburization of MoS_2 in the following stage. When using ZDDP in combination with MoDTC, the wear acceleration of a-C:H was significantly improved since a protective ZDDP-derived tribofilms are formed on the top surface and replace the previous surface of oxidized a-C:H layer. More importantly, the local stress concentration caused by increased surface roughness under severe wear can be obviously alleviated

[181-183], which weaken the effect of shear forces on the tribochemical reactions, such as the oxidation of a-C:H coatings and the carburization of MoS_2 into MoC.

8.5. Summary

Raman-based profilometry was employed in this study to identify the additive-derived tribofilms on a-C:H coatings based on their distinct optical properties. To demonstrate the effectiveness of Raman-based method, the chemical composition and structure of tribofilms were clarified by combining TEM, EDS, and EELS. The obtained results confirmed the dominating role of oxidized a-C:H layer in the growth process of ZDDP-derived tribofilms. This oxidation process catalysed by MoDTC-derived MoO_3 can transform a-C:H surface from Lewis base to Lewis acid, providing active growth sites for ZDDP tribofilms in the similar way happened on the oxidized ferrous surfaces. It gives direct evidence that the tribochemical reaction between ZDDP-derived products (phosphate-Lewis base) and a-C:H surfaces is driven by Lewis acid-base interaction rather than stress-dependent mechanism in view of the unobservable wear on the tribofilm formation areas of a-C:H surfaces. In addition, the lower durability of ZDDP tribofilms formed on a-C:H surfaces is attributed to the easy-shear capability of oxidized layer. These findings propose a new pathway for identifying additive-derived tribofilms formed on coating surfaces which can help gain fundamental insights into tribofilm growth mechanisms, and thus benefit a better understanding of the tribological mechanisms and the development of effective solid-liquid lubricating systems for diverse surface materials.

Chapter 9

Development of wear-sensing coating system on steel substrate for wear measurement via Raman-based profilometry

In this chapter, the silicon coatings with different crystallinity were developed by pulsed-DC magnetron sputtering method. The influence of gas pressure, cathode power, deposition temperature, and substrate-target distance on crystal size, crystalline content, surface roughness, and Raman intensity of silicon coatings was investigated via Raman spectroscopy, XRD and optical profilometer. After that, the wear-sensing coating system composed of a-C:H and crystalline silicon was deposited on steel substrate and employed to measure the coating wear. The results indicated that both Raman intensity and surface roughness increased with increasing the crystal size of silicon coatings. To realize accurate wear monitoring via Raman-based profilometry, a balance between high Raman intensity and low surface roughness was achieved by controlling the crystal size of silicon coatings.

9.1. Development of the sensing layer of crystalline silicon

In the previous chapter, a Raman-based profilometry was developed to achieve accurate coating thickness measurement. As displayed in Figure 9.1, this proposed approach is based on a bilayer structure: a top layer of a-C:H film is considered as a light attenuating and anti-wear layer while the underlayer of silicon serves as Raman-sensing layer. Through constructing the relationship between a-C:H thickness and the Raman intensity of silicon signal, coating thickness quantification method is established to quantify the a-C:H wear. In

this chapter, this bilayer structure is transferred on the steel substrate for realizing the coating wear measurement. The Raman intensity and surface roughness of silicon layers are two key factors for the Raman-based profilometry. For obtaining high Raman intensity, it is necessary to develop silicon coatings with high crystallinity by optimizing the deposition parameters (e.g., temperature, power, gas pressure). Meanwhile, the surface roughness of as-grown coatings should be controlled in a reasonable range as high roughness can result in big errors of wear measurement.

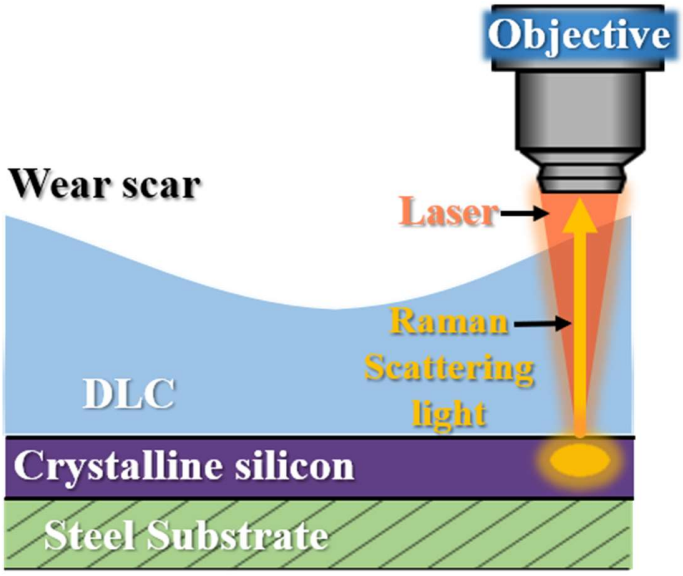

Figure 9.1. Schematic illustration of the Raman-based profilometry.

Here, a series of silicon coatings with different crystallinity were deposited on steel discs via pulsed-DC magnetron sputtering method as shown in Table 9.1. The influence of gas pressure, cathode power, temperature, and substrate-target distance on the crystallinity (crystal size and crystalline content) was investigated by combining XRD and Raman spectroscopy. Figure 9.2 displays the Raman spectra of silicon coatings deposited under different conditions. To calculate the crystalline content, three Gaussian peaks centred at 520, 505, and 480 cm^{-1} were used to fit the Raman spectra, which correspond to the crystalline, boundary, and amorphous phases, respectively [122, 127, 128]. A typical shape

fitting process of Raman spectrum is given in Figure 9.2c. The crystalline content is defined as the ratio of $(A_{crystalline}+A_{boundary})/(A_{crystalline}+A_{boundary}+A_{amorphous})$, where $A_{crystalline}$, $A_{boundary}$ and $A_{amorphous}$ are the integrated areas of crystalline, boundary, and amorphous phases. The crystalline contents and average Raman intensity are listed Table 9.1.

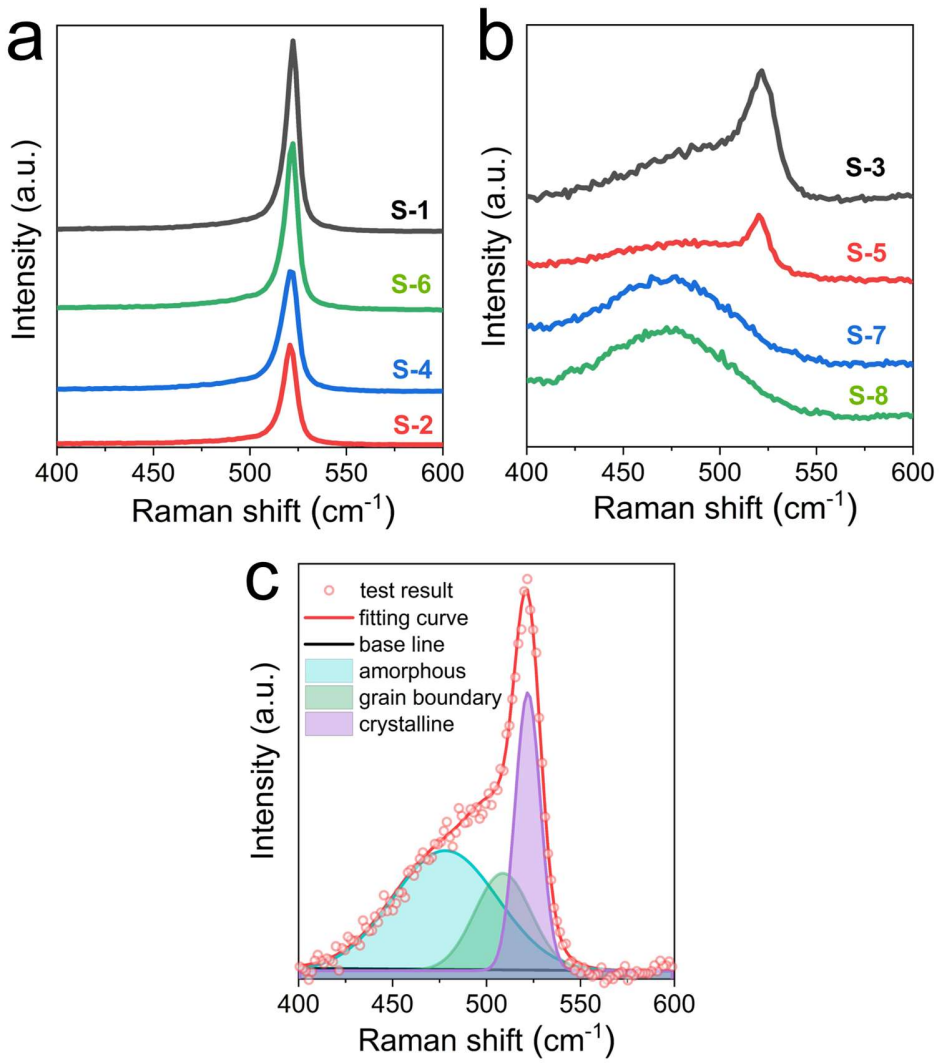

Figure 9.2. (a-b) Raman spectra of silicon coatings deposited via pulsed-DC magnetron sputtering deposition under different conditions. (c) Fitting curves by three Gaussians, corresponding to amorphous, grain boundary, and crystalline phases, respectively.

When the deposition temperature is up to 520 °C, the crystalline silicon coatings can be synthesized by adjusting the deposition parameters. It can be observed that by reducing the substrate-target (S-T) distance and increasing the cathode power and gas pressure, the

crystalline contents of silicon coatings increase obviously (above 93 %). The surface roughness values of silicon coatings are characterized via non-contact optical profilometer. Figure 9.3 displays the corresponding surface morphologies of silicon coatings with different crystallinity. With increasing the crystalline content, the surface roughness increases dramatically from 16.4 nm (*Ra*) of amorphous silicon coating to 1347 nm (*Ra*) of highly crystalline silicon coating. High crystalline content not only results in high Raman intensities but also high surface roughness. One interesting finding is that for the silicon coatings with similarly high-crystalline contents ranging from 93.5 to 97.8 % (S-1, S-2, S-4, and S-6), there are notable differences on the surface roughness values and Raman intensities (Table 9.1).

Table 9.1. Deposition parameters of silicon coatings

Sample ID	Pressure (mbar)	Power (kW)	Temp. (°C)	S-T (cm)	Ra (nm)	Cry. Size (nm)	Cry. Cont. (%)	Raman (Avg.)	CV (%)
S-1	6.0×10^{-3}	4	520	16.5	1347	111.1	97.8	18923.4	31.4
S-2	4.0×10^{-3}	4	520	16.5	62.9	32.7	93.5	8765.7	12.5
S-3	3.0×10^{-3}	4	520	16.5	32.6	-	49.7	-	-
S-4	4.0×10^{-3}	5	520	16.5	480	43.2	96.5	12699.1	47.5
S-5	4.0×10^{-3}	3	520	16.5	27.5	-	33.6	-	-
S-6	4.0×10^{-3}	4	520	15.5	320	71.8	94.3	16081.2	36.5
S-7	4.0×10^{-3}	4	520	20	17.3	-	0	-	-
S-8	4.0×10^{-3}	4	480	16.5	16.4	-	0	-	-

S-T, distance between substrate and target on the cathode. Cry. Size, average grain size of silicon crystal. Cry. Cont., crystalline content. Ra, surface roughness. Raman (Avg.), average values of Raman intensity of 15 test points on each sample. CV, coefficient of variation of Raman intensity.

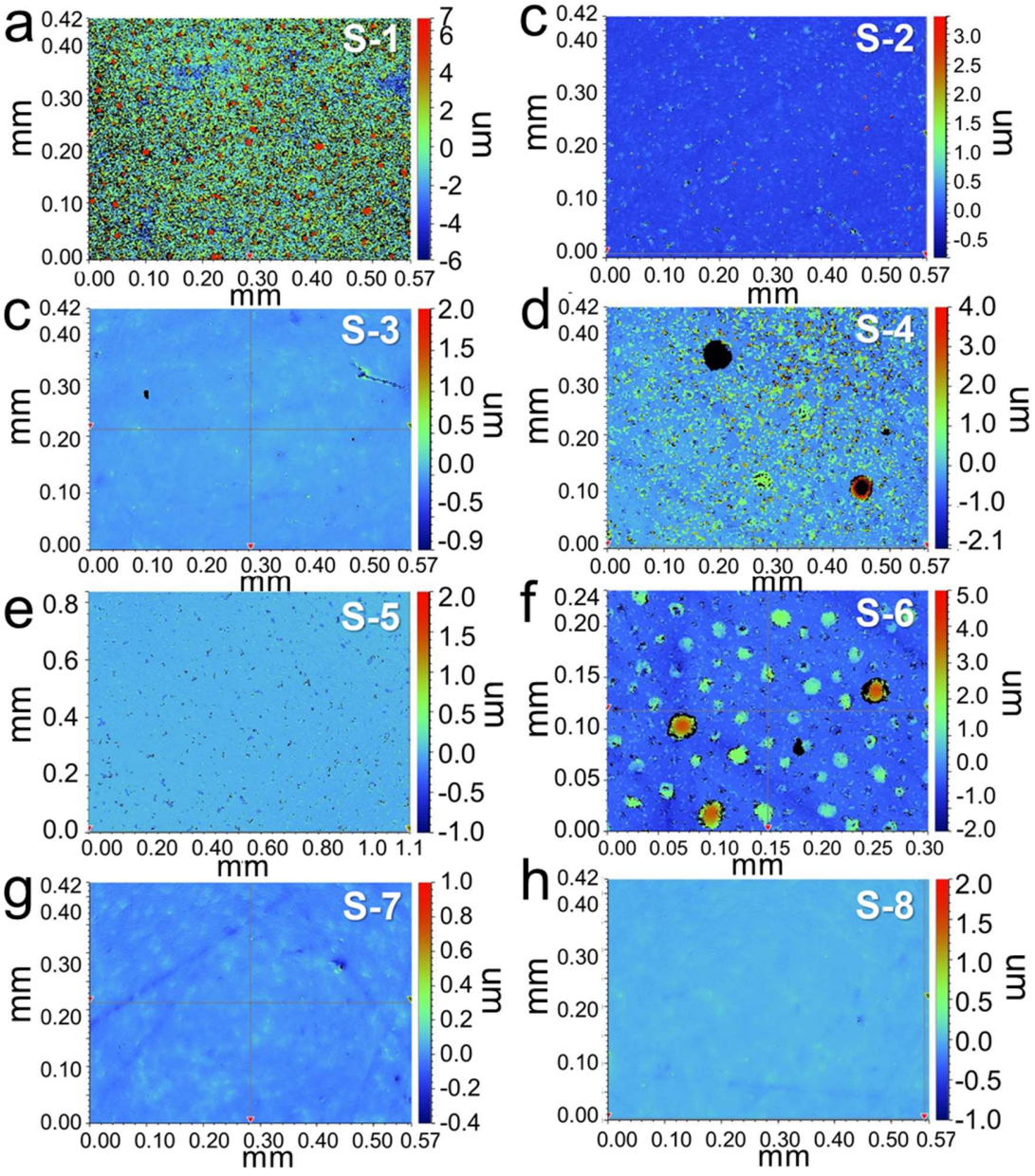

Figure 9.3. 3D optical images of silicon coatings deposited by pulsed-DC magnetron sputtering method under different deposition parameters which are listed in Table 9.1. (a, S-1. b, S-2. c, S-3. d, S-4. e, S-5. f, S-6. g, S-7. h, S-8.)

To clarify the key factor governing the Raman intensity and surface roughness, XRD is employed to study the crystal structure of the silicon coatings with high crystalline contents (S-1, S-2, S-4, and S-6). Figure 9.4 gives the corresponding XRD results after background subtraction. The diffraction peaks located at 28.4 º, 47.3 º, 56.2 º, and 69.2 º correspond to

the (111), (220), (311), and (400) planes of crystalline silicon [127]. The average grain sizes of these four crystalline silicon coatings were calculated from the three main peaks at (111), (220), and (311) based on the Scherrer equation, as shown in Table 9.1. The silicon coatings with highly crystalline content (S-1, S-2, S-4, and S-6) display notably different grain sizes ranging from 32.7 to 111.1 nm.

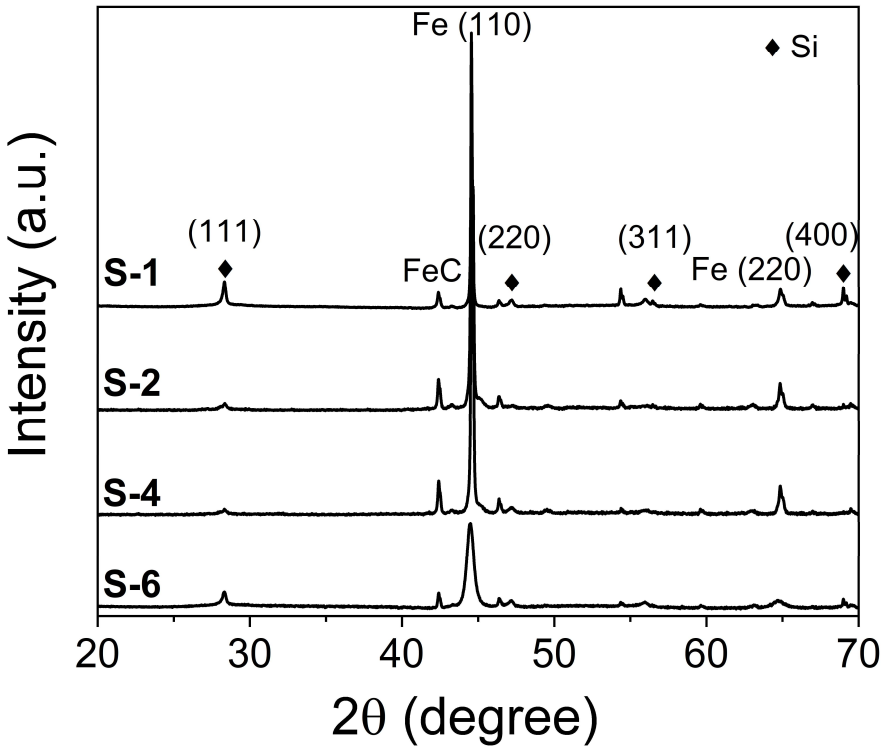

Figure 9.4. X-ray diffraction patterns of high crystalline silicon coatings (S-1, S-2, S-4, and S-6).

Figure 9.5 display the values of crystalline content, grain size, surface roughness and Raman intensity of the crystalline silicon coatings. Through comparison, it is found that the grain sizes rather than crystalline contents show high correlation with the surface roughness and Raman intensity. Specifically, the surface roughness and Raman intensity increase with grain size. It should be also pointed that with increasing the grain size, the coefficient of variation of Raman intensity obtained on a series of test points increases significantly

(Table 9.1), indicating the widening distribution of grain size of silicon crystals. The sputtered yield and energy of sputtered silicon atoms arriving at substrate was increased by reducing the S-T distance and increasing the gas pressure and cathode power in the coating deposition process, which not only promote the grain growth of silicon crystal but also lead to non-uniform grain growth, resulting in multimodal grain size distribution.

For improving the accuracy of wear measurement, the variation coefficient of Raman intensity should be reduced to avoid the big measurement errors. It is therefore suggested that the grain size of silicon coatings should be controlled at a reasonable value to reduce the measurement errors caused by high surface roughness and big variation of Raman intensities and provide high enough Raman intensity for achieving reliable wear-measurement. Through adjusting the grain size to ca. 32.7 nm by optimizing the deposition parameters, the silicon coating with low surface roughness at 62.9 nm, small variation coefficient of Raman intensity at 12.5% and Raman intensity of 8765.7 was obtained and denoted as S-2 in Table 9.1, which is employed as the sensing layer in the later section for constructing wear-sensing coating system on steel substrate to realize wear measurement via Raman-based profilometry.

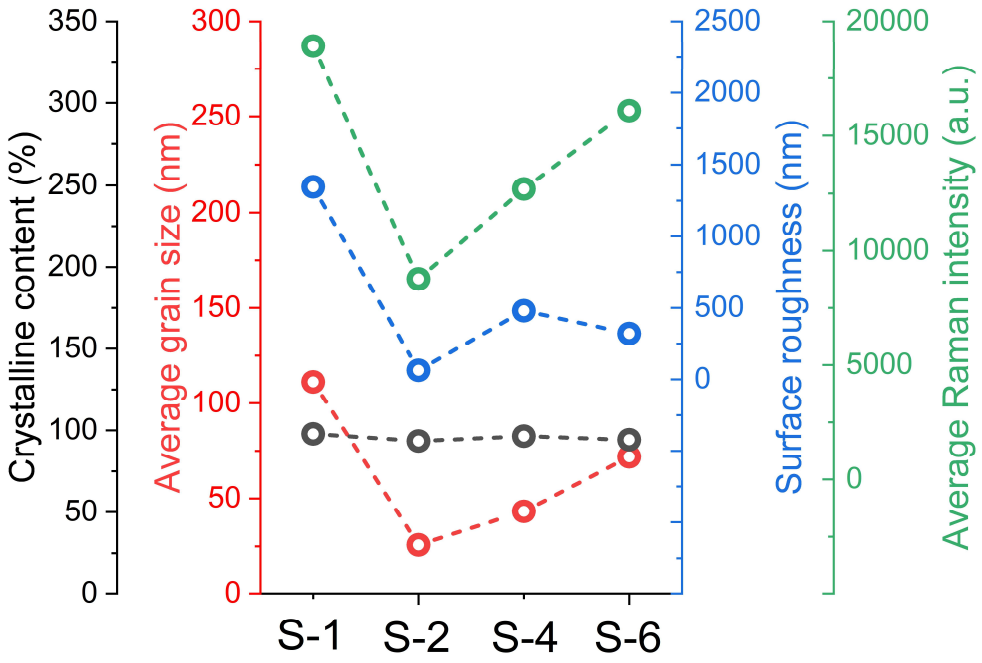

Figure 9.5. Image showing the relationship among crystalline content, grain size, surface roughness, and Raman intensity of silicon coatings (S-1, S-2, S-4, and S-6).

To further study the crystal structure of silicon coating and the influence of cathode power on the crystallinity, FIB with in-situ lift-out technique was used to fabricate cross-sectional lamellar specimens of silicon coating deposited on steel substrate for structure and composition characterization by TEM, FFT and EDS. As shown in Figure 9.6a, the bottom layer of silicon coating was deposited using the parameters of S-5 while the deposition condition of the top layer is same with S-4. The main difference is the cathode power (S-4, 5 kW; S-5, 3 kW). Figure 9.6b gives the corresponding EDS mapping (elements: Pt, Si, Fe) of the selected area in Figure 9.6a.

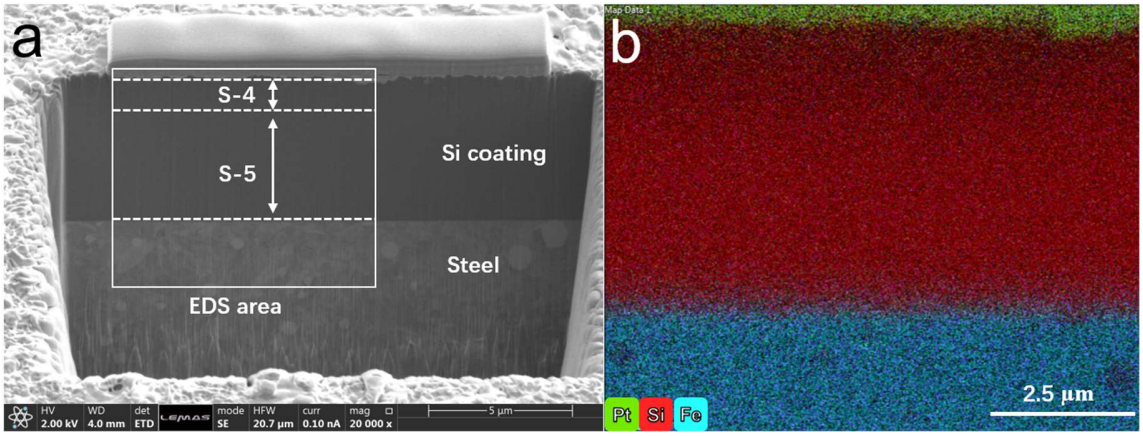

Figure 9.6. (a) SEM image showing the cross section of silicon coating deposited under different cathode powers on steel substrate. (b) The corresponding EDS mapping image of the selected area in (a).

Figure 9.7a displays the HRTEM image of selected area in Figure 9.6a. It can be observed that the silicon coating was transformed from amorphous to crystalline by increasing the cathode power from 3 to 5 kW. The formation of amorphous and crystalline silicon was also confirmed by FFT patterns, as shown in Figures 9.7b and c. In addition, HRTEM images containing detailed information about the crystal structure of silicon coatings deposited under high cathode power of 5 kW are given in Figures 9.7d and e. In the interface area between amorphous and crystalline layers, the obvious nanograins of several nanometers are observed, corresponding to the initial nucleation stage (Figure 9.7d). With increasing the deposition time, the grains with columnar structure were formed in the bottom area of S-4. In the top area of S-4, the recrystallized grain structure was observed as displayed in Figure 9.7e. The main reasons of existing two crystalline structures (i.e., columnar and recrystallized) can be ascribed to the gradually increased cathode power from 3 to 5 kW.

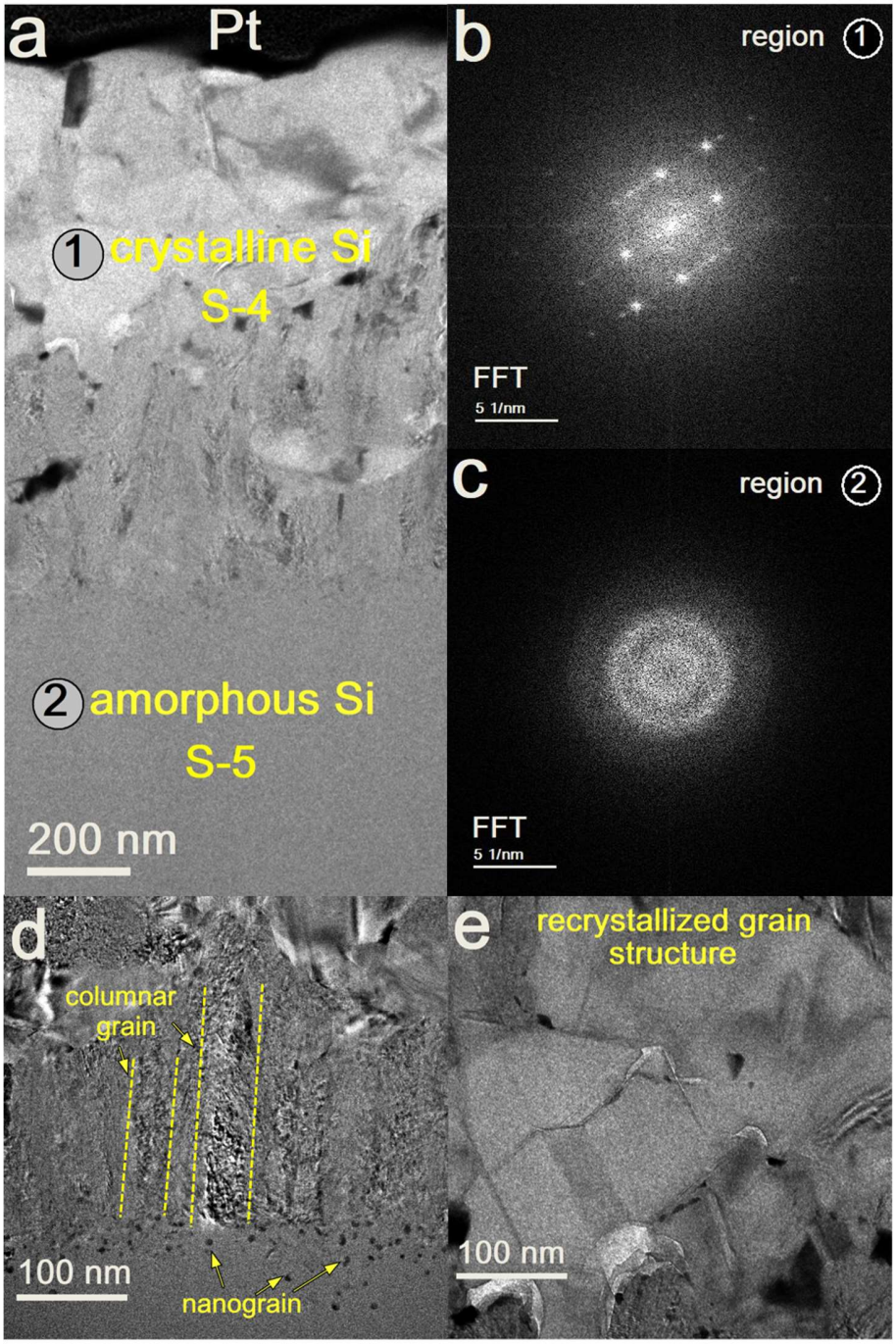

Figure 9.7. (a) HRTEM image showing the cross section of silicon coating deposited under different cathode power (S-4: 5 kW; S-5: 3 kW). (b) Fast Fourier transform (FFT) patterns clarifying the crystallinity of the marked area in (a). (c) and (d) HRTEM images of the bottom area and top area of crystalline silicon coating (S-4) deposited under high cathode power of 5 kW.

9.2. Deposition of wear-sensing coating system on steel substrate

In this section, a bilayer coating composed of a-C:H top layer and silicon sensing underlayer was deposited on steel substrate through PECVD and pulsed-DC magnetron sputtering. The a-C:H layer was deposited directly on silicon coating (S-2) via the same deposition condition in the chapter 4. Figure 9.8 shows the HRTEM image of the cross section of bilayer coating which was fabricated by FIB. It can be observed that the thickness of a-C:H was ca. 230 nm. In addition, the columnar grains were observed in the bottom area of silicon layer while recrystallized structure was formed on the top area. The crystal structure of S-2 is similar with that of S-4 in Figure 9.7. As shown in Table 9.1, the average Raman intensity of S-2 is 8765.2 which is high enough for the wear measurement via Raman-based profilometry. Meanwhile, compared with other crystalline silicon coatings, S-2 shows the lowest variation coefficient of Raman intensity and surface roughness.

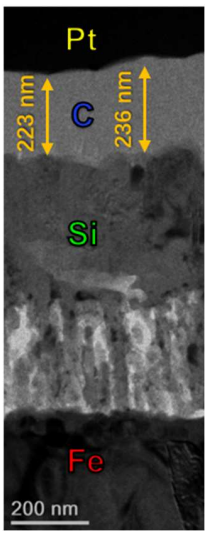

Figure 9.8. HRTEM image showing the bilayer structure of coating (top layer of a-C:H and bottom layer of crystalline silicon) deposited on steel substrate by combining PECVD and pulsed-DC magnetron sputtering.

To verify the bilayer structure of coating, EDS elemental mapping was used to characterize the chemical composition. Figure 9.9a shows the HRTEM image of the cross section of silicon coating. Figure 9.9b-e displays the corresponding EDS mapping images of elements Pt, C, Si and Fe, which demonstrate that the silicon layer and a-C:H layer were successfully deposited on steel substrate. In addition, the carbon element appearing in the Pt layer comes from the precursor gas used to deposit Pt in a FIB system.

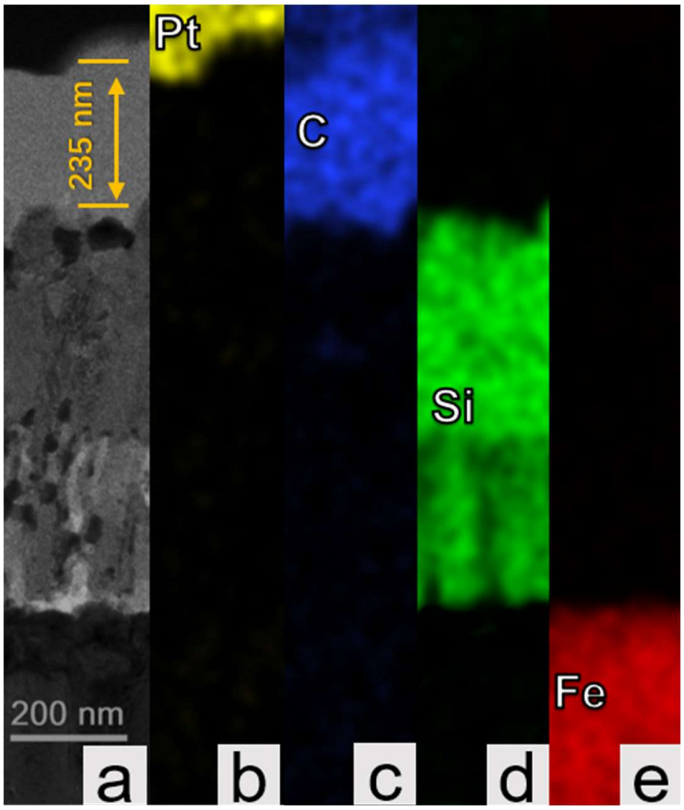

Figure 9.9. (a) HRTEM image showing bilayer structure of coatings deposited on steel substrate. (b-e) The corresponding EDXS elemental mapping images of Pt, C, Si and Fe.

9.3. Wear measurement based on wear-sensing coating system via Raman-based profilometry

A series of dry friction tests, with time ranging from 60 to 110 min, were conducted on the wear-sensing coating system deposited on steel substrate with the applied load of 1N (580

MPa), frequency of 2.5 Hz, stroke of 2mm, and ambient environment. The counterpart is steel ball. Figure 9.10 shows the friction curves under different test time. At the initial running-in stage, the friction coefficients were around 0.27, which gradually decreased to 0.15 after 30 min test.

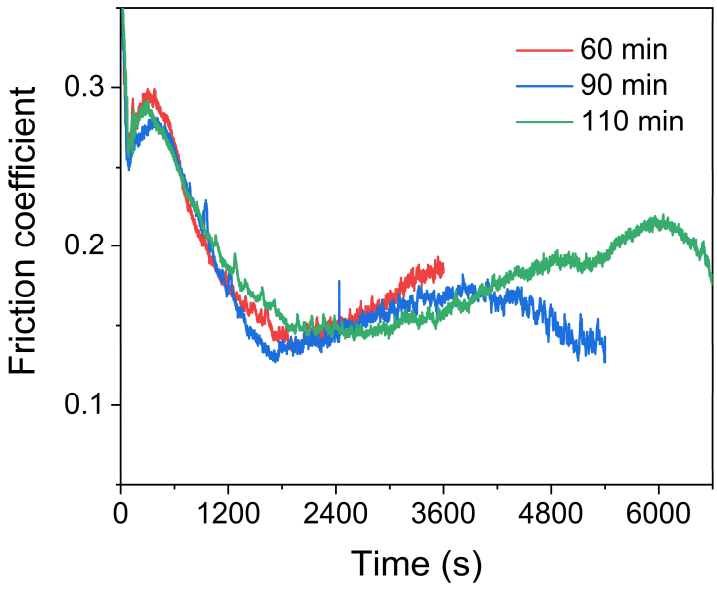

Figure 9.10. Friction curves of bilayer coating under different test time in the dry friction.

Here, to avoid the tribo-indued measurement errors of optical profilometer, an iridium layer with uniform thickness was deposited on the tribotested samples by DC magnetron sputtering to provide a top surface with consistent optical properties. Then, the optical profilometer was used to characterize the wear scars. This improved optical profilometry is used to provide an accurate wear information as a standard reference to verify the results obtained by Raman-based profilometry. In a typical process, the Raman-based profilometry was first used to quantify the wear depth of tribotested samples. Then, the improved optical profilometry (with the iridium layer on the top of coating) was employed to characterize the wear profiles.

The Raman line-scanning tests are conducted across the wear track and the Raman intensity of silicon signal was collected along the trace every 4 μm as shown in Figure 9.11. With knowing the optical parameters of a-C:H, the thickness of top a-C:H layer can be calculated based on the Raman intensity of silicon signal of crystalline silicon underlayer by the equation 5.5 as stated in chapter 5. After subtracting the thickness value of as-grown a-C:H layer of ca. 230 nm, the wear depth values along the line-scanning trace were obtained and presented as red points as displayed in Figure 9.13.

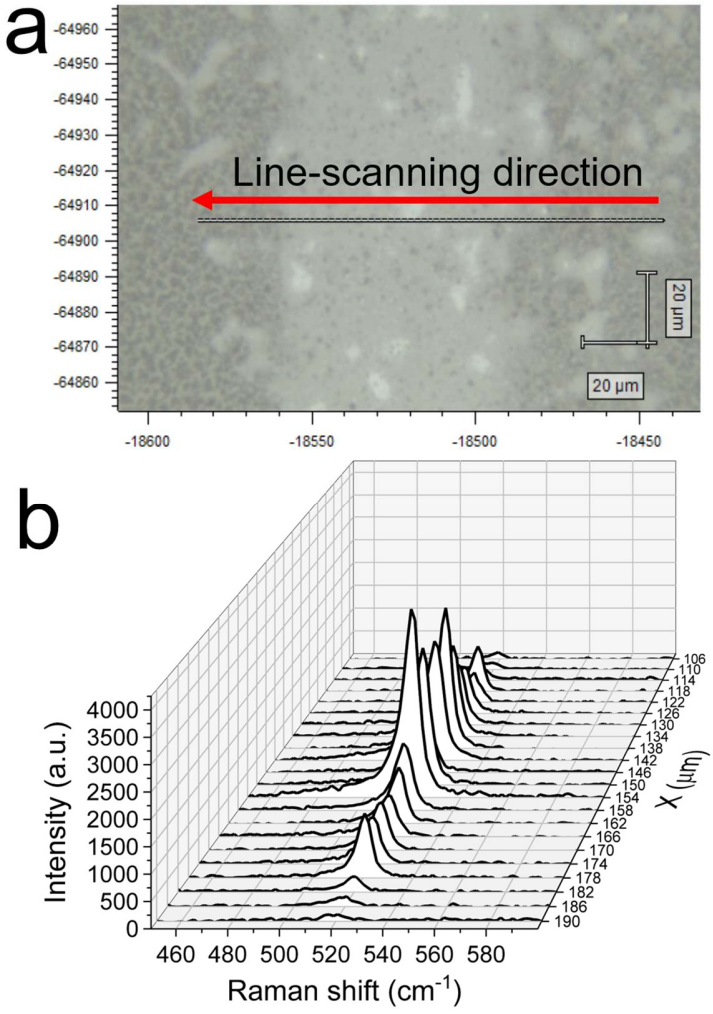

Figure 9.11. (a) Optical image of line-scanning trace of Raman spectroscopy across the wear track (tribo-test time: 90 mins). (b) Raman spectra of a series of silicon signals obtained from line-scanning.

Figure 9.12 displays the images of wear scars characterized by the improved optical profilometry. The corresponding wear profiles were presented as black lines in Figure 9.13. It can be observed that with increasing the test time from 60 to 110 min, the wear width and depth were increased obviously from ca. 75 to 120 μm and from ca. 130 to 225 nm, respectively.

Through comparison, it could be observed that the wear depth values of a-C:H layer obtained by Raman-based profilometry shows good alignment with that measured by improved optical profilometry. It is demonstrated that based on the wear-sensing coating system, Raman-based profilometry could provide accurate wear information. As this wear-sensing coating system could be deposited on the substrate with various materials and shapes, it may open a new pathway for realizing in-situ and real-time wear measurement in diverse engineering applications.

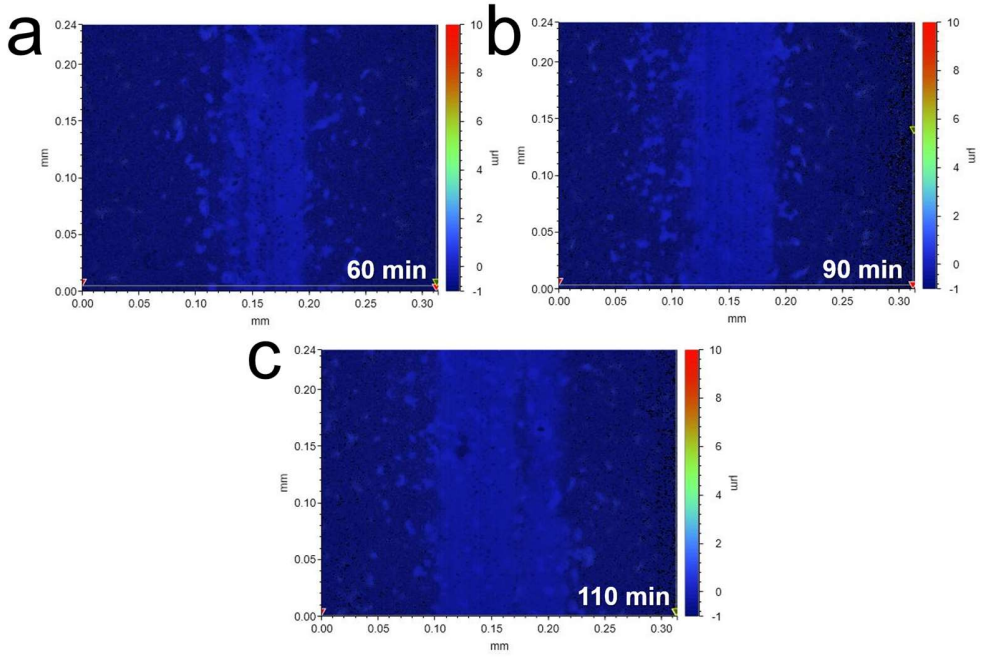

Figure 9.12. 3D optical microscopic images of wear scars on bilayer coating under different test time (a, 60 min; b, 90 min; c, 110 min).

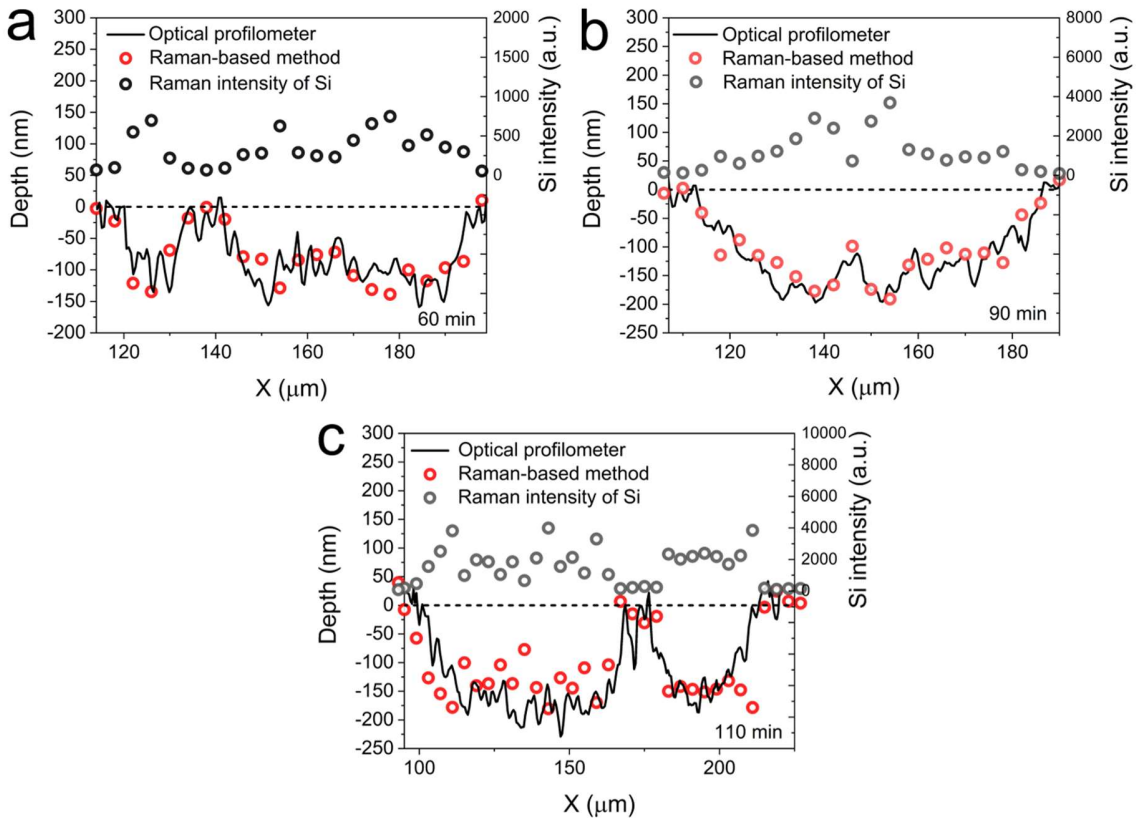

Figure 9.13. Comparison between calculated wear profiles obtained by Raman-based profilometry and wear profiles characterized by the improved optical profilometer (with the iridium layer on top) under dry friction (a, 60 min; b, 90 min; c, 110 min). Raman intensities of silicon signals were collected across the wear tracks.

9.4. Summary

The Silicon coatings with different crystallinity were deposited on steel substrates through pulsed-DC magnetron sputtering. The result indicated that the grain size of silicon crystal plays a dominating role in controlling the surface roughness, Raman intensity, and the variation coefficient of Raman intensity (CV), which are key factors for realizing the accurate wear measurement via Raman-based profilometry. By adjusting the deposition parameters to reducing the grain size to 32.7 nm, the crystalline silicon coating with low surface roughness and CV, and high Raman intensity was successfully deposited on steel substrate as the sensing layer. After depositing a-C:H on this silicon coating, the

wear-sensing coating system was constructed and the Raman-based profilometry was employed to measure the wear depth values across the wear track. Compared with the results deriving from optical profilometer, Raman-based method could provide accurate wear depth values based on the wear-sensing coating system. As this wear-sensing coating system could be deposited on the substrate with various materials and shapes, it may open a new pathway for realizing in-situ and real-time wear measurement in diverse engineering applications.

Chapter 10

Discussion on the key findings

10.1. The accuracy of Raman-based coating thickness measurement

The proposed coating thickness measurement based on the Raman signal of silicon sensing layer displays high accuracy compared with the non-contact optical profilometer, contact profilometer and the method based on the Raman signal of carbon of a-C:H coatings, as shown in Figure 10.1. The non-contact optical profilometer builds up a 3D map by collecting the array signals of light interference of reflected light. Due to its high sensitivity towards the optical signal, the variation of optical properties on the top surface (e.g., tribo-induced effect and tribofilm formation) can affect the intensity of the light signal, resulting in measurement errors. To avoid these errors, it is suggested to deposit an optical signal synchronization layer of iridium with uniform thickness and consistent optical properties on the tribo-tested samples before using an optical profilometer. The contact profilometer is employed to characterize the wear scars in this project. However, it is only used to verify the feature information of wear profile (e.g., height spikes) rather than the accuracy as its low resolution could result in obvious measurement errors. The remarkable errors of measurement results based on the Raman carbon signal of a-C:H is attributed to the bonding transformation of sp^3 (C-H) to sp^2 (C=C) under shear forces. As indicated in the former chapter, the Raman spectra of carbon are dominated by the scattering of the sp^2 phase due to its high polarizability. The slight enhancement of the sp^2 phase, especially

ordering or clustering, could result in a remarkable increase in Raman intensity, further leading to measurement errors in bonding transformation regions.

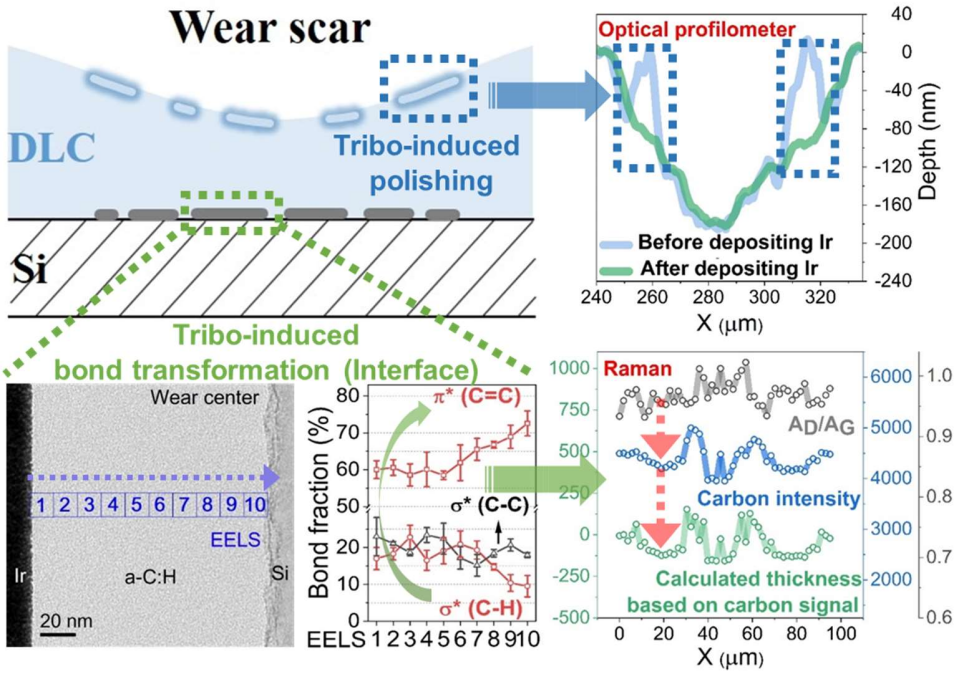

Figure 10.1. Comparison of the wear profile curves obtained by different methods (non-contact optical profilometer, Raman method based on carbon signal and silicon signal).

Meanwhile, it is necessary to clarify why the coating thickness method based on the Raman signal of silicon could avoid the remarkable errors caused by the tribo-induced bonding transformation. Table 10.1 shows the average values of EELS bonds fractions across the test areas. It can be observed that the average value of the sp^2 fraction in the unworn area is ~ 59%. In comparison, only a small increase of the sp^2 fraction appear in the side area and centre area (~ 60% for side area, ~ 63% for centre area). Therefore, the tribo-induced bonding transformation should have a slight effect on the optical properties of the whole coating and the final Raman intensity of the silicon signal. Considering the noticeable enhancement effect of sp^2 phase on Raman intensity of carbon signal, the method based on

the Raman signal of silicon is expected to provide a more accurate value of a-C:H thickness in a tribological contact.

Table 10.1. Average values of EELS C-bonds fractions of three targeted areas.

Bond	Unworn area	Side area	Centre area
sp^2 (c=c)	59 %	60 %	63 %
sp^3 (c-h)	21 %	18 %	17 %
sp^3 (c-c)	20 %	22 %	20 %

10.2. The bonding transformation from sp^3 (C-H) to sp^2 (C=C)

Figure 6.10 shows that the bottom layer of a-C:H coating in the centre of the wear scar underwent a bonding transformation from sp^3 (C-H) to sp^2 (C=C), leading to remarkable errors of measurement results based on the Raman signal of carbon. This critical finding further raises an interesting and important question of why bonding transformation was observed on the a-C:H/silicon interface rather than the top sliding interface which is subjected to the tribological contact. Based on previous findings of the tribo-chemical reaction of a-C:H under different test environments [166-168, 184, 185], the absence of bonding transformation on the sliding interface is attributed to the combined actions of easy-oxidation of a-C:H and easy-shear capability of the oxidation product during friction process.

Surface analysis of the oxide layer of a-C:H indicates that the oxidation resulted in the C-C or C-H bond dissociation and rearrangement of bond structure to disordered sp^2 phase, accompanied by the alteration of the mechanical properties which make the oxide layer more prone to wear. Especially under high oxygen pressure, the removal of transfer film (oxide layer) was almost entirely inside the wear scar, and loose wear debris could only be observed on the edge areas around the two ends of sliding direction [164, 168], which was

in accordance with our test results (Figure 10.2). Therefore, we could not observe the structural or phase transformation on the top surface of a-C:H coating.

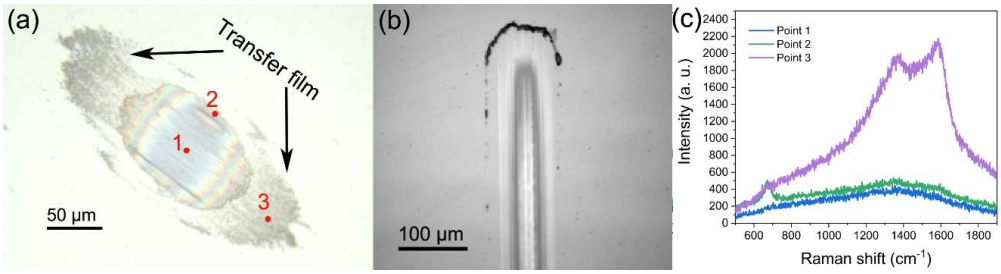

Figure 10.2. Optical images of wear scars on the steel counterpart ball (a) and a-C:H coating (b), and Raman spectra (c) on the marked points in (a).

On the other hand, TEM images in Figure 10.3 detected a sublayer with an increased nano-porous structure formed at the bottom area of a-C:H coating. As displayed in Figure 10.3c, a porous layer with thickness up to ~10 nm was observed in the unworn area (as-grown a-C:H), which should result from the thermally activated release of hydrogen from the a-C:H coating during the high temperature deposition process [186-190]. Besides, it was interesting to note that the porous sublayer in the sliding contact areas became more prominent with the thickness increasing to ~20nm after the tribological test (Figures 10.3a and b). As indicated in the literature, hydrogen emission was detected during friction from PECVD a-C:H coating as the main product of tribo-chemical degradation [160] and could result in a porous structure [191]. Meanwhile, the porous structure, especially more nanopores emerged in the wear centre, can trigger high stress concentration, and further promote the phase transformation during friction [130].

In addition, it should be pointed out that silicon is well known for its role in contributing to the formation of a porous microstructure (micro-void) in the $Si_{1-x}C_x$:H alloys [192-194]. Therefore, it is suggested that the stress concentration caused by structural evolution should play a pivotal role in the bonding transformation, where hydrogen atoms are cleaved from

C-H on the local stress-concentrated points, leaving C atoms rehybridized into disordered sp^2 carbon bonds, as the activation energy barrier for C-H to C=C is significantly lower than that for C-C to C=C [195-198].

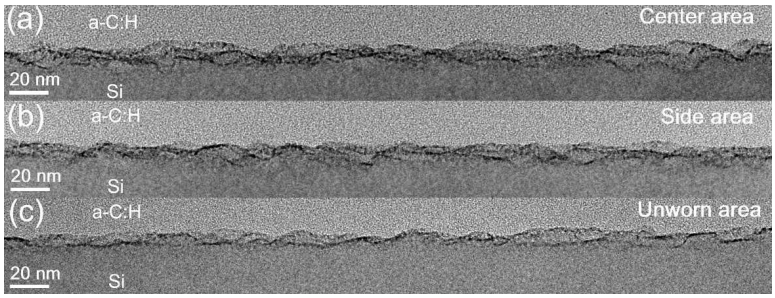

Figure 10.3. TEM images of the cross-sectional morphology of the interface areas between a-C:H and Si wafer from centre area (a), side area (b), and unworn area (c). The thickness of layer with nanovoid increase as it moves towards to wear centre.

10.3. The effect of MoDTC on wear acceleration of a-C:H coatings

As indicated in the literature review, the effect of MoDTC on wear acceleration of a-C:H under ambient environment has become one research hotspot during the past decade. It is well accepted that MoDTC-derived tribochemical products play a key role in this detrimental effect. To reveal the impact of tribochemical products, various surface analytical techniques have been applied to identify the composition and microstructure of MoDTC-derived tribofilms. Although significant progress has been achieved in understanding the chemical nature of tribofilms, the wear acceleration mechanisms are still not fully understood. The main reason is the difficulty in continuously or periodically obtaining the tribofilm composition during the wear process. It is well-known that the wear process is always accompanied by the formation and evolution of tribochemical products. In different wear-stages, there exist specific tribochemical products dominating the

tribological behaviour. It is therefore of great importance to verify the tribofilm composition in the correlated wear-stage. However, this remains a significant challenge for conventional surface analytical approaches due to their limitations in accessing the tribofilms in the friction process or low signal intensities of thin tribofilms with nanometers thickness.

In this project, the Raman-based profilometry is used to identify the MoDTC-derived products by monitoring the measurement deviations caused by the formation of tribochemical products with distinct optical properties. Based on the results, a two-stage wear process can be proposed to explain the wear acceleration mechanism. As shown in Figure 7.6, the measurement deviations, in the form of depth differences, increase remarkably in stage 2 in contrast with stage 1, indicating the formation of tribo-chemical products with lower transmittance in stage 2. Based on the optical properties of MoDTC-derived products, it is suggested that the main tribochemical products in stage 1 are MoS_2 and MoO_3, considering that MoS_2 is always formed accompanied by MoO_3 formation. The wear acceleration in stage 1 can be attributed to the catalytic effect of molybdenum oxides in the oxidation of a-C:H coating and the easy-shear capability of oxidation layers [163-165]. Due to the easy-shear capability of oxidation products, only a tiny oxidation layer remains on the surface with the thickness around several nanometers. Considering the large probe depth of Raman (~300 nm) and its high sensitivity towards sp^2-C phase, the bulk signal of a-C:H dominates the Raman spectra, explaining why we cannot detect the oxidation layer by Raman spectroscopy which is in line with the literature. However, MoO_3 formation has been confirmed based on the XPS analysis, due to the fact that the main probe depth of XPS is on the order of several nanometers.

In addition, it is suggested that the main product in stage 2 is MoC formed via the carburization of MoS_2 under the longer tribotest time as MoC displayed lower transmittance (higher reflectivity) than MoS_2. Specifically, the tribo-induced shear forces trigger PAO degradation into hydrocarbon fragments (carbon source) and generate heat for prompting the conversion of MoS_2 into hard MoC. MoC can trigger abrasive wear and speed up coating wear due to its high hardness. As shown in Figures 7.6 and 7.7, the wear in stage 2 is obviously increased compared with that in stage 1 due to the formation of hard MoC.

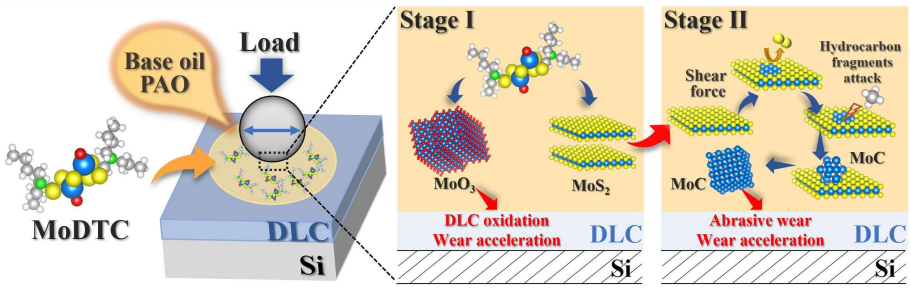

Figure 10.4. Schematic illustration of the two-stage wear process for clarifying the wear acceleration mechanisms of a-C:H films under MoDTC-lubricated condition.

10.4. Dominating role of oxidation layer in the growth of ZDDP-derived tribofilm

It is well accepted that friction and wear behaviours are dominated by tribofilms formed on contact surfaces. Gaining fundamental insights into the tribofilm growth mechanism can benefit a better understanding of the tribological mechanisms. As stated in the former chapters, ZDDP-derived tribofilm prefers to form on the steel surfaces on steel/DLC contacts based on the results of surface element content analysis. Meanwhile, it is interesting to note that the tribofilms formed on DLC surfaces are less durable than those

on ferrous surfaces. Although the reasons for this selective growth remain unknown, these findings clearly confirm the critical role of surface materials in the tribofilm growth.

For clarifying the governing factor of tribofilm growth in the friction process, the proposed Raman-based profilometry is employed to reveal the growth mechanism of ZDDP tribofilm. Since this proposed method is highly sensitive to the Raman signal, it is used to identify the additive-derived tribofilms formed on a-C:H based on the distinct optical properties of tribochemical products. It is well accepted that ZDDP can form surface-bonded pad-like tribofilms with a gradient structure with a short-chain glassy phosphate near the ferrous surface and a thin outer layer of long-chain polyphosphates. These glassy tribofilms derived from ZDDP hardly affect the Raman intensity due to the high transmittance, whereas the tribochemical products (e.g., MoS_2 and MoC) with lower transmittance (higher absorption coefficient or/and reflectivity than a-C:H) towards Raman signal can cause extra attenuation of Raman intensity and further remarkable measurement deviations of wear depth. Therefore, through comparing the results of wear profiles obtained by Raman-based method with that of optical profilometry, the compositions of tribofilms can be confirmed. Specifically, the ZDDP tribofilm formation can be detected by optical profilometer in the form of height rising, but it cannot be observed in the results of Raman-based method due to the high transmittance of ZDDP tribofilm. Based on the Raman-based method, it is found that no ZDDP tribofilm is detected on a-C:H when using ZDDP separately, while ZDDP-derived tribofilms can form on a-C:H surfaces when using ZDDP in combination with MoDTC. These results significantly benefit the deep understanding of the tribological behaviours of additives on steel/DLC contacts and the mechanisms of tribofilm growth.

As indicated in chapter 8, when ZDDP is used on the steel/a-C:H contact, ZDDP-derived tribofilms only form on the steel surface. Since the hardness of a-C:H is obviously higher

than steel, wear at the initial stage mainly happens on the steel surface and results in large nascent surfaces that is easily oxidized in the tribological process. These oxide areas provide active sites for the tribofilm growth of ZDDP based on Lewis acid-base interaction (Fe^{3+}-Lewis acid, phosphate-Lewis base). Given the Lewis base property of a-C:H, ZDDP tribofilm was formed on the steel surface rather than a-C:H. After that, wear mainly takes place on ZDDP tribofilm, due to its significantly low hardness. Since this wear process on steel surface will be repeated constantly when employing a-C:H as a counterpart, remarkable wear was observed on steel surface. In addition, since the friction behaviour depends on ZDDP tribofilms, the friction coefficient is close to the condition of ferrous / ferrous contacts with ZDDP as additive. When introducing MoDTC into the above lubricating oil, MoDTC-derived MoO_3 initiates catalytic oxidation of a-C:H. Based on EDX and EELS, the formation of oxidation layer on the top of a-C:H was confirmed, which can transform a-C:H surface from Lewis base to Lewis acid (oxidized a-C:H) according to HSAB principle. More importantly, the surface oxidation layer on a-C:H provides active sites for the tribochemical reaction with phosphate (Lewis base). The above results give direct evidence that the selective growth of ZDDP tribofilms on a-C:H surface in mild tribo-test conditions is driven by Lewis acid-base interaction rather than the stress-dependent mechanism in view of unobservable wear on the a-C:H surface.

10.5. Key factors in constructing the reliable wear-sensing coating system

Condition-based maintenance can effectively minimize the downtime caused by unpredicted failure, reduce the degree of over-engineering and premature replacement of machine parts, and ultimately directly impact the production competitiveness. Up to date,

most online monitoring approaches use indirect signals from diverse sensors to estimate the health status, such as acoustic emission, cutting force, vibration, and temperature. Since these signals only provide indicators of secondary effect, early failure detection at the component level remains a big challenge. Furthermore, their inherent drawbacks, deriving from signal noise and lack of directly detection information, always lead to the inevitable reduction in the measurement reliability and accuracy. As these indirect approaches are incapable of direct application in a distinct process and model retraining for the new condition is necessary, it is also crucial to consider the adaptability of newly developed techniques when changing application scenarios. Given these, there is an urgent need to find more powerful techniques to fulfil these challenges.

In this project, a Raman-based profilometry is developed to achieve accurate coating thickness measurement. This proposed approach is based on a bilayer structure: a top layer of a-C:H film and a sensing underlayer of silicon. To achieve the aim of in-situ and real-time wear measurement on the machine parts, the wear-sensing coating system composited of the above bilayer structure is developed on the steel substrates. Then wear measurement is carried out on tribotested samples. The Raman intensity and surface roughness of silicon layers are two key factors for realizing accurate wear measurement based on wear-sensing coating system. For obtaining high Raman intensity, it is necessary to develop silicon coatings with high crystallinity by optimizing the deposition parameters (e.g., temperature, power, gas pressure). Meanwhile, the surface roughness of as-grown coatings should be controlled in a reasonable range as high roughness can result in big errors of wear measurement.

Based on the results, it is suggested that the grain size of silicon coatings shows a high correlation with the surface roughness and Raman intensity. Specifically, the surface

roughness and Raman intensity increase with grain size. It should also be pointed out that with increasing the grain size, the coefficient of variation of Raman intensity obtained on a series of test points on the silicon coatings increases significantly, indicating the widening distribution of grain size. The sputtered yield and energy of sputtered silicon atoms arriving at the substrate can be increased by reducing the S-T distance and increasing the gas pressure and cathode power in the coating deposition process, which not only promote the grain growth of silicon crystal but also lead to non-uniform grain growth, resulting in multimodal grain size distribution.

For improving the accuracy of wear measurement, the variation coefficient of Raman intensity should be reduced to avoid the big measurement errors. It is therefore suggested that the grain size of silicon coatings should be controlled at a reasonable value to reduce the measurement errors caused by high surface roughness and big variation of Raman intensities and provide high enough Raman intensity for achieving reliable wear-measurement. Through adjusting the grain size to ca. 32.7 nm by optimizing the deposition parameters, the silicon coating with low surface roughness at 62.9 nm, small variation coefficient of Raman intensity at 12.5% and Raman intensity of 8765.7 was obtained, which is then employed as the sensing layer for constructing wear-sensing coating system on steel substrate to realize accurate wear measurement via Raman-based profilometry.

Chapter 11

Conclusions and Future work

11.1 Conclusions

In this project, a novel Raman-based profilometry has been developed to measure the coating wear based on the Raman signal from the silicon sensing layer. This proposed approach was successfully used to measure the coating wear under dry and oil-lubricated conditions. Meanwhile, since this method is highly sensitive towards the Raman signal intensity, it is employed to detect the formation of additive-derived tribofilms formed on coating surfaces based on their distinct optical properties. The results provide fundamental insights into the mechanisms of tribofilm formation and the tribochemical reactions between additives and a-C:H coatings. In view of the potential for in-situ and real-time wear monitoring of Raman-based profilometry, a wear-sensing coating system composed of crystalline silicon underlayer and a-C:H top layer has been developed on steel substrate by combining the pulsed-DC magnetron sputtering and PECVD. It is demonstrated that this coating system could provide accurate wear information based on Raman-based profilometry.

In summary, the key conclusions of this thesis are presented in the following:

- A Raman-based profilometry is developed based on two functional layers: the top a-C:H serves as light attenuating and anti-wear layer while the silicon substrate is employed as Raman sensing layer. Since the Raman intensity of silicon signal varied as a function of the a-C:H thickness, wear monitoring of a-C:H could be realized in the

friction process, giving the opportunity for in-situ wear measurement. Compared with the results deriving from the profilometer and Raman signal of carbon, the coating thickness quantification method based on the Raman signal of silicon provides more accurate wear profile in long term tribotests.

- The remarkable errors of non-contact optical profilometer was attributed to the tribo-induced variation of optical properties on the top surface of a-C:H film, while the obvious errors of the approach based on Raman signal of carbon was due to tribo-induced bonding transformation of sp^3 (C-H) to sp^2 (C=C) in the bonding transformation regions, resulting in noticeable enhancement effect of sp^2 C-phase towards Raman intensity of carbon signal.
- By introducing an additional attenuating-layer of oil film into the calculation process, this method enabled the possibility of monitoring coating wear under oil-lubricated conditions.
- The evolution process of MoDTC-derived tribofilms formed on the a-C:H coating surface is investigated using a combination of Raman-based profilometry, TEM, and FFT. The obtained results confirm that the remarkable deviations of Raman-based coating wear measurement are attributed to the tribofilm formation on the top surface of a-C:H due to their distinct optical properties compared with a-C:H.
- The formation of MoS_2 nanosheets is observed in the initial stage, which is further converted into nano-MoC via carburization reaction under the impact of shear forces. In combination with the previous studies about MoDTC-derived tribofilms, the MoDTC-induced wear process on a-C:H/steel contact could be divided into two stages. In the first stage, wear acceleration is attributed to the catalytic effect of molybdenum oxides (accompaniment of MoS_2 derived from MoDTC) in the oxidation of a-C:H and

the easy-shear capability of oxidation layers. Meanwhile, for the second stage, the tribo-induced MoS_2 carburization into hard MoC leads to abrasive wear, dominating the wear acceleration process.

- Raman-based profilometry is employed in this study to identify the additive-derived tribofilms of ZDDP on a-C:H coatings based on their distinct optical properties. The obtained results confirm the dominating role of the oxidation layer on the a-C:H surface in the growth of ZDDP-derived tribofilms. This oxidation process catalysed by MoDTC-derived MoO_3 can transform a-C:H surface from Lewis base to Lewis acid, providing active growth sites for ZDDP tribofilms.
- The tribochemical reaction between ZDDP-derived products (phosphate-Lewis base) and a-C:H surfaces is driven by Lewis acid-base interaction rather than stress-dependent mechanism in view of the unobservable wear on the tribofilm growth areas of a-C:H surfaces. In addition, the lower durability of ZDDP tribofilms formed on a-C:H surfaces than that on ferrous surfaces is attributed to the easy-shear capability of oxidation layer.
- The silicon coatings with different crystallinity are deposited on steel substrates by pulsed-DC magnetron sputtering method. The grain size of silicon crystal plays a dominating role in controlling the surface roughness, Raman intensity, and the variation coefficient of Raman intensity (CV), which are key factors for realizing accurate wear measurement via Raman-based profilometry.
- By adjusting the deposition parameters, the crystalline silicon coating with low surface roughness and CV, and high Raman intensity is successfully deposited on steel substrate as the sensing layer. After depositing a-C:H on this silicon coating, the wear-sensing coating system is constructed and Raman-based profilometry is

employed to measure the wear depth values. Compared with the results deriving from optical profilometer, Raman-based method could provide accurate wear depth values based on the wear-sensing coating system.

- The main limitations of this developed Raman-based profilometry are: 1, the additive-derived tribofilms can cause measurement errors under high concentration of additives in lubricating oil; 2, although it has been demonstrated that this Raman method could provide accurate wear information with oil film on coating surface, using oil with low transmittance may cause measurement errors in the in-situ test; 3, this developed method requires initial surface roughness under low level to prevent the high measurement errors.

11.2 Suggestions for future work

Several suggestions are proposed for future work in this research directions:

- Given the growing demand of automation, online monitoring capability is strongly required for wear measurement techniques. In this project, a Raman-based profilometry with strong potential of online monitoring is developed. It is suggested to conduct in-situ and real-time tribotests and use this proposed method to monitor the coating wear in the friction process.
- Considering that most of the existing liquid lubricants are tailored for ferrous-base surfaces, in-depth studies of the interaction between nonferrous surfaces and liquid lubricants are therefore essential for developing high-performance lubricating systems and understanding further mechanisms, such as tribochemical reactions on coating surfaces under additive-lubricated conditions. In this thesis, the Raman-based profilometry has been employed to study the formation mechanisms of tribofilms of

MoDTC and ZDDP and demonstrates its usefulness in detecting the tribochemical products based on the distinct optical properties. In view of this, it is suggested to use this proposed method to study the tribochemical reactions between diverse additives and coatings which can benefit the development and optimization of an effective solid−liquid lubricating system.

- The wear-sensing coating system composed of crystalline silicon and a-C:H has been developed in this project and used to measure the coating wear based on Raman-based profilometry. As this wear-sensing coating system could be deposited on the substrate of various materials and shapes, it is suggested to conduct research work based on this coating system in diverse engineering applications.

References

[1] Jia, P.; Rong, Y.; Huang, Y. Condition Monitoring of the Feed Drive System of a Machine Tool based on Long-Term Operational Modal Analysis. *Int. J. Mach. Tools Manuf.* **2019**,*146*, 103454.

[2] Castejón, M.; Alegre, E.; Barreiro, J.; Hernández, L. On-Line Tool Wear Monitoring using Geometric Descriptors from Digital Images. *Int. J. Mach. Tools Manuf.* **2007**, *47*, 1847-1853.

[3] Lee, G.; Kim, M.; Quan, Y.; Kim, M.; Kim, T. J. Y.; Yoon, H.; Min, S.; Kim, D.; Mun, J.; Oh, J. W.; Choi, I. G.; Kim, C.; Chu, W.; Yang, J.; Bhandari, B.; Lee, C.; Ihn, J.; Ahn S. Machine Health Management in Smart Factory: a Review. *J. Mech. Sci. Technol.* **2018**, *32*, 987-1009.

[4] Zhou, Y.; Wei, X. Review of Tool Condition Monitoring Methods in Milling Processes. *Int. J. Adv. Manuf. Technol.* **2018,** *96*, 2509-2523.

[5] El-Thalji, I.; Jantunen, E. A Summary of Fault Modelling and Predictive Health Monitoring of Rolling Element Bearings. *Mech. Syst. Signal Process* **2015,** *60-61*, 252-272.

[6] Scheffer, C.; Kratz, H.; Heyns, P.; Klocke, F. Development of a Tool Wear-Monitoring System for Hard Turning. *Int. J. Mach. Tools Manuf.* **2003,** *43*, 973-985.

[7] Nouri, M.; Fussell, B. K.; Ziniti, B. L.; Linder, E. Real-Time Tool Wear Monitoring in Milling using a Cutting Condition Independent Method. *Int. J. Mach. Tools Manuf.* **2015,** *89,* 1-13.

[8] Zhu, K.; San Wong, Y.; Hong, G. S. Wavelet Analysis of Sensor Signals for Tool Condition Monitoring: a Review and some new Results. *Int. J. Mach. Tools Manuf.* **2009**, *49*, 537-553.

[9] Shao, H.; Wang, H. L.; Zhao, X. M. A Cutting Power Model for Tool Wear Monitoring in Milling. *Int. J. Mach. Tools Manuf.* **2004**, *44*, 1503-1509.

[10] Fan, X.; Xue, Q.; Wang, L. Carbon-Based Solid-Liquid Lubricating Coatings for Space Applications-A Review. *Friction* **2015**, *3* (3), 191–207.

[11] Fan, X.; Wang, L.; Li, W.; Wan, S. Improving Tribological Properties of Multialkylated Cyclopentanes under Simulated Space Environment: Two Feasible Approaches. *ACS Appl. Mater. Interfaces* **2015**, *7* (26), 14359–14368.

[12] Zhu, S.; Yu, Y.; Cheng, J.; Qiao, Z.; Yang, J.; Liu, W. Solid/Liquid Lubrication Behavior of Nickel Aluminum-Silver Alloy under Seawater Condition. *Wear* **2019**, *420–421*, 9–16.

[13] Kosarieh, S.; Morina, A.; Lainé, E.; Flemming, J.; Neville, A. The Effect of MoDTC-Type Friction Modifier on the Wear Performance of a Hydrogenated DLC Coating. *Wear* **2013**, *302* (1–2), 890–898.

[14] Zou, Y. S.; Wu, Y. F.; Yang, H.; Cang, K.; Song, G. H.; Li, Z. X.; Zhou, K. The Microstructure, Mechanical and Friction Properties of Protective Diamond like Carbon Films on Magnesium Alloy. *Applied Surface Science* **2011**, *258* (4), 1624–1629.

[15] Haque, T.; Morina, A.; Neville, A. Influence of Friction Modifier and Antiwear Additives on the Tribological Performance of a Non-Hydrogenated DLC Coating. *Surface and Coatings Technology* **2010**, *204* (24), 4001–4011.

[16] Morina, A.; Zhao, H.; Mosselmans, J. F. W. In-Situ Reflection-XANES Study of ZDDP and MoDTC Lubricant Films Formed on Steel and Diamond like Carbon (DLC) Surfaces. *Applied Surface Science* **2014**, *297*, 167–175.

[17] Erdemir, A.; Ramirez, G.; Eryilmaz, O. L.; Narayanan, B.; Liao, Y.; Kamath, G.; Sankaranarayanan, S. K. R. S. Carbon-Based Tribofilms from Lubricating Oils. *Nature* **2016**, *536* (7614), 67–71.

[18] Wu, H.; Khan, A. M.; Johnson, B.; Sasikumar, K.; Chung, Y.-W.; Wang, Q. J. Formation and Nature of Carbon-Containing Tribofilms. *ACS Appl. Mater. Interfaces* **2019**, *11* (17), 16139–16146.

[19] De Feo, M.; De Barros Bouchet, MI.; Minfray, C.; Le Mogne, Th.; Meunier, F.; Yang, L.; Thiebaut, B.; Martin, J. M. MoDTC Lubrication of DLC-Involving Contacts. Impact of MoDTC Degradation. *Wear* **2016**, *348–349*, 116–125.

[20] Okubo, H.; Sasaki, S. In Situ Raman Observation of Structural Transformation of Diamond-like Carbon Films Lubricated with MoDTC Solution: Mechanism of Wear Acceleration of DLC Films Lubricated with MoDTC Solution. *Tribology International* **2017**, *113*, 399–410.

[21] Okubo, H.; Tadokoro, C.; Sumi, T.; Tanaka, N.; Sasaki, S. Wear Acceleration Mechanism of Diamond-like Carbon (DLC) Films Lubricated with MoDTC Solution: Roles of Tribofilm Formation and Structural Transformation in Wear Acceleration of DLC Films Lubricated with MoDTC Solution. *Tribology International* **2019**, *133*, 271–287.

[22] Muratore, C.; Clarke, D. R.; Jones, J. G.; Voevodin, A.A. Smart Tribological Coatings with Wear Sensing Capability. *Wear* **2008**, *265*, 913-920.

[23] Fang, L.; Yin, A.; Zhu, S.; Ding, J.; Chen, L.; Zhang, D.; Pu, Z.; Liu, T. On the Potential of Er-Doped AlN Film as Luminescence Sensing Layer for Multilayer Al/AlN Coating Health Monitoring. *J. Alloys Compd.* **2017**, *727*, 735-743.

[24] Wakelin, R. J. Tribology: The Friction, Lubrication, and Wear of Moving Parts.

Annu. Rev. Mater. Sci. **1974**, *4* (1), 221–253.

[25] Beloiu, D. M. Modeling and Analysis of Valve Train, Part I - Conventional Systems. *SAE International Journal of Engines* **2010**, *3* (1), 850–877.

[26] Czichos, H. Tribology. A systems approach to the science and technology of friction, lubrication and wear. Elsevier Scientific Publishing Co., **1978**.

[27] Szeri Andras, Z. Fluid film lubrication: Theory and design. Cambridge University Press, **1998**.

[28] Mang, T.; Bobzin, K.; Bartels, T. Industrial tribology: tribosystems, friction, wear and surface engineering, lubrication. John Wiley & Sons, **2011**.

[29] Holmberg, K.; Erdemir, A. Influence of Tribology on Global Energy Consumption, Costs and Emissions. *Friction* **2017**, *5* (3), 263–284.

[30] Sarkar, A.D. Friction and wear. New York: Academic Press, **1980**.

[31] Rizvi, Syed Q. A. A comprehensive review of lubricant chemistry, technology, selection, and design. West Conshohocken, PA: ASTM International, **2009**.

[32] Lansdown, A. Lubrication: a practical guide to lubricant selection. Elsevier, **2013**.

[33] Priest, M.; Taylor, C. M. Automobile Engine Tribology - Approaching the Surface. *Wear* **2000**, *241* (2), 193–203.

[34] Hamrock, B.J.; Dowson, D. Ball Bearing Lubrication, The Elastohydrodynamics of Elliptical Contacts. John Wiley & Sons, **1981**.

[35] Priest, M. Principles of Tribology- Introduction to Tribology and Real Surfaces. Work Unit 1, University of Leeds, **2005**.

[36] Spikes, H. The History and Mechanisms of ZDDP. *Tribology Letters* **2004**, *17* (3), 469–489.

[37] Srivastava, S.P.T.S.o.I. Advances in lubricant additives and tribology. New Delhi: Tech Books International in association with Tribology Society of India, **2009**.

[38] Neville, A.; Morina, A. Wear and chemistry of lubricants. In: Stachowiak, G. (ed.) in Wear-Materials, Mechanisms and Practice. Wiley & Sons.: London, **2005**.

[39] Rabinowicz, E. Friction and wear of materials. Wiley: New York, **1965**.

[40] Hirani, P. D. H. Module 3, wear mechanisms. **2014**.

[41] Kandeva, M.; Karastoyanov, D.; Vencl A. Advanced Tribological Coatings for HeavyDuty Applications: Case Studies. Sofia: Marin Drinov Academic Publishing House,

2016.

[42] Tsujimoto, A.; Barkmeier, W. W.; Fischer, N. G.; Nojiri, K.; Nagura, Y.; Takamizawa, T.; Latta, M. A.; Miazaki, M. Wear of Resin Composites: Current Insights into Underlying Mechanisms, Evaluation Methods and Influential Factors. *Japanese Dental Science Review* **2018**, *54* (2), 76–87.

[43] Zhang, H.; Zhou, L.; Zhang, Z. Transparent Wear-Resistant Multifunctional Polymeric Nanocoatings. In *Multifunctionality of Polymer Composites*; Elsevier, 2015; pp 573–587.

[44] Ramalho, A.; Miranda, J. C. The Relationship between Wear and Dissipated Energy in Sliding Systems. *Wear* **2006**, *260* (4–5), 361–367.

[45] Heinicke, G. Tribochemistry. John Wiley & Sons, **1984**.

[46] Beyer, M. K.; Clausen-Schaumann, H. Mechanochemistry: The Mechanical Activation of Covalent Bonds. *Chem. Rev.* **2005**, *105* (8), 2921–2948.

[47] Mattox, D.M. Handbook of Physical Vapor Deposition (PVD) Processing. William Andrew Publishing/Noyes, **1998**.

[48] Park, S.-I.; Quan, Y.-J.; Kim, S.-H.; Kim, H.; Kim, S.; Chun, D.-M.; Lee, C. S.; Taya, M.; Chu, W.-S.; Ahn, S.-H. A Review on Fabrication Processes for Electrochromic Devices. *Int. J. of Precis. Eng. and Manuf.-Green Tech.* **2016**, *3* (4), 397–421.

[49] Pierson, H.O.P.H.O. Handbook of chemical vapor deposition. Norwich, NY: Noyes Publications, **1999**.

[50] Gupta, K.; Jain, N. K.; Laubscher, R. Surface Property Enhancement of Gears. In *Advanced Gear Manufacturing and Finishing*; Elsevier, 2017; pp 167–196.

[51] Lee, D.-H.; Cho, N.-G. Assessment of Surface Profile Data Acquired by a Stylus Profilometer. *Meas. Sci. Technol.* **2012**, *23* (10), 105601.

[52] Poon, C. Y.; Bhushan, B. Comparison of Surface Roughness Measurements by Stylus Profiler, AFM and Non-Contact Optical Profiler. *Wear* **1995**, *190* (1), 76–88.

[53] Baysan, A.; Sleibi, A.; Ozel, B.; Anderson, P. The Quantification of Surface Roughness on Root Caries Using Noncontact Optical Profilometry-An in Vitro Study. *Laser Dent Sci* **2018**, *2* (4), 229–237.

[54] Hong, W.; Cai, W.; Wang, S.; Tomovic, M. M. Mechanical Wear Debris Feature, Detection, and Diagnosis: A Review. *Chinese Journal of Aeronautics* **2018**, *31* (5), 867–882.

[55] Sun, J.; Wang, L.; Li, J.; Li, F.; Li, J.; Lu, H. Online Oil Debris Monitoring of Rotating Machinery: A Detailed Review of More than Three Decades. *Mechanical Systems and Signal Processing* **2021**, *149*, 107341.

[56] Eberle, D. C.; Wall, C. M.; Treuhaft, M. B. Applications of Radioactive Tracer Technology in the Real-Time Measurement of Wear and Corrosion. *Wear* **2005**, *259* (7–12), 1462–1471.

[57] Scherge, M.; Pöhlmann, K.; Gervé, A. Wear Measurement Using Radionuclide-Technique (RNT). *Wear* **2003**, *254* (9), 801–817.

[58] Sidebottom, M. A.; Atkinson, C. A.; Campbell, K. L.; Babuska, T. F.; Junk, C. P.; Burch, H. E.; Krick, B. A. Perfluoroalkoxy (PFA)-α-Alumina Composites: Effect of Environment on Tribological Performance. Tribol Lett 2020, 68 (1), 14.

[59] Scharf, T. W.; Singer, I. L. Thickness of Diamond-Like Carbon Coatings Quantified with Raman Spectroscopy. *Thin Solid Films* **2003**, *440*, 138-144.

[60] Scharf, T. W.; Singer, I. L. Quantification of the Thickness of Carbon Transfer Films using Raman Tribometry. *Tribol. Lett.* **2003,** *14*, 137-145.

[61] Scharf, T. W.; Singer, I. L. Monitoring Transfer Films and Friction Instabilities with In-Situ Raman Tribometry. *Tribol. Lett.* **2003,** *14*, 3-8.

[62] Robertson, J. Diamond-like Amorphous Carbon. *Materials Science and Engineering: R: Reports* **2002**, *37* (4–6), 129–281.

[63] Ferrari, A. C.; Robertson, J. Interpretation of Raman Spectra of Disordered and Amorphous Carbon. *Phys. Rev. B* **2000**, *61* (20), 14095–14107.

[64] Ferrari, A. C.; Robertson, J. Raman Spectroscopy of Amorphous, Nanostructured, Diamond–like Carbon, and Nanodiamond. *Philosophical Transactions of the Royal Society of London. Series A: Mathematical, Physical and Engineering Sciences* **2004**, *362* (1824), 2477–2512.

[65] Coşkun, Ö. D.; Zerrin, T. Optical, Structural and Bonding Properties of Diamond-like Amorphous Carbon Films Deposited by DC Magnetron Sputtering. *Diamond and Related Materials* **2015**, *56*, 29–35.

[66] Sun, Y.; Huang, X.-Y.; Wang, H. Influence of Hydrogen Content on Optical and Mechanical Performances of Diamond-Like Carbon Films on Glass Substrate. *J. of Materi Eng and Perform* **2016**, *25* (4), 1570–1577.

[67] Casiraghi, C.; Ferrari, A. C.; Robertson, J. Raman Spectroscopy of Hydrogenated Amorphous Carbons. *Phys. Rev. B* **2005**, *72* (8), 085401.

[68] Robertson, J. Comparison of Diamond-like Carbon to Diamond for Applications. *phys. stat. sol. (a)* **2008**, *205* (9), 2233–2244.

[69] Rizzo, V. Z.; Mansano, R. D. Electro-Optically Sensitive Diamond-like Carbon Thin Films Deposited by Reactive Magnetron Sputtering for Electronic Device Applications. *Progress in Organic Coatings* **2011**, *70* (4), 365–368.

[70] Robertson, J. Properties of Diamond-like Carbon. *Surface and Coatings Technology*

1992, *50* (3), 185–203.

[71] Kosarieh, S.; Morina, A.; Lainé, E.; Flemming, J.; Neville, A. The Effect of MoDTC-Type Friction Modifier on the Wear Performance of a Hydrogenated DLC Coating. *Wear* **2013**, *302* (1–2), 890–898.

[72] Morina, A.; Neville, A.; Priest, M.; Green, J. H. ZDDP and MoDTC Interactions and Their Effect on Tribological Performance – Tribofilm Characteristics and Its Evolution. *Tribol Lett* **2006**, *24* (3), 243–256.

[73] Abdullah Tasdemir, H.; Wakayama, M.; Tokoroyama, T.; Kousaka, H.; Umehara, N.; Mabuchi, Y.; Higuchi, T. The Effect of Oil Temperature and Additive Concentration on the Wear of Non-Hydrogenated DLC Coating. *Tribology International* **2014**, *77*, 65–71.

[74] De Feo, M.; De Barros Bouchet, MI.; Minfray, C.; Esnouf, C.; Le Mogne, Th.; Meunier, F.; Yang, L.; Thiebaut, B.; Pavan, S.; Martin, J. M. Formation of Interfacial Molybdenum Carbide for DLC Lubricated by MoDTC: Origin of Wear Mechanism. *Wear* **2017**, *370–371*, 17–28.

[75] De Feo, M.; De Barros Bouchet, MI.; Minfray, C.; Le Mogne, Th.; Meunier, F.; Yang, L.; Thiebaut, B.; Martin, J. M. MoDTC Lubrication of DLC-Involving Contacts. Impact of MoDTC Degradation. *Wear* **2016**, *348–349*, 116–125.

[76] Okubo, H.; Sasaki, S. In Situ Raman Observation of Structural Transformation of Diamond-like Carbon Films Lubricated with MoDTC Solution: Mechanism of Wear Acceleration of DLC Films Lubricated with MoDTC Solution. *Tribology International* **2017**, *113*, 399–410.

[77] Okubo, H.; Tadokoro, C.; Sumi, T.; Tanaka, N.; Sasaki, S. Wear Acceleration Mechanism of Diamond-like Carbon (DLC) Films Lubricated with MoDTC Solution: Roles of Tribofilm Formation and Structural Transformation in Wear Acceleration of DLC Films Lubricated with MoDTC Solution. *Tribology International* **2019**, *133*, 271–287.

[78] Grossiord, C.; Varlot, K.; Martin, J.-M.; Le Mogne, T.; Esnouf, C.; Inoue, K. MoS_2 Single Sheet Lubrication by Molybdenum Dithiocarbamate. *Tribology International* **1998**, *31* (12), 737–743.

[79] Luo, X.; Zhao, Y.; Zhang, J.; Xiong, Q.; Quek, S. Y. Anomalous Frequency Trends in MoS_2 Thin Films Attributed to Surface Effects. *Phys. Rev. B* **2013**, *88* (7), 075320.

[80] Verble, J. L.; Wieting, T. J. Lattice Mode Degeneracy in MoS_2 and Other Layer Compounds. *Phys. Rev. Lett.* **1970**, *25* (6), 362–365.

[81] McDevitt, N. T.; Zabinski, J. S.; Donley, M. S.; Bultman, J. E. Disorder-Induced Low-Frequency Raman Band Observed in Deposited MoS_2 Films. *Appl Spectrosc* **1994**, *48* (6), 733–736.

[82] Frey, G. L.; Tenne, R.; Matthews, M. J.; Dresselhaus, M. S.; Dresselhaus, G. Raman

and Resonance Raman Investigation of MoS_2 Nanoparticles. *Phys. Rev. B* **1999**, *60* (4), 2883–2892.

[83] Li, H.; Zhang, Q.; Yap, C. C. R.; Tay, B. K.; Edwin, T. H. T.; Olivier, A.; Baillargeat, D. From Bulk to Monolayer MoS2: Evolution of Raman Scattering. *Adv. Funct. Mater.* **2012**, *22* (7), 1385–1390.

[84] Zeng, H.; Zhu, B.; Liu, K.; Fan, J.; Cui, X.; Zhang, Q. M. Low-Frequency Raman Modes and Electronic Excitations in Atomically Thin MoS_2 Films. *Phys. Rev. B* **2012**, *86* (24), 241301.

[85] Lee, C.; Yan, H.; Brus, L. E.; Heinz, T. F.; Hone, J.; Ryu, S. Anomalous Lattice Vibrations of Single- and Few-Layer MoS_2. *ACS Nano* **2010**, *4* (5), 2695–2700.

[86] Nayak, A. P.; Pandey, T.; Voiry, D.; Liu, J.; Moran, S. T.; Sharma, A.; Tan, C.; Chen, C.-H.; Li, L.-J.; Chhowalla, M.; Lin, J.-F.; Singh, A. K.; Akinwande, D. Pressure-Dependent Optical and Vibrational Properties of Monolayer Molybdenum Disulfide. *Nano Lett.* **2015**, *15* (1), 346–353.

[87] Livneh, T.; Sterer, E. Resonant Raman Scattering at Exciton States Tuned by Pressure and Temperature in 2 H-MoS_2. *Phys. Rev. B* **2010**, *81* (19), 195209.

[88] Sugai, S.; Ueda, T. High-Pressure Raman Spectroscopy in the Layered Materials 2H-MoS_2, 2H-$MoSe_2$, and 2H-$MoTe_2$. *Phys. Rev. B* **1982**, *26* (12), 6554–6558.

[89] Sahoo, S.; Gaur, A. P. S.; Ahmadi, M.; Guinel, M. J.-F.; Katiyar, R. S. Temperature-Dependent Raman Studies and Thermal Conductivity of Few-Layer MoS_2. *J. Phys. Chem. C* **2013**, *117* (17), 9042–9047.

[90] Thripuranthaka, M.; Kashid, R. V.; Sekhar Rout, C.; Late, D. J. Temperature Dependent Raman Spectroscopy of Chemically Derived Few Layer MoS_2 and WS_2 Nanosheets. *Appl. Phys. Lett.* **2014**, *104* (8), 081911.

[91] Lanzillo, N. A.; Glen Birdwell, A.; Amani, M.; Crowne, F. J.; Shah, P. B.; Najmaei, S.; Liu, Z.; Ajayan, P. M.; Lou, J.; Dubey, M.; Nayak, S. K.; O'Regan, T. P. Temperature-Dependent Phonon Shifts in Monolayer MoS_2. *Appl. Phys. Lett.* **2013**, *103* (9), 093102.

[92] Su, L.; Zhang, Y.; Yu, Y.; Cao, L. Dependence of Coupling of Quasi 2-D MoS_2 with Substrates on Substrate Types, Probed by Temperature Dependent Raman Scattering. *Nanoscale* **2014**, *6* (9), 4920–4927.

[93] Gosvami, N. N.; Bares, J. A.; Mangolini, F.; Konicek, A. R.; Yablon, D. G.; Carpick, R. W. Mechanisms of Antiwear Tribofilm Growth Revealed in Situ by Single-Asperity Sliding Contacts. *Science* **2015**, *348* (6230), 102–106.

[94] Martin, J. M.; Onodera, T.; Minfray, C.; Dassenoy, F.; Miyamoto, A. The Origin of

Anti-Wear Chemistry of ZDDP. *Faraday Discuss.* **2012**, *156*, 311.

[95] Spikes, H. The History and Mechanisms of ZDDP. *Tribology Letters* **2004**, *17* (3), 469–489.

[96] Martin, J.; Grossiord, C.; Varlot, K.; Vacher, B.; Igarashi, J. Synergistic effects in binary systems of lubricant additives: a chemical hardness approach. *Tribology Letters* **2000**, *8* (4), 193–201.

[97] Minfray, C.; Martin, J. M.; Barros, M. I. D.; Mogne, T. L.; Kersting, R.; Hagenhoff, B. Chemistry of ZDDP Tribofilm by ToF-SIMS. *Tribol. Lett.* **2004**, *17* (3), 351–357.

[98] Onodera, T.; Martin, J. M.; Minfray, C.; Dassenoy, F.; Miyamoto, A. Antiwear Chemistry of ZDDP: Coupling Classical MD and Tight-Binding Quantum Chemical MD Methods (TB-QCMD). *Tribol. Lett.* **2013**, *50* (1), 31–39.

[99] Martin, J. M. Antiwear mechanisms of zinc dithiophosphate: a chemical hardness approach. *Tribol. Lett.* **1999**, *6* (1), 1–8.

[100] Salinas Ruiz, V. R.; Kuwahara, T.; Galipaud, J.; Masenelli-Varlot, K.; Hassine, M. B.; Héau, C.; Stoll, M.; Mayrhofer, L.; Moras, G.; Martin, J. M.; Moseler, M.; De Barros Bouchet, MI. Interplay of Mechanics and Chemistry Governs Wear of Diamond-like Carbon Coatings Interacting with ZDDP-Additivated Lubricants. *Nat. Commun*. **2021**, *12* (1), 4550.

[101] Vengudusamy, B.; Green, J. H.; Lamb, G. D.; Spikes, H. A. Durability of ZDDP Tribofilms Formed in DLC/DLC Contacts. *Tribol. Lett.* **2013**, *51* (3), 469–478.

[102] Ueda, M.; Kadiric, A.; Spikes, H. ZDDP Tribofilm Formation on Non-Ferrous Surfaces. *Tribology Online* **2020**, *15* (5), 318–331.

[103] Haque, T.; Morina, A.; Neville, A. Influence of Friction Modifier and Antiwear Additives on the Tribological Performance of a Non-Hydrogenated DLC Coating. *Surface and Coatings Technology* **2010**, *204* (24), 4001–4011.

[104] Vengudusamy, B.; Green, J. H.; Lamb, G. D.; Spikes, H. A. Tribological Properties of Tribofilms Formed from ZDDP in DLC/DLC and DLC/Steel Contacts. *Tribology International* **2011**, *44* (2), 165–174.

[105] Sánchez-López, J. C.; Erdemir, A.; Donnet, C.; Rojas, T. C. Friction-Induced Structural Transformations of Diamondlike Carbon Coatings under Various Atmospheres. *Surface and Coatings Technology* **2003**, *163–164*, 444–450.

[106] Grischke, M.; Hieke, A.; Morgenweck, F.; Dimigen, H. Variation of the Wettability of DLC-Coatings by Network Modification Using Silicon and Oxygen. *Diamond and Related Materials* **1998**, *7* (2–5), 454–458.

[107] Kalin, M.; Velkavrh, I.; Vižintin, J.; Ožbolt, L. Review of Boundary Lubrication

Mechanisms of DLC Coatings Used in Mechanical Applications. *Meccanica* **2008**, *43* (6), 623–637.

[108] Yasuda, Y.; Kano, M.; Mabuchi, Y.; Abou, S. Research on Diamond-Like Carbon Coatings for Low-Friction Valve Lifters; 2003; pp 2003-01–1101.

[109] Mabuchi, Y.; Hamada, T.; Izumi, H.; Yasuda, Y.; Kano, M. The Development of Hydrogen-Free DLC-Coated Valve-Lifter. *SAE Transactions* **2007**, *116*, 788–794.

[110] De Barros Bouchet, MI.; Martin, J. M.; Le-Mogne, T.; Vacher, B. Boundary Lubrication Mechanisms of Carbon Coatings by MoDTC and ZDDP Additives. *Tribology International* **2005**, *38* (3), 257–264.

[111] Equey, S.; Roos, S.; Mueller, U.; Hauert, R.; Spencer, N. D.; Crockett, R. Tribofilm Formation from ZnDTP on Diamond-like Carbon. *Wear* **2008**, *264* (3–4), 316–321.

[112] Shah, A. V.; Meier, J.; Vallat-Sauvain, E.; Wyrsch, N.; Kroll, U.; Droz, C.; Graf, U. Material and Solar Cell Research in Microcrystalline Silicon. *Solar Energy Materials and Solar Cells* **2003**, *78* (1–4), 469–491.

[113] Filonovich, S. A.; Águas, H.; Busani, T.; Vicente, A.; Araújo, A.; Gaspar, D.; Vilarigues, M.; Leitão, J.; Fortunato, E.; Martins, R. Hydrogen Plasma Treatment of Very Thin P-Type Nanocrystalline Si Films Grown by RF-PECVD in the Presence of $B(CH_3)_3$. *Science and Technology of Advanced Materials* **2012**, *13* (4), 045004.

[114] Matsumura, H. Formation of Silicon-Based Thin Films Prepared by Catalytic Chemical Vapor Deposition (Cat-CVD) Method. *Jpn. J. Appl. Phys.* **1998**, *37* (Part 1, No. 6A), 3175–3187.

[115] Klein, S.; Finger, F.; Carius, R.; Dylla, T.; Rech, B.; Grimm, M.; Houben, L.; Stutzmann, M. Intrinsic Microcrystalline Silicon Prepared by Hot-Wire Chemical Vapour Deposition for Thin Film Solar Cells. *Thin Solid Films* **2003**, *430* (1–2), 202–207.

[116] Abe, Y.; Kawashima, S.; Fukushima, A.; Lu, Y.; Takeda, K.; Kondo, H.; Ishikawa, K.; Sekine, M.; Hori, M. Impact of Hydrogen Radical-Injection Plasma on Fabrication of Microcrystalline Silicon Thin Film for Solar Cells. *Journal of Applied Physics* **2013**, *113* (3), 033304.

[117] Yang, Y. H.; Abelson, J. R. Growth of Polycrystalline Silicon at 470 °C by Magnetron Sputtering onto a Sputtered Mc-hydrogenated Silicon Seed Layer. *Appl. Phys. Lett.* **1995**, *67* (24), 3623–3625.

[118] Makihara, H.; Tabata, A.; Suzuoki, Y.; Mizutani, T. Effect of the Hydrogen Partial Pressure Ratio on the Properties of Mc-Si:H Films Prepared by Rf Magnetron Sputtering. *Vacuum* **2000**, *59* (2–3), 785–791.

[119] Gerbi, J. E.; Voyles, P. M.; Treacy, M. M. J.; Gibson, J. M.; Abelson, J. R. Increasing Medium-Range Order in Amorphous Silicon with Low-Energy Ion

Bombardment. *Appl. Phys. Lett.* **2003**, *82* (21), 3665–3667.

[120] Jun, S.-I.; Rack, P. D.; McKnight, T. E.; Melechko, A. V.; Simpson, M. L. Direct-Current Substrate Bias Effects on Amorphous Silicon Sputter-Deposited Films for Thin Film Transistor Fabrication. *Appl. Phys. Lett.* **2005**, *87* (13), 132108.

[121] Shin, K. S.; Choi, Y. S.; Choi, I. S.; Setsuhara, Y.; Han, J. G. Nano-Crystalline Silicon Thin Films Grown by the Inductively Coupled Plasma Assisted CFUBM at Low Temperature. *Surface and Coatings Technology* **2010**, *205*, S227–S230.

[122] Fenske, F.; Reinig, P.; Selle, B.; Fuhs, W. Pulse-Sputter Deposition of Highly <100>-Oriented Crystalline Silicon Films. *Surface and Coatings Technology* **2003**, *174–175*, 801–804.

[123] Gerbi, J. E.; Abelson, J. R. Low Temperature Magnetron Sputter Deposition of Polycrystalline Silicon Thin Films Using High Flux Ion Bombardment. *Journal of Applied Physics* **2007**, *101* (6), 063508.

[124] Sivakumar, R.; Kumar, M.; Sanjeeviraja, C.; Som, T. Tuning Electro-Optical Properties of Pulsed Dc Magnetron Sputtered Indium Tin Oxide Thin Films: Effects of Pulsing Frequency and Annealing. *J Mater Sci: Mater Electron* **2017**, *28* (2), 1409–1418.

[125] Shin, K.; Acri, T.; Geary, S.; Salem, A. K. Biomimetic Mineralization of Biomaterials Using Simulated Body Fluids for Bone Tissue Engineering and Regenerative Medicine. *Tissue Engineering Part A* **2017**, *23* (19–20), 1169–1180.

[126] Senouci, D.; Baghdad, R.; Belfedal, A.; Chahed, L.; Portier, X.; Charvet, S.; Kim, K. H.; Roca i Cabarrocas, P.; Zellama, K. Hydrogen Related Crystallization in Intrinsic Hydrogenated Amorphous Silicon Films Prepared by Reactive Radiofrequency Magnetron Sputtering at Low Temperature. *Thin Solid Films* **2012**, *522*, 186–192.

[127] Smit, C.; van Swaaij, R. A. C. M. M.; Donker, H.; Petit, A. M. H. N.; Kessels, W. M. M.; van de Sanden, M. C. M. Determining the Material Structure of Microcrystalline Silicon from Raman Spectra. *Journal of Applied Physics* **2003**, *94* (5), 3582–3588.

[128] Jugdersuren, B.; Kearney, B. T.; Culbertson, J. C.; Chervin, C. N.; Katz, M. B.; Stroud, R. M.; Liu, X. The Effect of Ultrasmall Grain Sizes on the Thermal Conductivity of Nanocrystalline Silicon Thin Films. *Commun Phys* **2021**, *4* (1), 169.

[129] Downes, A.; Elfick, A. Raman Spectroscopy and Related Techniques in Biomedicine. *Sensors* **2010**, *10* (3), 1871–1889.

[130] Chen, X.; Zhang, C.; Kato, T.; Yang, X. A.; Wu, S.; Wang, R.; Nosaka, M.; Luo, J. B. Evolution of Tribo-Induced Interfacial Nanostructures Governing Superlubricity in a-C:H and a-C:H:Si Films. *Nat. Commun.* **2017,** *8,* 1675.

[131] Zhang, X.; Schneider, R.; Müller, E.; Gerthsen, D. Practical Aspects of the Quantification of sp^2-hybridized Carbon Atoms in Diamond-Like Carbon by Electron

Energy Loss Spectroscopy. *Carbon* **2016**, *102*, 198-207.

[132] Larkin, P. J. Infrared and Raman Spectroscopy: Principles and Spectral Interpretation. Elsevier: Waltham, MA, **2011**.

[133] Chu, P. K.; Li, L. Characterization of Amorphous and Nanocrystalline Carbon Films. *Mater. Chem. Phys.* **2006,** *96*, 253-277.

[134] Liang, H.; Kaufman, F.; Sevilla, R.; Anjur, S. Wear Phenomena in Chemical-Mechanical Polishing. *Wear* **1997,** *211*, 271-279.

[135] Zhao, Y. W.; Chang, L. A Micro-Contact and Wear Model for Chemical-Mechanical Polishing of Silicon Wafers. *Wear* **2002,** *252*, 220-226.

[136] Lu, X.; Yao, K.; Ouyang, J.; Tian, Y. Tribological Characteristics and Tribo-Chemical Mechanisms of Al-Mg-Ti-B Coatings under Water-Glycol Lubrication. *Wear* **2015,** *326-327*, 68-73.

[137] Xu, J.; Chen, X.; Grutzmacher, P.; Rosenkranz, A.; Li, J.; Jin, J.; Zhang, C.; Luo, J. Tribochemical Behaviors of Onion-Like Carbon Films as High-Performance Solid Lubricants with Variable Interfacial Nanostructures. *ACS Appl. Mater. Interfaces* **2019,** *11(28),* 25535-25546.

[138] Manimunda, P; Al-Azizi, A; Kim, S. H.; Chromik, R. R. Shear-Induced Structural Changes and Origin of Ultralow Friction of Hydrogenated Diamond-like Carbon (DLC) in Dry Environment. *ACS Appl. Mater. Interfaces* **2017,** *9,* 16704-16714.

[139] Kosarieh, S.; Morina, A.; Flemming, J.; Lainé, E.; Neville, A. Wear Mechanisms of Hydrogenated DLC in Oils Containing MoDTC. *Tribol Lett* **2016**, *64* (1), 4.

[140] Al-Jeboori, Y.; Kosarieh, S.; Morina, A.; Neville, A. Investigation of Pure Sliding and Sliding/Rolling Contacts in a DLC/Cast Iron System When Lubricated in Oils Containing MoDTC-Type Friction Modifier. *Tribology International* **2018**, *122*, 23–37.

[141] Topolovec-Miklozic, K.; Lockwood, F.; Spikes, H. Behaviour of Boundary Lubricating Additives on DLC Coatings. *Wear* **2008**, *265* (11–12), 1893–1901.

[142] Morina, A.; Neville, A.; Priest, M.; Green, J. H. ZDDP and MoDTC Interactions in Boundary Lubrication—The Effect of Temperature and ZDDP/MoDTC Ratio. *Tribology International* **2006**, *39* (12), 1545–1557.

[143] Neville, A.; Morina, A.; Haque, T.; Voong, M. Compatibility between Tribological Surfaces and Lubricant Additives—How Friction and Wear Reduction Can Be Controlled by Surface/Lube Synergies. *Tribology International* **2007**, *40* (10–12), 1680–1695.

[144] Gesheva, K.; Szekeres, A.; Ivanova, T. Optical Properties of Chemical Vapor Deposited Thin Films of Molybdenum and Tungsten Based Metal Oxides. *Solar Energy*

Materials and Solar Cells **2003**, *76* (4), 563–576.

[145] Sian, T. S.; Reddy, G. B. Optical, Structural and Photoelectron Spectroscopic Studies on Amorphous and Crystalline Molybdenum Oxide Thin Films. *Solar Energy Materials and Solar Cells* **2004**, *82* (3), 375–386.

[146] Al-Kuhaili, M. F.; Saleem, M.; Durrani, S. M. A. Optical Properties of Iron Oxide (α-Fe2O3) Thin Films Deposited by the Reactive Evaporation of Iron. *Journal of Alloys and Compounds* **2012**, *521*, 178–182.

[147] Wang, H.; Shen, J.; Qian, J. Magneto-Optic Faraday Rotation of Sputtered γ-Fe2O3 Film. *Journal of Magnetism and Magnetic Materials* **1988**, *73* (1), 103–105.

[148] De Temmerman, G.; Ley, M.; Boudaden, J.; Oelhafen, P. Study of Optical Properties of MoxC1−x Films. *Journal of Nuclear Materials* **2005**, *337–339*, 956–959.

[149] Feng, W.; Wang, R.; Zhou, Y.; Ding, L.; Gao, X.; Zhou, B.; Hu, P.; Chen, Y. Ultrathin Molybdenum Carbide MXene with Fast Biodegradability for Highly Efficient Theory-Oriented Photonic Tumor Hyperthermia. *Adv. Funct. Mater.* **2019**, *29* (22), 1901942.

[150] Dashora, A.; Ahuja, U.; Venugopalan, K. Electronic and Optical Properties of MoS2 (0001) Thin Films: Feasibility for Solar Cells. *Computational Materials Science* **2013**, *69*, 216–221.

[151] Min, Y.; He, G.; Xu, Q.; Chen, Y. Dual-Functional MoS2 Sheet-Modified CdS Branch-like Heterostructures with Enhanced Photostability and Photocatalytic Activity. *J. Mater. Chem. A* **2014**, *2* (8), 2578-2584.

[152] Lee, C.; Yan, H.; Brus, L. E.; Heinz, T. F.; Hone, J.; Ryu, S. Anomalous Lattice Vibrations of Single- and Few-Layer MoS_2. *ACS Nano* **2010**, *4* (5), 2695–2700.

[153] Li, X.; Zhang, J.; Wang, R.; Huang, H.; Xie, C.; Li, Z.; Li, J.; Niu, C. In Situ Synthesis of Carbon Nanotube Hybrids with Alternate MoC and MoS_2 to Enhance the Electrochemical Activities of MoS_2. *Nano Lett.* **2015**, *15* (8), 5268–5272.

[154] Spikes, H. Stress-Augmented Thermal Activation: Tribology Feels the Force. *Friction* **2018**, *6* (1), 1–31.

[155] Yin, X.; Wu, F.; Chen, X.; Xu, J.; Wu, P.; Li, J.; Zhang, C.; Luo, J. Graphene-Induced Reconstruction of the Sliding Interface Assisting the Improved Lubricity of Various Tribo-Couples. *Materials & Design* **2020**, *191*, 108661.

[156] Xu, J.; Luo, T.; Chen, X.; Zhang, C.; Luo, J. Nanostructured Tribolayer-Dependent Lubricity of Graphene and Modified Graphene Nanoflakes on Sliding Steel Surfaces in Humid Air. *Tribology International* **2020**, *145*, 106203.

[157] Zhao, J.; Huang, Y.; Li, Y.; Gao, T.; Dou, Z.; Mao, J.; Wang, H.; He, Y.; Li, S.;

Luo, J. Superhigh-Exfoliation Graphene with a Unique Two-Dimensional (2D) Microstructure for Lubrication Application. *Applied Surface Science* **2020**, *513*, 145608.

[158] Xu, X.; Xu, Z.; Sun, J.; Tang, G.; Su, F. In Situ Synthesizing Carbon-Based Film by Tribo-Induced Catalytic Degradation of Poly-α-Olefin Oil for Reducing Friction and Wear. *Langmuir* **2020**, *36* (35), 10555–10564.

[159] Argibay, N.; Babuska, T. F.; Curry, J. F.; Dugger, M. T.; Lu, P.; Adams, D. P.; Nation, B. L.; Doyle, B. L.; Pham, M.; Pimentel, A.; Mowry, C.; Hinkle, A. R.; Chandross, M. In-Situ Tribochemical Formation of Self-Lubricating Diamond-like Carbon Films. *Carbon* **2018**, *138*, 61–68.

[160] Rusanov, A.; Nevshupa, R.; Fontaine, J.; Martin, J.-M.; Le Mogne, T.; Elinson, V.; Lyamin, A.; Roman, E. Probing the Tribochemical Degradation of Hydrogenated Amorphous Carbon Using Mechanically Stimulated Gas Emission Spectroscopy. *Carbon* **2015**, *81*, 788–799.

[161] Ji, L.; Wang, J.; Teng, X.; Dong, H.; He, X.; Chen, Z. N,P-Doped Molybdenum Carbide Nanofibers for Efficient Hydrogen Production. *ACS Appl. Mater. Interfaces* **2018**, *10* (17), 14632–14640.

[162] Lv, C.; Huang, Z.; Yang, Q.; Wei, G.; Chen, Z.; Humphrey, M. G.; Zhang, C. Ultrafast Synthesis of Molybdenum Carbide Nanoparticles for Efficient Hydrogen Generation. *J. Mater. Chem. A* **2017**, *5* (43), 22805–22812.

[163] Alazizi, A.; Draskovics, A.; Ramirez, G.; Erdemir, A.; Kim, S. H. Tribochemistry of Carbon Films in Oxygen and Humid Environments: Oxidative Wear and Galvanic Corrosion. *Langmuir* **2016**, *32* (8), 1996–2004.

[164] Shi, J.; Gong, Z.; Wang, C.; Zhang, B.; Zhang, J. Tribological Properties of Hydrogenated Amorphous Carbon Films in Different Atmospheres. *Diamond and Related Materials* **2017**, *77*, 84–91.

[165] Afsharpour, M.; Mahjoub, A.; Amini, M. M. A Nano-Hybrid of Molybdenum Oxide Intercalated by Dithiocarbamate as an Oxidation Catalyst. *J Inorg Organomet Polym* **2008**, *18* (4), 472–476.

[166] Wang, D.-Y.; Chang, C.-L.; Ho, W.-Y. Oxidation Behavior of Diamond-like Carbon Films. *Surface and Coatings Technology* **1999**, *120–121*, 138–144.

[167] Al-Azizi, A. A.; Eryilmaz, O.; Erdemir, A.; Kim, S. H. Surface Structure of Hydrogenated Diamond-like Carbon: Origin of Run-In Behavior Prior to Superlubricious Interfacial Shear. *Langmuir* **2015**, *31* (5), 1711–1721.

[168] Fontaine, J.; Le Mogne, T.; Loubet, J. L.; Belin, M. Achieving Superlow Friction with Hydrogenated Amorphous Carbon: Some Key Requirements. *Thin Solid Films* **2005**, *482* (1–2), 99–108.

[169] Yang, M.; Marino, M. J.; Bojan, V. J.; Eryilmaz, O. L.; Erdemir, A.; Kim, S. H. Quantification of Oxygenated Species on a Diamond-like Carbon (DLC) Surface. *Applied Surface Science* **2011**, *257* (17), 7633–7638.

[170] Shi, J.; Gong, Z.; Wang, Y.; Gao, K.; Zhang, J. Friction and Wear of Hydrogenated and Hydrogen-Free Diamond-like Carbon Films: Relative Humidity Dependent Character. *Applied Surface Science* **2017**, *422*, 147–154.

[171] Kassim, K. A. M.; Tokoroyama, T.; Murashima, M.; Umehara, N. The Wear Classification of MoDTC-Derived Particles on Silicon and Hydrogenated Diamond-like Carbon at Room Temperature. *Tribology International* **2020**, *147*, 106176.

[172] Yoshida, Y.; Kunitsugu, S. Friction Wear Characteristics of Diamond-like Carbon Coatings in Oils Containing Molybdenum Dialkyldithiocarbamate Additive. *Wear* **2018**, *414–415*, 118–125.

[173] Afsharpour, M.; Mahjoub, A.; Amini, M. M. A Nano-Hybrid of Molybdenum Oxide Intercalated by Dithiocarbamate as an Oxidation Catalyst. *J. Inorg. Organomet. Polym.* **2008**, *18* (4), 472–476.

[174] Jäger, C.; Henning, Th.; Schlögl, R.; Spillecke, O. Spectral Properties of Carbon Black. *Journal of Non-Crystalline Solids* **1999**, *258* (1–3), 161–179.

[175] Bruley, J.; Madakson, P.; Liu, J. C. Characterization of CVD-Hydrogenated Diamondlike Thin Films on Silicon by EELS, RBS/Channeling and Nuclear Reaction Analysis. *Nuclear Instruments and Methods in Physics Research Section B: Beam Interactions with Materials and Atoms* **1990**, *45* (1–4), 618–621.

[176] Zong, E.; Wei, D.; Wan, H.; Zheng, S.; Xu, Z.; Zhu, D. Adsorptive Removal of Phosphate Ions from Aqueous Solution Using Zirconia-Functionalized Graphite Oxide. *Chemical Engineering Journal* **2013**, *221*, 193–203.

[177] Dreyer, D. R.; Jarvis, K. A.; Ferreira, P. J.; Bielawski, C. W. Graphite Oxide as a Carbocatalyst for the Preparation of Fullerene-Reinforced Polyester and Polyamide Nanocomposites. *Polym. Chem.* **2012**, *3* (3), 757.

[178] Equey, S.; Roos, S.; Mueller, U.; Hauert, R.; Spencer, N. D.; Crockett, R. Reactions of Zinc-Free Anti-Wear Additives in DLC/DLC and Steel/Steel Contacts. *Tribology International* **2008**, *41* (11), 1090–1096.

[179] Ward, L.; Junge, F.; Lampka, A.; Dobbertin, M.; Mewes, C.; Wienecke, M. The Effect of Bias Voltage and Gas Pressure on the Structure, Adhesion and Wear Behavior of Diamond Like Carbon (DLC) Coatings with Si Interlayers. *Coatings* **2014**, *4* (2), 214–230.

[180] Taylor, L. J.; Spikes, H. A. Friction-Enhancing Properties of ZDDP Antiwear Additive: Part I—Friction and Morphology of ZDDP Reaction Films. *Tribology*

Transactions **2003**, *46* (3), 303–309.

[181] Arola, D.; Williams, C. Estimating the Fatigue Stress Concentration Factor of Machined Surfaces. *International Journal of Fatigue* **2002**, *24* (9), 923–930.

[182] Leiro, A.; Kankanala, A.; Vuorinen, E.; Prakash, B. Tribological Behaviour of Carbide-Free Bainitic Steel under Dry Rolling/Sliding Conditions. *Wear* **2011**, *273* (1), 2–8.

[183] Teles, V. C.; de Mello, J. D. B.; da Silva, W. M. Abrasive Wear of Multilayered/Gradient CrAlSiN PVD Coatings: Effect of Interface Roughness and of Superficial Flaws. *Wear* **2017**, *376–377*, 1691–1701.

[184] Marino, M. Understanding Run-In Behavior of Diamond-Like Carbon Friction. *Langmuir* **2011,** *27,* 12702-12708.

[185] Kim, H. I.; Lince, J. R.; Eryilmaz, O. L.; Erdemir, A. Environmental Effects on the friction of Hydrogenated DLC Films. *Tribol. Lett.* **2006,** *21,* 53-58.

[186] Schenk, A.; Winter, B.; Biener, J.; Lutterloh, C.; Schubert, U. A.; Kuppers, J. Growth and Thermal Decomposition of Ultrathin Ion-Beam Deposited C:H Films. *J. Appl. Phys.* **1995**, *77(6),* 2462-2473.

[187] Ristein, J.; Stief, R. T.; Ley, L.; Beyer, W. A Comparative Analysis of a-C:H by Infrared Spectroscopy and Mass Selected Thermal Effusion. *J. Appl. Phys.* **1998,** *84(7),* 3836-3847.

[188] Malhotra, M.; Kumar, S. Thermal Gas Effusion from Diamond-Like Carbon Films. *Diamond Relat. Mater.* **1997,** *6(12),* 1830-1835.

[189] Jiang, X.; Beyer, W.; Reichelt, K. Gas Evolution from Hydrogenated Amorphous Carbon Films. *J. Appl. Phys.* **1990,** *68(3),* 1378-1380.

[190] Zecho, T.; Brandner, B. D.; Biener, J.; Kuppers, J. Hydrogen-Induced Chemical Erosion of a-C:H Thin Films: Product Distribution and Temperature Dependence. *J. Phys. Chem. B* **2001,** *105(26),* 6194-6201.

[191] Erdemir, A.; Donnet, C. Tribology of Diamond-Like Carbon Films: Recent Progress and Future Prospects. *J. Phys. D Appl. Phys.* **2006,** *39,* R311-R327.

[192] Williamson, D. L.; Mahan, A. H.; Nelson, B. P.; Crandall, R. S. Microvoids in Amorphous $Si_{1-x}C_x$:H Alloys Studied by Small-Angle X-Ray Scattering. *Appl. Phys. Lett.* **1989,** *55,* 783-785.

[193] Prado, R. J.; Bittencourt, D. R. S.; Tabacniks, M. H.; Fantini, M. C. A.; Carreño, M. N. P.; Pereyra, I. Distribution of Pores in *a*-$Si_{1-x}C_x$:H Thin Films. *J Appl Crystallogr* **1997**, *30* (5), 659–663.

[194] van Swaaij, R. A. C. M. M.; Berntsen, A. J. M.; van Sark, W. G. J. H. M.; Herremans, H.; Bezemer, J.; van der Weg, W. F. Local Structure and Bonding States in *a*-$Si_{1-x}C_x$:H. *Journal of Applied Physics* **1994**, *76* (1), 251–256.

[195] Mangolini, F.; Rose, F.; Hilbert, J.; Carpick, R. W. Thermally Induced Evolution of Hydrogenated Amorphous Carbon. *Appl. Phys. Lett.* **2013,** *103 (16),* 161605.

[196] Sattler, A.; Parkin, G. Cleaving Carbon-Carbon Bonds by Inserting Tungsten into Unstrained Aromatic Rings. *Nature* **2010,** *463 (7280),* 523-526.

[197] Jones, W. D. The Fall of the CC Bond. *Nature* **1993,** *364 (6439),* 676-677.

[198] Soltanahmadi, S.; Charpentier, T.; Nedelcu, I.; Khetan, V.; Morina, A.; Freeman, H. M.; Brown, A. P.; Brydson, R.; Eijk, M. C. P.; Neville, A. Surface Fatigue Behavior of a WC/aC:H Thin-Film and the Tribochemical Impact of Zinc Dialkyldithiophosphate. *ACS Appl. Mater. Interfaces* **2019,** *11,* 41676-41687.